STUDIES ON THE CHARACTERISTICS OF In_2O_3, $Ag_6Mo_{10}O_{33}$ AND Pd BASED MATERIALS TOWARDS SENSING DIFFERENT GASEOUS SPECIES

by

E. PRABHU

Enrolment No: CHEM02200804013

Indira Gandhi Centre for Atomic Research
Kalpakkam 603 102, Tamil Nadu, India

A thesis submitted to the
Board of Studies in Chemical Sciences
in partial fulfillment of requirements
for the Degree of

DOCTOR OF PHILOSOPHY

of

HOMI BHABHA NATIONAL INSTITUTE

August, 2015

Homi Bhabha National Institute

Recommendations of the Viva Voce Board

As members of the Viva Voce Board, we certify that we have read the dissertation prepared by **E. Prabhu** entitled **"Studies on the characteristics of In_2O_3, $Ag_6Mo_{10}O_{33}$ and Pd based materials towards sensing different gaseous species"** and recommend that it may be accepted as fulfilling the dissertation requirement for the Degree of Doctor of Philosophy.

Chairman: Dr. S. Anthonysamy Date:

Guide/Convener: Dr. T. Gnanasekaran Date:

Member: Dr. B. K. Panigrahi Date:

Member: Dr. K. Ananthasivan Date:

Member:Dr. V. Jayaraman Date:

Final approval and acceptance of this dissertation is contingent upon the candidate's submission of the final copies of the dissertation to HBNI.

I hereby certify that I have read this dissertation prepared under my direction and recommend that it may be accepted as fulfilling the dissertation requirement.

Date: Dr. T. Gnanasekaran

Place: (Guide / Convener)

STATEMENT BY AUTHOR

This dissertation has been submitted in partial fulfillment of requirements for an advanced degree at Homi Bhabha National Instituted (HBNI) and is deposited in the Library to be made available to borrowers under rules of the HBNI

Brief quotations from this dissertation are allowable without special permission, provided that accurate acknowledgement of source is made. Requests for permission for extended quotation from or reproduction of this manuscript in whole or in part may be granted by the Competent Authority of HBNI when in his or her judgment the proposed use of the material is in the interests of scholarship. In all other instances, however, permission must be obtained from the author.

E. Prabhu

DECLARATION

I, hereby declare that the investigation presented in the thesis entitled **“Studies on the characteristics of In_2O_3, $Ag_6Mo_{10}O_{33}$ and Pd based materials towards sensing different gaseous species”** submitted to **Homi Bhabha National Institute (HBNI)**, Mumbai, India for the award of **Doctor of Philosophy in Chemical Sciences** is the record of work has been carried out by me under the guidance of **Dr. T. Gnanasekaran**. The work is original and has not been submitted earlier as a whole or in part for a degree/diploma at this or any other Institution/University.

E. Prabhu

List of Publications

Journals

1. “Changes in carrier concentration and Debye length: Experimental evidence from van der Pauw Hall Measurements on NO_X sensing of In_2O_3”
   E. Prabhu , K.I. Gnanasekar, T.R. Ravindran, V. Jayaraman and T. Gnanasekaran,
   J. Electrochem. Soc., **169** (2014) B1 – B7.

2. “Preparation, characterization and NO_X sensing characteristics of sensor grade $CuInO_2$ thin films”
   E. Prabhu, K.I. Gnanasekar, V. Jayaraman, and T. Gnanasekaran, Mat. Sci. Forum 710, (2012) 727 – 732.

3. “Structural, electrical conductivity and transport studies on $Ag_6Mo_{10-X}W_XO_{33}$ (X = 0 – 1) – A class of silver ion conductors”
   E. Prabhu, K.I. Gnanasekar, V. Jayaraman and T. Gnanasekaran,
   J. Electrochem. Soc., 2015 (Under Review)

4. “Low temperature synthesis of metals and alloys of palladium and their hydrogen interaction behavior in argon”
   E. Prabhu, K.I. Gnanasekar, V. Jayaraman and T. Gnanasekaran.
   Int. J. Hydrogen Energy, 2015 (Manuscript under preparation)

5. “Analysis of Nano-structured In_2O_3 thin film NO_X sensor by AC impedance spectroscopy”
   C.R. Mariappan, **E. Prabhu**, K.I. Gnanasekar, V. Jayaraman & T. Gnanasekaran,
   IEEE Sensors 14, 3, (2014) 651 – 656

Published/Presented in National / International conferences / Symposia/ Workshops

1. "Selective detection of NH_3 by $Ag_6Mo_{10}O_{33}$ thick film by AC impedance spectroscopy"
   E. Prabhu, C.R. Mariappan, K.I. Gnanasekar, V. Jayaraman and T. Gnanasekaran, Proceedings of 1st International Symposium of Physics and Technology of Sensors, IEEE Xplore (2012)193-196

2. "Low temperature synthesis of Ni and Co substituted alloys of Pd and their hydrogen sensing characteristics"
   E. Prabhu, A. Sree Rama Murthy, I. Lakshmigandhan, Akash Singh, S. Murugesan, G. Panneerselvam, K.I. Gnanasekar, V. Jayaraman and T. Gnanasekaran, Proceedings of 2nd International Symposium of Physics and Technology of Sensors, IEEE Xplore (2015)83 – 87

3. In-situ Hall measurement study on In_2O_3 and its mechanism of NO_x sensing
   E. Prabhu, K.I. Gnanasekar, V. Jayaraman, T. R. Ravindran and T. Gnanasekaran
   IUMRS – ICA 2013, IISC, Bangalore 16 – 20 December 2013 (Best poster award)
   (Best paper award)

4. "Structural, electrical conductivity and transport studies on Ag6Mo10-xWxO33 (x = 0 – 1) – A class of silver ion conductors" **E. Prabhu**, K.I. Gnanasekar, V. Jayaraman and T. Gnanasekaran, Theme Meeting on Recent Trends in Materials Chemistry (RTMC-2013), VIT, Vellore, India, July 25 – 27, 2013. (Best oral presentation award)

5. Detection of reducing gases by $Ag_6Mo_{10}O_{33}$ thick film using impedance spectroscopy
   E. Prabhu, C.R. Mariappan, K.I. Gnanasekar ,V. Jayaraman and T. Gnanasekaran
   Chemistry Research Scholars Meet, IGCAR, Kalpakkam, 14 – 15 July 2011

With great pleasure I express my deep sense of gratitude
to my parents,
my wife and my son
and all my family members for
their constant help, affection, encouragement
and support
without which this thesis would not have come to this stage.

" If I have the belief
that I can do it,
I shall surely acquire
the capacity to do it
even if I may not have it
at the beginning "

Mahatma Gandhi

ACKNOWLEDGMENTS

I express my deepest gratitude to my research supervisor Dr. T. Gnanasekaran for giving me an opportunity to work in an exciting area. Without his insightful guidance and encouragement this thesis would never have been accomplished.

It gives me a great pleasure to express my deep sense of gratitude and thanks to Dr. V. Jayaraman and Dr. K.I. Gnanasekar for their concern, supervision and ever willing help in almost all aspects of my PhD work.

I would like to express my sincere thanks to my doctoral committee members Dr. S. Anthonysamy (Chairman), Dr. K.V.G. Kutty (Ex-Chairman), Dr. B.K. Panigrahi (member), Dr. K. Ananthasivan (member) for their technical assessment and suggestions.

My thanks to all my teachers who taught me various subjects at BARC training school, IGCAR. They helped me learning new concepts, which guided me to apply them in my research assignments.

I wish to record my sincere thanks to Dr. R. Asuvatharaman, Dr. G. Panneerselvam and Mr. Raja Madhavan for their continuous help in characterizing my samples using XRD.

My special thanks to Dr. R. Sudha, Dr. Shamima Hussain and Mr. Swapan Kumar Mahato, for their valuable help in doing surface morphology of the samples using SEM and EDX.

My special thanks to Mr. Sajal Ghosh and Dr. Rajesh Ganesan for helping in characterizing my samples in thermo gravimetric studies.

The cooperation rendered by Dr. S. Vijayalakshmi, Mr. J. K. Sekar, Mr. S. Sriram, Mrs. S. Annapoorani and Mrs. R. Uma Maheshwari in the analysis of my samples using AAS and ICPOES.

I profoundly thank my collaborators, Dr. T.R. Ravindran, for characterizing my samples using laser Raman spectroscopy and Dr. S. Murugesan and Dr. Aakash Singh for using the facility of PLD and thin film XRD.

I would like to thank Shri. K.A.S. Kutty, Shri. V. Suresh Kumar and their team for their continuous support in design and fabrication of mechanical facilities handled during my PhD period.

My appreciation to colleagues of Glass Blowing Facility, Chemistry Group, IGCAR for their skilled expertise in fabricating compact sensor facility which was used throughout of my PhD work.

I wish to acknowledge Dr. Chander shekar and Dr. Sulata Kumari Sahu for helping me in sending valuable literatures which are not available in IGCAR.

I thank Mr. A. Sree Rama Murthy, Mr. N. Sanil and Mr. N. Murugesan for their valuable scientific inputs throughout of this research period.

I would like to thank Mrs. P.C. Clinsha, Dr. Souman Das, Mr. Nair Afijith Ravindhranath, Mr. I. Lakshmi Gandhan, Mr. P. Madurai and Mr. M. Ravindhra Babu for their help and friendliness in the lab.

I thank all my colleagues, friends, research scholars of this centre, office staff who have helped me in various ways during this period.

I take immense pleasure in thanking Dr. R. Sridharan and Dr. M. Joseph for their valuable support.

I am grateful to Dr. P.R. Vasudeva Rao, Director, IGCAR for permitting me to use the various facilities of this centre to carry out this research work.

E. Prabhu

CONTENTS

CHAPTER 1

Introduction

CHAPTER 2

Experimental methods, principles and its applications

CHAPTER 3

Studies on interaction of In_2O_3 thin film towards NO_X to understand its interaction mechanism on the surface of In_2O_3 using Hall measurement & using AC impedance spectroscopy

CHAPTER 4

Preparation, characterization and gas sensing properties of $CuInO_2$ and $Cu_2In_2O_5$ thin films towards H_2, NH_3, PG and NO_X

CHAPTER 5

Preparation, characterization and sensing behavior of palladium, $Pd_{0.97}Ni_{0.03}$, $Pd_{0.93}Ni_{0.07}$, and $Pd_{0.91}Ni_{0.04}Co_{0.05}$ towards hydrogen at 300 K

CHAPTER 6

Studies on preparation and characterization of $Ag_6Mo_{10-X}W_XO_{33}$ (X = 0 – 2) and selective sensing behavior of $Ag_6Mo_{10}O_{33}$ thick film towards NH_3 by AC impedance technique

CHAPTER 7

Summary, conclusions and scope for future studies

SYNOPSIS

Clean air in the atmosphere is essential for the survival of life. Rapid industrialization and several natural processes release harmful chemicals to the ambient and pollute air, water and land. Use of fossil fuels and their inefficient combustion in industries and automobiles lead to the release of SO_2, CO, CO_2, NO, NO_2 and hydrocarbons to ambient air. Volcanic eruptions and vegetative decay also release gases like SO_2, H_2S, CH_4 and NH_3. Large quantities of gases like SO_2, H_2S and NH_3 are used in industrial processes and accidental release of these gases to ambient air will lead to severe pollution of air around these industries. In addition, H_2, H_2S and NH_3 can form explosive mixtures with oxygen in air and lead to undesirable consequences. Maximum permissible concentration of pollutants such as H_2S, NH_3, NO and NO_2 are in parts per million (ppm) range only and increase beyond these levels affects human health severely [1 – 8]. Hydrogen forms an explosive mixture with air when its concentration in the latter ranges between 4 and 75 %. Intense research and development activities are in progress for ensuring accident free industrial processes and to release the industrial and automobile exhausts to ambient only after their treatment. For continuous surveillance of the levels of these harmful gases in ambient air and also for detecting their accidental release, very sensitive analytical methods are needed. The conventional analytical instruments based on spectroscopic techniques (IR, UV and Visible radiations and mass), gas chromatography and electrochemical methods are capable of measuring trace levels of a single compound in a complex gas mixture with high precision and selectivity. However, these instruments are bulky, expensive and need preparation of the sample prior to its analysis and therefore cannot be easily deployed for mobile and field applications. Compact, portable, user-optimized and economic devices are needed for these applications.

In a Fast Breeder Reactor (FBR) circuit, hydrogen in argon cover gas needs to be monitored to detect any steam leak into liquid sodium under reactor start-up or low power operating conditions [9]. In the event of a steam leak in the steam generator of the reactor, sodium-water reaction would take place. This reaction, if not detected and stopped at its inception, could damage the steam generator itself. This detection is carried out by continuous monitoring of hydrogen evolved during sodium-water reaction which collects in argon cover gas over liquid sodium (and builds up from ppm level and could reach up to percentage). During operation of a hydrogen based fuel cell system, a leak of stored hydrogen gas into ambient air needs to be detected before it collects and reaches the explosive limits. Solid state chemical sensors with high selectivity and sensitivity towards hydrogen with large dynamic range are needed to meet these requirements.

Solid state chemical sensors are based on several different principles viz. optical, electrochemical, chemoresistive, gravimetric and magnetic. In chemoresistive sensors, electrical conductivity of the sensor material (which is generally in the form of a thin or thick film) is modulated by the presence and absence of a specific chemical that comes in contact with it. Semi conducting metal oxides is the popular choice for the sensor material and are being investigated for detecting the presence of trace level pollutants (which can be oxidizing gases such as NO, NO_2 or reducing gases such as H_2, H_2S, CO, CH_4 and NH_3) in ambient air or in other process gases [10]. Some of the challenges in developing sensors based on these metal oxides stem from their poor selectivity, effect of humidity on their performance and long-term drift in their output. With suitable choice of the oxide and optimized configuration and operating parameters of the sensor, these limitations can be overcome. When a chemical analyte interacts with the sensor material, processes like adsorption, diffusion, swelling and chemical reactions take place either on the surface or in bulk of the material. Understanding these intermediate processes would enable a proper choice of the sensor material to be made. It would also enable optimizing the operating parameters of the sensor so that along with high sensitivity and selectivity, fast response and recovery times can be achieved.

The major objective of this thesis is to investigate the sensing characteristics of indium oxide in well characterized thin film configuration towards NO and NO_2 (collectively called as NOx) and other pollutant gases. Intermediates formed on the surface of the film during its interaction with NO_X at temperatures between 450 and 698 K were identified by different techniques to understand the gas sensing mechanism. In addition, ternary oxides in the system Cu – In – O were also investigated. Copper oxide-indium oxide system forms two compounds, namely $CuInO_2$ $\left(=\frac{1}{2}Cu_2O.\frac{1}{2}In_2O_3\right)$ and $Cu_2In_2O_5$ $\left(=2CuO.1In_2O_3\right)$ involving +2 and +1 oxidation states of copper. Characteristics of the thin films of these compounds towards sensing trace levels of oxidizing and reducing gaseous pollutants were studied. Silver decamolybdate, $Ag_6Mo_{10}O_{33}$ has been earlier recognized as a good candidate material for sensing trace levels of NH_3. It possesses significant Ag^+ ion conductivity. However, measuring its electrical resistivity by common two probe technique leads to polarization due to steady transport of silver between the electrodes and drift in the sensor output. Measuring the resistance of $Ag_6Mo_{10}O_{33}$ thick film by alternating current (AC) technique and sensing pollutants such as NH_3, H_2, and petroleum gas (PG) were carried out. The effects of tungsten substitution in the electrical properties of $Ag_6Mo_{10-X}W_XO_{33}$ were investigated and discussed.

Metals such as Th, Ce, Zr, Ti and Pd are strong adsorbers of hydrogen and their physical properties such as density, electrical conductivity significantly vary due to the adsorption of hydrogen [11]. Among these metals, palladium has a high diffusion coefficient for hydrogen at near ambient temperatures (hence high adsorption and desorption rates) and its ability to dissolve large amounts of hydrogen before the precipitation of a second phase [12]. Hence, palladium and its alloys have been extensively investigated for detecting hydrogen in both trace as well as in percentage levels [13 – 15]. As part of this work, thin films of Pd, Pd-Ni and Pd-Ni-Co alloys were made and their characteristics of sensing hydrogen from percentage level down to ppm were studied.

The thesis is divided into seven chapters and a brief overview of individual chapters is presented below:

Chapter 1 : Introduction

This chapter briefs the need for a sensor, definition of a sensor and description of hazardous, toxic and flammable properties of gases and vapors. It also describes the principles behind different methods employed in the sensing of gases in the ambient. This chapter briefs the working principle of resistive materials (metal/metal oxide), their interaction with the pollutants, the advantages and their disadvantages in deploying them [8 – 10]. The objectives of the present investigations are listed below:

1. Studies on exposure of In_2O_3 thin film to NO_X to understand their interaction as a function of temperature by using AC impedance studies on In_2O_3.

2. Investigations on the interaction behavior of $Cu_2In_2O_5$ and $CuInO_2$ towards

flammable and hazardous gases.

3. Preparation, characterization and sensing behavior of palladium, $Pd_{1-x}Ni_x$ (0.03 – 0.10) and $Pd_{1-x-y}Ni_xCo_y$ (x = y = 0.05) towards hydrogen at 300 K.

4. Preparation and characterization of $Ag_6Mo_{10-X}W_XO_{33}$ (x = 0 – 2) and investigations on the selective sensing of $Ag_6Mo_{10}O_{33}$ thick film towards NH_3 by using the AC impedance technique.

Chapter 2 : Experimental methods, Principles and its Applications

This chapter describes the working principle of various methods employed in synthesizing the metals, alloys and metal oxides. This chapter provides a brief account of various characterization techniques like XRD, van der Pauw and Hall measurement, SEM, AFM, AC impedance spectroscopy and laser Raman spectroscopy employed for material characterization. The chapter also briefs various techniques and their principles engaged for the fabrication of materials investigated as gas sensing. The chapter covers the design and fabrication of facilities required for carrying out conductivity, ion transport studies and gas interaction studies of the materials taken for investigations.

Chapter 3 : Studies on interaction of In_2O_3 thin film towards NO_X to understand its interaction mechanism using Hall measurement and Laser Raman and AC impedance spectroscopic techniques

This chapter mainly covers the fundamental understanding of a metal oxide during its interaction with NO_X. At the outset, the deposition of In_2O_3 thin film by

PLD, its characterization using XRD and by laser Raman spectroscopy is presented in this chapter. The design, fabrication and installation of a high temperature van der Pauw and Hall measurement facility developed in-house for measuring conductivity (four probe), carrier concentrations and mobility of charge carriers in In_2O_3 thin film in the ambient of air and air containing different concentrations of NO_X in the temperature range 373 and 673 K are also described. The adsorption behavior of oxides of nitrogen on the surface of In_2O_3 thin film at different temperatures using laser Raman spectroscopy are elucidated. This chapter provides the evidence for the variation in the carrier concentration as well as changes in their mobility in In_2O_3 thin film caused by the strong electron affinity of NO_X with the chemisorbed oxygen. This chapter also discusses the variation in the dielectric property of In_2O_3 thin film brought about by its interaction with NO_X by using the AC impedance technique.

Chapter 4 : Preparation, characterization and gas sensing properties of $CuInO_2$ and $Cu_2In_2O_5$ thin films towards H_2, NH_3, PG and NO_X

This chapter mainly deals with selective sensing behavior shown by $CuInO_2$, a p-type semi-conducting metal oxide towards NO_X. The chapter highlights the use of p-type and n-type metal oxides for distinguishing reducing and oxidizing gases. This chapter discusses the deposition of a thin film of $CuInO_2$ under controlled oxygen pressure by using PLD at 823 K. It has been reported that the synthesis of $CuInO_2$ by solid state reaction is not thermodynamically feasible. This chapter elaborates the characterization of $Cu_2In_2O_5$ and $CuInO_2$ by using XRD, thermal analysis, AC impedance, AFM and XPS. The results pertaining to the studies on the interaction of H_2, NO_X, NH_3 and PG with $Cu_2In_2O_5$ and $CuInO_2$ thin films in the temperature range

448 and 698 K are discussed. The response of $CuInO_2$ thin film to the variation in the concentration of NO_X (2 to 24 ppm) was found to be linear. On the other hand $Cu_2In_2O_5$ showed a cross sensitivity with all the gases mentioned above.

Chapter 5 : Preparation, characterization and sensing behavior of palladium, $Pd_{0.97}Ni_{0.03}$, $Pd_{0.93}Ni_{0.07}$, and $Pd_{0.91}Ni_{0.04}Co_{0.05}$ towards hydrogen at 300 K

The main focus of this chapter is on the identification of palladium based alloys for sensing hydrogen at 300 K. Conditions for the preparation of nano palladium, nickel substituted palladium ($Pd_{1-X}Ni_X$ [x = 0, 0.05 & 0.1]) and cobalt and nickel substituted palladium ($Pd_{1-X-Y}Ni_XCo_Y$ [x = y = 0.05]) using low temperature reduction technique were optimized and presented. The nano-powders synthesized were characterized by using XRD, SEM, EDAX and AFM. This chapter discusses the thin film deposition of palladium and the alloys by using PLD. The interaction of these thin films with argon containing 2000 to 20000 ppm of hydrogen was studied by a four probe resistivity technique. The sensitivity of alloy thin films was found to increase with the nickel concentration in palladium in the nominal composition $Pd_{0.97}Ni_{0.03}$ and $Pd_{0.93}Ni_{0.07}$, when compared with palladium. At the same time, sensitivity of the nickel and cobalt co-substituted $Pd_{0.91}Ni_{0.04}Co_{0.05}$ thin film showed only marginally higher sensitivity towards hydrogen than pure palladium.

Chapter 6 : Studies on preparation and characterization of $Ag_6Mo_{10-X}W_XO_{33}$ (X = 0 – 2) and selective sensing behavior of $Ag_6Mo_{10}O_{33}$ thick film towards NH_3 by AC impedance technique

This chapter describes with the preparation of tungsten substituted silver molbdates $Ag_6Mo_{10-X}W_XO_{33}$ (X = 0 – 2.0). The substitution of tungsten in the position of molybdenum in $Ag_6Mo_{10}O_{33}$ is a preliminary investigation to understand the electrical properties of the tungsten substituted nominal compositions. The synthesized powders have been characterized by using XRD, normal and backscattered SEM, Wagner polarization and AC conductivity studies. From these studies, the effect of tungsten substitution in $Ag_6Mo_{10}O_{33}$ was elucidated. This chapter also describes preparation, characterization and sensing behavior of $Ag_6Mo_{10}O_{33}$ thick film towards NH_3, H_2 and PG. The characterization of this thick film was carried out by using XRD, SEM and EDX. This chapter elaborates the interaction behavior of the thick film with NH_3, H_2, NO_X and PG by using AC impedance spectroscopy at different frequencies and at different temperatures. The effect of the dipole moment, polarizability and electron transferring property of these gases with $Ag_6Mo_{10}O_{33}$ by using AC technique are briefly discussed. The AC impedance measurements facilitate selective response shown by $Ag_6Mo_{10}O_{33}$ thick film towards NH_3 as compared to the other gases.

Chapter 7 : Summary, conclusions and scope for future studies

This chapter summarizes the results discussed in chapters 3, 4, 5, and 6. In chapter 3, characterization techniques helped in proving the direct evidence of change in carrier concentration of In_2O_3 thin film due to adsorption of oxygen and NO_X. The presence of different N_YO_Z species at various temperatures on the surface of In_2O_3 elucidates the understanding of the reaction mechanism. Interaction studies of In_2O_3 thin film in argon and argon containing different concentrations of NO_X, H_2 and NH_3 are expected to provide better insight to the sensing mechanism. Chapter 4 discusses the merits of handling advanced thin film technique like PLD to deposit unstable $CuInO_2$ by suitably optimizing the parameters during deposition. Such deposited thin film showed selectivity towards NO_X at an operating temperature of 473 K. The measurements of carrier concentrations and carrier mobility of $Cu_2In_2O_5$ and $CuInO_2$ thin films using van der Pauw and Hall techniques in the presence of H_2, NH_3 and NO_X and using XPS will provide the experimental evidence for the nature of the carrier, formation of intermediates and analyte interaction mechanism.

The chapter 5 illustrated the novel method of synthesizing nano metal and alloys by soft-chemical reduction technique at 300 K. Thin films made using compacts of these powders by PLD showed linear behavior in sensitivity with towards hydrogen up to the concentration of 20000 ppm. Further studies on the interaction behavior of Pd and its alloys will be useful for identifying the compositions suitable for sensing hydrogen between the concentrations of 5 and 40000 ppm in argon/air streams.

In chapter 6, the initial investigations of electrical properties of tungsten substitution in $Ag_6Mo_{10}O_{33}$ indicated an enhancement in the silver ion conduction on comparing with $Ag_6Mo_{10}O_{33}$. Investigations on $Ag_6Mo_{10-X}W_XO_{33}$ [X = 0 – 0.5] as a catalyst for decomposition of ammonia will be useful. $Ag_6Mo_{10}O_{33}$ thick film showed selectivity towards NH_3 while conducting experiments using AC impedance technique. The nature of the polarizing property of NH_3 and its chemical reaction with $Ag_6Mo_{10}O_{33}$ altered the effective dielectric property of $Ag_6Mo_{10}O_{33}$, products and unreacted ammonia leading to selective sensing of NH_3. Further optimization studies are required to sense trace levels of ammonia.

Appendix 1

Appendix 1 deals with the characterization of nano metals and alloys prepared by low temperature chemical reduction technique. The powders have been characterized by XRD and their crystallite size was deduced by Scherrer equation. The surface morphology of the powders has been characterized using SEM and composition analyzed using EDX.

References

1. C. Baird, M. Cann, Environmental Chemistry, 4th edition, Clancy Marshall, USA (2008)

2. S.C. Bhatia, Text Book of Air Pollution and its Control, Atlantic publishers, India (2007)

3. W. Gopel, J. Hesse and J.N. Zemel, Sensors, Chemical and Biochemical Sensors Part I, Vol.2, VCH publishers, New York (1991)

4. W. Gopel, J. Hesse and J.N. Zemel, Sensors, Chemical and Biochemical Sensors Part II, Vol.3, VCH publishers, New York (1991)

5. P. A. Carson and C.J. Mumford, Hazardous Chemicals Handbook Butterworth – Heinmann Ltd, Linacre House, Jordon Hill, Oxford (1994)

6. D. J. Davis and G.T. Christianson, Firefighter’s Hazardous Materials Reference Book, Van Nostrans Reinhold, New York (1991)

7. S. A. Kharitnov, B.J.O. Connor, D. J. Evanas, P.J. Barnes, American J. Resp. Crit. Care Med, 151, 1894 (1995)

8. J. G. Mohler and Clarence R. Collier, Handbook of Hazardous Materials, Academic Press, USA (1993)

9. K. H. Mahendran, R. Sridharan, T. Gnanasekaran, G. Periaswami, Ind. Eng. Chem. Res. 37 (1998) 1398

10. K. Korotcenkov, Hand book of gas sensing materials, Vol I, Springer publications, New York, 2013

11. F. A. Lewis, The palladium hydrogen system, Academic press, New York, (1967) 65 – 66

12. R. C. Hughes and W. K. Schubert, J. Appl. Physics, 71 (1992) 542 – 544

13. E. Lee, J.M. Lee, J.S. Noh, J.H. Joe, B. Jung, W. Lee, Thin Solid Films, 519 (2010) 880 – 885

14. Y. J. Ou, W.W. Si, G. Yu, L.L. Tang, J. Zhang, Q.Z. Dong, J. Alloys and Compounds, 569 (2013) 130 – 135

15. J. H. Yoom, B.J. Kim, J.S. Kim, Sensors and Actuators B, 187 (2013) 540 – 545

LIST OF FIGURES

List of Tables

CHAPTER 1

Introduction

1.1 Introduction

1.1.1 Need for gas sensors for surveillance of the ambient and industrial processes

Environmental pollution can have severe effects on human health. The pollution could be due to natural processes like volcanic eruption, forest fires, and vegetative decay. Large volumes of H_2S are produced as byproduct in petrochemical industries. Similarly, large amounts of NH_3, NO and NO_2 (collectively called as NO_X) and SO_2 are being handled in acid and fertilizer plants. An accidental release of these gases into the ambient can result in severs environmental pollution [1 – 6].

Each pollutant has a very low threshold limit value (TLV) which is defined as the permissible concentration in air, to which workers can be exposed continuously, without adverse health effects, for a normal eight hours work per day and a forty four hours work per week. TLVs of some of the gaseous pollutants are given in Table 1.1. Some of the pollutants have odor and human nose can perceive their presence through their smell. The sensing of the gases by human nose is very complex. The nose can perceive the presence of a gas when present above a threshold concentration (called as olfaction limit) and this limit is partially dependent on properties such as shape, polarity, etc. of the molecule of the gas. However, human nose has some limitations. When the concentration of the pollutant in air is high, the sensing limit of the nose saturates and the nose, in fact, loses the sensing action. Some of the pollutants or the industrial process gases can be flammable and odorless. Gases like H_2, propane, butane, petroleum, etc. are under flammable gases. When such a flammable gas leaks in an industrial environment, it can accumulate to large levels in air. When its concentration in air exceeds the lower explosive limit (LEL) and is within the upper explosive limit (UEL), explosions can occur and damage the installations. The explosive limits of certain industrially important gases are also listed in Table 1.1. To mitigate the environmental pollution and/or the incidents of explosions, presence of these gases in ambient air need to be continuously monitored for detecting them well below their explosive limits and take the remedial measures.

Table: 1.1

Safety limits of hazardous and flammable gases

Gas	TLV limit (ppm)	Lower explosive limit (vol. %) (LEL)[1]	Upper explosive limit (vol. %) (UEL)[2]
NH_3	25	16	25
H_2S	10	4.3	44
NO	25	Not applicable	Not applicable
NO_2	0.2	Not applicable	Not applicable
H_2	-	4	75
Butane (C_4H_{10})	-	1.6	8.4
Propane (C_3H_8)	-	2.1	9.6

---

[1] LEL: The minimum concentration of gas or vapor mixed with air (% by volume, at room temperature) that will cause the propagation of flames when it comes in contact with a source of ignition.

[2] UEL: The maximum concentration of gas or vapour mixed with air (% by volume, at room temperature) that will cause the propagation of flames when it comes in contact with an ignition source.

The conventional instrumental methods of analysis such as mass spectroscopy, gas chromatography or optical techniques (e.g. IR and UV/Visible), etc. are capable of precisely analyzing a single species present in a complex gas mixture with high selectivity. However, these instruments are invariably bulky, very expensive, and they need frequent calibrations. In addition, sampling and analyzing would be elaborate leading to increase in analysis time. Analysis by these instruments is not truly on-line but is “batch analysis”. Chemical sensors operating on various principles such as optical, electrochemical, electrical (resistive), mass, magnetism, etc. can be used for the on-line analysis [7 – 9]. A chemical sensor is comprised of a receptor and a transducer. The receptor is the material which interacts with the analyte and results in a change of its properties (electrical resistance, work function, dielectric constant, electrode potential, mass, etc.), or emits heat or light. The transducer is the part of the sensor which transforms this change in properties into an electrical signal (i.e. sensor output). Among the various types of chemical sensors, chemo-resistive sensors, using thick or thin films of metal oxides or metals as receptors are promising candidates since they are relatively simple and very inexpensive. The difference in the resistances of the film in clean environment and in the environment containing the analyte is measured and correlated to the concentration of the analyte.

1.1.2 Desirable characteristics required for a gas sensor

The characteristics of a sensor are evaluated by the following criteria:

- Detection limit: It is the lowest concentration of the analyte that can be detected by the sensor under given conditions.

- Response time: It is calculated based on the time taken for the change in measurant from its initial value when the analyte is absent (background) to the stable value when the analyte is present.

- Recovery time: It is calculated based on the time taken for the measurant of the sensor in the presence of analyte to retrace back to its initial value after the analyte had been withdrawn from the environment.

- Baseline: It is the sensor response in a particular ambient (in the absence of the analyte) as a function of time. The baseline of the sensor should be stable and it should not be influenced by common changes in the ambient – for example changes of moisture or humidity, CO_2 and oxygen in air ambient.

- Sensitivity: It is the correlation involving the outputs of the sensor in the presence of analyte and in the absence of analyte in the ambient. The definition of sensitivity in the gas sensor field is different from that used in analytical chemistry (slope of the calibration curve i.e. signal / concentration). In case of chemoresistive sensors, it is defined as:

$$\text{Sensitivity}(\%) = \left(\frac{|R_a - R_g|}{R_a}\right) X100 = \frac{\Delta R}{R} X100 \qquad (1.1)$$

$$\text{Sensitivity (S)} = \left(\frac{R_a}{R_g}\right) \tag{1.2}$$

Where, 'R_a' is resistance of the receptor material in air and 'R_g' is resistance of the material in the presence of analyte. Sensitivity defined by eqn.1.1 is employed whenever the 'ΔR' of the sensor is high. When 'ΔR' exhibited by the sensor is low, sensitivity defined by eqn. 1.2 is used.

- Selectivity: It refers to the characteristics that determine whether the sensor can respond selectively to a group of analytes or to a single and specific analyte. The selectivity of a material to a particular analyte among other analytes is defined by eqn. 1.3:

$$\text{Selectivity} = \frac{\text{Sensitivity of the sensor towards the interfering analyte}}{\text{Sensitivity towards the desired analyte}} \tag{1.3}$$

The above characteristics of a chemo-resistive sensor are dependent on the thermophysical and thermochemical properties of the receptor material, geometrical configuration and temperature of operation of the sensor. An understanding of the sensing mechanism is essential to choose a suitable receptor material for a given analyte and tune its configuration and temperature of operation. Semiconducting metal oxides, which are used as receptors for gas sensing, are of two types: a) those which chemisorb oxygen on their surface when exposed to oxygen or oxygen containing environment and (b) which do not chemisorb oxygen but having labile lattice oxide ions. In chemoresistive sensors using the first category of oxides, the sensing action is the interaction of the chemisorbed oxygen with the analyte on the surface. In case of the sensors with the second category of oxides, the analyte interacts with the lattice oxygen which leads to a change in the stoichiometry resulting in the property change of the bulk material.

1.2.1 Interaction of analyte with chemisorbed oxygen (O_2^- and O^-)[Type I]

Semi-conducting metal oxides (SMO) are of two types — n-type and p-type oxides. In the n-type semi-conducting metal oxides, majority of the charge carriers are electrons, (e.g. $ZnO_{1-\delta}$, $SnO_{2-\delta}$, $In_2O_{3-\delta}$, etc.,) and in p-type oxides they are holes (e.g. $Ni_{1-X}O$, $Cr_{2-X}O_3$, etc.). For further discussion on gas sensing mechanism, indium oxide ($In_2O_{3-\delta}$) will be used as an example.

Indium oxide is an n-type semiconductor, with a wide band gap of 3.1 eV. Due to its wide band gap, one would expect it to be an insulator. However, experimental studies reviewed by King et al showed it to be n-type semiconductor [10]. The electronic conductivity in indium oxide is caused by the presence of oxygen deficiency ‘δ’ and is represented as $In_2O_{3-\delta}$. This non-stoichiometry is due to the existence of oxygen vacancies ($V_O^{\bullet\bullet}$) and the electrical-neutrality is maintained by electrons occupying the donor levels (In^{2+}). The schematics of the band structure of $In_2O_{3-\delta}$ are shown in fig. 1.1. The electrons from these donor levels can be readily excited into the conduction band leading to the observed electrical conductivity. The gas sensing mechanism of $In_2O_{3-\delta}$ can be understood by the adsorption of oxygen on the surface of the semiconducting oxide and its reaction with an analyte leading to changes in the conductivity of the oxide.

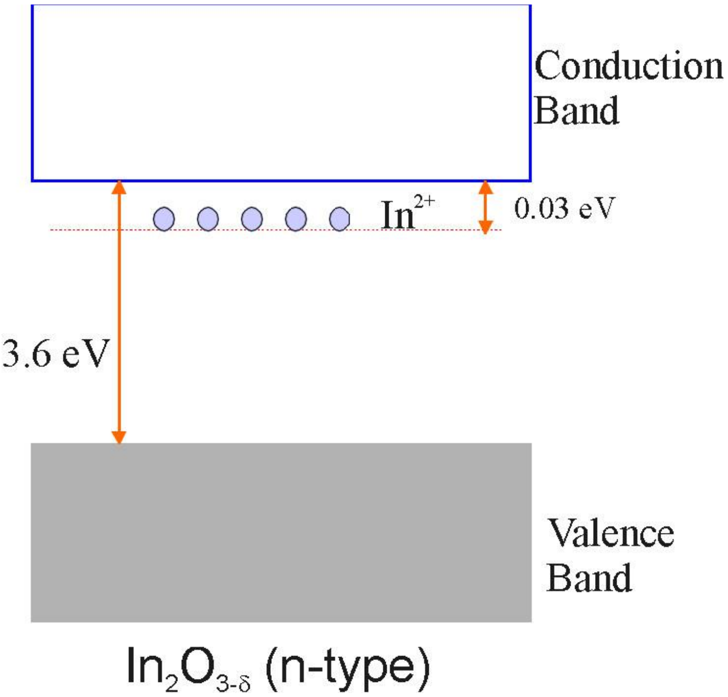

Fig. 1.1 Schematic of the energy band diagram of $In_2O_{3-\delta}$

When $In_2O_{3-\delta}$ is exposed to an oxygen containing environment, oxygen physisorbs on the surface of oxide and extracts electrons from it i.e. chemisorbs. Chemisorption of oxygen results in formation of different species of oxygen viz., O_2^-, O_2^{2-}, O^- & O^{2-} as shown in eqn. 1.4 [11 – 14]. The fraction of the specific oxygen species formed is dependant upon the temperature. In case of $In_2O_{3-\delta}$, the majority of the species is O_2^- in the temperature range of 323 to 473 K. Similarly, O^- is the major fraction in the temperature range of 473 to 573 K. At temperatures above 673 K, O^{2-} ion dominates [14].

$$O_{2(g)} \overset{323K-348K}{\rightleftharpoons} O_{2(physisorbed)} \overset{320K-473K}{\rightleftharpoons} O^-_{2(chemisorbed)} \qquad (1.4)$$

$$O^-_{2(chemisorbed)} \overset{448K-698K}{\rightleftharpoons} O^-_{(chemisorbed)} \overset{673K-873K}{\rightleftharpoons} O^{2-}_{(lattice)}$$

Figure 1.2 represents the schematics of the band and structural models of $In_2O_{3-\delta}$. 'E_F' and 'E_C' represent the Fermi level and lower edge of the conduction band of $In_2O_{3-\delta}$. Because of the abstraction of electrons by adsorbed oxygen, a space charge region (Λ_{air} or L) develops on the surface of the metal-oxide i.e. an electron-depleted region forms on oxide surface and is shown in fig. 1.2a. At the boundary across the two grains which have charge depleted regions, a potential barrier develops for the flow of charge [15]. This reflects as an increase in the electrical resistance of the surface of the oxide (which is generally in the form of a thin / thick film). This is shown in fig. 1.2c at ~ 673 K. Exposure of this surface to gases like carbon monoxide, leads to reaction of O^- ions with them. The trapped electrons are released back to the bulk during this process and thickness of depleted region reduces and its effect on potential barrier across the grains is shown in fig. 1.2b. The extent of reaction and the number of electrons released depend on the concentration of CO in air. The reduction in the height of potential barrier leads to reduction in surface resistance of the film. On re-exposure to clean air, the thickness of the depleted region increases again and hence the resistance. These sequences in surface resistance of the film are shown in fig. 1.2c.

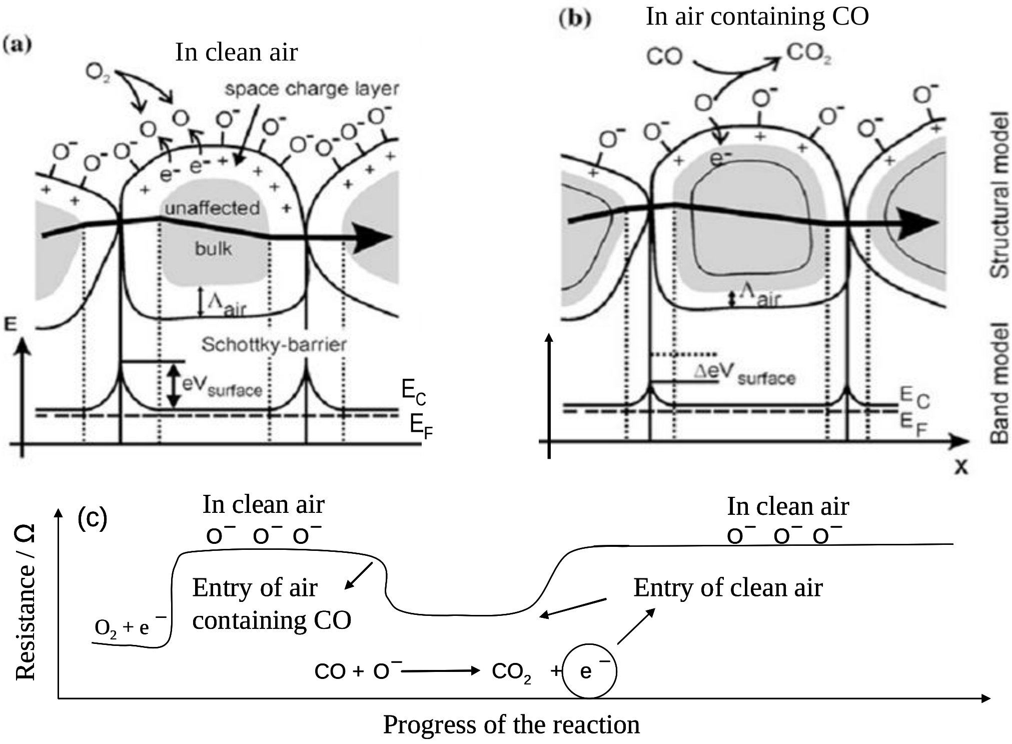

Fig. 1.2 Structural and band models for the intergranular percolation path of electron in $In_2O_{3-\delta}$ a) in clean air, b) air containing CO, and c) Schematics of the progress of the surface reactions on cyclic $In_2O_{3-\delta}$ in exposure to sequence of clean air and to air containing CO at ~ 673 K [15]

The processes that occur during the gas sensing action of the oxide materials can be considered by the following two simultaneous reactions: Equation 1.5 represents chemisorption of oxygen at different active sites on the surface of the oxide of bulk composition $MO_{X-\delta}$. Chemisorption changes the surface composition to "MO_X".

$$MO_{X-\delta} + \frac{\delta}{2} O_2 \rightarrow \text{"}MO_X\text{"} \qquad (1.5)$$

$$"MO_x"+R \rightarrow "MO_{x-\varepsilon}"+B \tag{1.6}$$

Equation 1.6 represents the reaction of reducing gas ‘R’ with “MO_X” to yield product ‘B’. The resulting composition of the oxide surface with lower chemisorbed oxygen would be “$MO_{x-\varepsilon}$”. Gas sensors are operated at a fixed temperature in air, where the oxygen concentration remains large and constant. The rates of these two reactions and the adsorption/desorption processes that precede and succeed them also need to be considered for understanding the gas sensing characteristics.

1.2.1.1 Sequence of steps occurring during the sensing action of SMO

The sequences of processes involved in gas sensing are:

1) Chemisorption of oxygen
2) Adsorption of analyte gas
3) Reaction between chemisorbed oxygen species and the analyte
4) Desorption of reaction product
5) Re-exposure of the oxide surface to clean air for oxygen to chemisorb

The first step in gas sensing is the physisorption of oxygen molecule on vacant active sites [S(□)] on the surface and is shown in eqn. 1.7.

$$S(\square)+O_2(gas)\xrightarrow{k_1}S(O_2)+\Delta H_1 \tag{1.7}$$

ΔH_1 is the enthalpy of formation (exothermic) of the physisorbed (neutral) oxygen species. For the accumulation of physisorbed oxygen on the surface, the condition is $|\Delta H_1| \geq k_BT$, where ‘k_B’ is Boltzmann constant and ‘T’ is the temperature. It is to be pointed out not all sites would be occupied by oxygen. The extent of occupation depends on the concentration of oxygen in air and the exothermicity of the process.

The next step is the capture of electron by the physisorbed oxygen molecule from the conduction band of the oxide and conversion to chemisorbed oxygen ion as shown in eqn. 1.8:

$$S\ (O_2) + e^- \xrightarrow{k_2} S\ (O_2^-) + \Delta H_2 \qquad (1.8)$$

ΔH_2 is the enthalpy of formation of the chemisorbed oxygen ion on the surface. When O^-, and O^{2-} adsorbates are formed at different temperatures (discussed earlier) heat of dissociation of oxygen molecule to oxygen atoms also need to be taken into account. It is to be pointed out that reaction shown in eqn. 1.5 is the sum of reactions shown in eqn. 1.7 and eqn. 1.8.

When the oxygen chemisorbed metal oxide is exposed to an analyte ‘R’, the analyte gets adsorbed on the vacant active sites as shown in eqn. 1.9.

$$S(\square)\ +\ R(gas) \xrightarrow{k_3} S(R) + \Delta H_3 \qquad (1.9)$$

Where, ΔH_3 is the enthalpy of physisorption (exothermic) of the process. $|\Delta H_3|$ needs to be greater or equal to k_BT, otherwise analyte would not accumulate on the surface. Since the concentration of the analyte R is very low compared to that of oxygen in air, for adsorption of R to be significant $|\Delta H_3| >> |\Delta H_1|$. Equation 1.10 shows the reaction between adsorbed R and chemisorbed oxygen ion.

$$S(O_2^-) + S(R) \xrightarrow{k_4} S(B^-) + S(\ \ ) + \Delta H_4 \qquad (1.10)$$

The species B^- is the charged reaction product and ΔH_4 is the enthalpy of the reaction (exothermic). For the fast response of the metal oxide towards the analyte gas, the above reaction should be very fast. Equation 1.11 shows the release of electron from the product (B^-) to oxide matrix.

$$S(B^-) + \Delta H_5 \xrightarrow{k_5} S(B) + e^- \tag{1.11}$$

Here, ΔH_5 is the enthalpy change for the removal of the electron (endothermic) from the product and transfer it to the oxide matrix. This step is an activated process and is a rate determining step. Equation 1.12, shows desorption of B from the surface and is again an endothermic process associated with heat of desorption 'ΔH_6'.

$$S(B) + \Delta H_6 \xrightarrow{k_6} S(\square) \tag{1.12}$$

As discussed earlier, for the sensing process to take place, the rate constants of the process shown in eqns. 1.7 and 1.8 (k_1 & k_2) should be lower than that rate constant of the process shown in eqn. 1.9 (k_3), because of large ratios of pO_2 / p_R involved in gas sensing (p_{O_2} and p_R are partial pressures of oxygen and analyte respectively in the ambient). The concentration of carriers (electrons) namely electrons in the surface region is determined by the reactions shown by eqn. 1.8 and eqn. 1.10. The reactions proceed until a steady state is established when their rates become equal as shown in eqn 1.13.

$$k_2 [S(O_2)] \; [e^-] = k_5 [S(B^-)] \tag{1.13}$$

Hence, at the steady state,

$$[e^-] \; = \; \frac{k_5 [S(B^-)]}{k_2 [S(O_2)]} \tag{1.14}$$

Concentration of adsorbed oxygen sites on the surface [S(O_2)] is very high compared to [S (B^-)] and since partial pressure of oxygen remains constant, S(O_2) is effectively constant. Hence, eqn 1.14 is reduced to eqn. 1.15:

$$\left[e^-\right] = \text{const.}\left[S(B^-)\right] \tag{1.15}$$

The concentration of the adsorbed product 'B^-', is proportional to partial pressure of reactant gas, 'P_R' as can be seen from eqns. 1.9 and 1.10. This shows that the concentration of electrons, in other words the conductivity of the oxide during the interaction with the analyte, would be proportional to partial pressure of the analyte gas as shown below:

$$[e^-] = \text{constant } P_R \tag{1.16}$$

In the above discussion, many simplifying assumptions have been made and hence the deduction that conductivity is proportional to 'P_R' is valid only under limited conditions. Generally conductivity is proportional to 'P_R^n', where $n \leq 1$.

1.2.2 Chemical reaction by the involvement of lattice oxygen (O^{2-}) [Type II]

Transition metal oxides like MoO_3, WO_3, etc. fall under this category. Data in literature shows that the gas sensing action of these oxides is mediated by lattice oxygen. These oxides are known to exhibit extensive non-stoichiometry. The deviation from stoichiometry is stabilized by the elimination of complete rows of anion point defects in specific crystallographic planes by simultaneous shear displacement and crystal structural collapse of the planes, by a mechanism called crystallographic shear (CS). The oxygen deficiency in the reduced oxide is incorporated by the formation of CS planes of edge-sharing octahedra in a specific crystallographic orientation. When an oxide is reduced, the driving force for the formation of CS planes is to lower the Gibbs energy of the system and preservation of the cation octahedral coordination [16 – 18].

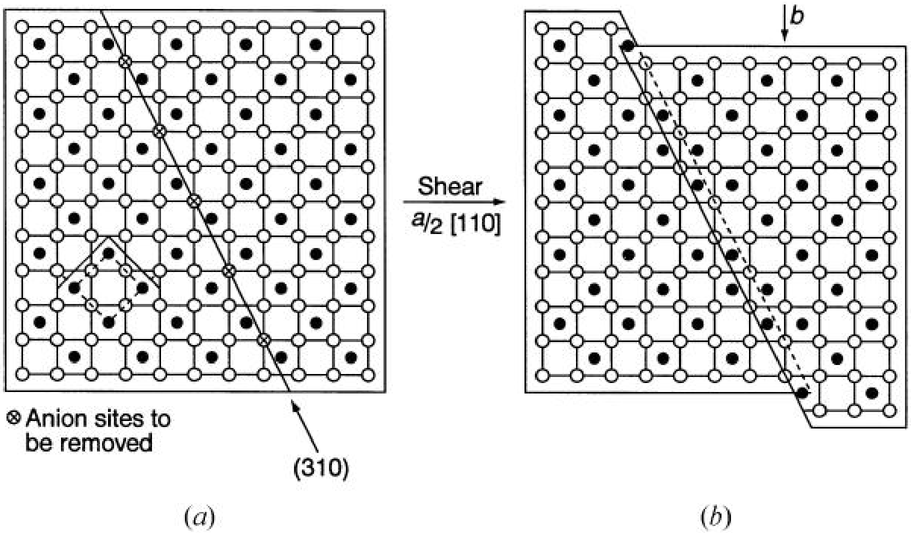

Fig.1.3 Principles of crystallographic shear (CS) in ReO_3: a) formation of anion vacancies; and b) elimination of the vacancies by crystal shear and collapse [19]

The WO_3 structure can be described as a slightly deformed ReO_3 structure, which consists of an infinite three dimensional arrangement of MO_6 octahedra, joined together by corner sharing (M stands for metal) as illustrated in fig.1.3a. If the crystal is cut along a lattice plane (a typical shear plane {310}), and is displaced as shown in fig.1.3b, an arrangement is obtained, where the octahedral along this plane are now joined by edges instead of the corners. This mechanism changes the composition along the plane, due to change in coordination [19].

The structure of MoO_3 is based on a series of bilayers that are oriented perpendicular to the [010] y axis as shown in fig.1.4a. Each bilayer consists of two sub layers of distorted MoO_6 octahedra to give three cystallographically inequivalent oxygen sites as shown in fig. 1.4b. Each bilayer interacts with the adjacent bilayer in the [010] direction through a weak non-covalent van der Waals interaction. There are no dangling bonds on the [010] surface. Oxygen positioned in these shear structures are in labile state [20 – 22].

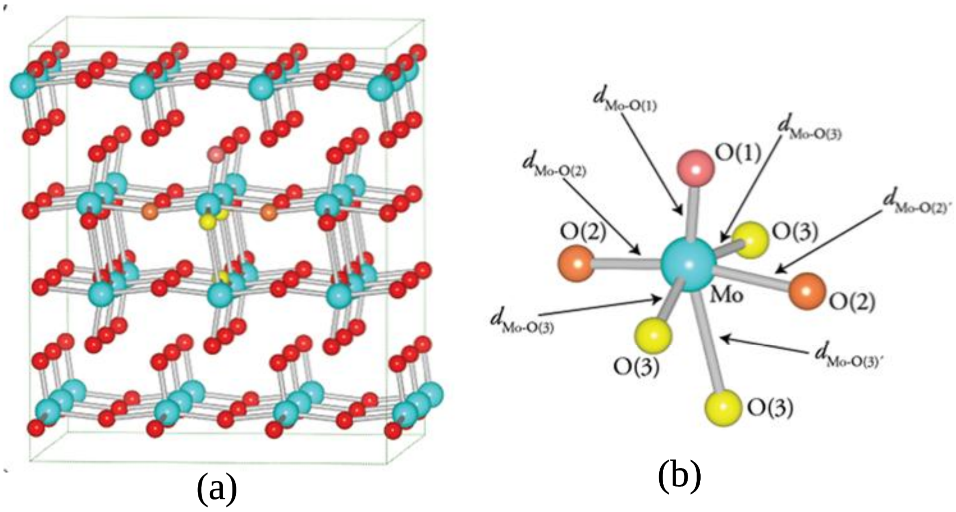

(a) (b)

Fig.1.4 a) Crystal structure of orthorhombic MoO_3 showing the layered structure along the (010) direction and b) Structure of MoO_6 distorted octahedra [21]

1.2.2.1 Sequence of steps in the sensing action of metal oxides with involvement of lattice oxygen

Molybdenum trioxide (MoO_3) has been well studied and proved to be a good catalyst for oxidation of organic compounds [23, 24]. Catalytic action of this oxide is shown to involve the participation of lattice oxygen [24]. The mechanism of this catalytic action was studied in detail by Mars-van Krevelen [18]. When thin / thick films of these oxides are used for gas sensing, the sensing would involve the following steps: (a) adsorption of the reactant (e.g. reducing gas) on the metal oxide surface (primary adsorption positions on the surface are co-ordinatively unsatisfied sites); (b) oxidation of the adsorbed reactant by the lattice oxide ions; (c) removal of charge from the oxidized product; (d) desorption of the oxidized product; and (e) replenishment of the vacant surface oxide site by the diffusion of oxygen from the bulk and by oxygen from air.

The co-ordinatively unsatisfied surface site is depicted as $M—O^{-}$ in the present discussions. The first step is the occupation of the reactant ‘R’ on the site $[S(M— O^{-})]$ of metal oxide, which is represented as $[S(\Delta)]$ and is shown in eqn. 1.17.

$$S(\Delta) + R(gas) \xrightarrow{k_7} S(M - O - R)^{-} + \Delta H_7 \qquad (1.17)$$

ΔH_7 is the (exothermic) enthalpy of formation of the species, $[S(M—O—R)^{-}]$. For this to occur, $|\Delta H_7|$ should be greater or equal to k_BT, where T is the temperature of operation of the sensor. The next step is the dissociation of the [O—R] from the surface site, generating vacant lattice oxide ion site $(L_O(\square))$ and release of electron to the matrix, as represented in eqn. 1.18.

$$S(M-O-R)^- + \Delta H_8 \xrightarrow{k_8} L_O(\square) + R-O\uparrow + e^- \qquad (1.18)$$

This process would be endothermic process as it is associated with dissociation and desorption of R—O species. For the material to exhibit good sensing characteristics, rate of this reaction should be very high. Equation 1.19 depicts the regeneration of the active oxide site [S(Δ)] from oxygen in air and this is expected to be exothermic reaction.

$$L_O[\square] + \frac{1}{2}O_2(\text{gas}) + e^- \xrightarrow{k_9} S(\Delta) + \Delta H_9 \qquad (1.19)$$

The rate of the reaction shown in eqn. 1.17 depends on the partial pressure of reactant 'p_R'. Similarly, the rate corresponding to regeneration of active oxide (eqn.1.19) depends on the partial pressure of oxygen in air. For the oxide to exhibit high sensitivity, the rate constant k_7 should be very high compared to those of reactions shown in eqn. 1.18 and 1.19. Also for good sensitivity and selectivity towards the analyte 'R', rate constant k_7 should be greater than k_9, because of large ratios of pO_2/p_R involved in gas sensing ('p_{O_2}' and 'p_R' are partial pressures of oxygen and analyte respectively in the ambient).

Sensing action of metal oxide film is realized by the measurement of change in its resistance in the presence of 'p_R'. The steady state equilibrium of the overall reaction depends on the rate of the analyte reaction (k_7) with metal oxide (eqn. 1.17) and formation of active oxide as shown by the eqn. 1.19.

$$k_7[R] = k_9[(pO_2)^{1/2}[e^-]] \tag{1.20}$$

$$[e^-] = \left(\frac{k_7[p_R]}{k_9(pO_2)^{1/2}} \right) \tag{1.21}$$

Also, the partial pressure of oxygen remains constant throughout the sensing action and thus, eqn 1.21 reduces to eqn. 1.22.

$$[e^-] = \text{constant } p_R \tag{1.22}$$

Thus, the change in electron concentration or change in conductivity is proportional to the partial pressure of the analyte species.

1.3 Hydrogen detection by metals

Hydrogen is consumed in large volumes in fertilizers, metal sintering plants, fuel in rockets, refineries, etc. Hydrogen is a flammable, colorless, and odorless gas. Hydrogen forms explosive mixtures in air when its concentration ranges between 4 and 74%. In a Fast Breeder Reactor (FBR) circuit, hydrogen in argon cover gas needs to be monitored to detect any steam leak into liquid sodium under reactor start-up or low power operating conditions. In the event of a steam leak in the steam generator of the reactor, sodium-water reaction would take place. This reaction, if not detected and stopped at its inception, could damage the steam generator itself. This detection is carried out by continuous monitoring of hydrogen evolved during sodium-water reaction which collects in argon cover gas over liquid sodium (and builds up from ppm level and could reach up to percentage). Sensors currently available in the market for monitoring hydrogen are pellistor, thermal conductivity detector (TCD), semi-conducting metal oxides, metal (Pd) coated film, etc. These products have their own advantages as well disadvantages. The pellistor is suitable for monitoring hydrogen up to 5 % [27]. The pellistor and SMO based sensors need the presence of a constant level of oxygen for the gas sensing process. Thermal conductivity detectors would work in a wide dynamic range, but they would work off-line (needs sampling) and need frequent calibration. The choice of selection of material for hydrogen detection is important. It should work at room temperature. The operating temperature of the sensor should not trigger fire during hydrogen leak in the ambient and online monitoring is preferable. In order to fulfill the above requirements and to work at room temperature, development of a material that should cover from ppm to percentage level and preferably both in air and also in inert atmosphere. Data in literature shows that palladium can be used to monitor hydrogen below 1% and would be operable in oxygen as well in inert ambient. The reports also show that the hydrogen detection range can be widened when palladium is alloyed with elements like Ag, Co, Ni, Au, etc. [28 – 30].

1.3.1 Mechanism of interaction of hydrogen with Palladium

Figure 1.5 shows the Lennard-Jones model in which the energy of the metal hydrogen system is plotted against a coordinate x, closely related to the distance of the adsorbate (H_2) from the surface [31]. Figure 1.5a shows physisorption of hydrogen molecule on the surface of palladium. The weak minimum Q_p (exothermic process) corresponding to heat of physisorption occurs at an appreciable distance. Gas molecules get physisorbed on the Pd surface without dissociation. The dissociation of H_2 molecule into fragments takes place when it is in the chemisorbed state. The interaction of hydrogen on palladium is a non-activated dissociative chemisorption process as seen from the fig.1.5a. Figure 1.5b shows the physisorption of hydrogen on the surface of Nickel. As seen from the figure, the cross over lines of the curves (1) and (2) result in activation energy, ‘E_a’ which is the energy needed for the physisorbed hydrogen molecule to get converted into chemisorbed state. Such processes would be facilitated by an increase in temperature (kinetic factor). The hydrogen interaction on nickel is activated chemisorption process.

Sequence of interaction of palladium with hydrogen begins with physisorption of hydrogen followed by its dissociation and then dissolution into solid phase. On dissolution of hydrogen, expansion of lattice and perturbation of electron mobility occur and they are correlated with the change in mass, volume or resistance of material. Generally, change in the resistance is employed as the measured parameter for sensing of hydrogen.

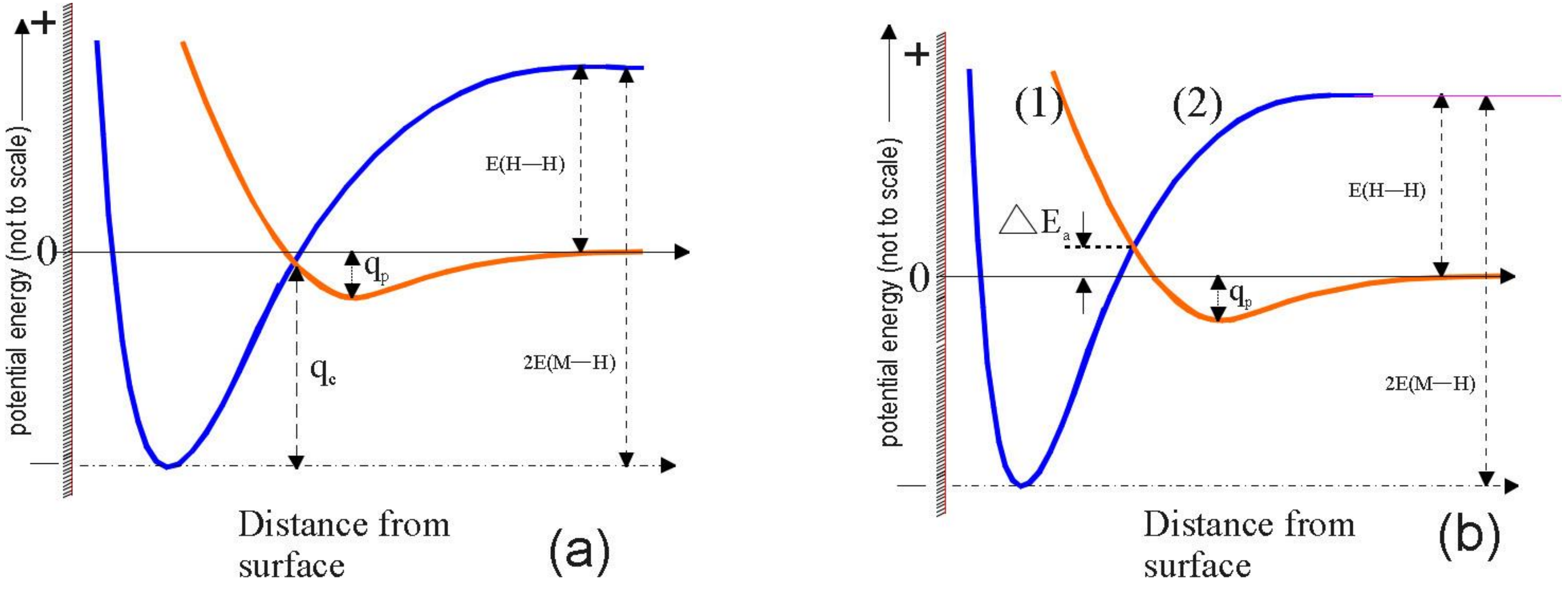

Fig.1.5 Types of interaction potential of H_2 on a) non activated disssociatve chemisorption of H_2 on Pd and b) activated dissociative chemisorption of H_2 on nickel [31].

1.4 Strategies to improve the gas sensing properties of type I and type II metal oxides

1.4.1 Effect of sensor morphology

The fundamental understanding of the interaction behavior of the materials towards analytes is carried out by fabricating the materials in the form of compact pellet called as bulk (dense or porous), thick (porous) and thin film. The sensor performance is critically influenced by four basic factors: (1) Geometry (sensor and electrode setup), (2) Dimensional (grain size, neck size and film thickness), (3) Crystallography (crystal shape, film texture, surface geometry and surface stoichiometry) and (4) Morphology (porosity, agglomeration, grain networks and intergrain contacts) [9]. In the view point of microstructure, two aspects are important. One is the nature of the adsorption sites and another is electrical transport properties.

Figure 1.6 shows the schematic representation of geometric surface (side view) of a pellet or bulk in the dense form. Two sides of the pellet are exposed to ambient (top and bottom) while the other two sides (left and right) are provided with electrodes. The two sides exposed to ambient have the carrier depleted regions due to chemisorption of oxygen and shown transparent in the figure. The shaded portion corresponds to the bulk and gases cannot access this region. Chemical interactions related to gas sensing are to take place on the two exposed surfaces. Since the bulk is unaffected by these processes, electrical current therefore flows through less resistive bulk. Hence, SMO’s in sintered dense pellet form possess poor sensitivity towards analyte [11].

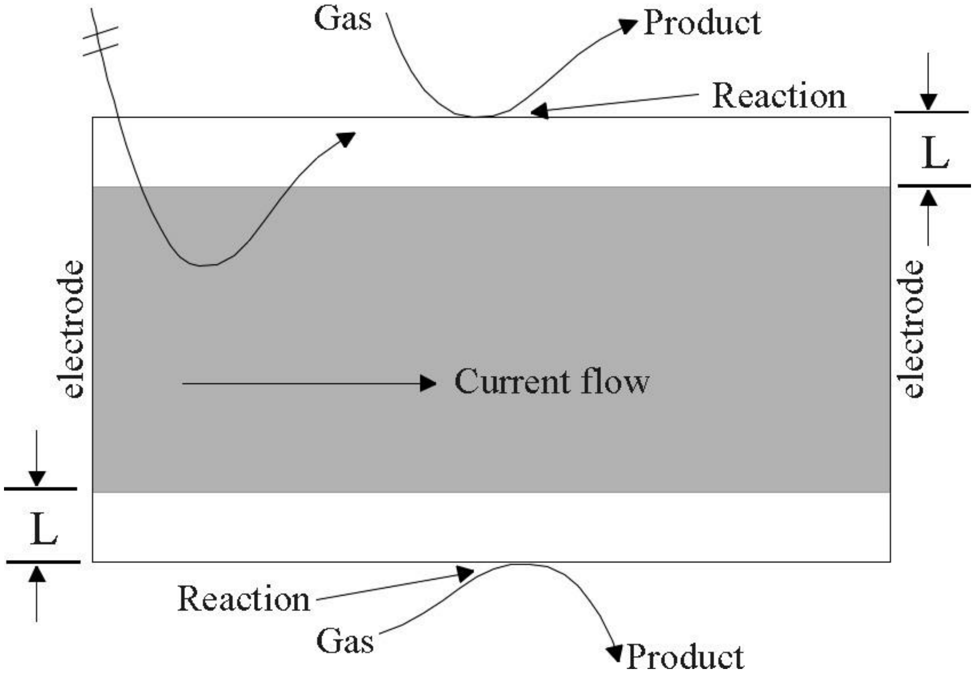

Fig. 1.6 Diagram showing the schematic representation of bulk semi-conducting metal oxide (side view) [15, 32]

Figure 1.7 show the schematics of porous network (porous pellet or porous thick film) of the SMO. Each grain has charge depleted surface. As mentioned earlier, potential barriers i.e. Schottky barriers develop at the grain boundaries where these surfaces are in contact with each other [11]. In porous layers, the gaseous species can penetrate deep into the bulk, which makes the active surface to be present on layers beneath the top layer also. These barriers hinder the free flow of electrons in the film and result in an increase in resistance (fig. 1.2c). The number of electrons which succeed in overcoming the potential barrier and accordingly, the conductance 'G' of the sensing layer is given by eqn. 1.23:

$$G \approx \exp\left(\frac{-eV_{sur}}{k_B T}\right) \tag{1.23}$$

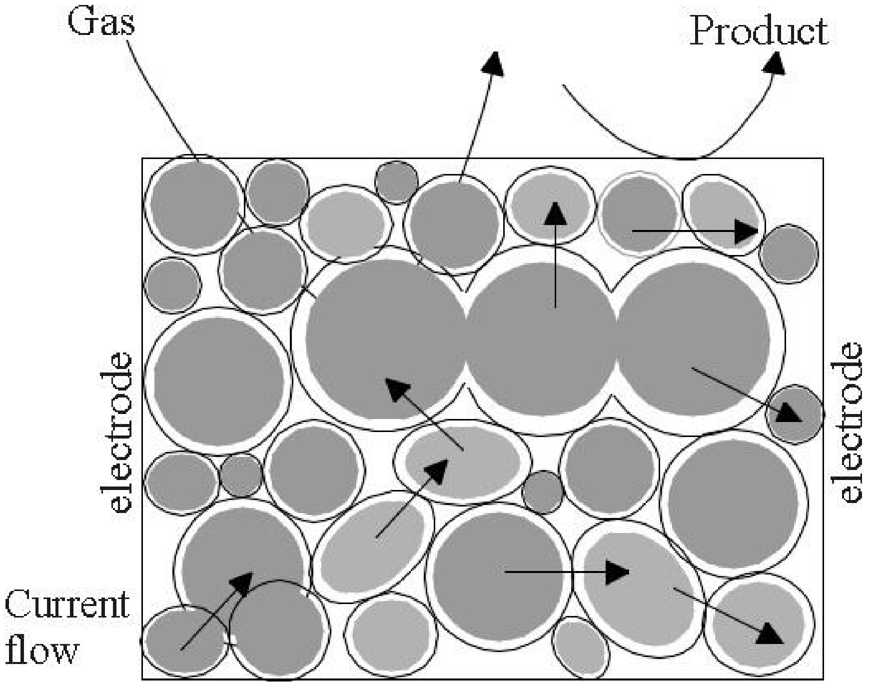

Fig. 1.7 Diagram showing the schematic of semi-conducting metal oxide in porous thick film [15, 32]

where, 'e' is charge of the electron, 'V_{sur}' potential barrier and 'T' is the temperature. Hence, in dense and porous network of these materials sensitivity mainly depends on the grain boundaries and size of the grain. The particle size is one critical parameter which influences the gas sensing properties of a material. Nano-particles are preferred, since they provide a large surface to volume ratio compared to microcrystalline counterparts. In nano-crystalline particles, dimension of the depletion layer would be comparable to the radius of the grain and hence the grains would be fully depleted of conduction-band electrons. The bulk conductivity of the interconnected grains becomes negligible and the conduction through the depleted layer dominates.

A semi-quantitative model was proposed by Rothschild and Komem to describe the effect of the grain size on the sensitivity of metal oxide gas sensors [33]. According to this model, the sensing material consists of partially sintered crystallites connected to their neighbors by narrow necks (fig. 1.8). The interconnected grains form larger aggregates and are connected to neighbors through the grain boundaries. Figure 1.8 shows the schematics of arrangement of spherical particles having uniform grain size ‘D’, neck size ‘X’ and space charge region ‘L’ [11].

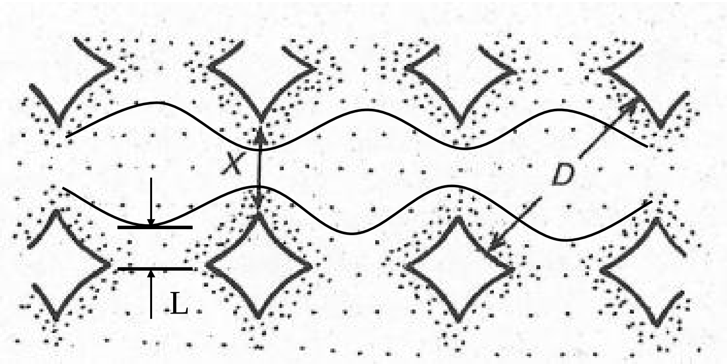

Fig. 1.8 Diagram showing the schematic of spherical particles having uniform grain size ‘D’, neck size ‘X’ and space charge region ‘L’ [11]

Three different cases have been modeled and are distinguished based on the relative sizes of ‘D’ and ‘L’. When D >> 2L, most of the crystallite volume is unaffected by the interaction of the gas phase on the surface (fig. 1.9). The predominant effect of the ambient gas on the conductivity is introduced via the potential barriers at the grain boundaries.

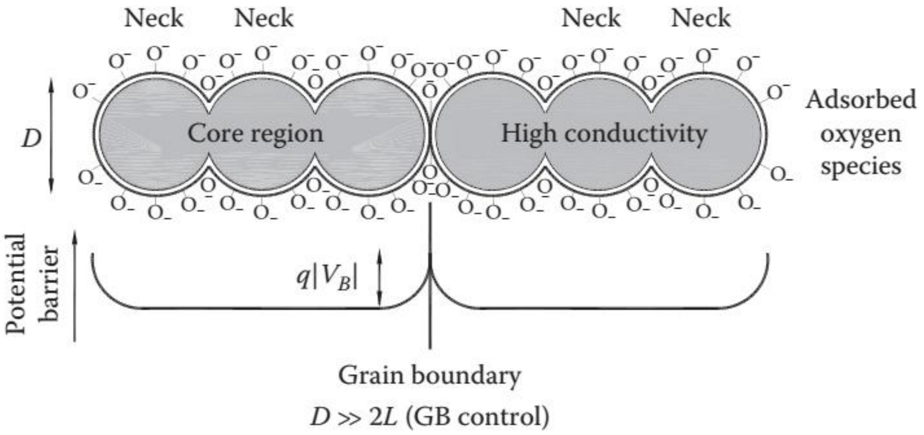

Fig. 1.9 Diagram showing the schematic model of the effect of grain boundary controlled crystallite size on the sensitivity of metal oxide when D >> 2L [34, 35]

The number of charge carriers in the bulk remains to be high. The fraction of the carriers that overcome the barrier under a potential gradient is also high and this results in high conductivity. Sensitivity of a sensor towards a gas is due to the modulation of the potential barrier across the grains in the presence and absence of the gas species in the ambient. Since the barriers do not have major influence on conductivity, the sensitivity would be low. In other words sensitivity is independent of grain size ‘D’ [35].

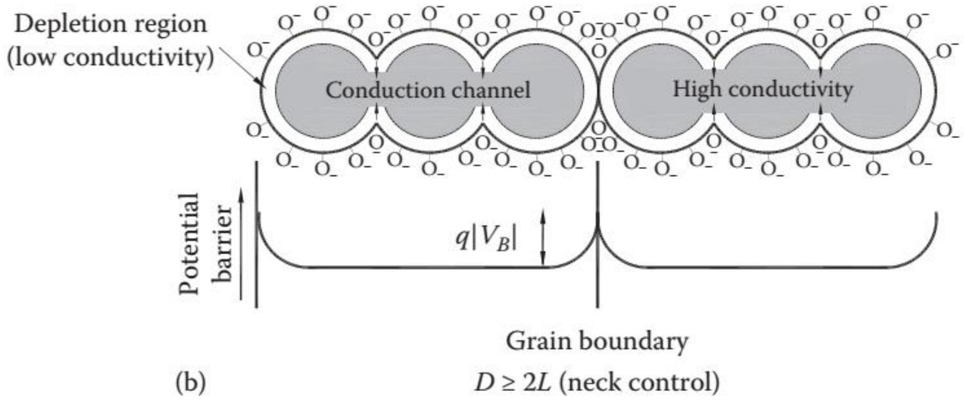

Fig. 1.10 Diagram showing the schematic model of the effect of neck controlled grain on the sensitivity of metal oxide when D ≥ 2L [34]

As the grain size decreases, the depletion region extends deeper into the grains. When D ≥ 2L, the depletion region surrounding each neck forms a constricted channel for conduction as shown in fig.1.10. The conductivity of the material under these conditions depends not only on the height of the potential barriers but also on the cross-sectional area (called neck size “X’) of those channels.

When D < 2L the depletion region extends throughout the grain and are almost completely depleted of charge carriers as shown in fig. 1.11. Also, the conduction channels between the grains do not exist. Thus, when D < 2L, both the carrier depletion in the entire grain and the existence of potential barriers at the grain boundaries determine the conductivity. In the presence and absence of a specific analytes in the ambient, large modulation in the number of carriers and potential barrier occur, leading to high sensitivity.

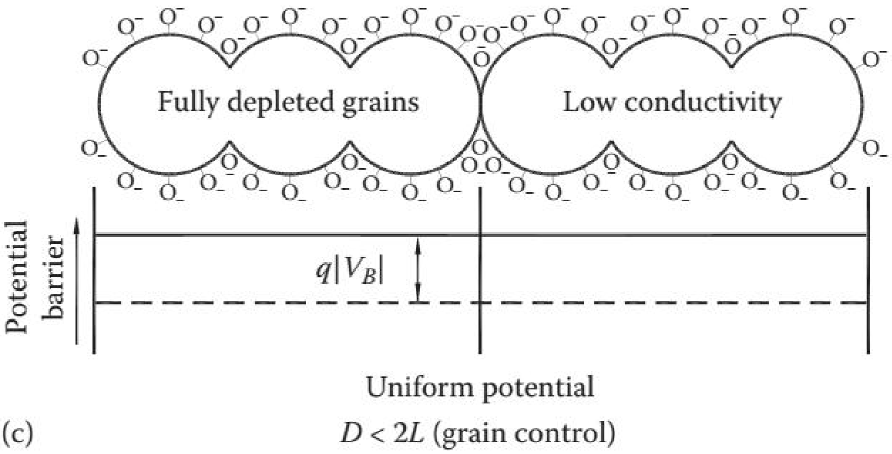

Fig. 1.11 Diagram showing the schematic model of grain controlled effect on the sensitivity of metal oxide when D < 2L [34]

1.4.2 Effect of incorporation of catalyst/additives and dopants

The enhancement of gas sensing properties of the semiconducting oxides by incorporating noble metals (Pd, Pt & Ag) and other metal oxides as foreign receptors has been well recognized since long and are used in the fabrication of practical sensors [36, 37]. By considering the catalytic and electrical properties of noble metals in conjunction with those of the properties of the semiconducting oxide used, Yamazoe et al proposed the role of additives in enhancing the sensitivity and selectivity either by chemical (Pt) or electronic sensitization (Pd, Ag, CuO, etc.) [38, 39]. The dopants such as Sb, Bi, Ga or In are added to balance the conductivity of the materials by increasing or reducing the number of carriers and thus maintain resistance at ranges measurable with common instrumentation.

1.4.3 Effect of temperature

Generally selectivity shown by a sensing material towards a gas in the presence of several other gases depends on the activation energy of the surface processes, temperature and nature of catalysts and additives employed. Generally, sensitivity exhibited by an oxide to a particular gas increases with increase in temperature. At low temperatures, the rate of the reaction between the chemisorbed oxygen / lattice oxide ions and the adsorbed analyte molecules would be slow because of the activation energy. Hence, sensor would exhibit low sensitivity. With increase in temperature, more reactants would cross the activation barrier and hence the reaction rate as well as the rate of electron transfer to SMO and desorption of the reaction product increase (eqn. 1.10 to eqn. 1.12). This would lead to higher sensitivity. However, at high temperatures, the analyte molecules would not accumulate on the surface, since the thermal energy of the species would be larger than the enthalpy of adsorption (c.f. eqn. 1.9: $|\Delta H_3 << k_BT|$). Hence, the reaction rate reduces. Thus the sensitivity towards an analyte gas would be low at high temperatures. The sensitivity would increase with increase in temperature, reaches a maximum and fall with further increase in temperatures. Addition of catalysts and additives / dopants can alter these processes. Similarly, conditions under which thin/thick films are made would alter the surface characteristics leading to changes in activation energies in the processes.

1.5 Strategies to improve the gas interaction behavior of metal/alloy

1.5.1 Effect of sensor morphology

The effect of gas on the metals was observed by measuring the gas solubility in metal or by observing the change in volume, mass or resistance during the gas interaction. The measurement of resistance is simple and direct. The resistance is generally measured using two probe technique. Using such technique, measurement of magnitude change in the resistance of metal during gas interaction is very small. This can be handled by two approaches. In the first approach, metal will be handled with different geometry by varying the length, width and thickness. In the second approach by handling such low resistance metal using four probe measurement technique. Better results can be obtained by employing a combination of both the approaches. The gas interaction behavior of the metal/alloy will get enhanced if it is made and employed as nanostructured thin film. Smaller the grain size higher the surface area and better the gas interaction.

1.5.2 Effect of substitution of an element in base metal

The substitution of an element (solute) in the base metal (solvent) leads to alloy formation. The gas interaction property of the synthesized alloy is different from the pure metal. The interaction behavior of the alloy depends on the size, structure and nature of the alloying element. The choice of solute dictates the gas interaction property.

1.5.3 Effect of temperature

Generally the sensitivity of gas interaction with metal/alloy decreases with increase in temperature. Lower the temperature better the physisorption of gas molecules on the surface of the metal/alloy. Similarly the response and recovery times of the metal during the gas interaction studies decrease with increase in temperature. The sensitivity of gas interaction behavior of a metal/alloy as a function of temperature is different for different metal/alloy. The operating temperature of metal/alloy as a sensor is important because a temperature beyond which metal get converted in to metal oxide. The unique sensing property of metal or alloy will be lost due to phase transformation.

1.6 Scope of the thesis

The aim of this thesis is to synthesize novel materials (metal oxides and alloys) by solid state reaction and by soft chemical routes. The synthesized compounds have been characterized using XRD, Laser Raman, XPS, AFM, SEM, van der Pauw, AC impedance and Hall measurements. The characterized compounds have been made in to bulk, thick and thin films using suitable techniques. Bulk pellets were mainly used for conductivity and transport number (ions and electrons) measurements. The advantages of thick film technique are simple, cheap, compact and quick way to initiate the experiments. The advantage of thin film is their larger surface area which would help in studying the surface conducting property of the materials. Such morphologically tailored materials were tested for their sensing towards H_2, PG, NH_3 and NO_X at different temperatures. Semi-conducting metal oxide thin films are probed with analytes to understand the interaction mechanism, kind of adsorbed species on the oxide surface at different operating temperatures. Similarly the role of electron carrier concentration and charge carrier mobility of semi-conducting metal oxide in air and in the presence of analyte has been measured using high temperature Hall measurement facility. Few transition metal oxides are metastable in nature. It is difficult to synthesis such compounds by solid state reaction. Such metastable compounds can be prepared under extreme non equilibrium condition using facility like pulsed laser deposition. Such synthesized compounds have been characterized and tested its performance towards different gases especially at low operating temperature.

Baseline stability is an important criterion to be checked for a gas sensing material. If there is a continuous drift in the baseline, it can lead to false indication of the presence of pollutant in the ambient. If a compound is a mixed conductor (M^+ & e^-), drift in the baseline is a probable feature due to transport of ions from one electrode to another. Even though the compounds show drift in their baseline, they performed as a selective sensing material towards an analyte. Such a mixed conducting compound has been synthesized and tested for its baseline stability by using suitable measurement technique. Thesis also covers a simple and novel technique to synthesize nano metals and nano alloys at room temperature. These alloys have been tested for their performance with different concentrations of H_2 at 300 K.

Indium oxide, In_2O_3 is a potential metal oxide for trace level detection of NO_X. The thesis begins with the interaction of In_2O_3 with NO_X. The deposition of In_2O_3 thin film by pulsed laser deposition (PLD) on different substrates, its characterization using X-ray diffraction (XRD) and laser Raman spectroscopy is presented. The design, fabrication and installation of in-house developed high temperature van der

Pauw and Hall measurement facility for measuring conductivity, carrier concentrations and charge carrier mobility of In_2O_3 thin film in the ambient of air, and air containing different concentrations of NO_X between the temperature of 373 and 673 K are described. The adsorption behavior of oxides of nitrogen on the surface of In_2O_3 thin film at different temperatures using laser Raman spectroscopy are elucidated The thesis also discusses about the measurement of resistance and capacitance of In_2O_3 thin film during its interaction with NO_X using AC impedance technique.

Thesis elaborates the preparation and characterization of thin films of $Cu_2In_2O_5$ and $CuInO_2$ using XRD, thermal analysis, AC impedance, AFM and XPS. It highlights the use of p-type and n-type metal oxides using their characteristics of interaction with reducing and oxidizing gases between 423 and 677 K.

The thesis also discusses the usefulness of palladium based alloys for sensing hydrogen at 300 K. Conditions for the preparation of nano powders of palladium, nickel substituted palladium ($Pd_{1-X}Ni_X$ [$x = 0, 0.05$ & 0.1]) and cobalt and nickel substituted palladium ($Pd_{1-X-Y}Ni_XCo_Y$ [$x = y = 0.05$]) using low temperature reduction technique are optimized and presented. It discusses the deposition of thin film of palladium and its alloys using PLD. Thesis covers studies on the interaction of palladium and alloys as thin film towards argon containing hydrogen in the region of 2000 and 20000 ppm by measuring the change in the resistance using four probe technique.

Silver decamolybdate (a mixed conductor with Ag^+ and e^-) is one among the various materials which can sense low concentrations of NH_3 in air. But the compound showed continuous drift in the baseline (resistance) value when DC current is passed through the material. During the process Ag^+ get transported and deposited.

In order to improve the baseline stability of $Ag_6Mo_{10}O_{33}$, two approaches have been employed. In the first approach, tungsten is used as substitute for molybdenum. It is known that tungsten forms WO_6 octahedra like MoO_6. It is expected that tungsten substitution for molybdenum may alter the silver ion mobility. Thesis elaborates the preparation of tungsten substituted nominal compositions $Ag_6Mo_{10-X}W_XO_{33}$ (X = 0 – 2). The tungsten incorporated compounds have been characterized using XRD, backscattering SEM, Wagner polarization and conductivity measurement using DC and AC technique.

In the second approach, resistance of $Ag_6Mo_{10}O_{33}$ is measured by AC impedance technique which would overcome the net transport of Ag^+ and decomposition of the material. Thesis continues with the preparation, characterization and sensing behavior of $Ag_6Mo_{10}O_{33}$ thick film towards NH_3, H_2 and PG by AC measurements technique between the temperature of 423 and 623 K. The effect of dipole moment and polarizing property of the gases with $Ag_6Mo_{10}O_{33}$ by the measurement conducted by AC are briefly discussed. The advantage of using AC technique to improve the baseline stability of a mixed conductor is highlighted.

CHAPTER 2

Experimental methods, principles and its applications

2.1 Introduction

This chapter deals with different preparative techniques adopted for the synthesis of sensor materials and with the principles of various characterization techniques employed. The chapter also describes the design and fabrication of the experimental facilities employed for testing these compounds.

This thesis work involves preparation, characterization and gas sensing characteristics of $Cu_2In_2O_5$, $CuInO_2$, pure and tungsten substituted $Ag_6Mo_{10}O_{33}$. Using pulsed laser deposition (PLD) technique, thin film of In_2O_3, $Cu_2In_2O_5$ and $CuInO_2$ were prepared and used for studies on gas sensing. Targets of In_2O_3 and $Cu_2In_2O_5$ (prepared by solid state reaction method) were used for these depositions. Pure Pd and alloys of Pd with Ni and Co were prepared using chemical reduction technique at 300 K. They were deposited as thin films using PLD. These metallic thin films were investigated for gas sensing with different concentrations of hydrogen at 300 K.

2.2. Powder synthesis technique

2.2.1 Solid state reaction or ceramic method

The most widely used method for the preparation of polycrystalline solids is mixing and heating of the respective reactants at high temperatures. For a favorable reaction, thermodynamic and kinetic aspects of the process need to be considered [36]. The three factors which influence the rate of the reaction are:

1) area of contact between the reacting solids (surface area)
2) rate of nucleation of the product phase and
3) rates of diffusion of ions through the various phases and especially through the product phase

During heating, reactants partially react to form a layer of a product (nuclei). The formation of nucleation is rather difficult probably due to large amount of structural reorganization is involved in forming the product. Bonds must be broken and reformed and atoms must migrate, perhaps over considerable distance (on an atomic scale). To get homogenous products and also to bring down reaction temperature below 1273 K, precursors such as carbonates, nitrates and ammonium salts are recommended in the solid state reactions. In the present work, $Cu_2In_2O_5$, $Ag_6Mo_{10}O_{33}$ and tungsten substituted nominal compositions $Ag_6Mo_{10-X}W_XO_{33}$ were prepared by solid state reaction method.

2.2.2 Low temperature chemical reduction method

Solid state reactions are suitable for the preparation of oxides and are not generally suitable for the synthesis of metallic alloys. Holt et al synthesized finely divided metals from their salt solutions using reducing agents at 300 K [37]. The technique is of particular interest in catalyst industry, where high surface area metals or their alloys are needed and are difficult to obtain by other methods. The preparation of a number of inter-metallic compounds from mixed salt solutions using boiling hydrazine and hypo-phosphorous acid has been accomplished. The advantages of the technique are the homogeneity of the product (atomic level substitution of alloying elements), low temperature processing and higher surface area of the product. Using this technique, palladium and nominal compositions of $Pd_{0.95}Ni_{0.05}$, $Pd_{0.9}Ni_{0.1}$, and $Pd_{0.9}Ni_{0.05}Co_{0.05}$ were prepared at 300 K in this thesis work.

Among various reducing agents, hydrazine and sodium borohydride are handled in various chemical industries due to their mild reducing property with components. Hydrazine is basic in nature; one mole of hydrazine can release four moles of electrons during the process of reduction in water [38]. The chemically active species of hydrazine is hydrazinium ion, $N_2H_5^+$. In sodium borohydride ($NaBH_4$), chemically active species is BH_4^-. One mole of $NaBH_4$ can supply eight moles of electrons during the reduction [39, 40]. The electron release by N_2H_4 and $NaBH_4$ during the reaction is shown in eqn. 2.1 and 2.2 respectively. Equations 2.3 and 2.4 show reactions that occurring during the reduction of palladium ion by hydrazine and nickel ion by sodium borohydride in water respectively.

$$N_2H_4 + 4OH^- \rightarrow N_2 + 4H_2O + 4e^- \tag{2.1}$$

$$BH_4^- + 8OH^- \rightarrow BO_2^- + 6H_2O + 8e^- \tag{2.2}$$

$$Pd^{2+} + \frac{1}{2}N_2H_4 + 2OH^- \rightarrow Pd + \frac{1}{2}N_2 + 2H_2O \tag{2.3}$$

$$2Ni^{2+} + 4BH_4^- + 12H_2O \rightarrow 2Ni + 14H_2 + 4B(OH)_3 \tag{2.4}$$

The limitation of handling sodium borohydride for the metal reduction in water is its vigorous reaction with water. Because of this simultaneous reaction with water and with metal ions, it is difficult to find the completion of the reduction of metal ions. In order to avoid this difficulty, water can be replaced with other solvents and carry out the reduction process at room temperature. In the past, reduction of metal ions has been carried out in solvents like ethanol, acetone, isopropyl alcohol, diglyme and diethylene glycol [41]. Acetone forms a hydrazone complex with hydrazine and metal ions in the solution. This complex is explosive in nature. Hence, use of hydrazine with acetone as solvent is not recommended. Acetone is less reactive with sodium borohydride. Hence, in this work, reduction of metal ions was carried out using sodium borohydride in acetone at 300 K.

The compositions (%) of nickel and palladium in $Pd_{0.95}Ni_{0.05}$, $Pd_{0.9}Ni_{0.1}$ and nickel, cobalt and palladium in $Pd_{0.9}Ni_{0.05}Co_{0.05}$ alloy were analyzed using atomic absorption spectroscopy. For the analysis, atomic absorption spectroscopy model; GBC Avanta PM, Austria was used. The presence of impurities (sodium and boron) in the alloys is also analyzed using inductively coupled plasma optical emission spectroscopy ICPOES Model: Horiba Jobin Yvon, France was employed.

2.3 X-ray Diffraction

The electrons in an atom coherently scatter light. The atoms in a crystal are arranged in a periodic arrangement and the distance between the atoms in the crystal are in a few Å. The wavelength of X-rays is similar to the distance between the atoms. Constructive interference of X-rays scattered by parallel planes of atoms will produce a diffraction peak when Bragg’s law is satisfied [42, 43]. Bragg’s law relates the wavelength of electromagnetic radiation (λ) to the diffraction angle (θ) and between these parallel planes spacing (d) in a crystalline sample and is shown by the eqn. 2.5:

$$n\lambda = 2d\sin\theta \qquad (2.5)$$

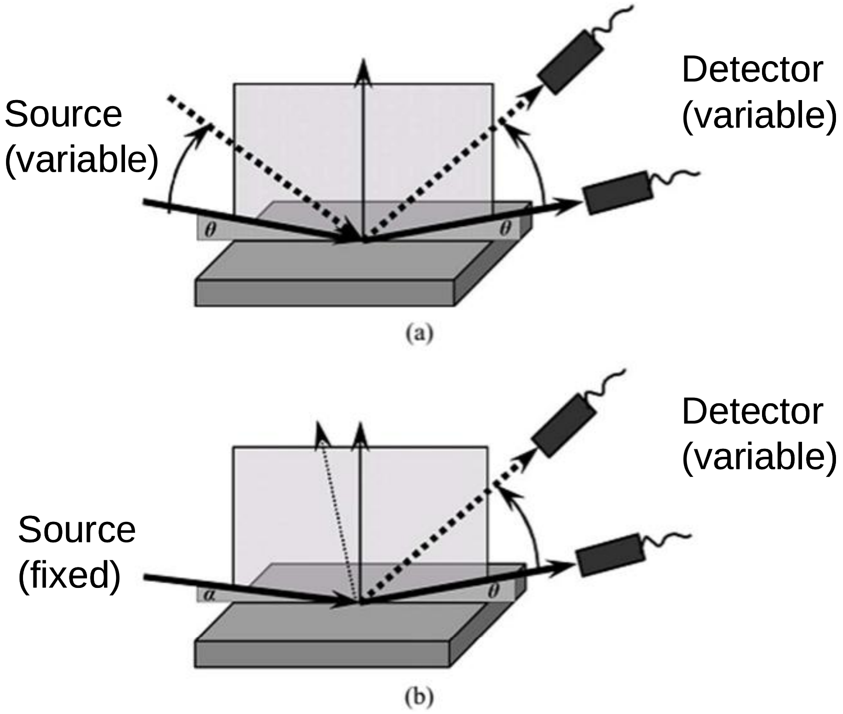

Fig. 2.1 X-ray diffraction of sample in the form of a) Powder – indicating the incidence and diffracted beam are in scanning mode and b) glancing incidence of thin film indicating fixed incidence and diffracted beam in scanning mode [44].

The scattering of X-rays from atoms produces a diffraction pattern, which contain information about the atomic arrangement within the crystal. The position of the diffraction peaks are determined by the distance between parallel planes of the atoms. Schematic of powder X-ray diffraction is shown in fig. 2.1a. The intensity of the diffraction peaks are determined by the arrangement of atoms in the entire crystal. A powder scan involves simultaneous moving the incident angle of X-rays by ‘θ’ and the detector angle by ‘2θ’, so that the incident angle of X-rays is always ½ of the angle between transmitted ray and the detector. However, X-rays with large glancing angles of incidence will go through a few to several hundred micrometers inside the material under investigation, depending on its radiation density, so that when it comes to thin film analysis, the beam penetration depth may be much greater than the sample thickness. The characterization of thin films using the conventional powder diffraction configuration generally produces weak signal from the film and intense signal from the substrate. Hence conventional XRD is rather not suitable for detailed study of thin film specimens. In order to overcome such limitation, glancing incidence configurations have been developed to render the XRD measurement more sensitive to the near surface region of the sample and minimize the substrate contribution.

In the glancing angle X-ray diffraction technique, geometry is modified to provide an ‘asymmetric’ diffraction, which allows access to small depth in the sample by varying the angle of incidence [44]. Schematic of glancing incidence X-ray diffraction is shown in fig. 2.1b. Thus, the incident beam goes over a long way over the film surface, reinforcing its diffraction pattern. Unlike conventional powder diffraction geometry, which observes planes parallel to the surface of the sample, in the case of glancing incidence XRD, crystal planes inclined with respect to the surface of the sample are observed; who’s normal is the bisector of the angle formed by the incident and the diffracted beam.

XRD patterns of $Cu_2In_2O_5$, $CuInO_2$, In_2O_3, $Ag_6Mo_{10}O_{33}$, $Ag_6Mo_{9.75}W_{0.25}O_{33}$, $Ag_6Mo_{9.5}W_{0.5}O_{33}$, palladium and its alloys were recorded using PANalytical, Model: X'Pert Pro MPD, at room temperature using CuKα radiation. For the characterization of Pd, $Pd_{0.93}Ni_{0.07}$, $Pd_{0.97}Ni_{0.03}$, and $Pd_{0.91}Ni_{0.04}Co_{0.05}$ thin films, glancing incidence X-ray diffraction (Cu Kα_1) was employed using INEL XRG-3000 Diffractometer. This diffractometer has the facility of parallel beam asymmetric geometry with a glancing angle incidence 5^{o} (ω) with an angular resolution of 0.0125^{o}.

2.4 Study of thermal behavior of materials

Thermal analysis involves the measurement of change in physical and chemical properties of materials especially enthalpy, heat capacity, coefficient of expansion and mass as a function of temperature. When the material under investigation undergoes stoichiometric changes under different ambient, a study of mass change phenomenon would provide an insight in to the types of intermediates formed and the kinetics of their formation. The three main thermal analytical techniques used to characterize the thermal properties of the materials are Thermo Gravimetric Analysis (TGA), Differential Thermal Analysis (DTA) and Differential Scanning Calorimetry (DSC). The detailed applications of handling such facilities are well dealt in the text books [45]. In the present work $Cu_2In_2O_5$ was characterized by thermogravimetry and differential thermal analyzer using SETSYS Evolution 16/18, M/s Setaram Instrumentation, Caliure, France.

2.5 Principle of thin film deposition (PLD) technique and its applications

Pulsed laser deposition is a thin film deposition technique, which uses short and intensive laser pulses to evaporate the material in a target. Most of the materials show strong absorption in the wavelength range of 200 to 400 nm. Hence, if a laser light of wavelength in this region is used, the penetration depth into the target material will be short and removal of thin layers would be possible [46 – 48]. During laser ablation, high intensity laser pulses of short wavelength are focused using focusing lenses on the surface of the target. On the surface, they are partially absorbed and the absorbed radiation is immediately converted into electronic excitations. The excited electrons transfer their energy to the lattice within a few picoseconds resulting in heating of the surface to a depth of 1/α, where 'α' is the characteristic optical absorption coefficient of the material.

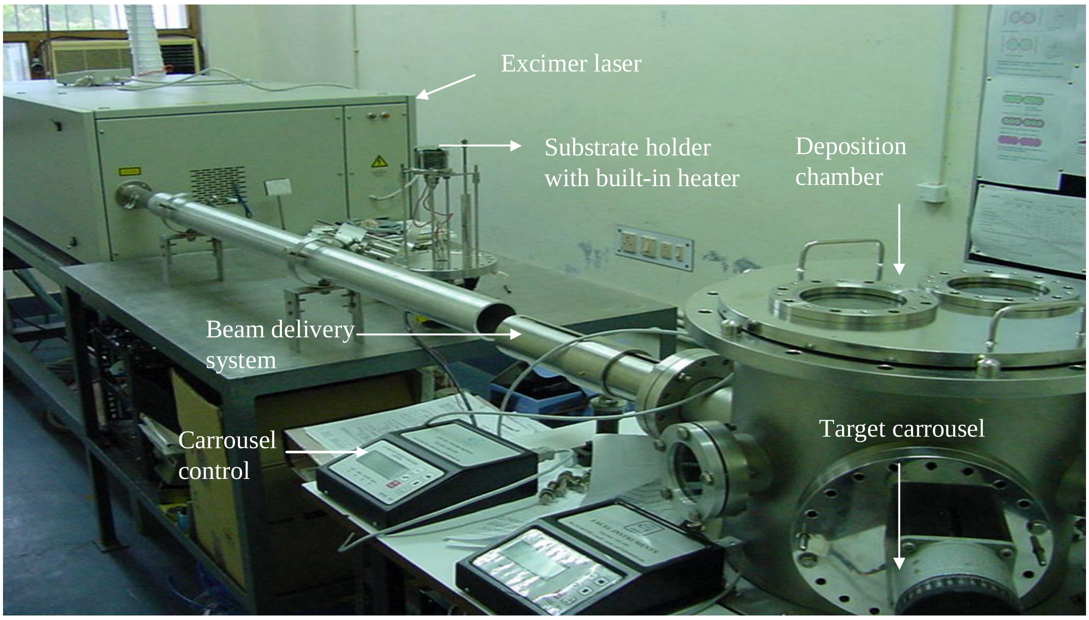

Fig. 2.2 Photograph of PLD facility used in the present investigations

The thermal diffusion length for a material, l_{ther} is given by $l_{ther} = 2\sqrt{Dt}$, where D is the thermal diffusivity and t is the pulse duration. If thermal diffusivity 'D' is smaller than 1/ α, then the sample will be heated down to a depth of 1/ α independent of the pulse duration. Ideally the plasma plume produced should have the same stoichiometry as the target if one wants to grow a film of the correct composition. For example, if the target surface was heated slowly, say by absorbing the light from a continuous wave laser source, and then this would allow a significant amount of the incident power to be conducted into the bulk of the target. The subsequent melting and evaporation of the surface would essentially be thermal i.e.

the difference between the melting points and vapor pressures of the target constituents would cause them to evaporate at different rates so that the composition of the evaporated material would change with time and would not be representative of the target.

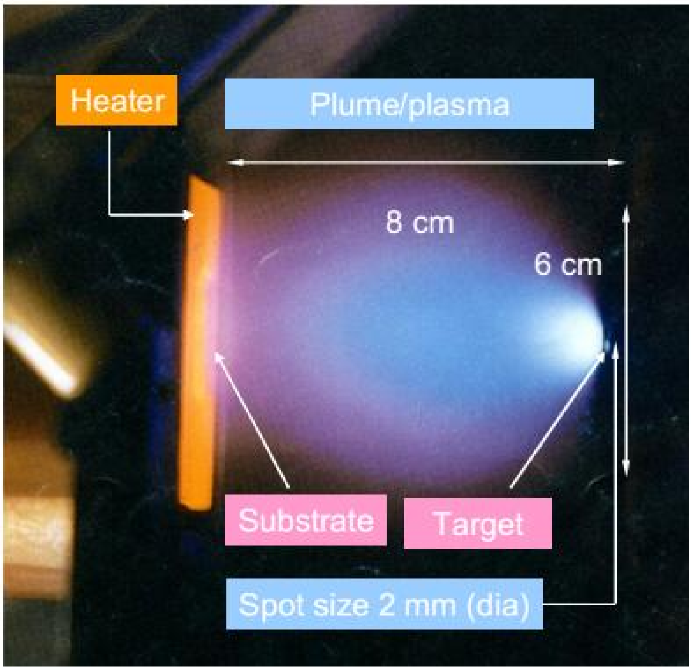

Fig. 2.3 Plume / Plasma generated during Laser – Target interaction

The incongruent evaporation leads to films with different stoichiometry from the target. To achieve congruent evaporation, the energy from the laser must be dumped onto the target surface rapidly, to prevent a significant transport of heat into the subsurface material, so that the melting and vapor points of the target constituents are achieved simultaneously. The high laser power density is most readily achieved with a pulsed or Q-switched source focused to a small spot on the target. If the energy density is below the ablation threshold for the material, then no material will be removed at all, though some elements may segregate to the surface. In the present work thin films were deposited using an excimer laser (KrF; λ = 248 nm, M/s Lumonics, Canada) having pulse width of 30 ns operating at 20 Hz.

The photograph of the PLD assembly used in this work is shown in fig. 2.2. The laser from the source is passed through an optical window of a SS vacuum chamber and is focused on the surface of the target. The chamber is pumped down by a turbo molecular pump and has provisions to let in gases at a precisely known flow rate. Using a gate valve mounted between the vacuum chamber and the turbo molecular pump, and by maintaining a constant flow of oxygen into the chamber, the chamber could be maintained at different pressures of oxygen. Through the ports provided in the chamber, a target holder and substrate holders are mounted. The target holder is rotatable using a DC motor so that ablation is not confined to one spot on the target but is uniformly spread out on its surface. Interaction of laser beam with the target material causes the ejection of luminous plume as shown in fig. 2.3. Materials from the laser plume are then allowed to re-condense on a substrate attached to a substrate holder. The substrate can be heated to desired temperature by means of a heating facility provided in the substrate holder and this enhances the film growth process on the substrate. Conditions, such as substrate temperature, oxygen partial pressure, energy density at the laser spot etc. need to be optimized for growth of films. The conditions employed in each case are presented in the respective chapters. Substrates used for the deposition of thin film are polycrystalline alumina, sapphire and silicon. In this work In_2O_3, $Cu_2In_2O_5$, $CuInO_2$, Pd, $Pd_{0.93}Ni_{0.07}$, $Pd_{0.97}Ni_{0.03}$, and $Pd_{0.91}Ni_{0.04}Co_{0.05}$ were deposited using PLD.

2.6 Laser Raman Spectroscopy technique - principle and its applications

Inelastic scattering of light by atomic vibrations in molecules, liquids and solids, discovered by C.V. Raman in 1928, is known as Raman scattering. It is a non-destructive chemical analysis technique, which provides detailed information about chemical structure, phase and polymorph, crystallinity and gas interaction mechanism with the surface [49].

In Raman spectroscopy, the sample is irradiated by intense beam of frequency 'ω_o' in the UV-Visible region, and the scattered light is collected and analysed. The scattered light consists of two parts; one is the Rayleigh scattering part which is intense and has the same frequency as the incident beam 'ω_o'. On the other hand, the second part is called Raman scattering which is very weak (10^{-10} of the incident beam) and has frequencies $\omega_o \pm \omega_p$, where ω_p, is the characteristic vibrational frequency of the system. The $\omega_o - \omega_p$, is called the Stokes line, whereas the $\omega_o + \omega_p$ are anti-Stokes lines. Hence, in Raman spectroscopy, the vibrational frequency ω_p is measured as a shift from the incident photon frequency ω_o. Under normal conditions, the population of phonons in a solid at ground state is much larger than that at first excited state which is governed by Maxwell-Boltzmann distribution law. Therefore, the Stokes lines are stronger than anti-Stokes lines. Although, both the lines give the same information, it is in practice to measure only the Stokes side of the Raman spectrum.

Laser Raman spectroscopic technique was employed to characterize In_2O_3 thin film. The characterization was done for the thin film in air and in the presence of air containing NO_X using Renishaw micro Raman spectrometer (M/s InVia, Germany) at ambient temperature. 514.5 nm Argon ion laser was used as the excitation source, which was focused to 1 µm spot size by a 50 X microscope objective.

2.7 Atomic Force Microscope - principle and its applications

Atomic Force Microscopy is one of the best nondestructive physical techniques for surface characterization of various types of samples and specifically for studying morphology of thin films. It gives a clear picture of the arrangement of grains and its average size in a solid crystal surface [50]. It comprises a micro cantilever that is allowed to move along the surface of the sample. The cantilever tip is often made of silicon oxynitride with a thin coating of gold for better reflection of light. A laser beam is allowed to fall on the tip of the micro cantilever while probing the topography of the sample surface. The cantilever moves deflecting the laser beam, which in turn is collected by the surrounding photodiodes and sent to the detector for analyzing. The process of characterization can be either in contact or non – contact or semi – contact mode with the sample surface. The non – contact mode is more useful since the tip of cantilever doesn't touch the sample surface and hence doesn't affect the morphology. The force of interaction between the tip of cantilever and the sample atoms is shown by the eqn. 2.6.

$$f = \frac{1}{2\pi}\sqrt{\left(\frac{k}{\mu}\right)} \tag{2.6}$$

where ‘f’ is the resonance frequency, ‘k’ is the force constant and ‘μ’ is the reduced mass which is given by $\left(\mu = \frac{(m_1 \, x \, m_2)}{(m_1 + m_2)}\right)$. Here, m_1 and m_2 are the masses of atoms in sample and the cantilever tip respectively. The resonance frequency of the micro cantilever is generally kept constant by varying the amplitude of its vibrations. This interaction is controlled by a feedback loop connected to the cantilever holder uniformly with the sample surface. In the present work, surface morphology of In_2O_3, $Cu_2In_2O_5$, $CuInO_2$, Pd, $Pd_{0.93}Ni_{0.07}$, $Pd_{0.97}Ni_{0.03}$, and $Pd_{0.91}Ni_{0.04}Co_{0.05}$ thin films were analyzed using Atomic Force Microscope, Model Solver Pro of M/s NT – MDT, Russia.

2.8 X-ray Photoelectron spectroscopy - principle and its applications

X-ray photoelectron spectroscopy (XPS) is a surface analysis technique in which a solid surface in vacuum is irradiated with X-rays (200-2000 eV) to produce photoelectrons by direct transfer of energy from the X – ray photons to core-level electrons in the atoms of the sample [51, 52]. The kinetic energy of the photoelectrons, KE, would be equal to the ($h\nu - BE$) where ν is the frequency of the X-rays used, h is the Planck’s constant and BE is the binding energy of the electrons in the shell. Kinetic energy distribution of the emitted electrons is measured using an electron energy analyzer and photo electron spectrum is obtained. The observed binding energy for an ejected electron is the fingerprint of an electron in the core level of an element. Electrons in the ‘s’ orbital will appear as singlet in the XPS spectrum whereas the electrons in the other orbital will appear as doublets due to spin orbit coupling. Binding energy of lower ‘j’ value in doublet would be higher (BE $2p_{1/2}$ >

$BE2p_{3/2}$) and the energy separation between the doublets would increase with increase in atomic number. Shift in the original binding energy values occur depending on the nearby coordinating atoms/groups and this is called chemical shift. Chemical shift due to the difference in the chemical environment of a particular atom gives an idea about the coordination structure in the lattice. A shift in BE values can also be caused by the surface charging of the samples, which arises due to the insulating nature of the samples and this is usually corrected with a standard reference such as carbon and gold.

In the present work, X-ray photoelectron spectra of the samples were recorded using XPS system of M/s SPECS, Germany. The facility is equipped with a reaction chamber, in which sample can be heated to a maximum of 873 K by an infrared lamp in desired gas ambience and can be evacuated to 10^{-8} mbar subsequently for transferring to analysis chamber through a gate valve without exposing it to the air ambient. Monochromatic Al K_{α} (1486.6 eV) radiation was used for excitation at a constant power of 400 W. The hemispherical Phoibos 150 mm analyser equipped with 1D – delay line detector was operated in Fixed Analyser Transmission (FAT) mode with constant pass energy of 50 eV throughout the measurements. The spectrometer work function was adjusted to Au $4f_{7/2}$ peak centered for metallic gold located at a binding energy of 84.0 eV using electron gun operated at 1 eV with an emission current of 2.3 μA for charge correction of the specimen. Survey scans were recorded with an energy step of 1 eV in the energy range 1000 - 4 eV, whereas selected regions were recorded with an energy step of 0.05 eV and dwell time of 0.1 s/step. All the selected region recordings were averaged out for 5 scans. The vacuum level inside analysis chamber was maintained around 10^{-10} mbar throughout all the measurements.

Most of the semi-conducting metal oxides exhibits non – stoichiometry. This non-stoichiometry arises due to the presence of the mixed valence states of the metals in the metal oxides. The gas interaction studies and existence of mixed oxidation states of metals in metal oxides elucidated from XPS are helpful to confirm whether the compound is n-type or p-type semiconductor. In this work, oxidation states of $Cu_2In_2O_5$ and $CuInO_2$ thin films were investigated.

2.9 Scanning Electron Microscope - principle and its applications

Electron microscopy has been a valuable materials characterization tool which has contributed greatly to biology, medicine and material science. The wide spread use of electron microscopes is because it permits the observation and characterization of materials on nanometer (nm) to micrometer (μm) scale [53, 54].

In scanning electron microscope an accelerated electron beam is moved over the specimen surface in sequence of closely spaced lines. Interaction of electron beam with matter causes various physical phenomena such as absorption, reflection, backscatter and diffraction. In addition to the above said physical phenomena, it also causes the emission of low energy secondary electrons and X - rays. In SEM the effects due to the secondary emission and backscattered electrons are measured. The emission of secondary and backscattered electrons varies from point to point depending on the variations in the composition or topography of the sample. The effects due to this are converted to an electrical signal, amplified and displayed as modulations of brightness on the cathode ray tube. The magnification of the resultant image is determined by the ratio of the distance travelled by the recording beam in a given time interval to that travelled by the synchronously deflected scanning beam in the same time interval.

Energy dispersive X-ray spectroscopy (EDX)is one of the salient features of SEM and can be used to determine the elemental composition of the surface of the samples. When electrons from incident beam interact with atoms on the surface, secondary electrons from inner shells of the atoms are ejected out. Electrons from outer shells will drop in to the vacant levels of the inner shells and this result in the emission of X – rays characteristic of the atom. Hence, by measuring the energy of these characteristic X – rays, information about the elemental composition of the sample can be obtained. Since these X – rays are formed by the interaction of electron beam with the atoms on the sample surface and the penetration depth of electron beam are very low, the deduced composition corresponds to very narrow surface dimensions (ca. 0.5 × 0.5 μm area and to a depth of 0.5 to 2 μm). Hence a surface scan can be made and compositional variations in the sample can be derived.

In the present work, morphologies of $Ag_6Mo_{10}O_{33}$, $Ag_6Mo_{9.75}W_{0.25}O_{33}$, $Ag_6Mo_{9.5}W_{0.5}O_{33}$, and $Ag_6Mo_{9.0}W_{1.0}O_{33}$ were investigated using Ultra 55 Scanning Electron Microscopy, Germany. The compositional variation of the sample was analyzed using EDX.

2.10 Surface profiler - principle and its applications

Surface profiler or profilometer is an instrument used to measure the surface profile of thick or thin film in order to quantify its smoothness and uniformity. A surface profiler can measure small surface variations in vertical stylus displacement as a function of position. In surface profiler, a diamond stylus is moved vertically in contact with a sample and then moved laterally across the sample for a specified distance and specified contact force according to a user-programmed scan length and speed. A typical profilometer can measure small vertical features ranging in height from 10 nm to 1 mm. The height position of the diamond stylus generates an analog signal which is converted into a digital signal stored, analyzed and displayed. The radius of the diamond stylus ranges from 20 nm to 25 μm and the horizontal resolution is controlled by the scan speed and data signal sampling rate. In the present investigations, thicknesses of metal oxides in the form of thick and thin film were measured using profilometer Dektak^3 of M/s Veeco, USA. The thickness of thin films of In_2O_3, palladium, $Pd_{0.93}Ni_{0.07}$, $Pd_{0.97}Ni_{0.03}$, and $Pd_{0.91}Ni_{0.04}Co_{0.05}$ and thick film of $Ag_6Mo_{10}O_{33}$ were measured.

2.11 Characterization based on electrical measurement techniques

Electrical behavior of the materials is generally carried out by direct current (DC) and alternating current (AC) techniques. DC is a unidirectional flow of movement of electric charge carriers. Using DC, measurement of resistance (R) or resistivity (ρ) of the material is primary step in knowing about its electrical properties. The material resistivity depends on the free electron and hole densities ‘n’ and ‘p’, and the electron (μ_n) and hole mobilities (μ_p) as shown in eqn. 2.7.

$$\rho = \frac{1}{q(n\mu_n + p\mu_p)} \tag{2.7}$$

2.11.1 Measurement of resistance using direct current (DC) Technique

2.11.1.1 Two probe measurement

The two probe technique is one of the most commonly employed techniques for measuring the resistance of the materials [55]. The method would appear to be easier to implement, because only two probes need to be manipulated. But, the interpretation of the measured data is more difficult. It employs the constant-current method to measure the resistance, which sources a current to the device under test and measures the voltage. Resistance is then calculated and displayed using the known current and measured voltage. The measurement of total resistance (R_T) of the sample between the two probes is given in eqn. 2.8. The schematic of the two probe arrangement is shown in fig. 2.4.

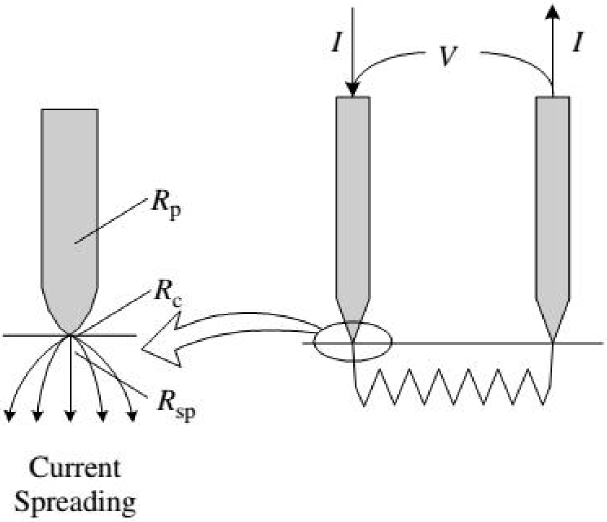

Fig. 2.4 Two probe arrangement showing the probe resistance R_P, the contact resistance R_C and the spreading resistance R_{SP} [55].

$$R_T = \frac{V}{I} = 2R_P + 2R_C + 2R_{SP} + R_S \tag{2.8}$$

Here, R_P is the probe resistance, R_C the contact resistance at each metal/sample contact, R_{SP} the spreading resistance under each probe, and R_S the sample resistance. In DC measurements, generally R_C and R_{SP} are assumed to be identical. The contact resistance arises from the mechanical metal probe contacting the semiconductor. The spreading resistance accounts for the resistance encountered by the current when it flows from the small metal probe into the semiconductor and from the semiconductor to the probe. The polarization of charges and/or ions at the respective electrodes will occur during DC measurements. In the two probe measurement each probe serves as a current and as a voltage source. The two probe technique is suitable only to those materials whose resistances are above kΩ. In this work, the resistances of In_2O_3 thin film, $Ag_6Mo_{10}O_{33}$, $Ag_6Mo_{9.75}W_{0.25}O_{33}$ and $Ag_6Mo_{9.5}W_{0.5}O_{33}$ were measured using 34970A, M/s Agilent Data Acquisition Switch Unit, Malaysia.

2.11.1.2 Four probe measurement

The technique involves bringing four equally spaced probes in contact with a material of unknown resistance as shown schematically in fig. 2.5. The two outer probes (1, 4) are used for sourcing current and the two inner probes (2, 3) are used for measuring the resulting voltage drop across the surface of the sample [55]. Here S_1, S_2 and S_3 are the distances between the probes. The four probes eliminate measurement errors due to the probe resistance, the spreading resistance under each probe, and the contact resistance between each metal probe and the semiconductor material. Because a high impedance voltmeter draws little current, the voltage drops across the probe, spreading and contact resistance are very small. The four probe resistivity of the sample is calculated using the eqn. 2.9:

$$\rho = F(s,t)\frac{\Delta V}{I} \tag{2.9}$$

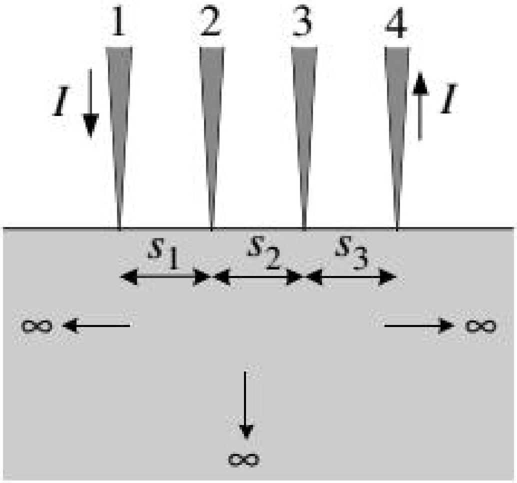

Fig. 2.5 Schematic of collinear four probe for current and voltage flow measurement [55]

Here, ‘ΔV’ is the measured differential voltage and ‘I’ is the applied current. Here ‘F’ is the correction factor, ‘s’ is the distance between the probes and ‘t’ the sample thickness. Since the measurements are made on finite areas, correction factors have to be incorporated based on the sample geometry. This correction factor depends on the sample thickness, edge effects and the location of the probe on the sample. Other considerations that need to be considered for accurate four probe measurements are the spacing of the probes and temperature effects. Small spacing differences in probe spacing can cause the resistivity values to vary widely across a sample surface.

A high quality four point head is necessary to get repeatable and reliable resistivity values. The limitation encountered in four probe technique was modified by van der Pauw [56].

2.11.2 Four probe measurement of resistivity using van der Pauw technique

The van der Pauw technique is suitable for flat sample (fig. 2.6) and would be applicable if the following conditions are obeyed.

1. The contacts are at the circumference of the sample.
2. The contacts are sufficiently small.
3. The sample is homogenous in thickness.
4. The surface of the sample is singly connected, i.e., the sample does not have isolated holes.

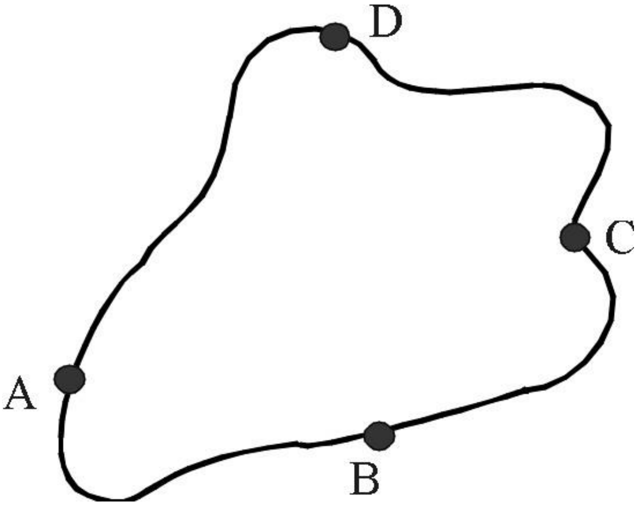

Fig. 2.6 Schematic of a typical sample of arbitrary shape with four small contacts to measure specific resistivity by van der Pauw and Hall measurements [56]

Schematic of a van der Pauw configuration is shown in fig. 2.6. A flat sample of a conducting material of arbitrary shape with successive contacts A, B, C and D fixed on arbitrary places along the circumference is considered such that the above-mentioned conditions are fulfilled [57]. We define the resistance $R_{AB,\ CD}$ as the potential difference $V_D - V_C$ between the contacts D and C per unit current passing through the contacts A and B. The current enters the sample through the contact A and leaves it through the contact B. Similarly we define the resistance $R_{BC,\ DA}$ and the following relationship would be valid (eqn. 2.10):

$$\exp(-\pi R_{AB,CD}\, d/\rho) + \exp(-\pi R_{BC,DA}\, d/\rho) = 1 \qquad (2.10)$$

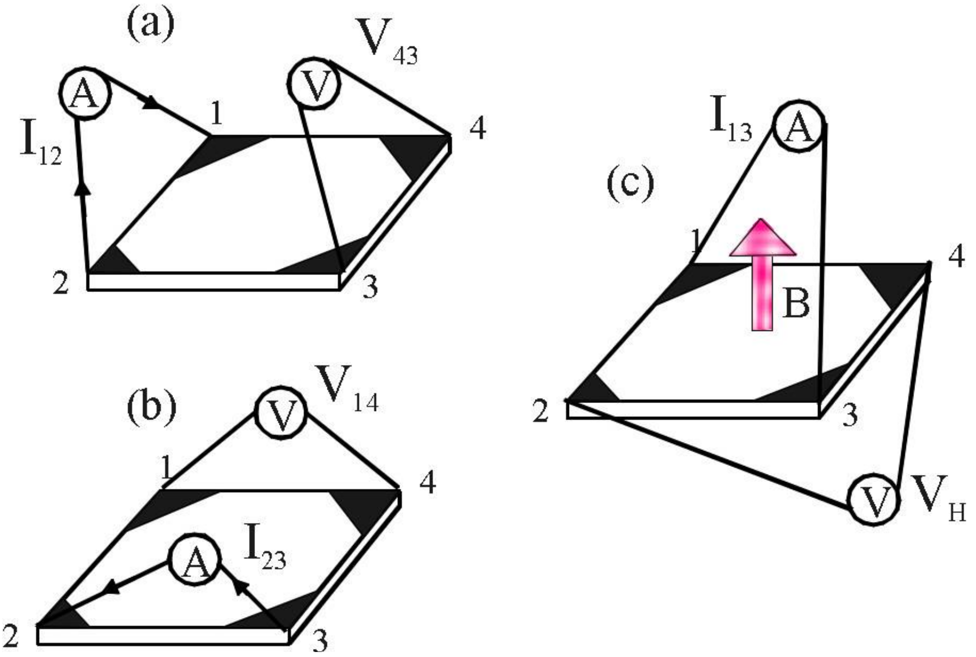

Fig. 2.7 Schematic of a van der Pauw configuration used in the determination of the two characteristic resistances R_A and R_B a) current (1,2) and volt (4,3), b) current (2,3) and volt (1,4) and c) current (1,3) and volt (2,4) [57]

where ‘ρ’ is the specific resistance of the material and ‘d’ is the thickness of the sample. In order to obtain the two characteristic resistances, one applies a dc current ‘I’ into contact 1 and draws out of contact 2 and measures the voltage V_{43} from contact 4 to contact 3 as shown in fig. 2.7a. Next, one applies the current I into contact 2 and draws out of contact 3 while measuring the voltage V_{14} from contact 1 to contact 4 (fig. 2.7b). R_A and R_B are calculated by means of the following eqn. 2.11:

$$R_A = \frac{V_{43}}{I_{12}} \text{ and } R_B = \frac{V_{14}}{I_{23}} \tag{2.11}$$

From eqn. 2.10, 'ρ' can be represented as in eqn. 2.12.

$$\rho = \frac{\pi d}{\ln 2}\left(\frac{(R_{AB,CD} + R_{BC,DA})}{2}\right) f\left(\frac{R_{AB,CD}}{R_{BC,DA}}\right) \tag{2.12}$$

Here, 'f' is the geometric factor. Better results are obtained when the geometric factor is maintained unity ('f' becomes unity if we choose a perfect square shaped geometry).

2.11.3 Carrier concentration determination using Hall measurement

The objective of the Hall measurement in the van der Pauw technique is to determine the sheet carrier (electrons) density 'n' by measuring the Hall voltage 'R_H'. The Hall voltage measurement consists of a series of voltage measurements with a constant current I and a constant magnetic field B applied perpendicular to the plane of the sample shown in fig. 2.8. The principle is based on Hall effect. When a conductor is placed in a magnetic field and a current passed through it, an electric field will be produced, the direction of which is normal to both the current and magnetic field directions. This phenomenon, discovered by E.T. Hall in 1879 is known as Hall effect [55].

The Hall effect is an important tool for the characterization of materials particularly semiconductors. It provides a direct determination of both the sign of charge carriers, e.g. electron or holes and their concentrations in a given sample. The basic setup is shown in fig.2.8. A thin strip (thickness δ) of the material to be studied is placed in a magnetic field B oriented at right angles to the strip.

A current I is arranged to flow through the strip from left to right, and the voltage difference between the top and bottom of the sample is measured. Assuming the voltmeter probes are vertically aligned, the voltage difference is zero, when B = 0 (‘B’ is magnetic field).

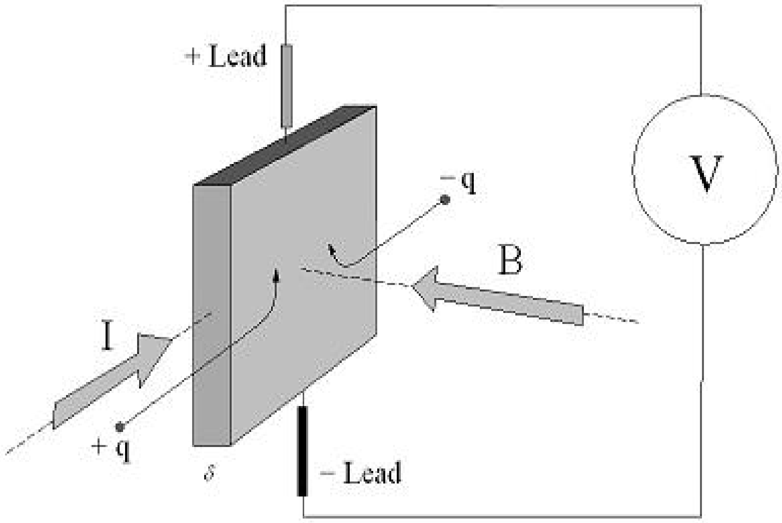

Fig. 2.8 Schematics of Hall effect measurement for a semi-conducting material

The current ‘I’ flows in response to an applied electric field, with its direction established by convention. However, on the microscopic scale ‘I’ is the result of either positive charges moving in the direction of ‘I’, or negative charges moving in the opposite. In either case, the magnetic Lorentz force (q x v x B) causes the carriers to curve upwards. Here, ‘q’ is the charge of the electron and ‘v’ is velocity experienced by the electron due to applied field. Since, the charge cannot leave the top or bottom of the strip, a vertical charge imbalance builds up in the strip. This charge imbalance produces a vertical electric field, which counteracts the magnetic force, and a steady-state situation is reached. The vertical electric field can be measured as a transverse potential difference on the voltmeter. The voltage developed is given by the following relationship [58]:

$$R_H = \frac{IB}{ne} \qquad (2.13)$$

where ‘R_H’ is Hall voltage and ‘I’ is the current.

If the carriers are electrons (q = -e), they accumulate on the top of the strip and the voltmeter would read a negative potential difference. Alternately, should the carriers be holes (q = +e), a positive voltage would be measured.

In order to measure the Hall voltage ‘R_H’, a current I is forced through the opposing pair of contacts 1 and 3 and the Hall voltage ‘R_H’ (= V_{24}) is measured across the remaining pair of the contacts 2 and 4 of the sample geometry shown in fig. 2.7c. Once the Hall voltage ‘R_H’ is acquired, the sheet carrier electron density ‘n’ can be calculated ‘n’ = IB/qR_H from the known values of ‘I’, ‘B’ and ‘q’. From the measured four probe resistivity (ρ) using van der Pauw method and charge carrier density (n) calculated from Hall voltage, mobility of the carrier in the sample can be calculated using the eqn. 2.14:

$$\mu = \frac{1}{\rho}\left(\frac{1}{ne}\right) \qquad (2.14)$$

2.11.4 Setting up of van der Pauw test facility

To measure four probe resistivity, carrier concentrations and mobility of electrons in the samples under investigation, van der Pauw and Hall measurements test facilities were indigenously designed, fabricated and installed as part of the thesis work. For the measurement of four probe resitivity of the sample, suitable sample holder and chamber (SS 316) were made with necessary gas inlet, outlet and electrical contacts. The schematics of the sample positioned over the heater along with electromagnet and Hall measurement facility is shown in fig. 2.9. The SS chamber is fixed to the frame of the electromagnet and is provided with a tilt adjustment so as to align the sample to be perpendicular to the direction of the magnetic field. The heater is a non – inductively wound resistive wire so that no net magnetic field emanates from it during heating of the samples.

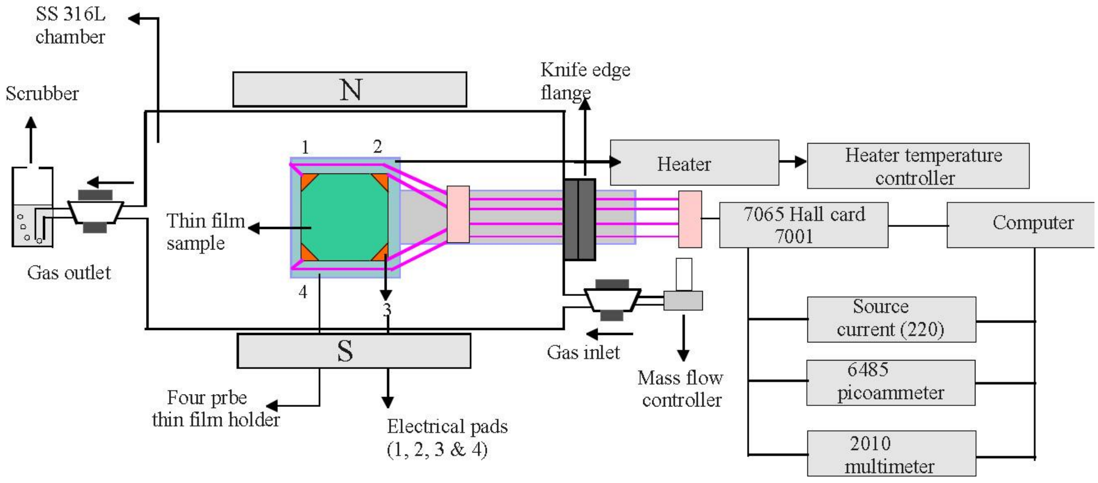

Fig. 2.9 Schematics of Hall measurement facility

The temperature of the sample is measured using a thermocouple mounted inside the chamber. The electromagnet has a pole gap of 60 mm and it is capable of providing a uniform magnetic field of 1T inside the gap. The electromagnet is provided with a switching facility for automated reversal of the magnetic field. The magnetic field in the gap is measured using a Hall probe (Group 3, DTM – 150 Digital Teslameter, USA). The presence of any longitudinal/transverse temperature gradients in the thin film would generate thermo voltages, which may get superimposed on the measured Hall voltage. Hence, the substrate containing thin film is placed in constant temperature zone of the stainless steel chamber, where the temperature stability is ± 1 K. The sample is positioned perpendicular to applied magnetic field inside the SS chamber. The photograph of external view of four probe thin film facility along with electromagnet is shown in fig. 2.10.

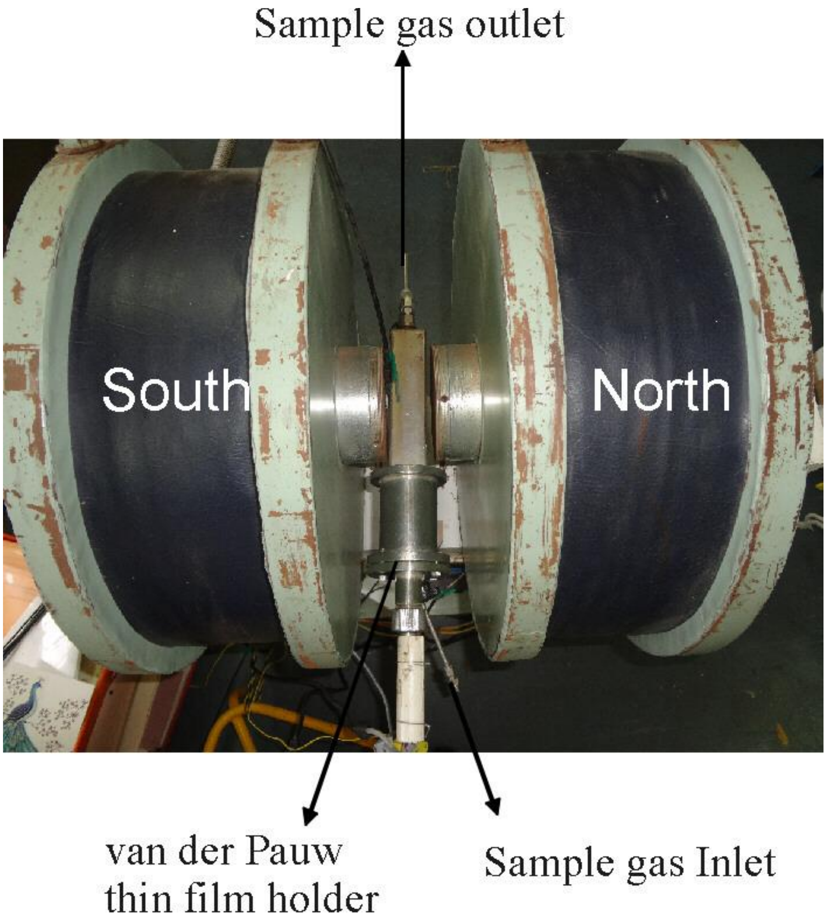

Fig. 2.10 Photograph of four probe van der Pauw thin film facility along with electromagnet for handling Hall measurements

A programmable current source (M/s Keithley Instruments, Model 220) is used for sourcing the current through any two out of the four terminals. A picoammeter (M/s Keithley Instruments Model 6485) is used to measure the current passing through the thin film specimen. The voltage that developed across the other two terminals of the thin film specimen is measured using a multimeter (M/s Keithley Instruments, Model 2010).

A Hall voltage card (M/s Keithley Instruments, Model 7065), which operates on van der Pauw is used in the high density switching system (M/s Keithley Instruments Model 7001) scanner for switching the currents and voltage terminals through the software program. All these instruments are integrated and interfaced with a personal computer using GPIB card and a program was written for automation. To avoid the voltage signal arising from the deviation from orthogonality of the magnetic field and current directions, the polarities of the current and magnetic fields were reversed and the measurements are taken again.

The four probe resistivity, carrier concentrations and charge carrier mobility of In_2O_3 thin film was measured using van der Pauw and Hall measurement facility in air and in air containing NO_X between 373 and 673 K.

2.11.5 Measurement of resistance by two probe alternating current (AC) technique - theory and its application

In AC technique, the current periodically reverses its direction, usually sinusoidally at certain frequency or range of frequencies. The term is also used to describe alternative voltages.

For measuring impedance of the sample a small amplitude sinusoidal (ac) signal is applied to perturb the sample and the frequency response is recorded as impedance and phase angle [36, 59]. The applied potential is given by eqn. 2.15 and the output current from the system is also sinusoidal which is given by eqn. 2.16:

$$E = E_0 \exp(j\omega t) \tag{2.15}$$

$$I = I_0 \exp(j\omega t + \phi) \tag{2.16}$$

According to Ohm's law, impedance (Z) of the circuit at any frequency (ω) can be shown by eqn. 2.17 to 2.20.

$$Z^* = \frac{E}{I} = \left(\frac{E_0}{I_0}\right)\exp(-j\phi) \tag{2.17}$$

$$= Z \exp(-j\phi) \tag{2.18}$$

$$= Z\cos\phi - jZ\sin\phi \tag{2.19}$$

$$Z^* = Z^{'} - jZ^{''} \tag{2.20}$$

where, $Z^{'} = Z\cos\phi$ and $Z^{''} = Z\sin\phi$, $j = \sqrt{-1}$. Z' and Z" are respectively real and imaginary parts of the impedance. The phase difference (ϕ) is represented by the eqn. 2.21.

$$\phi = \tan^{-1}\left(\frac{Z^{''}}{Z^{'}}\right) \tag{2.21}$$

Table: 2.1

The inter relationship of impedance, admittance, permittivity and electric modulus parameters [36]

Immittance	Symbol	Relation	Complex form
Impedance	Z^*	-	Z’-jZ”
Admittance	Y^*	$1/Z^*$	Y’+jY”
Permittivity	ε^*	$1/j\omega C_0Z^*$	ε’-jε‘
Electric modulus	M^*	$j\omega C_0Z^*$	M’+jM“

The impedance spectroscopy is also called immittance spectroscopy and it is used to measure the behavior of the materials in terms of the complex impedance (Z^*), complex admittance (Y^*), complex permittivity (ε^*) and complex modulus (M^*). The inter relationship of above four parameters are given in Table 2.1 where, $C_0 = \varepsilon_0\left(\frac{A}{L}\right)$, $\varepsilon_0 = 8.854\times10^{12}\,F/m$, $\omega = 2\pi f$ and $\frac{A}{L}$ is cell constant, A is the area of the sample and L is the thickness of the sample.

If the sample is a pure resistor ‘R’, the DC current ‘I’ it under an applied field, ‘E’, is given by ohm’s law (eqn. 2.22).

$$I = \frac{E}{R} \tag{2.22}$$

A pure capacitor does not allow the passage of a DC current but does allow a frequency dependent ac current as shown by eqn. 2.23.

$$I = j\omega CE \tag{2.23}$$

where, ω is the angular frequency $(\omega = 2\pi f)$ and $j = \sqrt{-1}$. Suppose AC current is passed through the sample and it is represented by the eqn. 2.24. Here, Z is the impedance.

$$I = \frac{E}{Z} \tag{2.24}$$

Figure 2.11a and 2.11b show the impedance behavior of a pure resistor and a capacitor as a function of frequency. Figure 2.11c shows the circuit containing a resistance and a capacitance in series. The total impedance of the circuit is represented in eqn. 2.25 – 2.28.

$$Z^* = R + \frac{1}{j\omega C} \tag{2.25}$$

$$= R - \frac{j}{\omega C} \tag{2.26}$$

$$\text{(or)} \qquad Z^* = Z' - jZ'' \tag{2.27}$$

$$\text{where} \quad Z' = R \text{ and } Z'' = \frac{1}{\omega C} \tag{2.28}$$

The resultant impedance plot for R and C in series is represented by a vertical line parallel to the imaginary axis intersecting the real axis at R, as shown in fig.2.11c. Figure 2.11d shows the circuit containing a resistance and a capacitance in parallel. The total impedance of the circuit is represented by eqn. 2.29 – 2.33.

$$Z^* = \left(\frac{1}{R + j\omega C} \right)^{-1} \tag{2.29}$$

$$= \frac{R}{(1 + j\omega RC)} \tag{2.30}$$

$$= \left\{ \frac{R}{\left(1+(\omega RC)^2\right)} \right\} - \left\{ \frac{j\omega RC}{\left(1+(\omega RC)^2\right)} \right\} \tag{2.31}$$

or

$$Z^* = Z' - jZ'' \tag{2.32}$$

where, $Z' = \frac{R}{\left(1+(\omega RC)^2\right)}$ and $Z'' = \frac{\omega RC}{\left(1+(\omega RC)^2\right)}$ (2.33)

As seen from the fig. 2.11d, the intersection of the semicircle with the real axis at a point R gives the bulk resistance of the material. The equation of the semicircle with radius R/2 and centre at R/2, 0 is shown by eqn. 2.34.

$$\left(Z' - \frac{R}{2} \right)^2 + Z''^2 = \frac{R^2}{4} \tag{2.34}$$

From the impedance, resistance and capacitance components can be calculated and are given in eqn. 2.35 and eqn. 2.36.

$$R = \frac{(Z'^2 + Z''^2)}{Z'} \tag{2.35}$$

$$C = \frac{-Z''}{\omega(Z'^2 + Z''^2)} \tag{2.36}$$

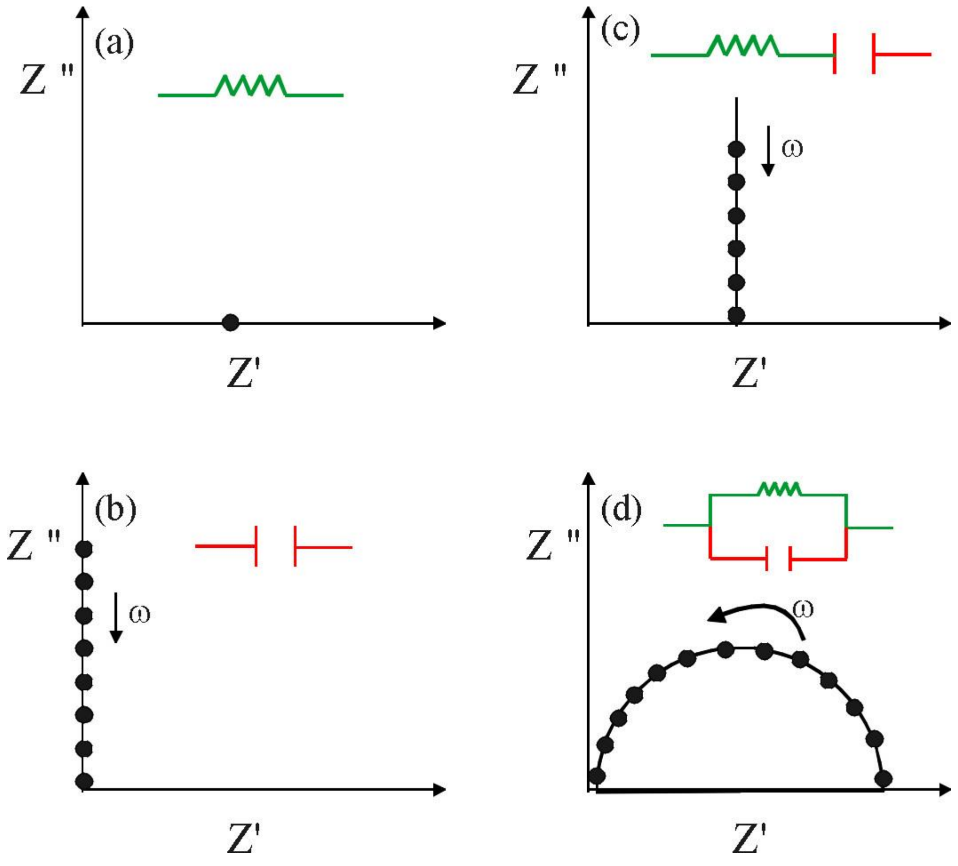

Fig. 2.11 Impedance pattern for a) resistor, b) capacitor, c) R and C in series and d) R and C in parallel [36].

2.11.6 Representation of an impedance spectrum (IS) for a solid ionic conductor

A typical impedance spectrum for a solid ionic conductor sandwiched between two identical electrodes has 3 arcs in the complex plane plot shown in fig. 2.12. The respective arcs can be identified with each elementary process experimentally. The first frequency arc (bulk) is proportional to sample length and density (by a factor of 1.2) and is attributed to the bulk or grain interior process. The frequency dispersion shows a linear response to applied signal amplitude. This arc is observed at low and medium temperatures.

The low frequency arc (interface) is inversely proportional to the electrode area and is attributed to the electrode / electrolyte interfacial process. This responds non – linearly to applied signal amplitude. This arc is observed at high temperatures. The impedance due to this is termed as Warburg impedance. This is manifested as a spike in an impedance spectrum. Electrode / electrolyte interfacial frequency dispersion is sensitive to the methods of attaching the electrode to the electrolyte. Variations of this arc are reported when the electrodes were deposited by coating and by sputtering.

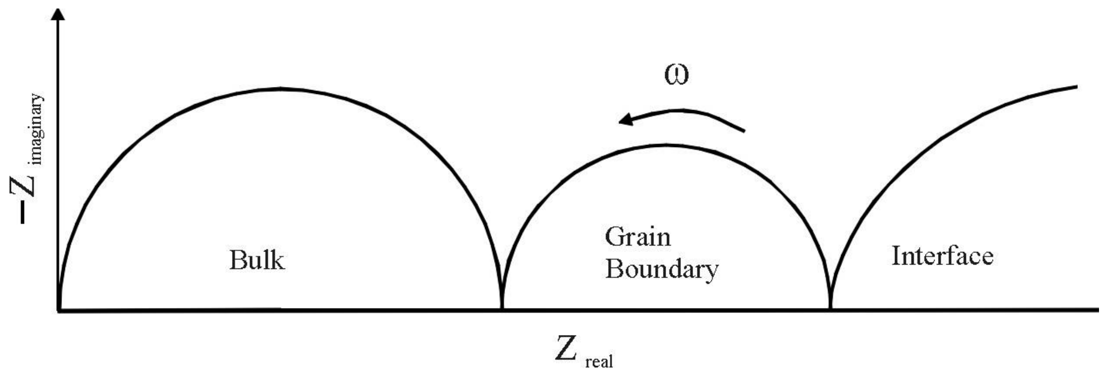

Fig. 2.12 Typical impedance spectrum for a polycrystalline calcia stabilized zirconia solid electrolyte

The intermediate arc (grain boundary) is associated with the grain boundary conductance and the micro structural effects. The arc disappears for a single crystal. The arc depends on the sample history such as cooling, quenching, annealing or aging. The response is strongly dependent on the microstructure of the sample. Presence of a second phase or an impurity affects this arc. This is observed at low and medium temperatures. At higher temperatures this arc merges with the high frequency arc of the bulk.

2.12 Dielectric property - theory and its application in material characterization

Every material has a unique set of electrical characteristics that are dependent on its dielectric properties. A material is classified as dielectric; it has the ability to store energy when a DC external field is applied [60]. The dielectric material increases the storage capacity of the capacitor by neutralizing charges at the electrodes. The increase in capacitance of the dielectric is related to dielectric constant and is given by the eqn. 2.37.

$$k' = \varepsilon_r' = \frac{C}{C_o} \tag{2.37}$$

Here, ‘C’ is the material capacitance and ‘C_O’ is the capacitance in vacuum. k' and ε_r' are defined as the dielectric constant or permittivity of the material. Dielectric constant can also be represented by the symbol ‘ϵ_S’. The dielectric constant depends strongly on the frequency of the alternating electric field or the rate of change of the time-varying field. It also depends on the structure, material imperfections, orientations, as well as on other physical parameters including temperature, pressure, etc.

The measurement of dielectric constant by AC technique is defined by a complex quantity (ϵ^*) and is represented by the eqn. 2.38:

$$\varepsilon^* = \varepsilon_r' - \varepsilon_r'' \tag{2.38}$$

Here, ε_r' is a real part of permittivity, a measure of storage of electrical energy where as ε_r'' is an imaginary part of the permittivity loss from the material. The dielectric displacement D occurring in a dielectric material is given by the eqn. 2.39. Here, ‘ε_o’ is dielectric permittivity in vacuum (ε_o) and ε^* is complex dielectric permittivity.

$$D = \varepsilon^* \varepsilon_0 E \tag{2.39}$$

A dielectric material is made up of atoms or molecules that possess one or more of five basic types of electric polarization. They are electronic, ionic, dipolar, spontaneous and interface or space charge polarization. The approximate time scales for the polarization process for a material is shown in fig. 2.13.

Each polarization process has a specific frequency range. As the frequency increases, the slow mechanisms drop out in turn, leaving the faster ones to contribute to polarization. Usually, the electronic polarizability is measured in the visible or UV region, and the ionic polarizability in the IR region. The time required for electronic polarization is about 10^{-15} s and around 10^{-13} s for ionic polarizabilitiy. Both atomic and electronic polarizability are coming under induced polarizability. If the polarizability occurs only due to applied external field in a material, it is called induced polarizability. The induced polarizability is caused by local electric field, which distorts a neutral distribution of charges.

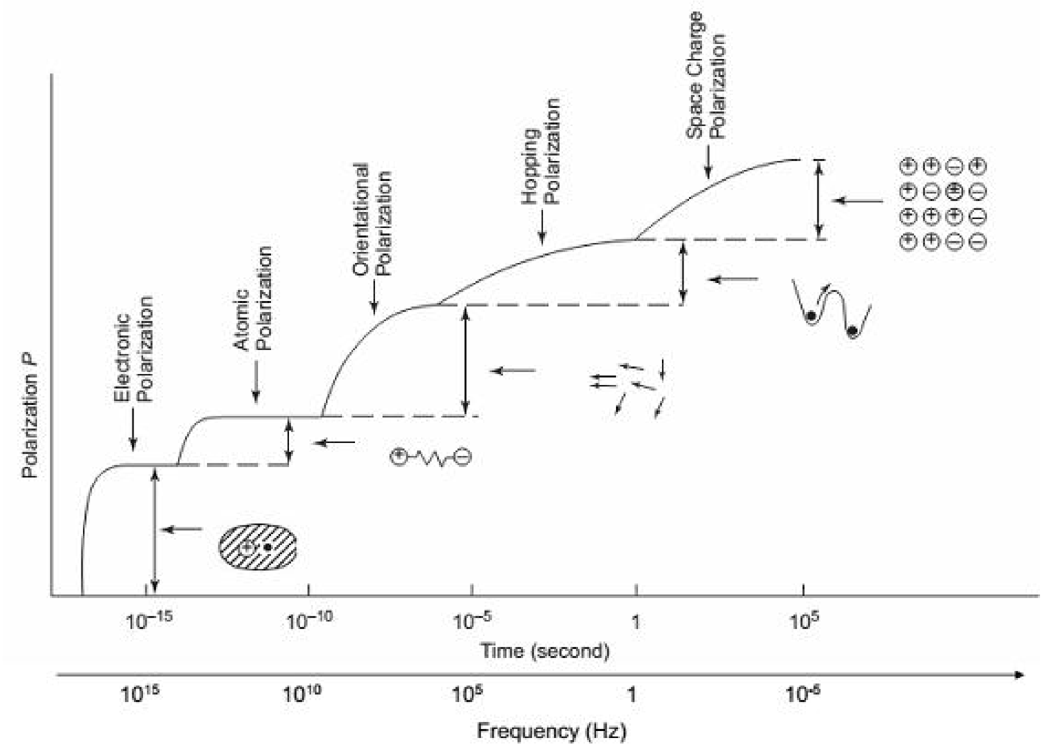

Fig. 2.13 The variation of different types of polarization with time under a step-function electric field ‘F’ [60]

The orientation polarizability occurs in the time scale of 10^{-8} — 10^{-5} s. It occurs in the materials composed of molecules with an asymmetrical structure in which the centroid of the negative charge and that of the positive charge are not coincident. They possess permanent dipole moment in the absence of an external field. The directions of these permanent dipole moments are randomly distributed in the material. An electric field will cause them to reorient towards the direction of the field, resulting in orientational polarization.

In a dielectric material, localized charges (ions and vacancies, or electrons and holes) can hop from one site to the neighboring site, creating so-called hopping polarization. It occurs in the time scale of 10^{-5} — 1 s. The space charge polarization happens in the region of 1 — 10^{5} s. It arises due to accumulation or depletion of charges or carriers at the electrode-electrolyte interface.

Polarizability is temperature and frequency dependent process. It decreases with increase in temperature as shown eqn 2.40. The relation between the dielectric function and polarizability 'α' was derived by Mossoti and Clausius is shown in eqn. 2.41. Where 'M', 'ρ', 'ϵ_o', 'ϵ_s', 'N_A', 'μ' and 'K_B' and 'T' are molecular weight, density, sample dielectric constant, dielectric constant in vacuum, Avogadro number, dipole moment, Boltzmann constant and temperature (K). The change in the polarizability (α) of a material will reflect in the change in dielectric constant 'ε_S' of the material (eqn. 2.41). The change in dielectric constant of the material can be observed as the change in the chemical properties of the material.

$$\alpha = \frac{\mu^2}{3kT} \tag{2.40}$$

$$\frac{\varepsilon_s - 1}{\varepsilon_s + 2}\frac{M}{\rho} = \frac{1}{3}\frac{N_A}{\varepsilon_O}(\alpha + \frac{\mu^2}{3k_B T}) \tag{2.41}$$

In this work, change in the dielectric property of the material was measured by observing change in the capacitance of the material using AC measurements by interacting them with polarizing and non-polarizing gases at different temperatures as shown in eqn. 2.36 at different frequencies. In this work the change in the capacitance of $Ag_6Mo_{10}O_{33}$ thick film was carried out in the presence of different concentrations of NH_3, PG, and H_2 between the temperatures of 523 and 623 K using SI 1287 Electrochemical interface and SI 1260 Impedance / Gain phase analyzer from M/s Solartron analytical UK.

2.13 Facility for measuring electrical conductivity using AC impedance technique

The electrical conductivity of the materials can be measured by both DC and AC measurement techniques. DC technique measures the total conductivity of the sample. The total conductivity is nothing but, sum of the bulk conductivity of the sample and conductivity exhibited at electrode-electrolyte boundaries on both sides of the sample. But, AC measurement can distinguish the various conducting behavior exhibited by the compound by sweeping as a function of frequency.

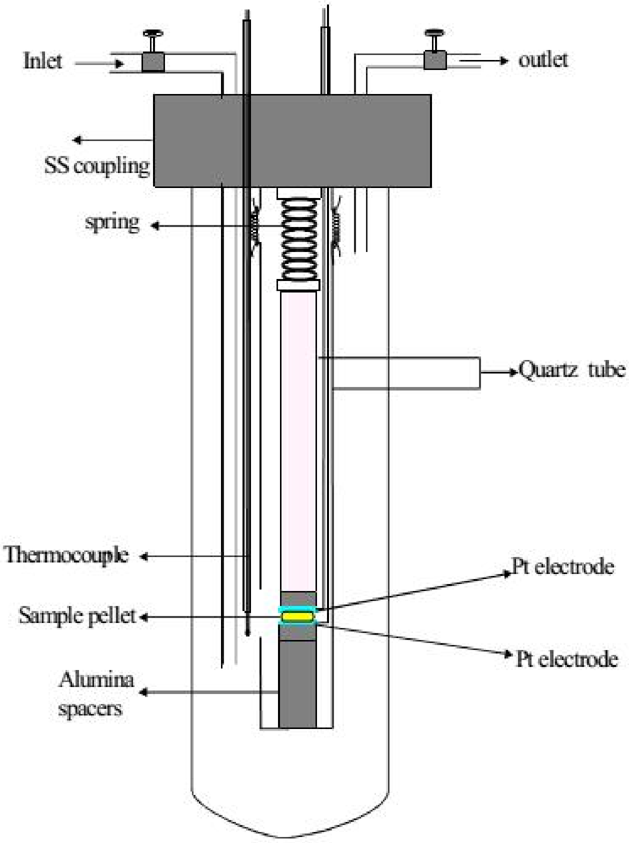

Fig. 2.14 Schematic representation of the set up employed for electrical conductivity measurements

In AC impedance method, conductivity of the sample is measured using frequency response analyser (Model SI 1255 of Solartron, M/s Schlumberger, UK) coupled with an electrochemical interface (Model SI 1286 of Solartron, M/s Schlumberger, UK) in the frequency range of 1 Hz - 1MHz in different ambient. The set up used for mounting a pellet and measuring its conductivity is shown in Fig.2.14. This consists of a one end closed (~ 12.5 mm OD and 11 mm ID) quartz tube having a cut-out at the closed end. The sample pellet sandwiched between two platinum electrodes was placed at the bottom of this quartz tube through the cut-out. Alumina discs placed below the bottom electrode and on top of the upper electrode. The open end of the quartz tube was secured to a stainless steel (SS) coupling through a O-ring sealed fitting. Two springs, which hang from the (SS) coupling, connected to this quartz tube using two hooks provided in the tube. Another quartz tube (OD: ~ 10 mm) closed flat at both ends was placed over the stack of sample pellet and alumina discs. An additional spring was kept between the SS coupling and the top of the closed inner quartz tube.

This arrangement of springs holds the platinum electrodes well pressed on the sample pellet. Platinum wires of 1 mm thickness were attached to the platinum foils served as electrical leads. These leads were insulated using alumina beads and tubes, and were taken through O-ring sealed fittings provided at the top of the SS coupling. A stainless steel sheathed type K thermocouple was positioned close to the sample pellet by using another O-ring sealed fitting present in the SS coupling. This sample holder assembly was placed inside a bigger quartz tube (~ 45 mm diameter), which was also connected to the SS coupling through an O-ring seal. The SS coupling had tubes for gas inlet and outlets provided with needle valves. The whole set up was kept inside the isothermal zone of a vertical resistance furnace. The temperature of the sample was controlled to ± 1 K at a chosen temperature using a PID controller. Using frequency response analyzer, impedance of $Cu_2In_2O_5$ (bulk), $Ag_6Mo_{10}O_{33}$ (bulk and thick film), $Ag_6Mo_{9.75}W_{0.25}O_{33}$, $Ag_6Mo_{9.5}W_{0.5}O_{33}$ (bulk) were measured is the frequency range of 1 MHz and 1 Hz at different temperatures.

2.14 Transport number measurement using Wagner polarization technique

In solid electrolytes major charge carriers would be ions, but in some cases significant concentration of carriers can be either electrons or holes. Hebb [61] and Wagner [62] devised a method to measure the conductivity due to electrons or holes in these materials particularly when their contribution to total conductivity is low. This method is called as ion blocking method and is also called as the DC polarization or Wagner's asymmetric polarization method. In this method, a small DC voltage signal 'V' below the decomposition potential is applied to the sample, which is sandwiched between an electrode reversible to the conducting ion and an inert electrode, which blocks the flow of ions. Ionic migration will occur in the sample until the cell is completely polarized. After the cell becomes completely polarized, the residual current is carried only by the electrons or holes present in the ionic solid, while the initial value of conductivity is due to ions and electrons and / or holes.

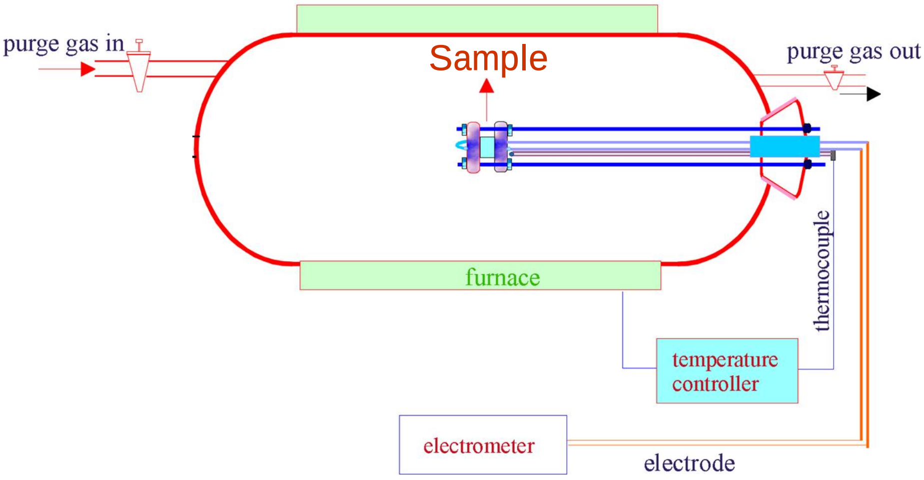

Fig. 2.15 Schematic representation of the set up employed for the measurement of transport number of the sample using Wager polarization technique.

The schematic of the glass facility employed for the measurement of transport number of the sample is shown in fig. 2.15. The facility is having the provision of gas inlet and outlet to conduct experiments in different ambient. The glass facility is positioned inside a nichrome furnace which can be operable from 300 to 673 K. The temperature of the sample was controlled to ± 1 K at a chosen temperature using a PID controller. The cell configuration is shown in eqn. 2.42. In the steady state, current is due to electrons / holes only. From these measured currents, the ionic and electronic transport numbers of the solid can be calculated. The ionic transport number is the fraction of the total current (cationic, anionic, and electronic) as shown by eqn. 2.43 and eqn. 2.44.

$$(-)\,\mathrm{Au\,(or)\,Pt\,/\,Sample\,/\,Pt\,(or)\,Au}\,(+) \tag{2.42}$$

$$t_i = \sigma_i /(\sigma_i + \sigma_e) \tag{2.43}$$

$$\text{Similarly, } t_e = \sigma_e/(\sigma_i + \sigma_e) \tag{2.44}$$

In the present work, transport number of silver in $Ag_6Mo_{10}O_{33}$, $Ag_6Mo_{9.75}W_{0.25}O_{33}$ and $Ag_6Mo_{9.5}W_{0.5}O_{33}$ was measured between the temperature range of 473 K and 673 K using Keithley (Model No. 6517) electrometer.

2.15 Gas interaction studies of materials - fabrication of sensors and test facilities

2.15.1 Thick film principle, fabrication and experimental facility

The thick film is a technique by which the material in the form of viscous paste is employed on a base is made of glass, silicon, alumina, etc. Generally the thickness of the film will be in the range of a few micrometers [63]. The technique is usually employed to print a pattern (custom design) by coating through a mask on a ceramic or glass substrate followed by heating. A typical thick film screen consists of a finely woven mesh of stainless steel, nylon or polyester, mounted under tension on a metal or wooden frame. The mesh is coated with a ultra-violet (UV) light sensitive emulsion onto which the pattern can be formed. The property of emulsion film gets modified on exposure to UV light. The finished stencil has open mesh areas through which the desired pattern can be printed and is held in position at a distance of around 0.5 mm from the top surface above the substrate. The ink is placed on the screen and a squeegee traverses the screen under pressure, thereby bringing it into contact with the substrate and also forcing the ink through the open areas of the mesh. The required pattern is thus, left on the substrate.

The screen printable ink or paste consists of a sample dispersed in a binder. The binder is a mixture of resin made up of α-terpineol and ethyl cellulose in volatile solvent like 2(2-butoxyethoxy) ethyl acetate. The substrates are the physical support of the thick film. One of the most employed substrates in thick film technology is alumina (96% Al_2O_3).

2.15.2 Thick film preparation

The sample for the thick film studies was prepared by mixing finely ground powder with a proprietary organic base in the ratio of 1:1.5. The paste was mixed thoroughly and maintained at 283 K. Polycrystalline alumina wafers of 0.5 mm thickness were used as the substrate, and a screen printer model Dek J 1202 of M/s Kyoritsu Mfg. Co. Ltd., Japan was used to make the thick films.

Prior to printing of the thick film of the sample, a serpentine platinum heater pattern was printed on one side of the alumina substrate. The platinum conducting paste (Part No. 9141) was purchased from M/s DuPont, UK. The screen printed thick film was fired at 1173 K for 5 h. The photograph of Pt heater is shown in fig. 2.16b. Necessary connecting gold or platinum pads were screen printed on top side of the alumina substrate in order to take the electrical leads for heater as well as for the thick film. The thick film, which was screen printed on two electrical pads is shown in fig. 2.16a. The screen printed film was first heated at 373 K for 1 h to remove the volatile organic compounds followed by heating at 773 K in air for 24 h.

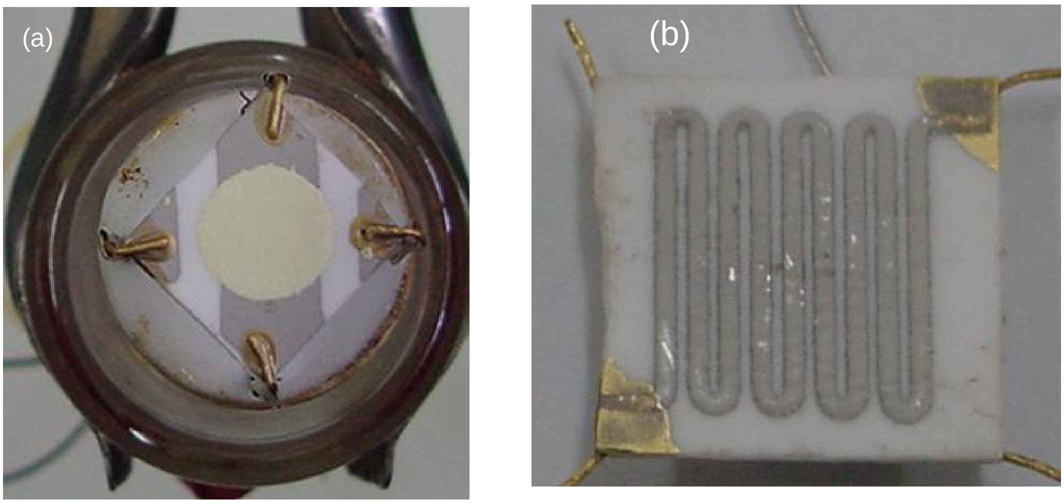

Fig. 2.16 Photograph showing a) screen printed thick film (top view) and b) screen printed Pt heater film (bottom view)

Figure 2.17 shows the photograph of test chamber made of glass for testing thick or thin film samples. The volume of the glass chamber is 50 ml, and has provisions for gas injection port, air inlet and outlet. The thick/thin film samples were housed inside this chamber and all the four electrical leads are connected for the measurement. The gas interaction studies were carried out by introducing known volume of the analyte gas into the chamber.

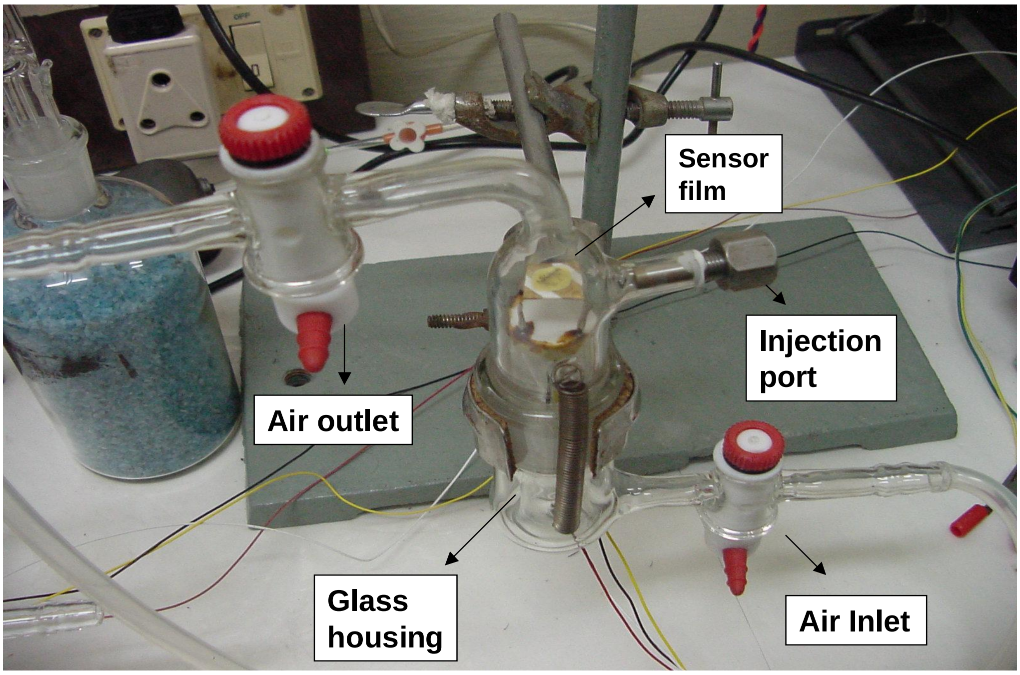

Fig. 2.17 Photograph of test chamber for gas interaction studies of thick or thin film in static air

Figure 2.18 shows miniature test facility made of stainless steel to perform the interaction studies of thick or thin film in the presence of analyte in continuous flowing condition. As seen from the fig. 2.17 and fig.2.18, there is no provision to measure the sample temperature. The platinum heater itself is source for measuring the sample temperature. Before initiating the experiment platinum heaters were calibrated as a function of temperature.

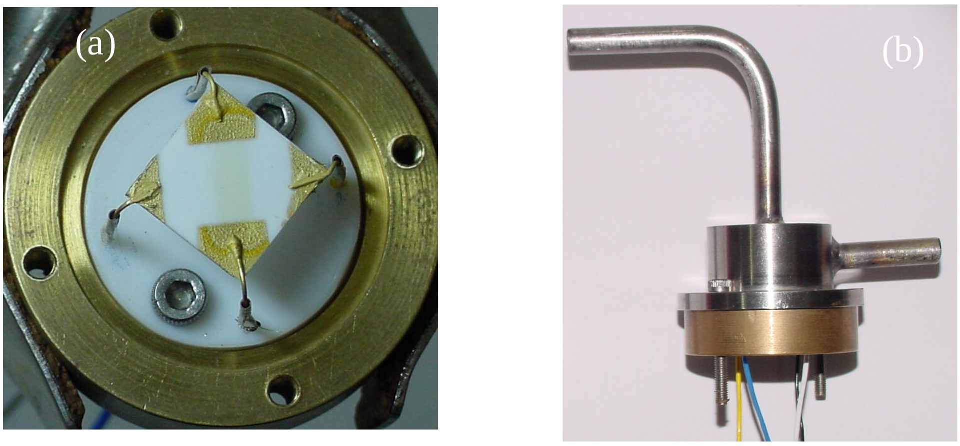

Fig. 2.18 Photograph of a) top view of thin film deposited on Al_2O_3 substrate and b) thin film assembled in SS housing for dynamic gas interaction studies.

For calibration, Pt heater was positioned inside the furnace and the furnace was heated to 773 K at a heating rate of 5 K per minute. Using the electrical leads attached to the platinum heater, its resistance was measured externally between 300 and 773 K. After completing the measurement of resistance of the heater in the mentioned temperature range, a calibration plot is made by plotting the platinum heater resistance as a function of temperature. Typical plot obtained in the present work is shown in fig. 2.19. After completing the heater calibration, thick or thin film was made on the top side of alumina substrate. Using a power supply, appropriate voltage was applied to the platinum heater to establish a required temperature of operation. The gas interaction studies of $Cu_2In_2O_5$ and $CuInO_2$ was carried out using the glass facility shown in fig. 2.17. The gas interaction studies of $Ag_6Mo_{10}O_{33}$ thick film with different concentrations of NH_3, H_2 and PG was carried out using the facility shown in fig. 2.18 in dynamic condition.

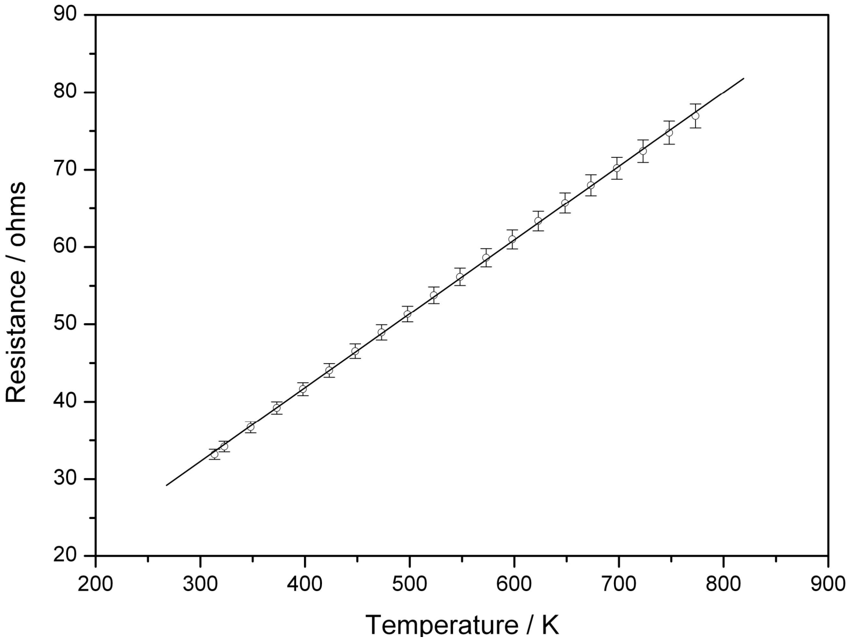

Fig. 2.19 Resistance of Pt heater on Al_2O_3 substrate as a function of temperature [Error bar: < 1.5%]

In order to conduct gas interaction studies of the samples in dynamic operation, mass flow controllers were employed. For this purpose, respective mass flow controllers were calibrated between the flow rates of 0 – 50 ml/min. independently at 300K.

CHAPTER 3

Studies on interaction of In_2O_3 thin film towards NO_X to understand its interaction mechanism on the surface of In_2O_3 using Hall measurement and using AC impedance spectroscopy

3.1 Introduction

Semi-conducting metal oxides exhibit a change in conductivity in the presence of trace levels of oxidizing or reducing gases and this property has been exploited for applications as gas sensors. Among the various mechanisms proposed for gas sensing, the widely accepted mechanism emphasizes the role of various species of chemisorbed oxygen viz., O_2^-, O_2^{2-}, O^- & O^{2-} formed as a result of transfer of carriers from the conduction/valence band of the semiconductor [11 – 13]. The relative fraction of each of this oxygen bearing species is dependant on the temperature and the species which control the surface conductivity at a chosen temperature determine the mechanism of gas sensing. Infra Red (IR), Temperature Programmed Desorption (TPD) and Electron Paramagnetic Resonance (EPR) studies have shown O_2^- to be stable below 473 K [14]. The relative fraction of O^- would be high in the temperature range of 473 K to 773 K and temperatures above 773 K, O^{2-} ion dominates. The chemical interaction of the reducing gases (H_2, H_2S, NH_3, etc.) with the chemisorbed oxygen species releases the electrons back to the conduction band and increase of conductivity of an n-type semiconductor. Just the opposite mechanism is proposed for interaction of these n-type semi-conductors with oxidizing gases (NO_2, Cl_2, O_3 etc.) [64 – 68]. In order to realize enhanced interaction by these gases, metal oxides must have large surface area. This is achieved in practice by using thin film technology. Among many thin film deposition techniques, pulsed laser deposition technique has superior capability to grow nano-structured thin films of multi-component oxides on substrates like alumina, SiO_2, quartz, etc. Among various metal oxides, SnO_2, WO_3, and In_2O_3 are well known semi-conducting metal oxides for sensing of low concentrations of pollutants. Studies to understand the gas sensing behavior of these metal oxides towards oxidizing or reducing gases and their signal transduction mechanism are still continuing [69 – 72]. The gas sensing mechanisms involve surface phenomenon, and hence probing the changes in conductivity and carrier concentration in the presence of the trace levels of the pollutant gas provides a meaningful insight into the mechanism of the gas sensing.

This chapter discusses the deposition of In_2O_3 thin film using PLD and characterizing the film using XRD, AFM, Laser Raman and Impedance spectroscopic techniques. Among the gases, NO_X was chosen; its interaction behavior with In_2O_3 was undertaken in this chapter. Using a high temperature facility, Hall coefficient and four probe conductivity were measured by van der Pauw technique. Changes in carrier density and charge carrier mobility in air and air containing NO_X were also studied and their results will be discussed. The chapter also discusses the adsorption behavior of NO_X on the surface of In_2O_3 using laser Raman spectroscopy at different temperatures. Finally, the chapter also discusses two probe AC impedance studies of In_2O_3 thin film in air and in presence of different concentration of NO_X at different operating temperature.

3.2 Experimental

The targets for the pulsed laser deposition of In_2O_3 thin film were made from the high purity powders of In_2O_3 (99.9%, M/s Aldrich, USA). The powders were pelletized into discs of 15 mm diameter and ~ 3 mm thickness and then sintered at 1273 K for about 48 h in air. Thin films of In_2O_3 were deposited on 10 × 10 mm polished alumina substrates. A KrF laser (M/s Lumonics, Canada) operating at a wavelength of 248 nm was used for pulsed laser deposition. The optimized conditions for the growth of In_2O_3 thin film by PLD are given in Table 3.1. Before depositing the thin film on the substrate, gold electrical pads were screen printed on four corners of the substrate for four probe measurements. The details of the screen printing of electrical pads have been discussed in Chapter 2.

The deposited thin films were analyzed by X-ray diffraction using PANalytical, Model: X'Pert Pro MPD, at room temperature using CuKα radiation. The thicknesses of In_2O_3 thin films were measured using profilometer Dektak^3 of M/s Veeco, USA. The morphologies of the films were studied using Atomic Force Microscope model Solver Pro, M/s NT – MDT, Russia. Two probe DC conductivity of the thin film was measured using 34970A, M/s Agilent Data Acquisition Switch Unit, Malaysia in clean air and in air containing 25 ppm of NO_X at 573 K. 1 % NO_X was used for the experiment. Mass flow controllers (M/s Aalborg, USA) were used to pass clean air and air containing known levels of NO_X through the gas inlet of the thin film housed chamber at a constant flow rate of 50 ml/min. The gas let out from the chamber was passed through a solution of sodium carbonate to scrub the NO_X completely. The change in DC conductivity of the thin film in the presence of 25 ppm of NO_X was carried out in the above mentioned chamber. Four probe electrical conductivity and Hall coefficient of In_2O_3 film were measured using van der Pauw technique. Hall coefficient measurement system which was designed, fabricated and installed as part of this work has been described in Chapter 2. The conductivity and Hall coefficients were measured in the temperature range of 373 to 673 K in flowing clean air and air containing 25 ppm of NO_X. These measurements were also carried out at a fixed temperature of 623 K in flowing air containing different NO_X levels (5 to 75 ppm).

Table: 3.1

In-situ growth parameters for pulsed laser deposition of In_2O_3 thin film

S. No.	Deposition conditions	
1.	Target	In_2O_3
2.	Fluence (J cm^{-2})	4 - 5
3.	Repetition rate (Hz)	10
4.	Pre-ablation (min.)	5
5.	Ablation (min.)	20 – 30
6.	Pressure (mbar of oxygen)	2×10^{-1}
7.	Substrate-Target distance (cm)	4 – 5
8.	Substrate Temperature (K)	773
9.	Substrate	Polished polycrystalline alumina

In order to identify NO_X based surface adsorbed species, Raman spectrum was recorded at room temperature on In_2O_3 thin film, which was exposed to air containing 1000 ppm of NO_X at 398 K for 15 min. and cooled to room temperature in the same environment. The experiment was also conducted at 448 K and 573 K by exposing the thin film to 1000 ppm of NO_X for 15 min to investigate any changes in the adsorbed species. For comparison, laser Raman spectrum of In_2O_3 prior to exposure to 1000 ppm of NO_X was also recorded at room temperature. These spectra were recorded using Renishaw micro Raman spectrometer (M/s InVia, Germany) at ambient temperature. 514.5 nm Argon ion laser which was focused to 1 µm spot size by a 50 X microscope objective was used as the excitation source. The impedance of In_2O_3 thin film was measured using Model SI 1260, Solartron, UK over the frequency range 1.0 MHz – 10 Hz, with an applied V_{rms} of 50 mV. These measurements were carried out in the temperature range of 548 – 698 K in air and in the presence of different concentrations of NO_X. The design, fabrication and gas testing facilities have been discussed in Chapter 2.

3.3 Results and Discussion

3.3.1 Characterization of In_2O_3 thin film using XRD

Figure 3.1a shows the XRD pattern of In_2O_3 target used for deposition of thin films. All the reflections were indexed as those of the cubic phase of In_2O_3 (JCPDS # 06 – 416). Fig. 3.1b shows the XRD pattern of In_2O_3 thin film on polished alumina substrate with the reflections of (211), (222), (400), (411), (332) and (431) planes of In_2O_3 as indexed in Fig. 3.1a. The reflections at 38.15 and 44.35^o are from gold (electrical pad) and the other peaks shown in Fig.3.1b are due to alumina substrate. Fig. 3.2a and 3.2b show the AFM images of the film, recorded over the scan areas of 10 µm × 10 µm and 4.5 µm × 4.5 µm respectively. The AFM images show that the film consists of grains with an average size of 75 to 100 nm. The thicknesses of the In_2O_3 thin films were around 100 nm (Measurement accuracy: ± 5%). The photograph of PLD deposited In_2O_3 thin film on square shaped alumina substrate is shown in fig. 3.2c.

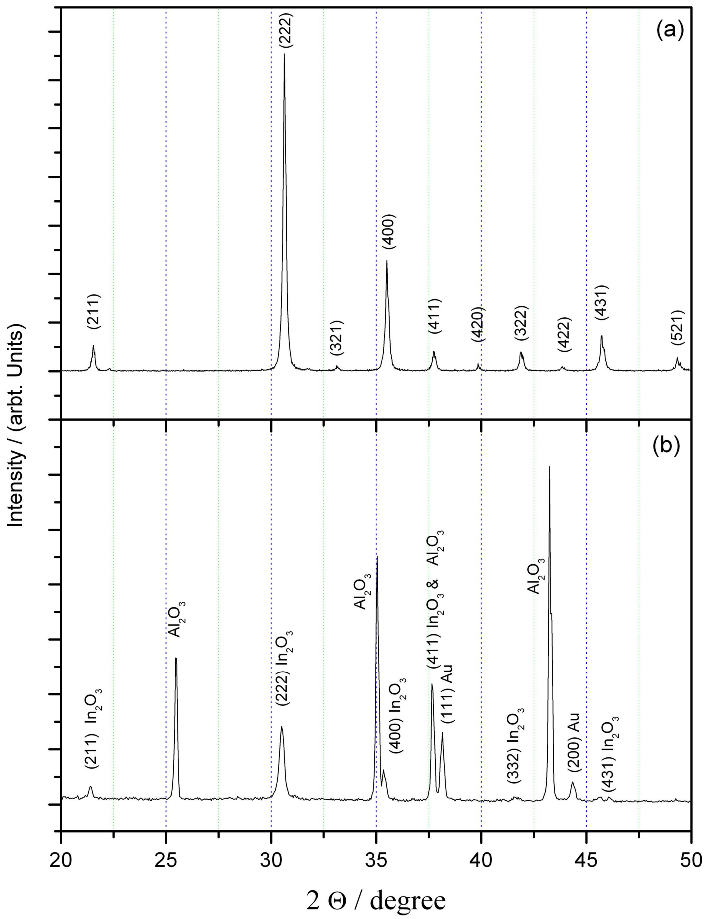

Fig. 3.1 X-ray diffraction patterns of (a) In_2O_3 powder and (b) In_2O_3 thin film on Al_2O_3 substrate

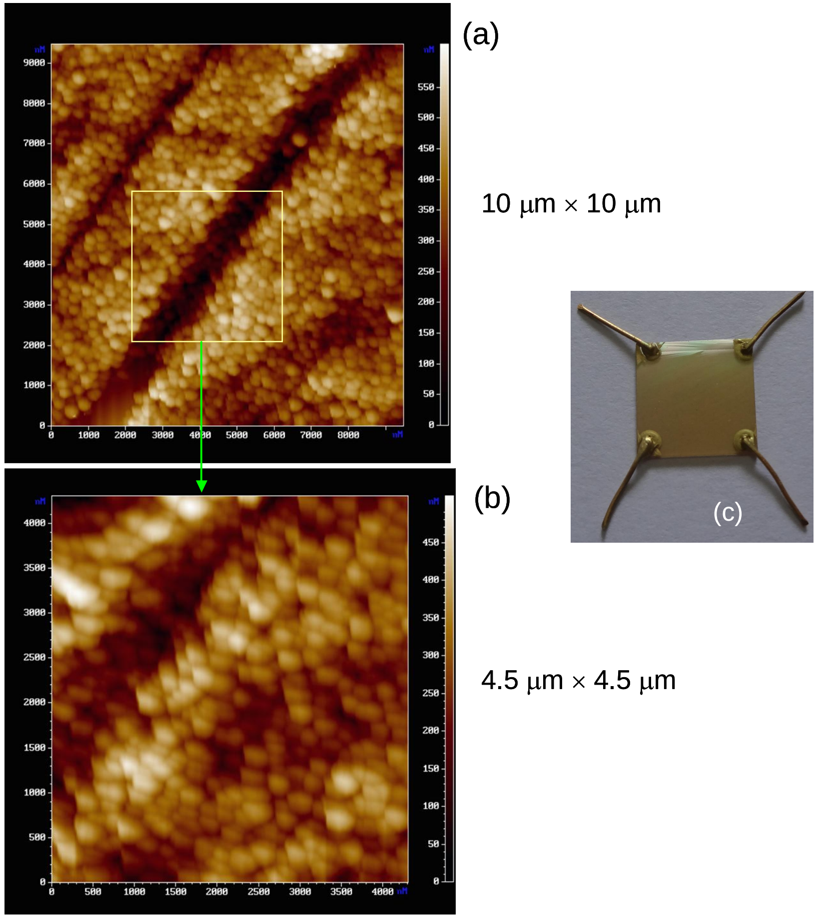

Fig. 3.2 AFM micrographs of In_2O_3 thin film deposited at 773 K on polished Al_2O_3 substrate over scanned area of (a) 10 μm × 10 μm, (b) 4.5 μm × 4.5 μm and c) photograph of In_2O_3 thin film

3.3.2 Two probe DC conductivity studies on In_2O_3 thin film on exposure to air containing NO_X

Earlier studies have shown a high sensitivity by In_2O_3 thin film towards 2 ppm of NO_X at 473 K. However, its recovery time was several hours [73]. Although sensitivity to NO_X continued to be high at 523 K, response and recovery times were again unacceptably long - 400 and 2500 s respectively. At 573 K the response and retrace times were considerably low (60 and 300s respectively) although sensitivity was reduced marginally. Based on these experimental results, temperature of 573 K was chosen for the present study.

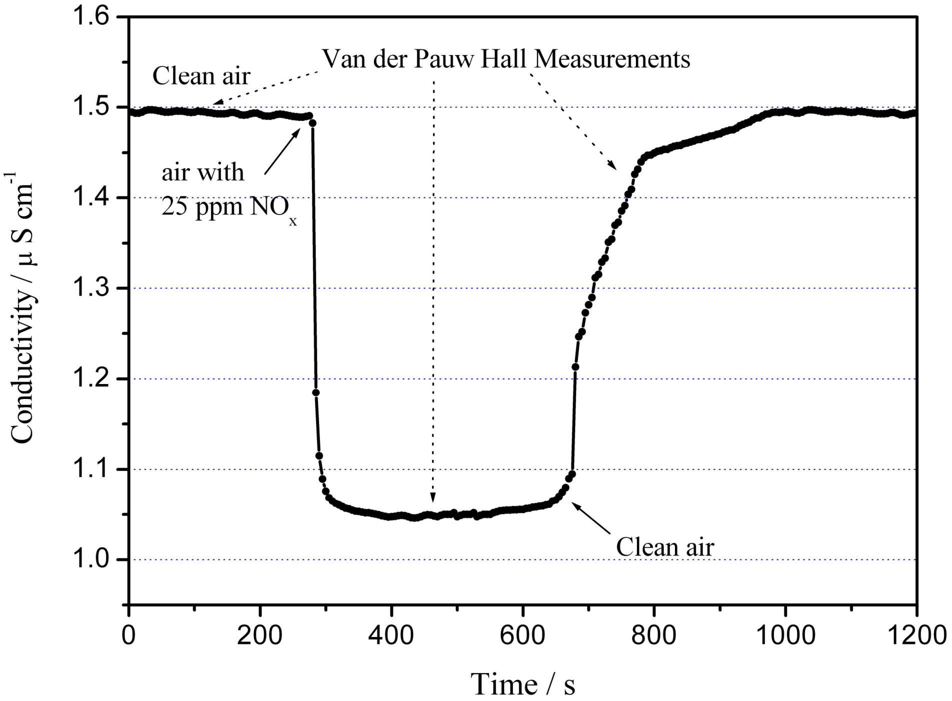

Fig. 3.3 Transient changes in conductivity by two probe as a function of time for thin film of In_2O_3 exposed to 25 ppm of NO_X in air at 573 K.

Figure 3.3 shows the transient changes in two probe DC conductivity of In_2O_3 thin film at 573 K. The baseline conductivity of the thin film in clean air was acquired for a specified time. Then, with the help of a mass flow controller, air containing 25 ppm of NO_X was introduced into the sensor chamber. On exposure to NO_X, conductivity of the film decreased sharply and attained a stable value. Then, the chamber was purged with clean air. The conductivity of the film traced back to the original value in about five minutes.

3.3.3 Measurement of four probe conductivity, carrier concentration and charge carrier mobility and Hall coefficient as a function of temperature using van der Pauw technique

Figure 3.4a shows the plot of logarithmic conductivity (four probe conductivity) of In_2O_3 thin film as a function of inverse temperature in clean air and in air containing 25 ppm of NO_X. Data corresponding to the conductivity measurement of In_2O_3 thin film is shown in Table. 3.2. As seen from the figure, conductivity in clean air follows Arrhenius behavior throughout the temperature interval of 373 to 673 K and the activation energy for this conductivity is 0.13 (± 0.02) eV. It is reported that in the temperature range of 323 to 873 K, three surface adsorbed oxygen species exist which control the conductivity of the semiconducting oxide [14]: Depending upon the temperature, one or more of these adsorbed species will be in dynamic equilibrium with oxygen in air.

$$\begin{gathered} O_{2(g)} \overset{323K-348K}{\rightleftharpoons} O_{2(physisorbed)} \overset{320K-473K}{\rightleftharpoons} O^{-}_{2(chemisorbed)} \\ O^{-}_{2(chemisorbed)} \overset{448K-698K}{\rightleftharpoons} O^{-}_{(chemisorbed)} \overset{673K-873K}{\rightleftharpoons} O^{2-}_{(lattice)} \end{gathered} \qquad (3.1)$$

Conductivity of the film in air containing 25 ppm of NO_X shows the presence of two distinct regions. The conductivity values are also lower than those observed in clean air. The plot of ln σ versus reciprocal temperature is found to be linear in the temperature range of 473 to 673 K, indicating the Arrhenius behavior. Below 473 K, ln σ is seen to decrease sharply and deviates from linear relation. The activation energy deduced for the conductivity for the linear region (above 473 K) was found to be 0.13 (± 0.02) eV. As the activation energy in clean air and in air containing 25 ppm of NO_X remains unchanged, the mechanism of electrical conduction is likely to be the same in the temperature range of 473 to 673 K. However, at temperatures below 473 K the deviation from the linearity implies that the mechanism of electrical conduction in the presence of NO_X in air is different from that in clean air. Further inference about the mechanism of conduction was deduced from Hall coefficient data.

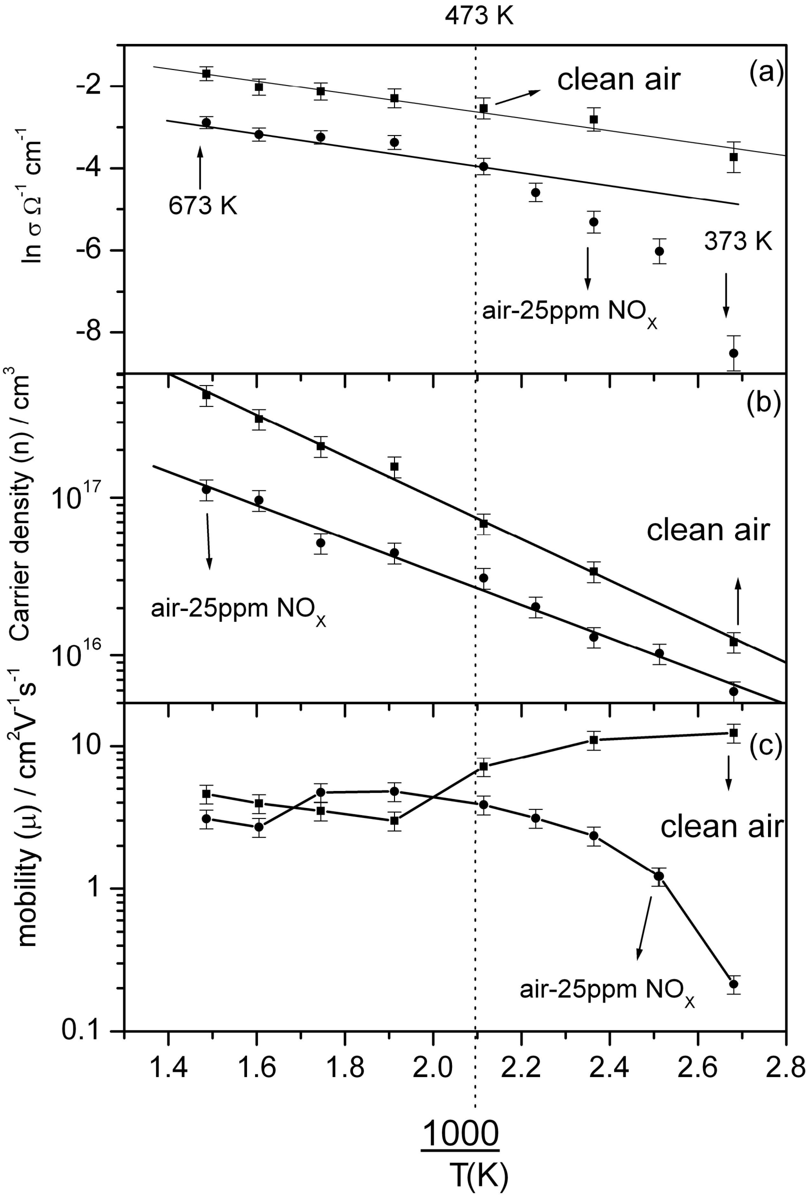

Fig. 3.4 a) Conductivity, b) carrier concentration and c) carrier mobility of In_2O_3 thin film in [■] clean air and [●] air containing 25 ppm of NO_X as a function of 1/T (vertical dotted line shows the deviation in conductivity and carrier mobility) [Error bar: < 1.0 %]

Table: 3.2

Conductivity (σ), carrier concentration (n) and charge carrier mobility (μ) of In_2O_3 thin film in clean air and in the presence of air containing 25 ppm of NO_X as a function of temperature (K)

Temperature (K)	1000/T	Conductivity (σ) of In_2O_3 thin film (Ω^{-1} cm^{-1})		Carrier concentration (n) of In_2O_3 thin film (cm^{-3})		Charge carrier mobility (μ) of In_2O_3 thin film ($cm^2V^{-1}s^{-1}$)	
		Clean air	Air containing 25 ppm of NO_X	Clean air	Air containing 25 ppm of NO_X	Clean air	Air containing 25 ppm of NO_X
673	1.48	1.48	0.055	4.46×10^{17}	1.12×10^{17}	4.61	3.08
623	1.60	1.14	0.041	3.14×10^{17}	9.64×10^{16}	3.95	2.69
573	1.74	0.99	0.038	2.11×10^{17}	5.15×10^{16}	3.51	4.71
523	1.91	0.87	0.034	1.56×10^{17}	4.46×10^{16}	2.99	4.79
473	2.11	0.68	0.019	6.85×10^{16}	3.09×10^{16}	7.15	3.86
448	2.23	-	0.011	-	2.04×10^{16}	-	3.12
423	2.36	0.44	0.004	3.41×10^{16}	1.31×10^{16}	11.02	2.34
398	2.51	0.23	0.002	-	1.02×10^{16}	-	1.22
373	2.68	-	0.0002	1.21×10^{16}	5.89×10^{15}	12.35	0.21

Figure 3.4b shows the variation of log n as a function of reciprocal temperature (where n is the carrier concentration) for the In_2O_3 film in clean air and in air containing 25 ppm of NO_X. Data corresponding to carrier concentration of In_2O_3 thin film is shown in Table. 3.2. When air containing NO_X is the environment, carrier concentration in the film is significantly reduced compared to the concentration in clean air environment. Electron affinity of NO_2 is (2.2 eV) higher than that of oxygen (0.45 eV) [74]. Hence carrier concentration of In_2O_3 in air containing NO_X is likely to be lower than in clean air since more electrons would get trapped on the surface, as shown by the eqn. 3.2:

$$NO_2 + e^- \rightleftharpoons NO^-_{2\,(ads)} \tag{3.2}$$

As seen from the figure, log n vs 1/T is linear in clean as well as in air containing 25 ppm of NO_X in the entire temperature range i.e. 373 to 673 K. This is in contrast to the two distinct regions observed for the variation of log σ with 1/T in air containing 25 ppm of NO_X (compare fig. 3.4a and fig. 3.4b). Since conductivity is related to carrier concentration and its mobility ($\sigma = n\,e\mu$), mobility of the electrons could play a key role for this behavior. The charge carrier concentration 'n' was calculated using the eqn. 3.3.

$$\mathrm{n} = \frac{\mathrm{IB}}{\mathrm{eR_H}} \tag{3.3}$$

where 'I' is current in ampere, 'B' is magnetic field in Gauss, 'e' is the charge of an electron and 'R_H' is Hall voltage. The mobility of the carrier in the sample can be calculated using the eqn. 3.4.

$$\mu = \frac{1}{\rho}\left(\frac{1}{ne}\right) \qquad (3.4)$$

Figure 3.4c shows the variation of log μ with 1/T in clean air and in air containing 25 ppm of NO_X. Mobility of the electrons in the film exposed to clean air remains nearly constant in the temperature range of 673 to 473 K (4 $cm^2V^{-1}s^{-1}$ at 673 K to 2 $cm^2V^{-1}s^{-1}$ at 473 K). Below 473 K, the mobility tends to increase slightly. This pattern is similar to the results reported for SnO_2 films in an identical temperature range [75]. On exposure of the film to air containing 25 ppm of NO_X, the mobility of the carrier remains comparable to that in clean air (3 $cm^2V^{-1}s^{-1}$ in clean air at 673 K and 5 $cm^2V^{-1}s^{-1}$ air containing 25 ppm of NO_X at 473 K). Data corresponding to the charge carrier mobility of In_2O_3 thin film is shown in Table. 3.2. Hence, in the temperature range of 473 to 673 K, the observed decrease in the conductivity of the film in air containing NO_X is due to the reduction in the value of 'n' i.e., the concentration of the charge carrier. However, at temperatures below 473 K, the mobility shows a sharp decrease, while the variation of log n with 1/T did not show any significant change. Hence the reason for non-linear variation of log σ vs 1/T below 473 K originates from mobility of the surface adsorbed species. To explore the characteristics of the surface adsorbed species, laser Raman spectroscopic studies were carried with the In_2O_3 thin film in clean air and in air containing NO_X.

3.3.4 Characterization of NO_X based species on In_2O_3 thin film using laser Raman spectroscopy

Figure 3.5a shows the laser Raman spectrum of In_2O_3 thin film coated on Al_2O_3 substrate and exposed to air containing 1000 ppm of NO_X at 573 K. For comparison, the Raman spectrum of In_2O_3 thin film exposed to clean air is shown in fig.3.5b. To enable better analysis, Raman spectrum was background corrected and normalized. The Raman lines at 132.9, 308.2, 493.5 and 633.2 cm^{-1} arise from In_2O_3, whereas the Raman lines at 379, 415.7, 427.5, 449.2, 576.2, 644.9, 749.3 cm^{-1} correspond to α - Al_2O_3 substrate as marked in Fig. 3.5a [76 – 79]. A broad but new feature was observed between 1200 and 1500 cm^{-1} [Fig. 3.5(a)]. To view this portion of the spectrum clearly, the spectrum magnified in the wavenumber region of 1200 – 1500 cm^{-1} is shown as inset in Fig. 3.5a. Peak fitting using Lorentian function yields a peak center of 1363 cm^{-1}, which is the characteristic N-O stretch of the antisymmetric mode of nitro species, ν_{asym} (NO_2) [80].

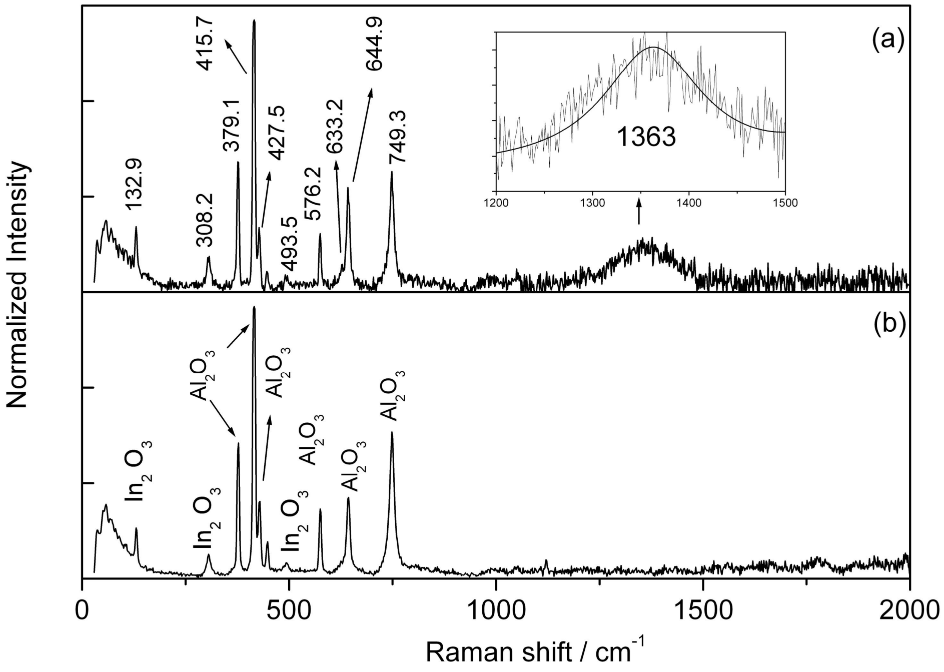

Fig. 3.5 Laser Raman spectrum of In_2O_3 thin film recorded at room temperature a) exposure to 1000 ppm of NO_X in air at 573 K, b) In_2O_3 thin film deposited on alumina substrate at 773 K and Inset – zoomed portion of Raman band: antisymmetric stretching of NO_2 (1363 cm^{-1})

To understand the temperature dependency of interaction of NO_X with In_2O_3 below 573 K, thin film was exposed to air containing 1000 ppm NO_X at 398 and 448 K. In each case Raman spectrum was recorded. Figures 3.6 and 3.7 show normalized laser Raman spectrum obtained at 398 and 448 K, respectively. The spectra are nearly identical. The magnified spectra in the wavenumber region of 900 – 1200 cm^{-1} are shown as insets in each figure. Both the spectra show characteristic features at 983, 1052, and 1123 cm^{-1} although their peak intensities are different. The Raman shift in the region of 980 – 984 cm^{-1} is attributed to monodentate nitrate (NO_3^-) bonded through oxygen with the surface of In_2O_3 [80]. The shift at 1052 cm^{-1} is due to the free nitrate NO_3^- formed as a result of NO_X interaction with the surface chemisorbed oxygen ions (O_2^- & O^-) [79 – 81]. At temperatures below 473 K, O_2^- and O^- are in dynamic equilibrium.

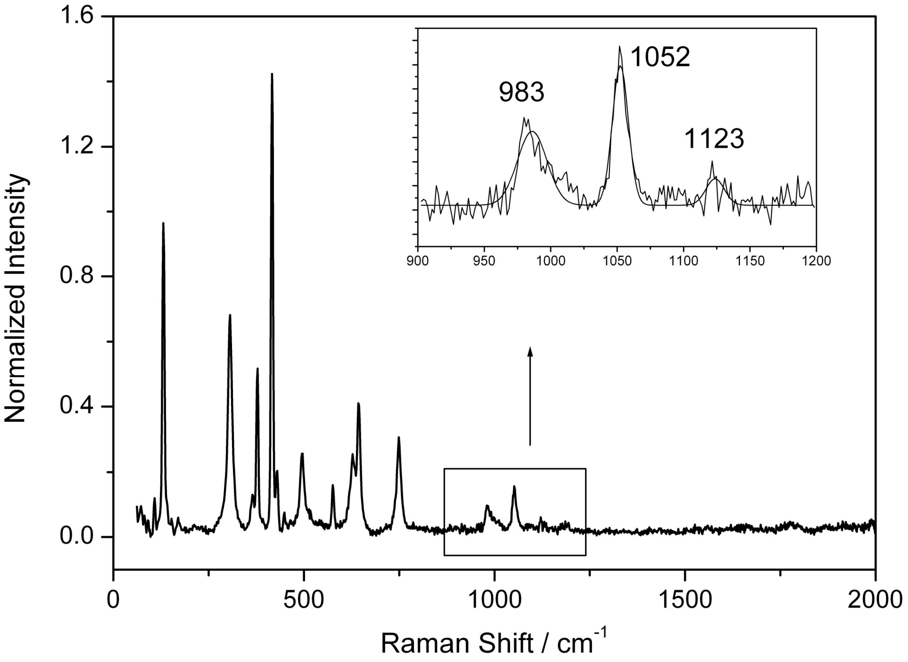

Fig. 3.6 Laser Raman spectrum of In_2O_3 thin film exposed to 1000 ppm of NO_X in air at 398 K. Inset: Magnified portion of Raman band: Monodentate nitrate (983 cm^{-1}), free nitrate (1052 cm^{-1}), $(NO)_2$ dimer or $(NO)_2^{2-}$ (1123 cm^{-1})

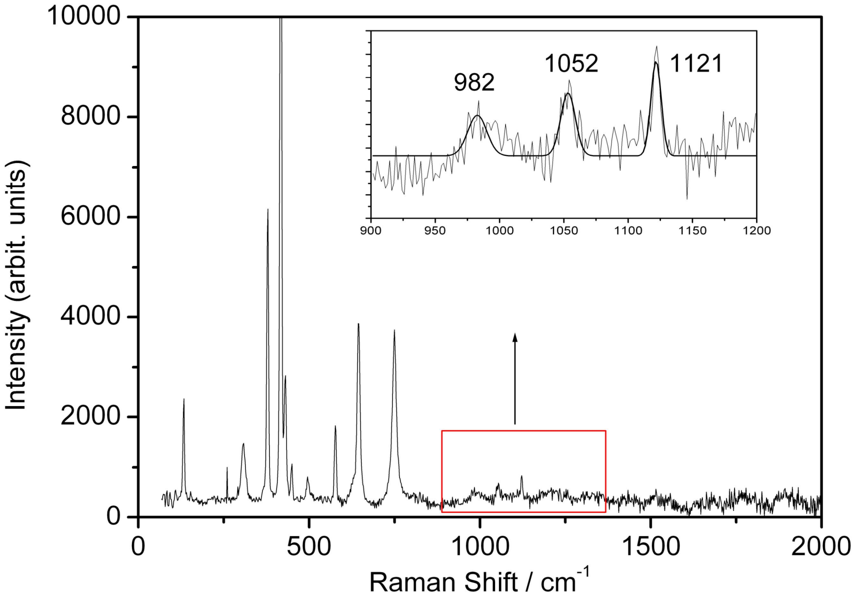

Fig.3.7 Laser Raman spectrum of In_2O_3 thin film exposed to 1000 ppm of NO_X in air at 448 K. Inset: Magnified portion of Raman band: Monodentate nitrate (982 cm^{-1}), free nitrate (1052 cm^{-1}), $(NO)_2$ dimer or $(NO)_2^{2-}$ (1123 cm^{-1})

The peak at 1123 cm^{-1} in both fig. 3.6 and 3.7 is attributed to the dimers of NO represented as $(NO)_2$ [79, 82]. Studies by Tsukahara et al on the reaction of nitric oxide with oxygen molecule showed that these dimers to be in equilibrium with NO below 473 K [83, 84]. The reaction between nitric oxide and oxygen is a third order reaction as shown by eqn. 3.5 [85].

$$2\ NO + O_2 \longrightarrow 2\ NO_2 \quad \Delta G^o_{RX,298K} = -70.44\, kJ/mol\, of\, O_2 \tag{3.5}$$

Data in literature on the kinetics of reaction of nitric oxide with oxygen shows that concentration of NO_2 and dimer $(NO)_2$ decreases with increase in temperature [3] The presence of $(NO)_2^{2-}$ (dimer of NO) on the surface of In_2O_3 thin film after its exposure to NO_X at 398 as well as at 448 K is seen from laser Raman spectra.

Literature shows that the adsorption of NO_X on oxide surfaces proceeds via (a) monodentate nitrate through oxygen in NO_3^- (structure represented in Table 3.3), (b) free nitrate (NO_3^-), (c) $(NO)_2$ dimer as $(NO)_2^{2-}$, (d) nitro species (NO_2) etc., as given in Table. 3.3. Among the species indicated, presence of a particular adsorbed species depends on the temperature. These species are in ionized state on In_2O_3 surface.

Ogawa et al reported the interaction of ethanol with nanograins of SnO_2 [86]. Authors proposed a schematic model for the potential barrier exhibited SnO_2 due to oxygen chemisorption. Such model was proposed for In_2O_3 thin film and is shown in fig. 3.8.

---

[3]

$$2NO \xrightleftharpoons{K_1} (NO)_2 \quad \text{(fast)} \tag{I}$$

$$(NO)_2 + O_2 \xrightarrow{k_2} 2\,NO_2 \quad \text{(slow and rate determining step)} \tag{II}$$

$$\left(\frac{dNO_2}{dt}\right) = k_2K_1[NO]^2\,[O_2] \tag{III}$$

K_1 is the equilibrium constant for the reaction shown in eqn. (I) and k_2 is the rate constant for reaction (II). Dimerization (I) is an exothermic reaction and hence K_1 decreases with increase in temperature [84]. Therefore the rate of formation of NO_2 decreases with increase in temperature.

Table: 3.3

Species arising from the adsorption of NO_X on In_2O_3 thin film

Species observed from Raman measurement	Observation from present studies Wavenumber (cm^{-1})	Literature report	
		Wavenumber (cm^{-1})	Reference
Monodentate nitrate through oxygen in NO_3 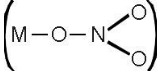	980 – 984	970 – 1035	[80]
Free nitrate (NO_3^-)	1052	1049 – 1052	[79 – 81]
Dimer of NO $[(NO)_2^{2-}]$	1120	1120	[79, 82]
Antisymmetric stretching of NO_2 [ν_{asym} (NO_2)]	1363	1360 – 1380	[80]

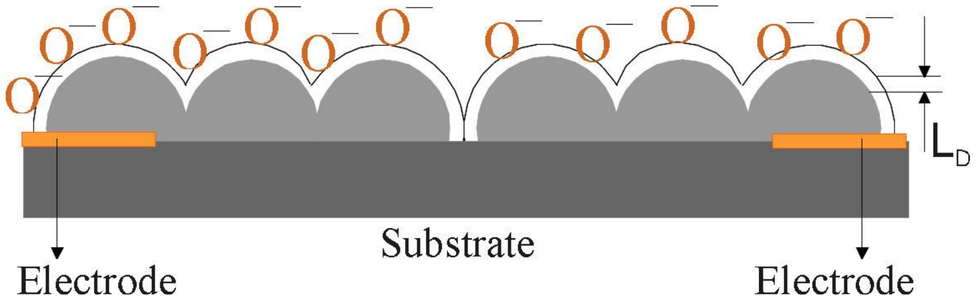

Fig. 3.8 Schematic model of channel height modulation due to chemisorbed oxygen ion on the surface of In_2O_3 thin film

Figure 3.9 shows the schematic representation of change in the potential barrier height of In_2O_3 (chemisorbed oxygen ion surface) during its interaction with NO_X above 473 K. As seen from the figure, NO_X gets chemisorbed on the surface as nitro species (NO_2) along with chemisorbed oxygen ion. The presence of NO_2 along with chemisorbed oxygen ion on the thin film surface doesn’t change the mobility of carrier in In_2O_3 above 473 K when compared with carrier mobility of the film in air.

No change in carrier mobility above 473 K may probably due to effect of temperature (above 473 K) of n-type In_2O_3.

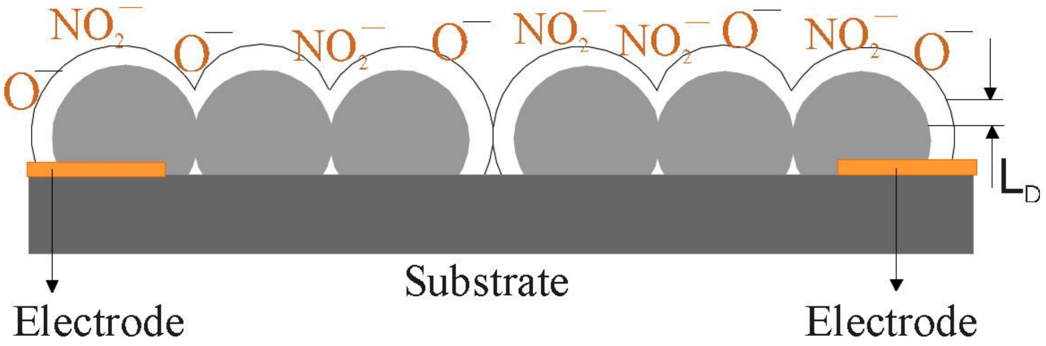

Fig. 3.9 Schematic model of channel height modulation by abstraction of electron by NO_2 along with chemisorbed O^- on the surface of In_2O_3 thin film

Figure 3.10 shows the schematics of potential barrier height of In_2O_3 thin film in the presence of NO_X below 473 K. The decrease in carrier mobility of In_2O_3 thin film in the presence of NO_X below 473 K when compared with air is probably due to the presence of different kinds of species namely NO_3^-, $(NO)_2$, and NO_2 along with chemisorbed oxygen species (O_2^- & O^-) on the surface is likely modified the surface barrier height in such a way that the mobility decreased sharply at lower temperatures. These NO_X species are probably responsible for the change in activation process for the carrier concentration of In_2O_3 thin film below 473 K.

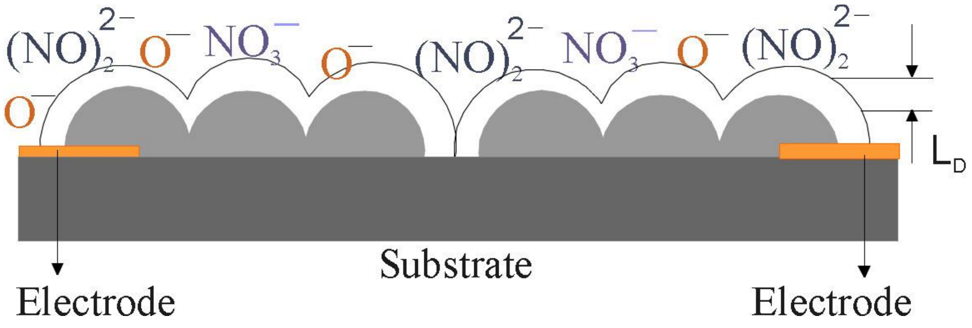

Fig. 3.10 Schematic model of channel height modulation by abstraction of electron by NO_2 and NO_3^- along with chemisorbed O^- on the surface of In_2O_3 thin film

3.3.5 Measurement of conductivity and carrier concentrations of In_2O_3 in different concentrations of NO_X

To understand the influence on the conductivity and carrier concentration of In_2O_3 thin film during its interaction with different concentrations of NO_X in air, it was exposed to air containing different concentration of NO_X between 5 and 75 ppm at 623 K. Data corresponding to the conductivity and carrier concentration of In_2O_3 thin film at 623 K as a function of NO_X concentration is shown in Table. 3.4. Figure 3.11a shows the variation of conductivity of the film on this exposure at 623 K. It is seen that the conductivity decreases with increasing concentration of NO_X in air. Similarly, the carrier concentration (Fig. 3.11b) also reduces with increase in NO_X concentration. This confirms that the mechanism of NO_X sensing proceeds through trapping the mobile carriers (electrons) on the surface of the semiconductor by the adsorbed NO_X species, as proposed.

Table: 3.4

Conductivity and carrier concentration of In_2O_3 thin film in the presence of different concentration of NO_X at 623 K

Concentration of NO_X (ppm)	Conductivity (σ) of In_2O_3 thin film (Ω^{-1} cm^{-1})	Carrier concentration (n) of In_2O_3 thin film (cm^{-3})
5	0.091	4.07×10^{17}
10	0.067	2.14×10^{17}
25	0.052	1.19×10^{17}
50	0.049	5.56×10^{16}
63	0.045	2.81×10^{16}
75	0.042	2.15×10^{16}

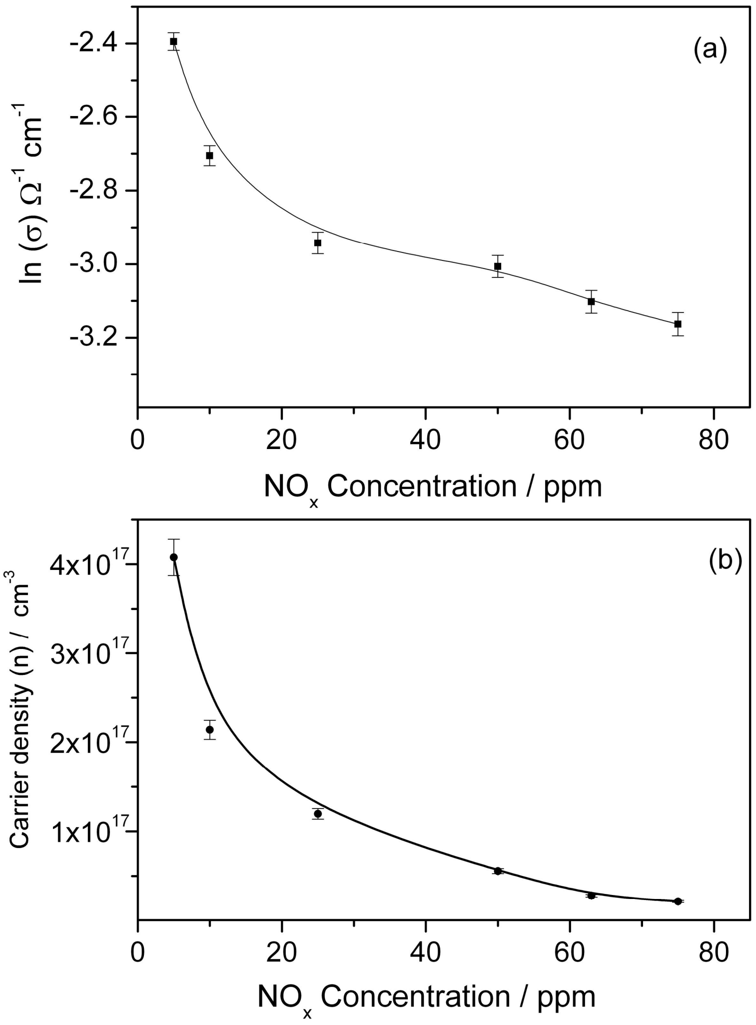

Fig. 3.11 a) Conductivity and b) carrier concentration as a function of concentration of NO_X in air at 623 K (Error bar: < 1.5 %)

3.3.6 Measurement of Debye length of In_2O_3 in clean air and air containing NO_X as a function of temperature

As mentioned earlier, the In_2O_3 thin film consists of uniformly sized grains with average size 75 – 100 nm. The thickness of the depletion over the grains would vary with the nature of the adsorbed species. The charge depletion layer represented at first approximation by the Debye length (L_D: defined as the distance in semiconductor over which local electric field affects distribution of free charge carriers; L_D, decreases with increasing concentration of free charge carriers in the materials) in clean air and in air containing 25 ppm of NO_X was calculated for In_2O_3 at different temperatures from the measured carrier concentration using the following eqn. 3.6 [12]:

$$L_D = \sqrt{\frac{\varepsilon_o \, \varepsilon_r \, k T}{e^2 \, n}} \tag{3.6}$$

where 'ε_o' is the permeability of free space (a vacuum), 'ε_r' is the permittivity of the material, 'k' is the Boltzmann constant, 'T' is the temperature (K), 'e' is the electronic charge and 'n' is the carrier concentration measured for the In_2O_3 thin film from Hall measurements. With $k = 1.380 \times 10^{-23}$ J/K, $\varepsilon_0 = 8.854 \times 10^{-12}$ $C^2/J \cdot m$, $\varepsilon_r = 8.9$ for In_2O_3, $e = 1.602 \times 10^{-19}$ C, L_D for In_2O_3 when exposed to air containing 25 ppm of NO_X was calculated at different temperatures.

Figure 3.12 shows the plot of L_D versus $T^{0.5}$. L_D in clean air is 36 nm at 373 K, which decreases gradually to 8 nm at 673 K (Fig. 3.12a). Calculated Debye length data corresponding to In_2O_3 thin film in clean air and in the presence of air containing 25 ppm of NO_X as a function of temperature is shown in Table. 3.5.

Table: 3.5

Calculated Debye length of In_2O_3 thin film

in air and in the presence of air containing 25 ppm of

NO_X as a function of temperature (K)

Temperature (K)	Debye length (nm)	
	Clean air	Air containing 25 ppm of NO_X
673	15.9	8.0
623	16.5	9.2
573	21.7	10.7
523	22.3	11.9
473	25.5	17.1
448	30.5	-
423	37.1	22.9
398	40.7	-
373	-	36.1

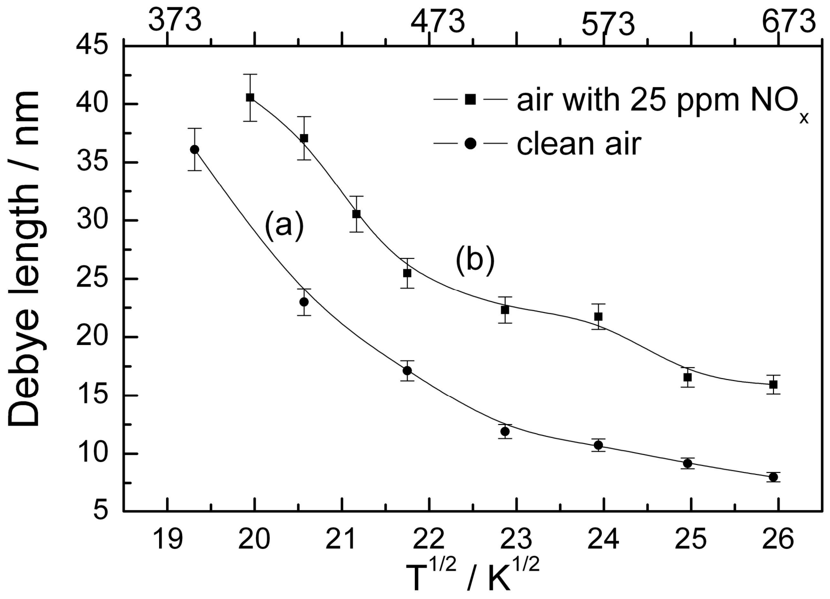

Fig. 3.12 Plot of Debye length (L_D) of In_2O_3 as a function of temperature ($T^{1/2}$): (a) in air and (b) 25 ppm of NO_X in air [Error bar: < 1.0 %]

The large value of carrier concentration varying from 10^{16} to 10^{18} cm^{-3} controls the L_D as compared to that of temperature (273 – 673 K) giving rise to the pattern shown in Fig. 3.12. Upon exposure to 25 ppm of NO_X, the same dependence is obtained, but with a constant difference. Here, L_D starts from 41 nm at 398 K and decreases to 16 nm at 673 K (Fig.3.12b). The increase in L_D of In_2O_3 in the presence of 25 ppm of NO_X compared with that of the values in air clearly indicates that there is an increase in the thickness of depletion region of In_2O_3 thin film due to adsorption of different species of NO_X, which in turn raises the barrier height. This leads to a decrease in the carrier mobility at lower temperatures [Fig.3.4c].

3.3.7 Interaction of In_2O_3 thin film in air and in the presence of NO_X using AC impedance technique

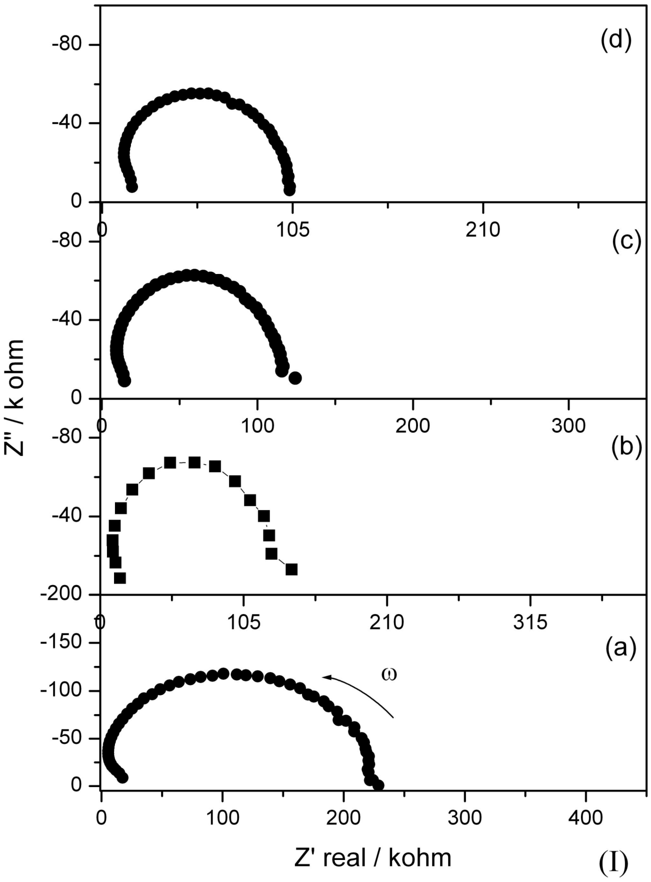

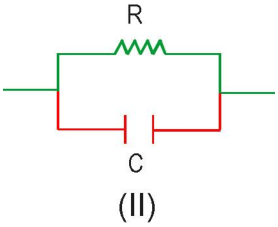

Fig. 3.13 AC impedance plot of In_2O_3 thin film in clean air
I; a) 548 K, b) 598 K, c) 648 K and d) 698 K.
II; Modelled R & C components of In_2O_3 thin film

Figure 3.13 (I) shows the Nyquist (Z' vs Z") impedance plots of In_2O_3 thin film between 546 K and 698 K in air (Frequency range: 1 MHz to 1 kHz). From the semicircular pattern obtained, equivalent circuits were modelled. This model offered an equivalent circuit with parallel combination of resistor (R) and capacitor (C) [C is a space charge capacitance] shown in fig. 3.13 (II). The deposited In_2O_3 thin film is of nano-structured and each grain is uniformly well connected as seen from AFM images shown in fig. 3.2. A space charge region is built on the surface because of the capture of electrons by oxygen from air to form chemisorbed oxygen ions on it as shown by the eqn. 3.1. The values of R and C components of In_2O_3 thin film deduced from the model are given in Table 3.6. It is observed that, R decreases with increase in temperature while only a marginal increase in capacitance is observed with increase in temperature.

Table: 3.6

Calculated 'R' and 'C' of In_2O_3 thin film using Zview® (version 2.70) program

Temp. (K)	R (Mohm) (± 1 %)	C (pF) (± 1 %)
548	0.25	3.52
598	0.12	3.84
648	0.11	3.91
698	0.1	4.20

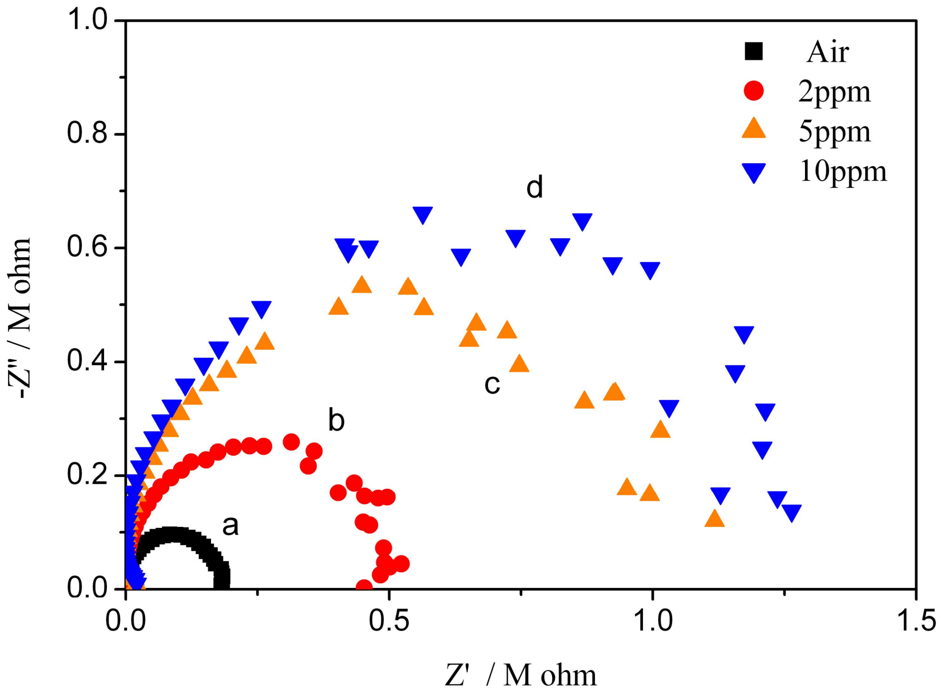

Fig. 3.14 Impedance plot of In_2O_3 thin film at 598 K; a: clean air, b: c: and d : air containing 2, 5 & 10 ppm of NO_X

Figures 3.14a to d show the impedance plots (Z' vs Z") of In_2O_3 thin film measured between 1 MHz to 1000 Hz in air and air containing 2, 5 and 10 ppm of NO_X at 598 K. The impedance data shown in figs. 3.14b to d were measured after admitting air containing known concentrations of NO_X was introduced into the chamber in which the thin film was housed. Figure shows there is a gradual increase of diameter of the semicircle in air containing different concentrations of $NO_{X.}$ It is to be noted that during the impedance measurement, frequency was varied from 1 MHz to 1000 Hz. Ling Chen et al also made similar observation during their experiments with 1% Ag doped WO_3 in air containing 40 ppm of NO_X and in clean air at 623 K [87]. In fact, because of interaction of the film with NO_X, both R and C components change with time. To deduce useful information, it is preferable to fix the frequency of measurement. For choosing the appropriate frequency, the resistance and capacitance of the In_2O_3 thin film in clean air were deduced from the impedance data from fig. 3.14a using eqn. 3.7 and 3.8:

$$R = \frac{(Z'^2 + Z''^2)}{Z'} \tag{3.7}$$

$$C = \frac{-Z''}{\omega(Z'^2 + Z''^2)} \tag{3.8}$$

The variation of resistance and capacitance of In_2O_3 thin film in clean air as a function of frequency at 598 K is shown in fig. 3.15a and b (log-log plot of R & C vs frequency (Hz)). As seen from fig. 3.15a, the measured resistance of the film in air was frequency independent in the frequency range of 1 kHz to 316 kHz. Above 316 kHz, a gradual decrease of the resistance was observed with increase in frequency. Figure 3.15b shows that the measured value of capacitance of the film was independent of frequency in the frequency range of 32 to 630 kHz. Below 30 kHz, a gradual decrease in measured capacitance was observed with decrease in frequency. Hence, the measured values of R and C of the thin film were frequency independent in the frequency range of 32 and 315 kHz. For measuring the impedance of In_2O_3 thin film during its interaction with NO_X in air and deduce the time dependent resistance and capacitance values, a frequency 32 kHz was chosen. Experiments were conducted at 598 K. The stability of R and C components of In_2O_3 thin film in clean air as a function of time was monitored for a period of 1.5 h. and the data deduced are shown in fig. 3.16a and 3.16b. As seen from the figure, no drift was observed in the resistance as well as in the capacitance of the thin film.

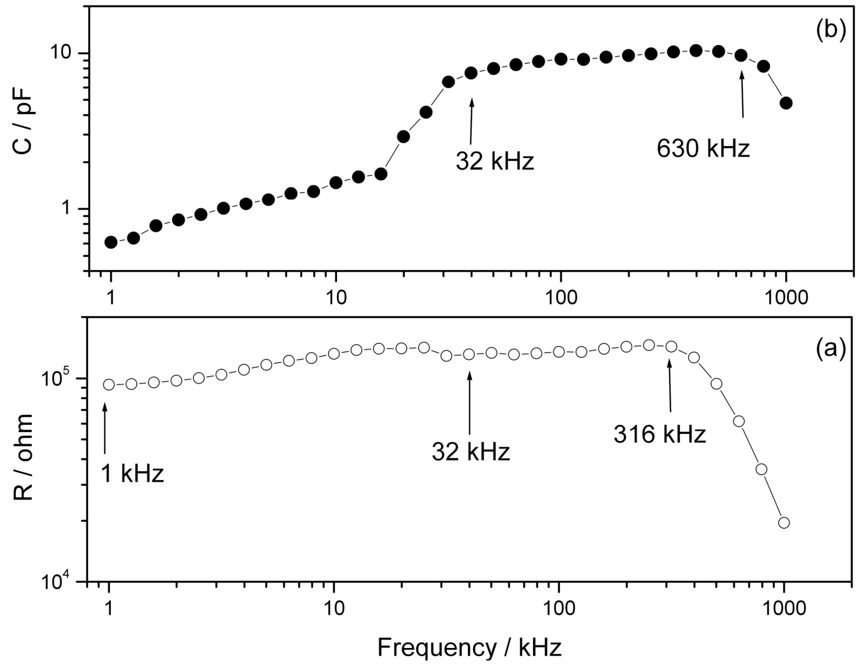

Fig. 3.15 log –log plot of resistance (a) and capacitance (b) as a function of frequency of In_2O_3 thin film in air at 598 K.

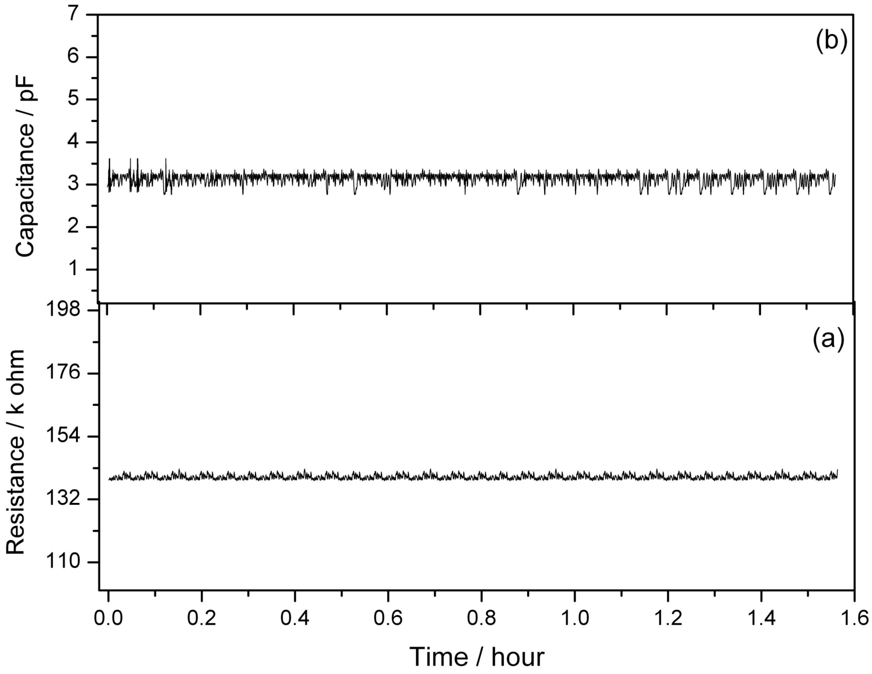

Fig. 3.16 Baseline measurement of a) resistance and b) capacitance of In_2O_3 thin film at 598 K as a function of time in air measured at frequency of 32 kHz.

Figure 3.17a and b show the typical change in the resistance and capacitance of the In_2O_3 thin film at 598 K as a function of time when exposed to air containing 5 ppm of NO_X. Resistance and capacitance values first increased and after about 250 to 300 s, they remained stable. On replacing the air containing NO_X with clean air, the resistance of the film gradually decreased and finally retraced to the value in clean air. From these data, the response and recovery times (t_{90}) of resistance and capacitance components of In_2O_3 thin film were calculated. From the calculation the response time for change in resistance and capacitance are around 50 and 160 s. The recovery time for both resistance and capacitance are between 7 and 8 minutes respectively.

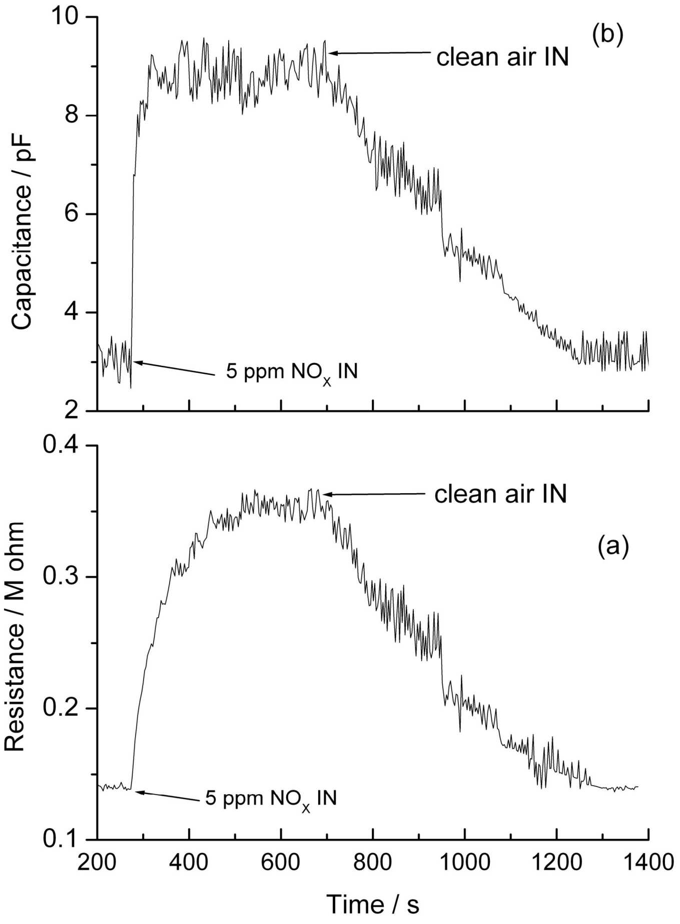

Fig. 3.17 Typical change in the response of a) resistance and b) capacitance of In_2O_3 thin film at 598 K as a function of time towards 5 ppm of NO_X in air measured at frequency of 32 kHz

Figure 3.18 shows the plot of sensitivity (%) computed from resistance and with capacitance data for the In_2O_3 thin film at 598 K as a function of NO_X concentration in air. As seen in the figure, sensitivity of the film was 68 % even for 2 ppm of NO_X in air. The sensitivity gradually increased to 83% when NO_X concentration was 20 ppm. In the case concentration range studied i.e. 2 to 24 ppm the net change in sensitivity per unit concentration of NO_X is 0.81. Variation of capacitance of the film with increase in NO_X concentration is shown in fig. 3.18 and is not linear. A first order polynomial could be used for fitting the capacitance changes.

The sensitivity based on capacitance change was 30 % when NO_X was 2 ppm. It increased to 71% when NO_X concentration was 20 ppm. To understand the cross sensing characteristics of the In_2O_3 thin film towards other gases, its impedance was measured on exposure to 5000 ppm of H_2 and PG in air. The film did not show any change in the resistance and capacitance during its exposure to air containing H_2 or PG.

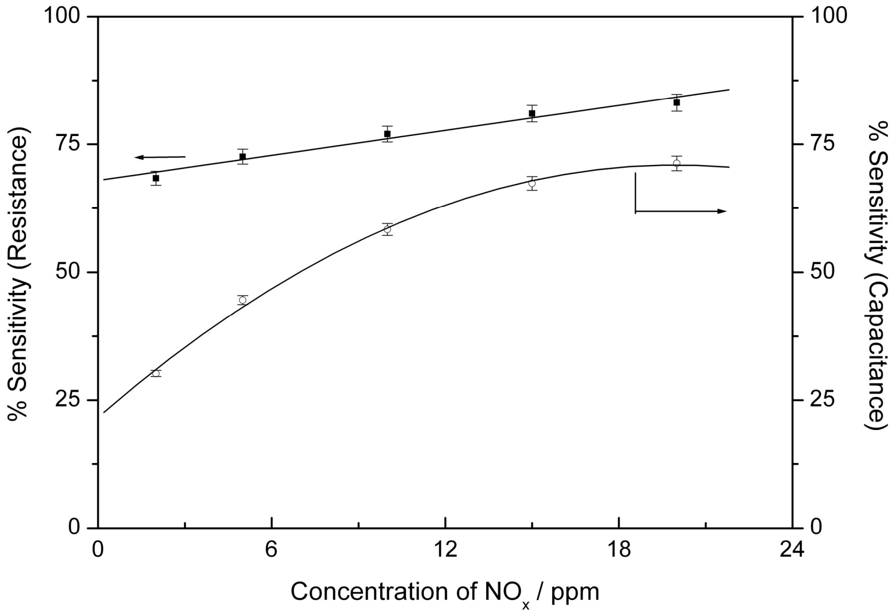

Fig. 3.18 Calibration traces obtained using a) resistance and b) capacitance changes towards various concentrations of NO_X using In_2O_3 thin film at 598 K (f: 32 kHz) [Error bar: < 1.5%]

The sensing mechanism of metal oxides was understood by the reaction between semiconductor surface and analyte in the atmosphere, which changes the conductivity of semiconductor at a particular temperature. The change in the conductivity of the semiconductor in the gaseous environment may be attributed to the adsorption mechanism: The oxygen from the atmosphere adsorbs and extracts electrons from the semiconductor. A space charge region on the surface of the metal-oxide is built, resulting in an electron-depleted surface layer due to the electron transfer from the semiconductor surface to oxygen. The decrease in carrier concentration due to capturing of these charges by oxygen from air resulted in increase in Debye length (L_D) of In_2O_3 thin film (10 nm) at 598 K in fig. 3.12. It is well known that NO_2 is exhibiting both polarizing ($\alpha = 3.02$) and dipole moment ($\mu = 0.316$) character [88]. The electron withdrawing nature of NO_2 abstracts charges (eqn. 3.2) resulted in further increase in L_D to 19 nm as seen from Fig. 3.12. The increase in the resistance exhibited by In_2O_3 thin film in the presence of air containing NO_X (fig. 3.17) is more than in clean air is primarily due to abstraction of charge carriers by NO_X from the surface of In_2O_3 thin film. The increase in the capacitance of the thin film is related with the change in the ratio of carrier concentration (n) due to abstraction of charges by NO_X and the change in barrier height (V_b) of In_2O_3 thin film.

It is well known that capacitance (C) is related to electron concentration, and barrier height (V_b) as shown by the eqn. 3.9 (Equation 3.9 was adopted from the measurement of Schottky barrier height (V_b) in metal-semiconductor junction) [89].

$$C \propto \left(\frac{n}{V_b}\right)^{1/2} \tag{3.9}$$

Ponce et al observed and reported the change in the capacitance of SnO_2 thick film during the film interaction with CO [90]. Author correlated such effect with carrier concentration (n) and barrier height (V_b). Xiaoayan Zhou also reported the effect of capacitance change of ZnO nanorods during the interaction of ethanol by correlating with parameters shown in eqn. 3.9 [91].

Chandra sekar et al published their results on the change in the DC resistance of In_2O_3 thin film towards 100 ppm of H_2 and PG in air between the temperatures of 475 and 675 K [73]. The thin film showed a resistance change in the presence of 100 ppm of H_2 and PG at 598 K by DC. But, in the present studies, In_2O_3 thin film did not responded to 5000 ppm of H_2 and PG in clean air at the fixed frequency of 32 kHz at 598 K. The reason for not responding to hydrogen and PG is not understood from the present investigations.

3.4 Conclusions

The four probe conductivity, charge carrier concentrations and charge carrier mobility of In_2O_3 thin film in air was compared with NO_X at different temperatures using high temperature van der Pauw and Hall measurement technique. The decrease in four probe conductivity and carrier concentration of In_2O_3 thin film in the presence of NO_X by comparing its behaviour in air was determined experimentally. The results from Hall studies indicated the change in the trends in conductivity, carrier concentrations and carrier mobility of the film between 373 and 673K. But, it doesn't provide the reason for variation in the behaviour shown by the film in the presence of NO_X when compared with its behaviour in air. Raman spectroscopic studies provide the characteristic signature evidence of different NO_X adsorbing species on the surface of In_2O_3 thin film at different temperatures during its interaction. The presence of different N_XO_Y species adsorbed on the surface at different temperatures is responsible for the variation in the conductivity and mobility of In_2O_3 thin film.

Apart from understanding the mechanism of different adsorbing species of NO_X with In_2O_3, the effect of NO_X adsorption on electrical properties of the film was observed by AC impedance technique in air and in the presence of NO_X. The thin film showed good selectivity towards NO_X in the presence of other gases like H_2 and PG. The increase in the film resistance in the presence of NO_X is the clear indication that it is occurring due to abstraction of unoccupied charges by electron withdrawing NO_X on the surface of In_2O_3. The observation of increase in the capacitance of In_2O_3 thin film during its interaction with NO_X is due to change in the ratio of carrier concentration and barrier height of In_2O_3.

CHAPTER 4

Preparation, characterization and gas sensing properties of $CuInO_2$ and $Cu_2In_2O_5$ thin films towards H_2, NH_3, PG and NO_x

4.1. Introduction

Indium oxide is an n-type semi-conducting metal oxide with band gap energy of 3.5 eV. A film of In_2O_3 or any other n – type oxide exhibits an increase in resistance when exposed to trace levels of NO_X [92 – 94]. This increase in resistance is due to entrapment of charge carriers (electrons) of these oxides at the gas – solid interface resulting in a sharp fall in their concentration [95]. When the film resistance exceeds giga ohms, one requires very expensive and sophisticated instruments for measurements. This problem can be circumvented by the use of a film of a suitable p-type semi-conducting oxide as gas sensing material. With holes as the majority carriers, they would exhibit an opposite effect. $CuInO_2$ is a p-type semi-conducting oxide, which belongs to the general family of $A^+B^{3+}O_2$ ($A^+ = Cu^+$ or Ag^+ ; $B^{3+} = Al^{3+}$, Ga^{3+}, In^{3+}, Cr^{3+}) and has a delafossite structure [96 – 100]. Compounds exhibiting 'delafossite' structures are transparent conducting oxides (TCO) which are being explored for their application in optoelectronic devices [96].

Gas sensing properties of $CuInO_2$ has not been studied so far and this was taken up in the present investigation. Preparation of $CuInO_2$ in air invariably leads to the formation of $Cu_2In_2O_5$, which is found to behave like n-type semiconductor (from the present studies). Oxidation state of copper is +1 in $CuInO_2$, while in $Cu_2In_2O_5$, it is +2. When processed in air, copper gets oxidized from +1 to +2 state and therefore oxygen partial pressure needs to be controlled for the synthesis of $CuInO_2$. Delafossite structure of $A^+B^{3+}O_2$ is shown in Fig. 4.1. It can be described as the alternate stacking of BO_2 layers of edge-sharing BO_6 octahedra and planes of A^+ cation arranged as a planar triangular network [103, 104]. The A^+ cation has dumb-bell coordination with two oxygen anions from the planes above and below as marked in the Fig. 4.1. Depending on the manner of stacking of the BO_2 and A layers, structural variants with hexagonal or rhombohedral symmetry can be formed. $CuInO_2$ exhibits oxygen non-stoichiometry [101]. Since indium is present at its highest oxidation state of +3 in this compound, the non-stoichiometry arises due to the presence of Cu^{2+} in the lattice.

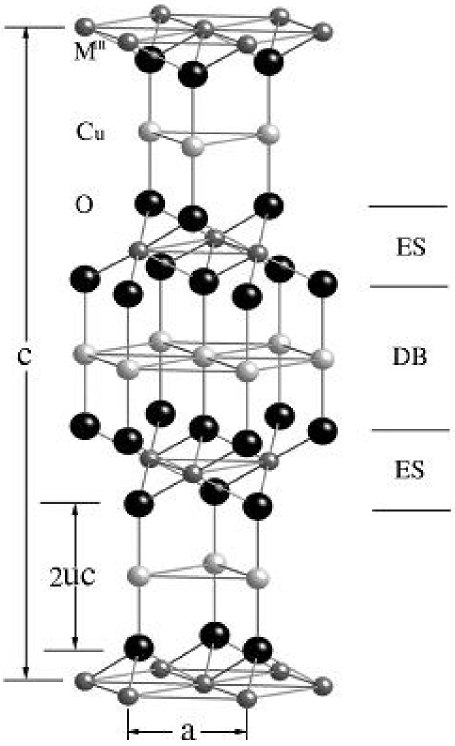

Fig. 4. 1 Crystal structure of delafossite-type ($A^+B^{3+}O_2$) copper indium oxide, where A: Cu^+ and B: In^{3+} , ES: Edge Sharing, DB: dumb-bell [102]

This chapter discusses the preparation of $CuInO_2$ and $Cu_2In_2O_5$ its characterization using XRD, XPS, AFM, AC impedance spectroscopy and its gas sensing characteristics towards H_2, NH_3, PG and NO_X in the temperature range of 423 to 677 K.

4.2. Experimental

4.2.1 Preparation of thin films of $Cu_2In_2O_5$

$Cu_2In_2O_5$ was synthesized by conventional solid state route. Calculated quantities of CuO and In_2O_3 were mixed and calcined in air at 1223 K for about 24 h. The resulting product was ground, pelletized and again heated at 1223 K for another 24 h. This process was repeated three times in order to get homogeneous product. The product was ground thoroughly and characterized using XRD. The powder was made in the form of pellets and was used as target for the preparation of thin films of $Cu_2In_2O_5$ using PLD (deposition conditions for the formation of $Cu_2In_2O_5$ are given in Table. 4.2).

The $Cu_2In_2O_5$ thin film was characterized using XRD, AFM and XPS. The interaction behavior of thin films of $Cu_2In_2O_5$ and $CuInO_2$ with H_2, petroleum gas (PG), NH_3 and NO_X gases was studied in the temperature region of 498 – 677 K. The impedance of bulk $Cu_2In_2O_5$ was measured in the temperature region of 473 – 693 K in the ambient of air, oxygen and in argon. The experimental facilities for all the studies and its principles have been discussed in Chapter 2.

4.2.2 Preparation of thin films of $CuInO_2$

Preparation of $CuInO_2$ powder in air by solid state route by heating a stoichiometric mixture of Cu_2O and In_2O_3 yielded $Cu_2In_2O_5$ instead of $CuInO_2$ [105, 106]. This was due to the oxidation of Cu_2O to CuO, which took place in air. Similar observations were made in the present investigations also. Therefore, preparation of $CuInO_2$ required controlled oxygen partial pressure in order to retain copper in +1 oxidation state. Garlea et al synthesized $CuInO_2$ by chemical exchange process by heating a mixture of CuCl and $NaInO_2$ in a sealed, evacuated silica tube at 873 K [106]. These authors carried out thermogravimetric analysis of $CuInO_2$ in oxygen ambient. The results of these experiments showed a gradual uptake of oxygen by $CuInO_2$ above 473 K and it got completely converted to $Cu_2In_2O_5$ (based on weight gain) above 823 K. These studies indicate that $CuInO_2$ would not be stable in air above 473 K. Data on thermochemical properties of $CuInO_2$ and $Cu_2In_2O_5$ are reported in literature [107].

To examine the stability of $CuInO_2$ in air and feasibility of its preparation by thermal decomposition of $Cu_2In_2O_5$, oxygen partial pressure of the equilibrium below were calculated:

$$\mathrm{Cu_2In_2O_5} \rightleftharpoons \mathrm{2CuInO_2} + 1/2\mathrm{O_2} \quad \mathrm{(RX1)} \tag{4.1}$$

Calculations were made for the temperature range of 473 – 873 K. The Gibbs energy change of the above equilibrium is given below:

$$\Delta G_{RX1} = 2\Delta G^{o}_{f,T} < \mathrm{CuInO_2} > + 1/2RT\ln pO_2 - \Delta G^{o}_{f,T} < \mathrm{Cu_2In_2O_5} > = 0 \tag{4.2}$$

Yao et al estimated the Gibbs energy of formation of $CuInO_2$ (s) and $Cu_2In_2O_5$ (s) from copper and indium oxides shown by eqn. 4.3 and eqn. 4.4 [107].

$$\mathrm{Cu_2O + In_2O_3 \rightarrow 2CuInO_2} \quad \mathrm{(RX2)} \tag{4.3}$$

$$\mathrm{2CuO + In_2O_3 \rightarrow Cu_2In_2O_5} \quad \mathrm{(RX3)} \tag{4.4}$$

By incorporating the Gibbs energy of formation of Cu_2O (s), CuO (s) and In_2O_3 (s), Gibbs energy of formation of $CuInO_2$ and $Cu_2In_2O_5$ can be obtained, as shown below [85]:

$$2\Delta G^{o}_{f,T} < CuInO_2 > = \Delta G^{o}_{RX2,T} + \Delta G^{o}_{f,T} < Cu_2O > + \Delta G^{o}_{f,T} < In_2O_3 > \tag{4.5}$$

$$\Delta G^{o}_{f,T} < Cu_2In_2O_5 > = \Delta G^{o}_{RX3,T} + 2\Delta G^{o}_{f,T} < CuO > + \Delta G^{o}_{f,T} < In_2O_3 > \tag{4.6}$$

Gibbs energy of formation of $CuInO_2$ is calculated using the eqn. 4.7 given below:

$$\begin{aligned}\Delta G_{RX1} &= \Delta G^{o}_{RX2} + \Delta G^{o}_{f,T} < Cu_2O > + \Delta G^{o}_{f,T} < In_2O_3 > \\ &\quad + 1/2RT\ln pO_2 - \Delta G^{o}_{RX3} - 2\Delta G^{o}_{f,T} < CuO > - \Delta G^{o}_{f,T} < In_2O_3 >\end{aligned} \tag{4.7}$$

$$\begin{aligned}0 = \Delta G_{RX1} &= \Delta G^{o}_{RX2} - \Delta G^{o}_{RX3} + \Delta G^{o}_{f,T} < Cu_2O > - 2\Delta G^{o}_{f,T} < CuO > \\ &\quad + 1/2RT\ln pO_2\end{aligned} \tag{4.8}$$

$$\Delta G_{RX1} = -22.0217T + 1.74T\log T + 304940.3 + 9.512122T\log pO_2 = 0 \tag{4.9}$$

By incorporating data in eqn 4.9, the oxygen partial pressures of equilibrium (eqn. 4.1) were calculated for temperature range of 473 to 873 K and are shown in Table 4.1. When $Cu_2In_2O_5$ (s) is heated at a chosen temperature in a gaseous environment with oxygen partial pressures below the listed value, it is expected to decompose to $CuInO_2$. The calculated oxygen partial pressures are extremely low indicating that $Cu_2In_2O_5$ would be stable in air (p_{O_2} = 0.21 atm) and its thermal decomposition in air cannot be the route to synthesize $CuInO_2$.

Table: 4.1

Estimated oxygen partial pressure for the decomposition of $Cu_2In_2O_5$ to $CuInO_2$ as a function of temperature

Temperature (K)	pO_2 (atm.)
473	10^{-70}
573	10^{-58}
673	10^{-50}
773	10^{-44}
823	10^{-41}
873	10^{-39}

For experimental confirmation of these calculations, thermogravimetric analysis of $Cu_2In_2O_5$ in oxygen atmosphere was carried out. Figure 4.2 shows the TG/DTA trace when the temperature of the sample was increased from 300 to 1223 K at a rate of 5 K per min. A very small weight loss was observed between 300 and 420 K. This weight loss may probably be due to the presence of physisorbed moisture evolved from the sample. There was no other thermal event in the entire temperature range (exothermic or endothermic). The trend exhibited in the heating run by the compound was again exhibited in the cooling run (fig. 4.3) at the cooling rate of 5 K per min.

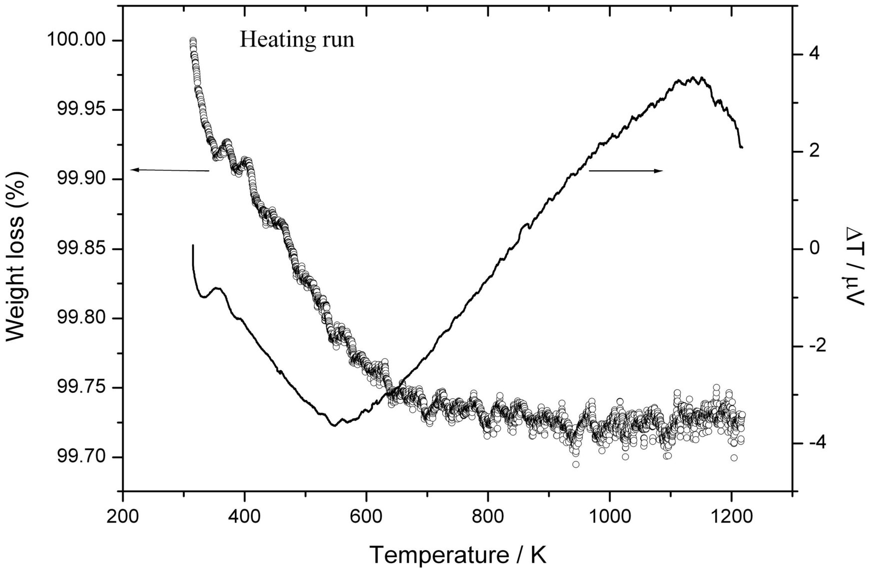

Fig. 4.2 Thermogravimetric and differential thermal analysis traces of $Cu_2In_2O_5$ during heating run

From the results obtained from quenching and thermal analysis of $Cu_2In_2O_5$, it is clear that the compound does not decompose during the heating process, showing its stability.

Additionally, a sample of $Cu_2In_2O_5$ was taken in quartz tube and heated in air at 1223 K for a period of 5 hours followed by quenching to room temperature in air. The quenched sample was characterized by XRD. This result reaffirms the stability of $Cu_2In_2O_5$ in air at 1223 K.

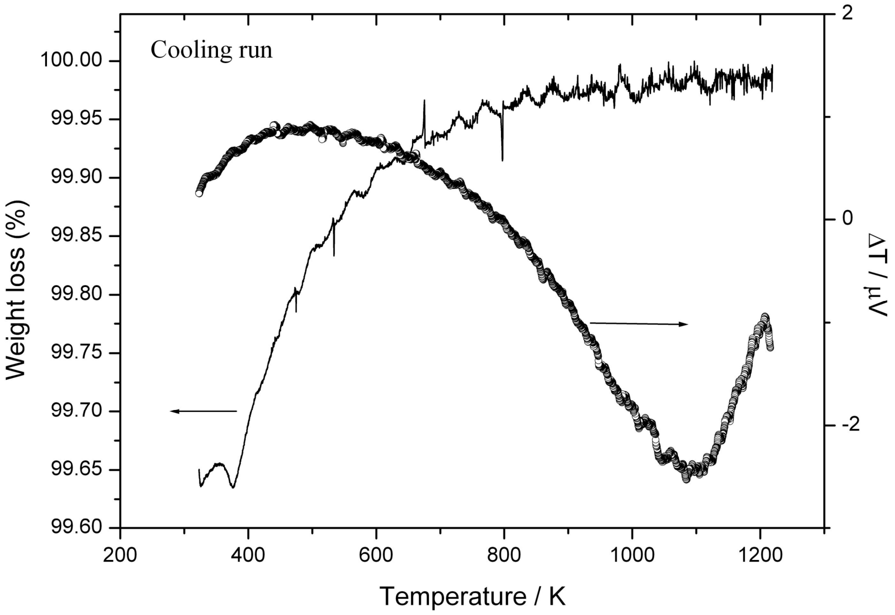

Fig. 4.3 Thermogravimetric and differential thermal analysis traces of $Cu_2In_2O_5$ during cooling run

PLD technique is known to stabilize certain phases in thin film form, which otherwise are not amenable for the conventional synthetic routes. The extreme non-equilibrium conditions, which prevail during deposition such as high fluence, repetition rate, growth temperature and low oxygen partial pressure, are exploited for this purpose. In the present work also $CuInO_2$ thin film was also deposited by PLD. The deposition of thin film of $CuInO_2$ by PLD has been reported in the literature, which requires narrow synthetic parameters [105, 108 & 109]. For this deposition, $Cu_2In_2O_5$ was used as the target. The optimized conditions for this thin film deposition are given in Table. 4.2. In Cr–O system, CrO_2 is metastable under ambient systems. Guinneton et al deposited CrO_2 thin film on sapphire substrate using Cr_8O_{21} as the target by maintaining an oxygen pressure of 0.15 mbar at 573 K [110].

The films were deposited on polycrystalline alumina and sapphire substrates. The films where characterized by XRD, AFM and XPS. Their sensing characteristics towards H_2, petroleum gas (PG), NH_3 and NO_X were studied in the temperature region of 423 to 473 K.

Table: 4.2

In-situ growth parameters for pulsed laser deposition of thin films of $CuInO_2$ and $Cu_2In_2O_5$ using $Cu_2In_2O_5$ as target

Deposition conditions	$CuInO_2$	$CuIn_2O_5$
Fluence (J cm^{-2})	4 - 5	4 - 5
Repetition rate (Hz)	10	10
Pre-ablation (min.)	5	5
Ablation (min.)	20 – 30	20 – 30
Pressure (mbar of oxygen)	5×10^{-2}	2×10^{-1}
Substrate-Target distance (cm)	4 – 5	4 – 5
Substrate Temperature (K)	823	773
Substrate	Polycrystalline alumina and sapphire	Polycrystalline alumina and sapphire

4.3. Results and Discussion

4.3.1 Characterization of bulk $Cu_2In_2O_5$ and $Cu_2In_2O_5$ thin film by XRD

The XRD pattern of $Cu_2In_2O_5$ powder prepared at 1223 K is shown in Fig. 4.4(a). All the reflections were indexed for the monoclinic phase [Space group P2(3)] of $Cu_2In_2O_5$ [JCPDS # 75-0579]. The XRD pattern of the thin film deposited using PLD on polycrystalline Al_2O_3 substrate is shown in Fig. 4.4b. The XRD pattern of the Al_2O_3 substrate is also shown in Fig. 4.4(c). The reflections marked (310), (420), $(\bar{2}21)$, (201), (121), (411), (311), $(\bar{3}80)$ match with those of $Cu_2In_2O_5$. In addition to these peaks, the reflections from the Al_2O_3 substrate are also seen, which are marked * in Fig. 4.4 (b).

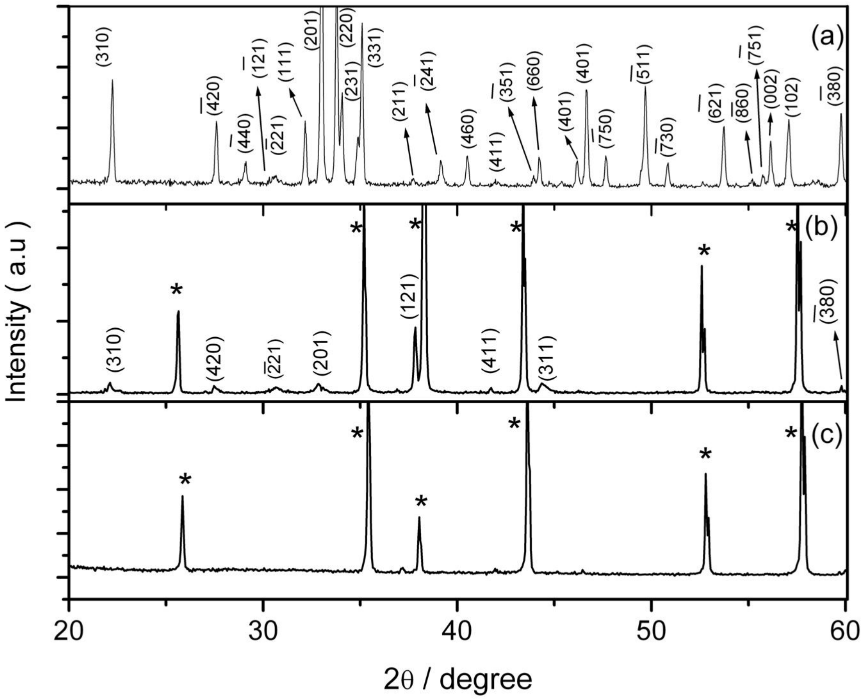

Fig. 4.4 X-ray diffraction patterns of a) bulk $Cu_2In_2O_5$, b) $Cu_2In_2O_5$ thin film and c) alumina substrate (* corresponds to reflections of Al_2O_3)

4.3.2. Characterization of $CuInO_2$ thin film by XRD

Figure 4.5(a) shows the XRD pattern of $CuInO_2$ thin film deposited on alumina substrate at 823 K. The reflections of (006), (012), and (104) corresponding to rhombohedral symmetry [$R\bar{3}m(166)$] of $CuInO_2$ (JCPDS # 53-0954) [105, 107]. The other strong intense peaks belong to alumina substrate are marked * as in the fig. 4.5 (b). The reflections at $2\theta = 44.62^o$ and 64.71^o arise from the gold electrodes. No other lines were found, implying that the deposited $CuInO_2$ is pure and is stabilized in thin film form.

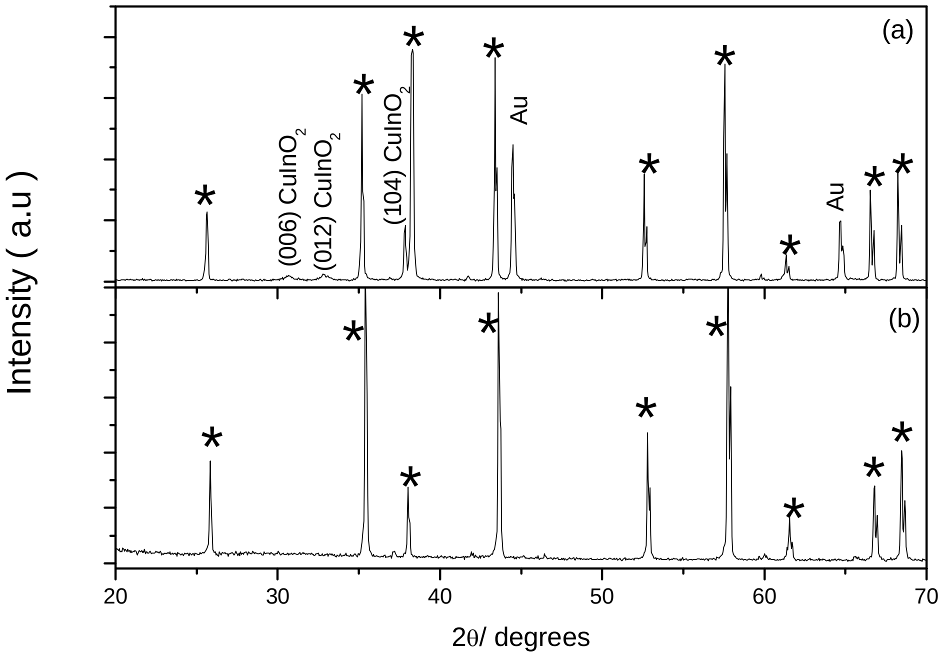

Fig. 4.5 X-ray diffraction pattern of a) rhombohedral symmetry of $CuInO_2$ thin film and b) alumina substrate (* corresponds reflections of Al_2O_3)

4.3.3. Surface Morphology of $CuInO_2$ and $Cu_2In_2O_5$ thin films

Figures 4.6a and 4.6b shows the AFM images of $CuInO_2$ thin film deposited on sapphire substrate. The images show that the thin film has porous network of uniform grains with an average grain size of 300 nm. Figures 4.7a and 4.7b show the AFM images of $Cu_2In_2O_5$ thin film deposited on sapphire substrate. The images show that the film has uniform grains of porous network. The average size of the grains is around 500 nm.

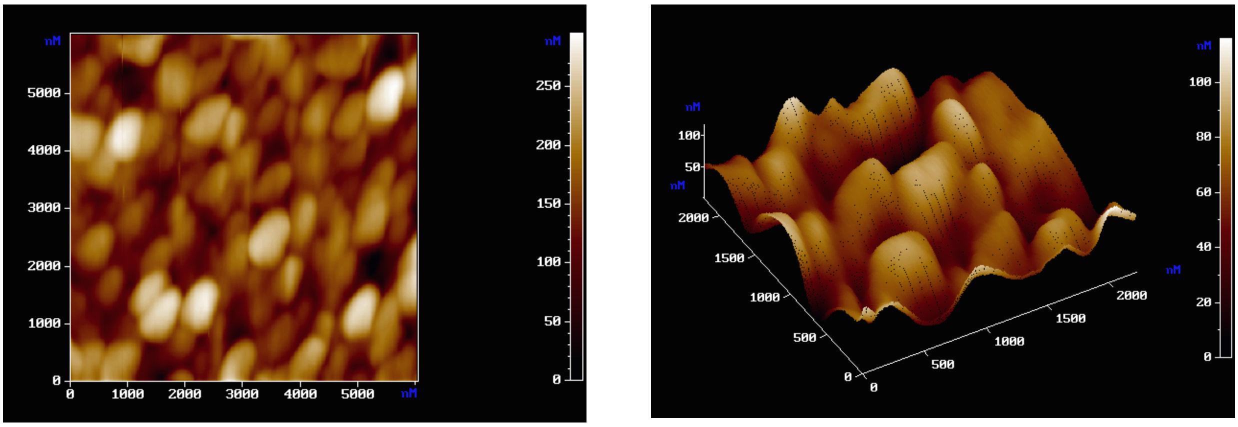

Fig. 4.6 AFM images of CuInO_2 thin film; a) 2D and b) 3D image on sapphire substrate

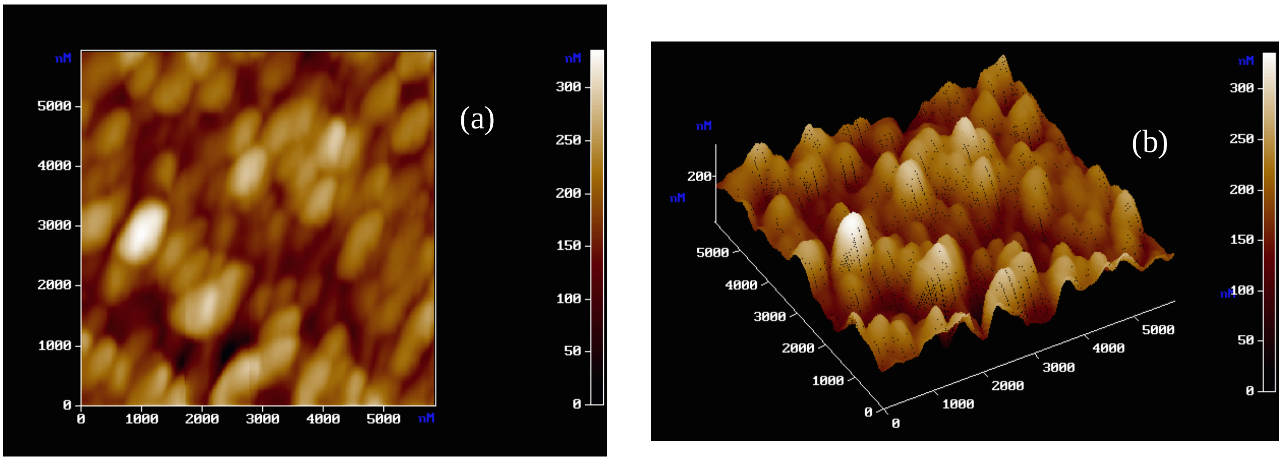

Fig. 4.7 AFM images of $Cu_2In_2O_5$ thin film; a) 2D and b) 3D image on sapphire substrate

4.3.4. Core shell XPS studies on CuInO_2

XPS patterns of In 3d and Cu 2p levels of CuInO_2 thin film was recorded at room temperature. Figure 4.8 shows the Shirley background corrected XPS pattern of In-3d level in CuInO_2 thin film. The data was fitted using Gaussian functions and the overall spectrum synthesized from the fitted components gives a correlation coefficient of 0.99. Parameters, such as full width at half maximum (FWHM), peak positions and satellite peak positions are given in Table 4.3. The $3d_{5/2}$ peak of indium appears at 444.6 eV with its component $3d_{3/2}$ at 452.1 eV separated from each other by the spin orbit coupling constant of 7.5 eV [102, 111]. A single peak with its centre at 444.6 eV is fitted for indium $3d_{5/2}$. This spectrum shows that indium is present in a single valence state of In^{3+} in $CuInO_2$.

Table: 4.3

Binding energy, satellite peak position and FWHM of $CuInO_2$ thin film deduced from XPS studies

Material	Peak	Oxidation state	BE (eV)	Satellite Peak (eV)	FWHM (eV)
$CuInO_2$	$Cu2p_{3/2}$	Cu^{2+}	933.6	939.8 942.7	1.78 1.54 1.27
	$Cu2p_{1/2}$	Cu^{2+}	952.9	960.9	1.82 1.22
	$Cu2p_{3/2}$	Cu^{+}	931.7	-	1.77
	$Cu2p_{1/2}$	Cu^{+}	951.5	-	1.78
	$In3d_{5/2}$	In^{3+}	444.6	-	1.89
	$In3d_{3/2}$	In^{3+}	452.1	-	1.87

XPS spectrum of Cu-2p level of copper in $CuInO_2$ thin film was also recorded and the spectrum is shown in Fig. 4.9. $Cu2p_{3/2}$ peak appears at 931.7 eV and its component $Cu2p_{1/2}$ appears at 951.5 eV, both these peaks indicate the presence of copper in Cu^{+} state. In addition to these peaks, satellite peaks are present at the higher binding energy side of the spectrum with reduced intensity [112 – 114]. This shows that Cu^{2+} is also present in $CuInO_2$.

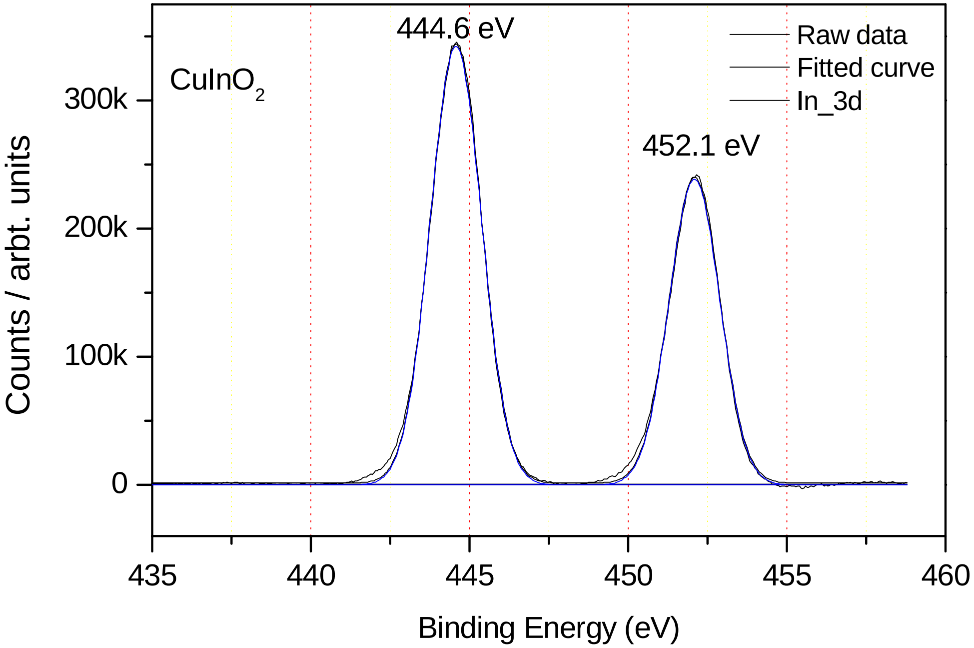

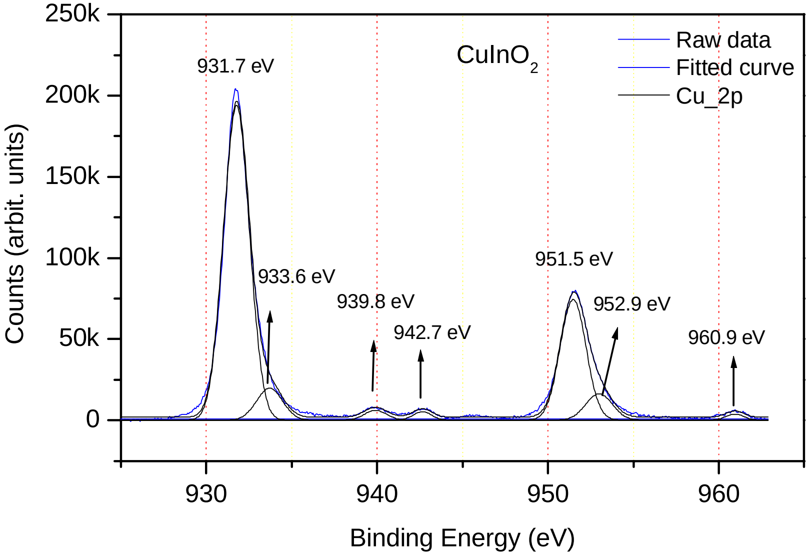

Fig. 4.8 XPS pattern of In – 3d level of indium in CuInO$_2$ thin film

Fig. 4.9 XPS pattern of Cu – 2p in CuInO$_2$ thin film

4.3.5. Core shell XPS studies on thin films of $Cu_2In_2O_5$

XPS patterns of In 3d and Cu 2p level of $Cu_2In_2O_5$ thin films were recorded to elucidate the oxidation states of copper and indium. The Shirley background corrected XPS pattern of In-3d level recorded at room temperature is shown in Fig. 4.10. The data was fitted using Gaussian functions and the overall spectrum synthesized from the fitted components gives a correlation coefficient of 0.99. The various parameters such as full width at half maximum (FWHM), peak positions and satellite peak positions of the curves are given in Table 4.4. The $3d_{5/2}$ peak of indium of $Cu_2In_2O_5$ appears at 444.8 eV with its component $3d_{3/2}$ at 452.3 eV separated from each other by the spin orbit coupling constant of 7.5 eV. A single peak with its centre at 444.8 eV is fitted for indium $3d_{5/2.}$ It is evident from XPS studies that indium is present in a single oxidation state of 3+ in $Cu_2In_2O_5$.

The Shirley background corrected XPS spectrum of Cu-2p level of copper in $Cu_2In_2O_5$ thin film is shown in Fig. 4.11. The Cu-2p pattern of $Cu_2In_2O_5$ was fitted with Gaussian functions and the overall fit gives a correlation coefficient of 0.99. The Cu $2p_{3/2}$ peak in $Cu_2In_2O_5$ appears at 932.9 eV with its component Cu $2p_{1/2}$ peak at 952.8 eV. These peaks are accompanied by shake-up satellite peaks appearing at 940.2 eV, 942.5 eV and at 961.8 eV respectively at the higher binding energy side of the spectrum [112 – 114]. Based on the positions of Cu $2p_{3/2}$ and Cu $2p_{1/2}$ peaks, determination of the oxidation states of copper is difficult. However, peaks accompanying the Cu $2p_{3/2}$ and Cu $2p_{1/2}$ were used to differentiate the oxidation states of copper. Satellites arise due to the charge transfer process taking place between the ligand and the Cu^{2+} which is a d^9 system. This cannot take place for Cu^+, which is a d^{10} system as the 'd' shell is completely filled and therefore satellites peaks cannot be observed.

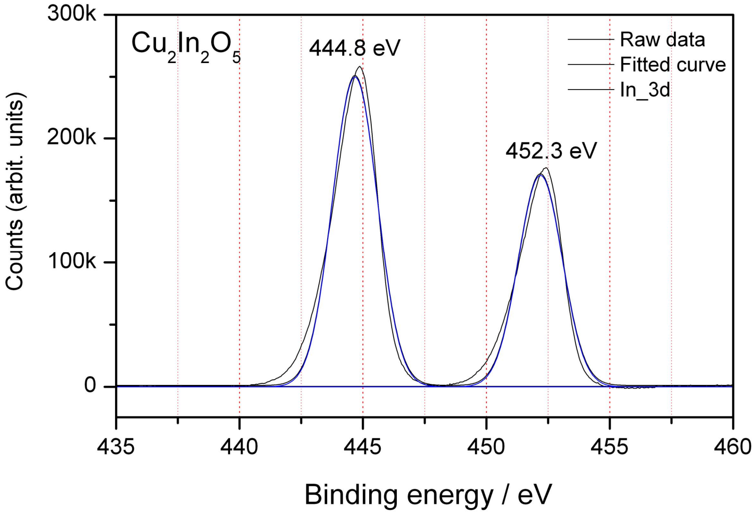

Fig. 4.10 XPS pattern of In – 3d level of indium in $Cu_2In_2O_5$ thin film

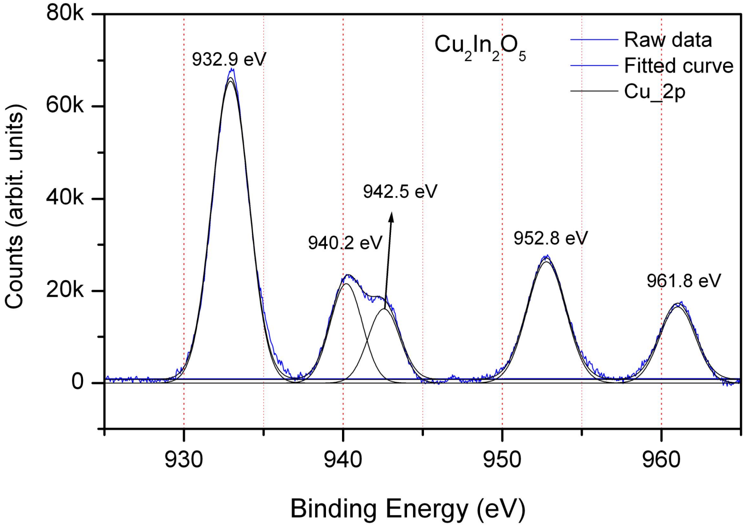

Fig. 4.11 XPS pattern of Cu – 2p level in $Cu_2In_2O_5$ thin film

Table: 4.4

Binding energy, satellite peak position and FWHM of $Cu_2In_2O_5$ thin film deduced from XPS studies

Material	Peak	Oxidation state	BE (eV)	Satellite peak (eV)	FWHM (eV)
$Cu_2In_2O_5$	$Cu2p_{3/2}$	Cu^{2+}	932.9	940.2 942.5	2.72 2.35 2.35
	$Cu2p_{1/2}$	Cu^{2+}	952.8	961.8	2.85 2.62
	$In3d_{5/2}$	In^{3+}	444.8	-	2.13
	$In3d_{3/2}$	In^{3+}	452.3	-	2.08

4.3.6. Gas sensing characteristics of $CuInO_2$ thin film towards analytes

The gas sensing properties of $CuInO_2$ thin film towards trace levels of H_2, PG, NH_3 and NO_x between the temperature of 373 and 473 K were studied. There was no response even for 500 ppm of H_2, PG, and NH_3 in air at 373 and 473 K. However, response to NO_X could be observed at 423 K onwards and it was significant at 473 K showing the selectivity. The gas sensing with $CuInO_2$ thin film was restricted up to 473 K, since it absorbs oxygen from air above this temperature [106]. However, a few experiments were carried out at 598 K to understand its response and cross-sensitivity towards H_2 and PG.

Since the threshold limit values of NO_2 and NO are 3 and 25 ppm respectively, sensing characteristics of $CuInO_2$ thin film was recorded for NO_X concentration of 3 and 24 ppm in air at 423, 448 and 473 K. Figure 4.12 shows the transient changes in resistance of the film at 473 K for different concentrations of NO_X. On introduction of NO_X into the chamber containing thin film, the resistance of the film decreased sharply and reached a stable resistance. The chemisorption of NO_X abstracts the minority carriers (p-type) resulting in an increase in hole carrier density, which manifests in terms of a decrease in resistance for $CuInO_2$. The p-type behavior is due to the presence of Cu^{2+} in $CuInO_2$ which leading to creation of holes in the valence band. After the interaction, resistance of the film retraced back to the original value upon flushing the chamber with clean air. The sensitivity of $CuInO_2$ thin film towards NO_X increases with increase in the concentration of NO_X as seen from the Fig. 4.12.

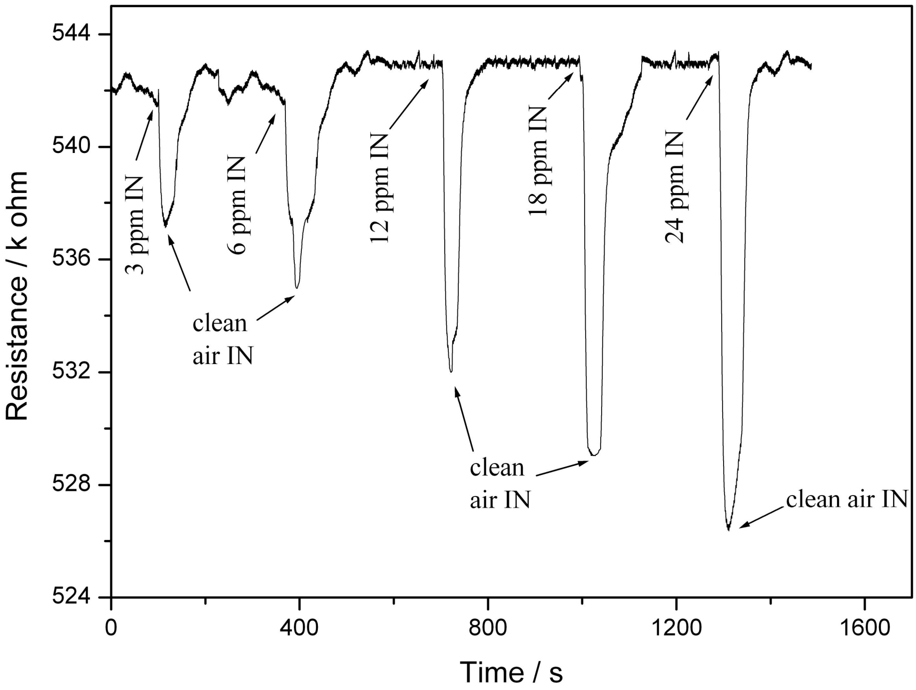

Fig. 4.12 Transient changes in resistance of $CuInO_2$ thin film as a function of time towards different concentrations of NO_X at 473 K

The response and recovery times for sensing of different concentrations of NO_X by $CuInO_2$ thin film are shown in the Table 4.5. The data in the table shows that response and recovery times of $CuInO_2$ thin film increase with increase in concentration of NO_X. The reasons for the increase in response and recovery times as a function of NO_X concentration are not understood presently. The experiments were repeated at least three times and the results established the reproducibility of response and recovery times.

Table: 4.5

Response and recovery time of $CuInO_2$ thin film in the presence of NO_X at 473 K

Concentration of NO_X (ppm)	Response time (s)	Recovery time (s)
3	15	50
6	18	60
12	21	70
18	25	80
24	28	105

As mentioned earlier, $CuInO_2$ thin film did not show any response towards low concentrations of H_2 and PG up to 473 K. To understand the sensing characteristics of $CuInO_2$ thin film towards reducing gases (as opposed to the oxidizing NO_X gas), it was exposed to air containing large concentrations of H_2 and PG (typically 1000 ppm) at 598 K. The resistance of the film was observed to increase on its exposure towards 1000 ppm of PG unlike the observed decrease on exposure towards NO_X (Fig. 4.13).

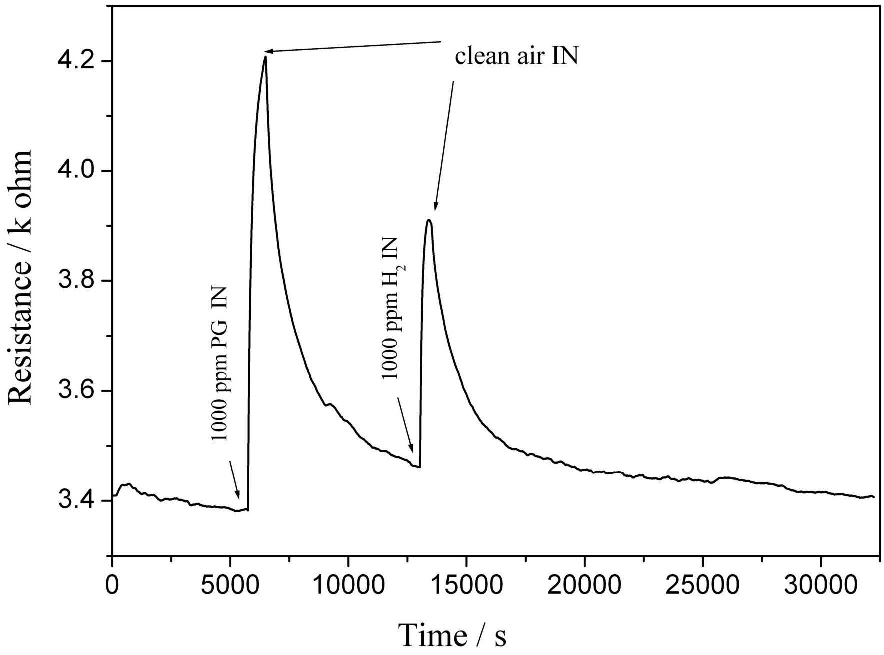

Fig. 4.13 Transient changes in resistance of $CuInO_2$ thin film as a function of time at 598 K towards 1000 ppm of PG and 1000 ppm of H_2

Similar observation was made with 1000 ppm of H_2 in air. This shows that the reducing and oxidizing gases can be distinguished by their opposite patterns of response. Using the data obtained from the gas sensing studies of $CuInO_2$ towards different concentrations of NO_X, variation of sensitivity as a function of concentration of NO_X (ppm) was plotted and is shown in fig. 4.14. Sensitivity varies linearly in the concentration range of 3 to 24 ppm of NO_X and the linear least square fit has a correlation coefficient of 0.99.

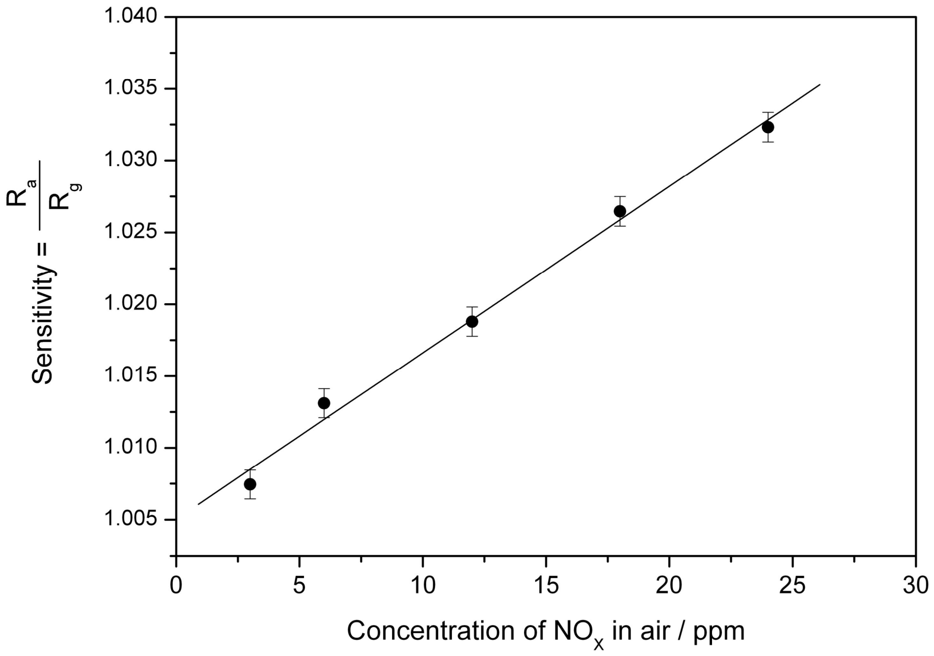

Fig. 4.14 Calibration plot of sensitivity of $CuInO_2$ thin film towards different concentrations of NO_X (ppm) in air at 473 K; R_a: Resistance of $CuInO_2$ thin film in air; R_g: Resistance of $CuInO_2$ thin film in the presence of NO_X in air [Error bar: < 0.5%]

After completing the gas interaction studies between the temperature of 448 K and 598 K, the thin film was once again characterized using XRD. This XRD pattern completely matched with XRD pattern of the as-deposited film shown in Fig. 4.5(a), indicating the retention of $CuInO_2$ phase during gas sensing experiments.

4.3.7. Gas sensing characteristics of $Cu_2In_2O_5$ thin film

Variation of sensitivity exhibited by $Cu_2In_2O_5$ thin film towards 500 ppm of NH_3, H_2, PG and NO_X in air at different temperatures is shown in Fig. 4.15. At 490 K, the sensitivity was 40 % towards 500 ppm of NH_3 and it gradually increased to 55 %

at 593 K. Thereafter sensitivity decreased systematically with increase in operating temperature reaching a minimum value of about 20 % at 683 K. As seen from the figure more or less a similar trend was observed for H_2. The sensitivity was about 10 % towards 500 ppm of PG at 490 K, which marginally increased with increase in temperature and showed a maximum sensitivity at 650 K as seen from Fig. 4.15. For NO_X, the sensitivity was 5 % at 490 K, which gradually increased with increase in temperature. A maximum sensitivity of 23 % was observed at 677 K. As seen from the figure, $Cu_2In_2O_5$ thin film exhibits higher sensitivity towards H_2 and NH_3 than with PG and NO_X. The material didn't show selectivity towards any of the analyte gases studied. The gas interaction studies of $Cu_2In_2O_5$ thin film was not continued below 498 K since the resistance of the film was beyond the measurable range of the instrument (Model: Agilent 34970A).

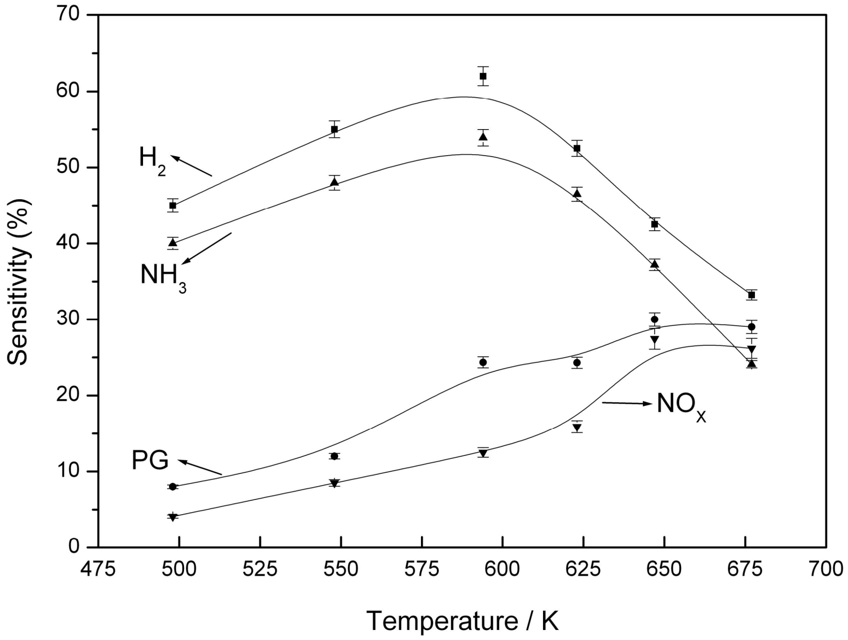

Fig. 4.15 Sensitivity as a function of operating temperature for the compound $Cu_2In_2O_5$ thin film for the gases (■)H_2, (▲) NH_3, (●) PG and (▼) NO_x [Error bar: < 1.5%]

The response and recovery times towards the interaction of $Cu_2In_2O_5$ thin film with the chosen gases are shown in Table.4.6. As seen from the table, the response and recovery times exhibited towards sensing of all these gases are in the range of minutes. The response and recovery times for sensing of H_2 and NH_3 are found to be generally higher than those towards sensing of PG and NO_X. The reasons for variation in the response and recovery times towards these gases are not known from the present studies.

Table: 4.6

Response and recovery times of $Cu_2In_2O_5$ thin film towards the mentioned analytes (in minutes)

Gas 500 ppm each	Temperature (K)											
	498 K		548 K		594 K		623 K		647 K		677 K	
	Res. time	Rec. time	Res. time	Rec. time	Res. time	Rec. time	Res. time	Rec. time	Res. time	Rec. time	Res. Time	Rec. Time
H_2	3	8	3	6	2	5	2	4	2	3	1	2
PG	2	2	2	3	2.5	4	2	4	3	2.5	4.5	2
NO_X	2	2	2.5	3	3	4	2.5	3.5	2	3.5	2	3
NH_3	3.5	9	3	8	2.5	7	2	6	2	6	2	5

Figure 4.16 shows the typical response characteristics of $Cu_2In_2O_5$ thin film towards 1000 ppm of NO_x in air at 677 K. During the exposure of the film towards air containing 1000 ppm of analyte, the resistance of the film increases until it reaches a stable resistance in the presence of NO_x as seen from the fig. 4.16. On re-exposure to clean air, resistance of the film traces back to its base resistance observed in air before introducing the sample gas. All these processes are depicted in fig. 4.16. Figure 4.17 shows the response behavior of $Cu_2In_2O_5$ thin film towards 500 ppm of PG at 677 K. This material showed a decrease in resistance in the presence of PG, which is just opposite in response exhibited by NO_x. On flushing out the environment of chamber with clean air, the resistance of the compound retraces back to the baseline value as shown in fig. 4.17.

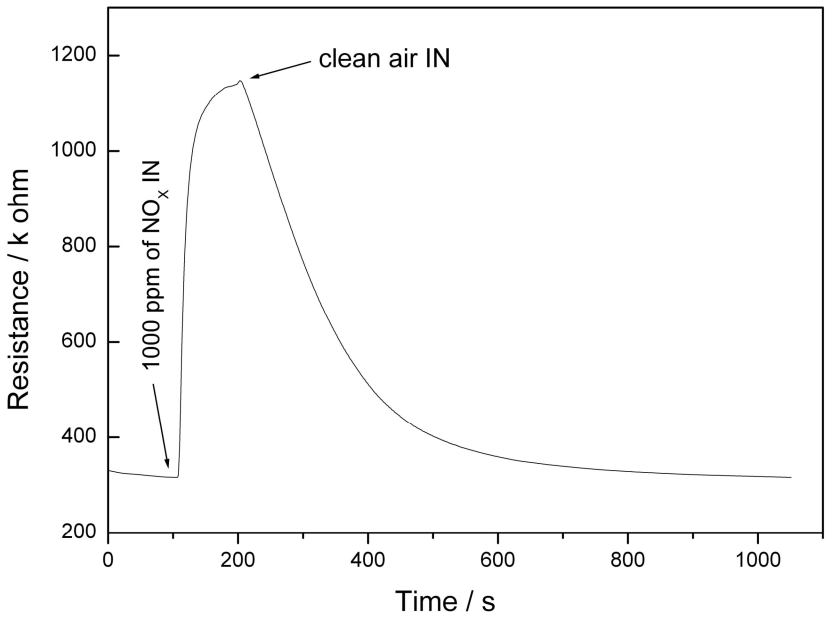

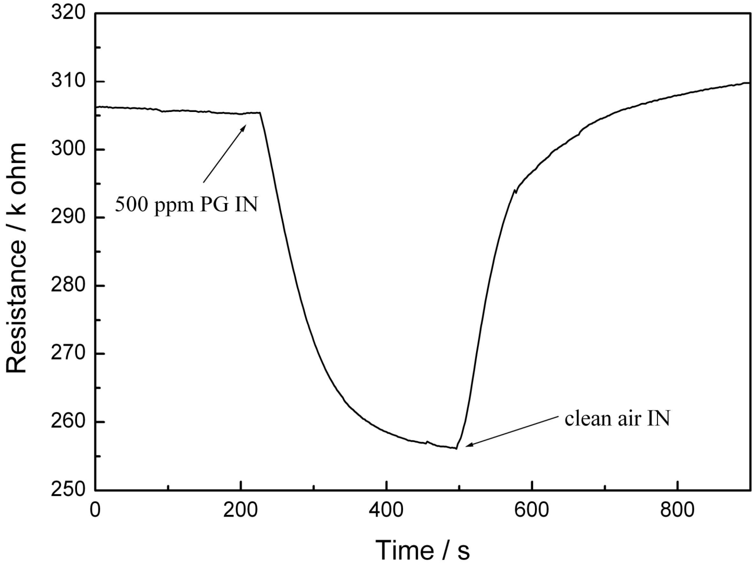

Fig. 4.16 Typical response characteristics of $Cu_2In_2O_5$ thin film towards 1000 ppm of NO_x in air at 677 K

Fig. 4.17 Typical response characteristics of $Cu_2In_2O_5$ thin film towards 500 ppm of PG in air at 677 K

4.4. Sensing mechanism of $CuInO_2$ and $Cu_2In_2O_5$

Data presented in the earlier sections indicate that $CuInO_2$ is present in metastable form at least up to 473 K, although it is thermodynamically predicted to be unstable in air even at lower temperatures.

The gas interaction studies of semi-conducting n-type metal oxides like SnO_2 and In_2O_3 exhibit a decrease in resistance in the presence of reducing gas (H_2) and an increase in resistance in the presence of oxidizing gas like O_3, NO_2 etc. [115, 116]. $Cu_2In_2O_5$ also exhibited similar response characteristics towards the reducing and oxidizing gases, implying that it could be an n-type semiconductor and the sensing was mediated by chemisorbed oxygen.

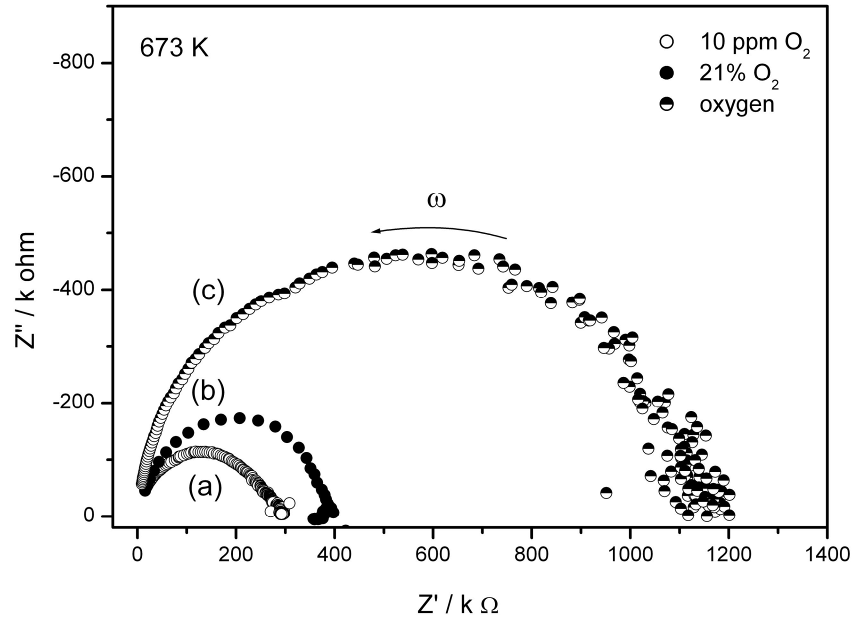

Fig. 4.18 Two probe AC impedance plot of $Cu_2In_2O_5$ pellet in a) argon containing 10 ppm of O_2 b) air and c) oxygen at 673 K

The effect of oxygen partial pressure on the conductivity of $Cu_2In_2O_5$ was carried out in the ambient of 10 ppm of O_2, air and oxygen between the temperature of 473 and 693 K using AC impedance technique. Typical AC impedance plots of $Cu_2In_2O_5$ pellet in the ambient of argon containing 10 ppm of O_2, air and oxygen atmosphere at the operating temperature of 673 K is shown in fig. 4.18. The compound showed a single semicircle in all the ambient and the circles are depressed owing to the dependence of both C and R on frequency. From the intercept of the circles with the x-axis at the low frequency end, the impedance of $Cu_2In_2O_5$ was calculated using Z view® (version 2.70) program and from the plot it is clear that, the impedance of $Cu_2In_2O_5$ increases with increase in oxygen partial pressure.

Figure 4.19 shows the plot of logarithmic electrical conductivity obtained from the AC impedance measurement of bulk $Cu_2In_2O_5$ as a function of temperature in air, oxygen and argon containing 10 ppm of oxygen in the above mentioned temperature region. The activation energy for the conduction process in argon containing 10 ppm of oxygen is 0.37 ± 0.02 eV, in air it is 0.36 ± 0.01 eV and in oxygen 0.35 ± 0.01 eV. These experimental results clearly proved that there was no large variation in activation energy for conduction in gas ambient with differing oxygen partial pressures. The marginal increase in conductivity of $Cu_2In_2O_5$ from oxygen to argon containing 10 ppm oxygen is probably due to the change in the surface coverage of chemisorbed oxygen on the surface. This behavior by $Cu_2In_2O_5$ in different oxygen partial pressure is similar to that of n-type SnO_2 in different pO_2 values [117]. Such n-type behavior showed by $Cu_2In_2O_5$ from the gas interaction studies, it implies that there is a very small fraction of Cu^+ is present in the compound, which is below the detection limit of XPS.

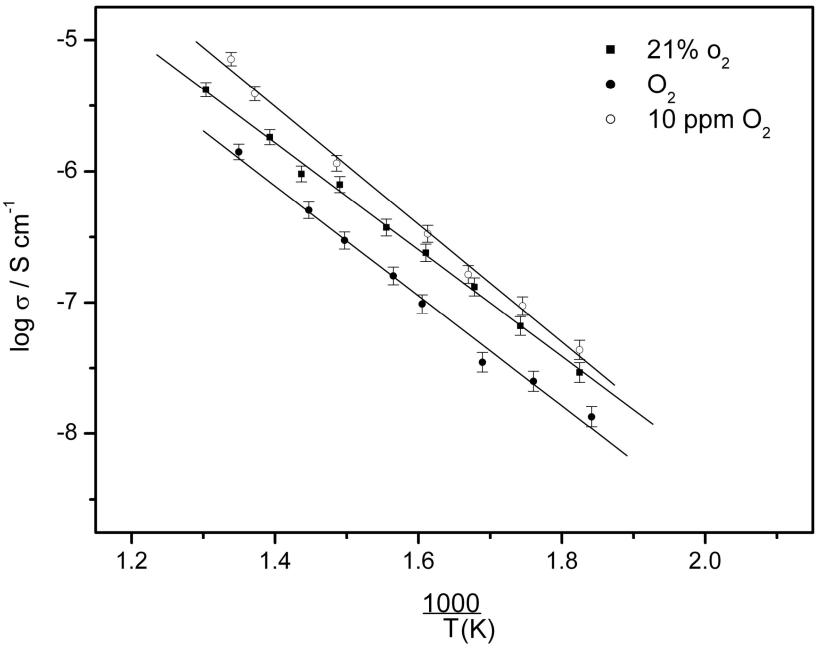

Fig. 4.19 Arrhenius plot of bulk $Cu_2In_2O_5$ as a function of 1000/T (K): (■) 21 % O_2, (●) O_2 and (○) 10 ppm O_2 [Error bar: < 1.0 %]

$CuInO_2$ with Cu^+ ‘ d^{10} ’ configuration behaves as an intrinsic semiconductor with a band gap of 3.2 eV. It is reported that doping $CuInO_2$ with a divalent Ca^{2+} for copper (Ex. $Cu_{1-x}Ca_xInO_2$) introduces acceptor levels close to the valence band and enhances the p-type conductivity in $Cu_{1-x}Ca_xInO_2$ [102]. Results of XPS studies in the present work provide evidence for the presence of a small fraction of Cu^{2+} in $CuInO_2$, which also provides evidence for its p-type behavior. The interaction of NO_X with $CuInO_2$ thin film leads to decrease in resistance [fig. 4.12], whereas its interaction with $Cu_2In_2O_5$ film leads to increase in resistance [fig. 4.16]. NO_X being an oxidizing gas interacts with the surface thereby trapping the electrons of the solid as shown by eqn. 4.10:

$$NO_2 + e^- \rightleftharpoons NO_2^- \qquad (4.10)$$

The higher electron affinity of NO_2 (2.20 eV) as compared to that of oxygen (0.43 eV) justifies the possibility of such a reaction taking place on the surface [74]. It is proposed that the chemisorption of NO_X leads to removal of electrons from acceptor level to form surface states with NO_2^-. Extraction of electrons from acceptor levels leads to increase in hole carrier density, which manifests as decrease in resistance. On the contrary, in case of $Cu_2In_2O_5$, reducing gas reacts with the chemisorbed oxygen ion and releases the trapped electrons back to the conduction band and overall process is represented by the eqn. 4.11 and eqn. 4.12.

$$2H_2 + O^-_{2\,ad} \rightleftharpoons 2H_2O + 2e^-(semiconductor) \tag{4.11}$$

$$H_2 + O^-_{ad} \rightleftharpoons H_2O + 2e^-(semiconductor) \tag{4.12}$$

The interaction of hydrogen with chemisorbed oxygen leads to an increase in carrier concentration and hence a decrease in resistance for $Cu_2In_2O_5$ [fig. 4.17]. For a p-type $CuInO_2$, the chemical interaction of a reducing gas with chemisorbed oxygen leads to the release of the electrons, which is expected to annihilate the holes resulting in an increase in resistance [fig. 4.13].

4.5. Conclusions

The thin film of $CuInO_2$ was deposited using $Cu_2In_2O_5$ by PLD in a controlled oxygen pressure at 823 K. The gas interaction studies of $CuInO_2$ thin film towards reducing and oxidizing gases represents the deposited thin film exhibits p-type semi-conducting behavior. The XPS results provide the evidence of Cu^{2+} along with Cu^+ in $CuInO_2$ corroborates the p-type semi-conducting behavior shown by $CuInO_2$ thin film.

The thin film showed good selectivity towards NO_X among H_2, NH_3 and PG even at very low operating temperature of semi-conducting metal oxide. It showed linear in sensitivity towards NO_X between the concentrations of 3 and 24 ppm. The deposited $CuInO_2$ thin film is metastable between the temperature of 473 and 598 K.

The response behavior of $Cu_2In_2O_5$ with reducing and oxidizing gases (H_2, PG, NH_3 and NO_X) are similar to those of n-type semiconducting oxides like SnO_2. The compound exhibited a poor selectivity for the gases investigated. XPS results showed that copper and indium in $Cu_2In_2O_5$ were in +2 and +3 oxidation state respectively. The n-type response exhibited by the compound is probably due to the interaction of the gases with surface chemisorbed oxygen.

CHAPTER 5

Preparation, characterization and sensing behavior of palladium, $Pd_{0.97}Ni_{0.03}$, $Pd_{0.93}Ni_{0.07}$, and $Pd_{0.91}Ni_{0.04}Co_{0.05}$ towards hydrogen at 300 K

5.1 Introduction

Hydrogen gas is widely used in industrial processes. It has unusual properties in comparison to other combustible gases and vapors. It has a very low density (0.082 kg/m^3 at 300 K) and boiling point (20.39 K). It has a high diffusion coefficient in air (0.61 cm^2/s). Hydrogen acts as a strong reducing agent, possesses high permeability through most of the materials and forms explosive mixtures in air when its concentration ranges between 4 and 74% [3]. Hence, special precautions need to be taken to monitor any accidental release of hydrogen into air in industrial plants. Most of the commercially available chemo-resistive sensors for hydrogen exhibit high cross sensitivity towards other gases albeit their high hydrogen sensitivity [26]. Further, the dynamic range of these sensors is not very large. A sensor capable of selectively measuring hydrogen in air from ppm to ~ 2% levels is desirable for initiating safety related alarms and actions. Similarly, there is a need of a hydrogen sensor to detect below 2% in argon plenum of sodium handling facilities in nuclear reactors. Therefore, new materials need to be developed and deployed as sensors. Elements like Zr, Ti, V, Nb, and Pd are known to dissolve large amounts of hydrogen and data in literature shows the solubility of hydrogen in palladium at 300 K to be the highest [118, 119]. Physical properties of palladium such as its density and electrical resistivity vary with the dissolved hydrogen concentration. Variation of the resistance of palladium metal (or its alloys) in suitable configurations can be exploited for hydrogen sensing applications. Since metals have very low resistivity, the configuration adopted should enable precise measurement of the low resistance and its variations during the gas sensing process. Thin films of palladium (or its alloys) in a serpentine configuration can be employed for these purposes.

Figure 5.1 shows the phase diagram of Pd-H system [120]. At a given temperature T, hydrogen dissolves in palladium to form an interstitial solid solution α (region A to B). As the amount of dissolved hydrogen increases, a limiting concentration of hydrogen in the α phase is reached i.e. α phase gets saturated with hydrogen (α_{max}). Further addition of hydrogen to the system (in region B to C) leads to precipitation of another interstitial solid solution of hydrogen in palladium (labeled as β_{min} in the Fig. 5.1) with simultaneous conversion of α_{max} to β_{min}. After the entire α_{max} is converted to β_{min}, additional hydrogen gets dissolved in the β phase (in region C to D). Both α and β phase are based on FCC structure of palladium. With increase in temperature, solubility of hydrogen in α phase increases while that in β phase decreases. The two-phase region closes at the critical temperature of 566 K (293^{o}C) where the atom fraction of hydrogen in the solid solution is ~ 0.225.

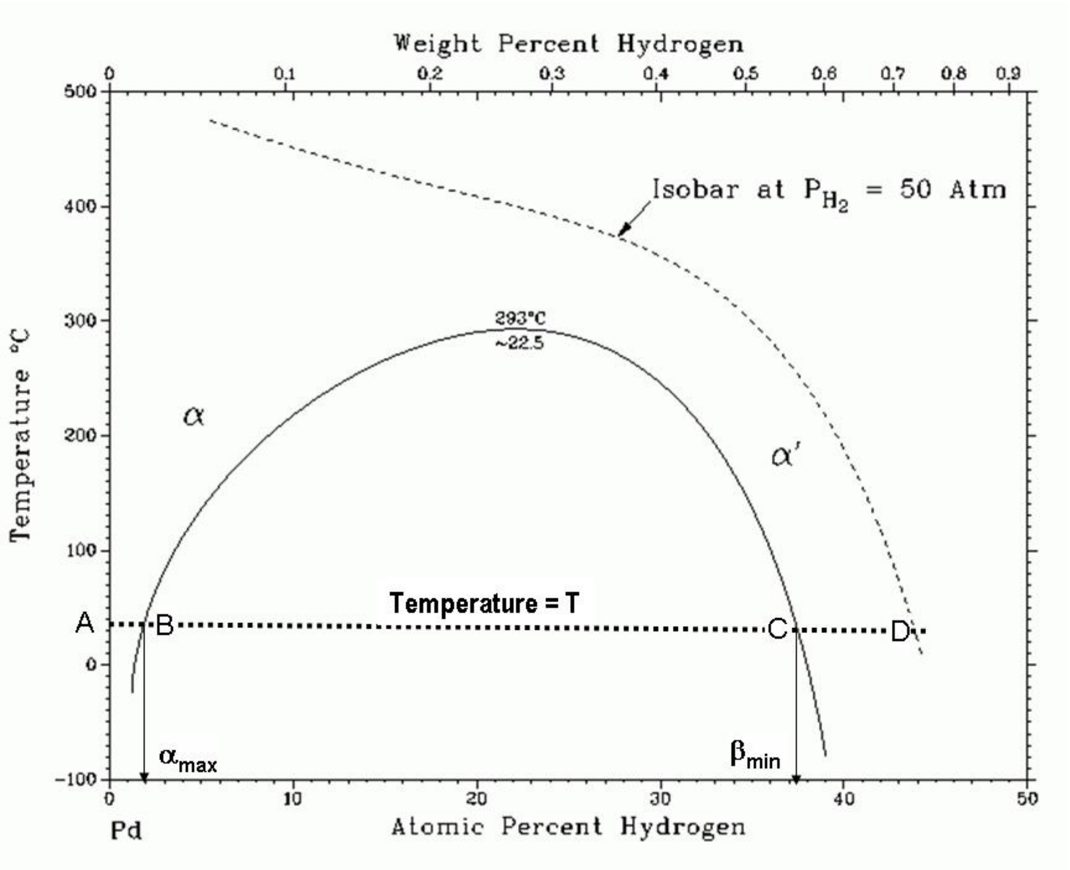

Fig. 5.1 Phase diagram of the palladium – hydrogen system [120]

In the region A–B where hydrogen is present as interstitial solid solution in α phase, the following equilibrium exists:

$$\tfrac{1}{2}\ H_2(g) \Leftrightarrow [H]_\alpha \tag{5.1}$$

The equilibrium constant K of the reaction can be expressed as:

$$K = \frac{a_H}{p_{H_2}^{1/2}} \tag{5.2}$$

where a_H is the thermodynamic activity of hydrogen in the α phase and p_{H_2} is the equilibrium hydrogen partial pressure. If N_H is the gram-atom fraction and γ_H is the activity coefficient of hydrogen in the α phase, activity of hydrogen can be expressed as below:

$$a_H = N_H \gamma_H = K\, p_{H_2}^{1/2} \tag{5.3}$$

Henry's law is obeyed at low levels of dissolved hydrogen i.e. γ_H is independent of N_H. Under these conditions,

$$N_H = \left(\frac{K}{\gamma_H}\right) p_{H_2}^{1/2} = K_s\, p_{H_2}^{1/2} \tag{5.4}$$

where K_s is a constant at a given temperature. Equation 5.4 is the expression for Sievert's law, which states that the concentration of hydrogen (N_H) present as solid solution in a metal at a given temperature varies linearly with square root of the equilibrium hydrogen partial pressure [121]. In the region B–C of the phase diagram given in Fig.5.1, α and β phases coexist and establish the following equilibrium:

$$\alpha_{max} + x\,H_2\,(g) \Leftrightarrow \beta_{min} \tag{5.5}$$

The value of x in the above equation varies with temperature since the compositions of α_{max} and β_{min} are temperature dependent, as shown in Fig.5.1. In the region C–D the β phase is in equilibrium with hydrogen gas:

$$\tfrac{1}{2}\ H_2(g) \Leftrightarrow [H]_\beta \tag{5.6}$$

At 300 K, the atom fractions of hydrogen in α_{max} and β_{min} are 0.017 and 0.376 respectively.

The pressure-composition diagram of the Pd-H system at 300 K is shown in Fig.5.2. It is known that Sievert's law is valid in the α phase of Pd–H system at low temperatures [28]. The plateau hydrogen partial pressure in gas phase when α_{max} and β_{min} phases coexist is ~ 9 x 10^{-3} atm (9000 vppm). It is to be pointed out that this plateau pressure is lower than the desired upper limit of hydrogen to be monitored by a sensor (2 % = 20,000 vppm). At 2% hydrogen partial pressures, entire α phase would be converted to β phase. Since the difference in densities of hydrogen saturated α phase i.e. α_{max} and that of β phases are high (Pure Pd: 12.02g/cc, α_{max}: 11.96 g/cc and β_{min}: 10.98 g/cc), the films of metal would be disintegrated during the sensing processes. Hence, it is desirable to have only α phase during the entire gas sensing concentration regime. Properties of alloys of Pd need to be explored to extend the hydrogen partial pressure in gas phase to 2% without any precipitation of β phase. The required characteristics of the alloying element are:

1. Its atomic radii should be close to that of Pd (within ± 5%). The crystal structure of the alloying element and Pd should be same (or closely similar) so that they form a solid solution (Hume-Rothery Rules).
2. It should not form any intermetallic compound with Pd.
3. It should not form any stable hydride.

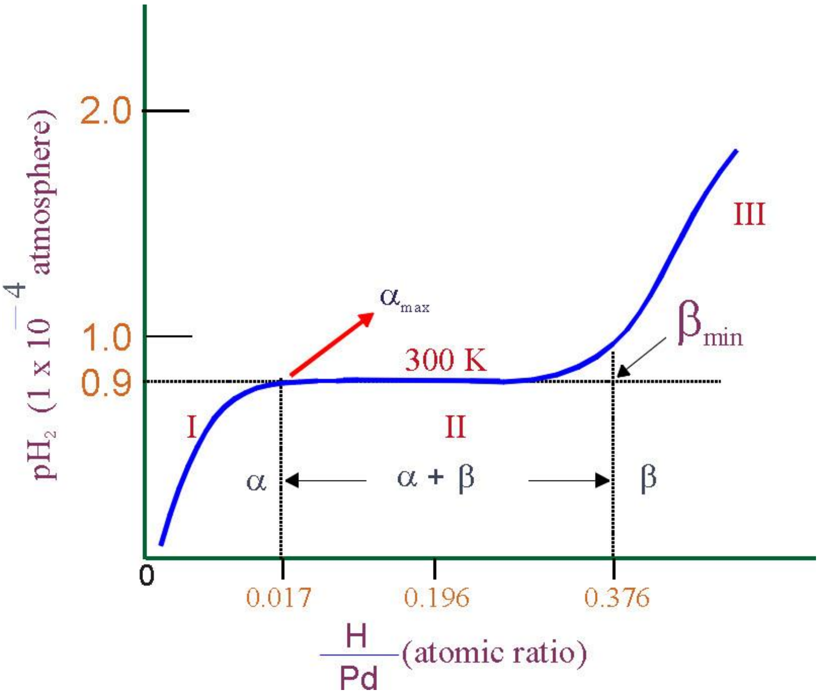

Fig. 5.2 Pressure composition phase diagram of the palladium – hydrogen system at 300 K (redrawn from the reference [28])

Electrical resistivity of metals is dependent on their electronic configuration, temperature and the impurity levels in them. Valence electrons of the metal atoms in the condensed phase are delocalized and are free to move in the lattice of metal ions. These conduction electrons flow under an electric potential gradient. During their flow, the electrons get scattered by the thermally vibrating ionic cores and by the imperfections (structural defects, impurity atoms, etc.) and this scattering is the origin of the resistivity of the metal. According to the empirical rule by Matthiesen [122], the total resistivity of a crystalline metallic specimen is the sum of the resistivity due to thermal agitation of the ionic core of the lattice and the resistivity due to the presence of defects in the crystal (grain boundaries, dislocations, vacancies and impurity atoms). Influence of defects other than impurity atoms is weak and hence the total resistivity of a metal can be expressed as:

$$\rho_{total} = \rho_{thermal} + \rho_{impurity} \tag{5.7}$$

The resistivity of a pure metal '$\rho_{thermal}$' is reciprocal of its conductivity 'σ' and according to classical free-electron theory the resistivity is given by eqn. 5.8 given below:

$$\rho_{thermal} = \frac{1}{\sigma_{thermal}} = \frac{m v_o}{n e^2 \ell} \tag{5.8}$$

where 'v_o' is the average velocity of the electron under unit potential gradient, 'e' is its charge, 'm' is its mass and 'ℓ' is its mean free path and 'n' is the number of free conduction electrons per unit volume. $\frac{v_o}{\ell}$ is the time taken for the electron to spend between two successive collisions and is called the relaxation time, represented as 'τ'. The observed variation of resistivity is due to a change in electron mean free path. When a solute 'B' (impurity) enters into the lattice of the metal 'A' (solvent), changes in the structural and electrostatic periodicities occur. Because of these distortions, the mean free path during scattering of the electrons alters and hence their relaxation time changes. The resistivity of the alloy AB can be represented as below:

$$\rho_{\mathrm{total}} = \rho_{\mathrm{thermal}} + \rho_{\mathrm{impurity}} = \rho_{\mathrm{thermal}} + \rho_{\mathrm{B}} = \frac{1}{\sigma_{\mathrm{thermal}}} + \frac{1}{\sigma_{\mathrm{B}}} = \frac{m}{ne^2\tau_{\mathrm{thermal}}} + \frac{m}{ne^2\tau_{\mathrm{B}}} \tag{5.9}$$

Variation of ρ_B with the concentration of the impurity is generally represented by the Nordheim rule [122]:

$$\rho_{\mathrm{impurity}} = C\, N_B(1 - N_B) \tag{5.10}$$

where N_B is the atom fraction of B in the alloy AB and C is the Nordheim's coefficient, also called as solution resistivity coefficient. The value of C depends on the chemical properties, crystal structure and atomic radii of solvent A as well as those of solute B. In case of dilute solutions, $(1 - N_B) \sim 1$. For example, hydrogen solubility in α phase in Pd-H system (i.e. α_{max}) at 300 K is 0.017 atom fraction and hence equation 5.10 can be written as,

$$\rho_H = C\, N_H \tag{5.11}$$

Using Sievert's law in the α phase given by eqn. 5.4, the contribution to the total resistivity by dissolved hydrogen can be written as,

$$\rho_H = CK_S pH_2^{1/2} = K'\, p_{H_2}^{1/2} \tag{5.12}$$

where $K' = C\,K_s$ = a constant at a given temperature. When an alloy of palladium, e.g. Pd-Ni is used as the sensor material, the total resistance of the film in equilibrium with hydrogen in the gas phase can be written as below (cf. 5.9):

$$\rho_{\mathrm{total}} = \rho_{\mathrm{thermal}} + \rho_{\mathrm{solute}} + \rho_H = \frac{1}{\sigma_{\mathrm{thermal}}} + \frac{1}{\sigma_{\mathrm{solute}}} + \frac{1}{\sigma_H} = \frac{m}{ne^2\tau_{\mathrm{thermal}}} + \frac{m}{ne^2\tau_{\mathrm{solute}}} + \frac{m}{ne^2\tau} \tag{5.13}$$

By application of Nordheim rule for (substitutional solid solution of) Ni and Sievert's law for (dilute interstitial solid solution of) H, the net resistivity can be expressed as below:

$$\rho_{\mathrm{total}} = \rho_{\mathrm{thermal}} + \rho_{\mathrm{solute}} + \rho_H = \rho_{\mathrm{thermal}} + C_{Ni}\, N_{Ni}\,(1 - N_{Ni}) + K' P_{H_2}^{1/2} \tag{5.14}$$

Since $\rho_{thermal} + C_{Ni} N_{Ni} (1 - N_{Ni}) = \rho_{alloy}$ is constant at a given temperature and for a fixed composition of the alloy,

$$\rho_{total} = \rho_{alloy} + K' P_{H_2}^{1/2} \tag{5.15}$$

Difference in resistivity in the presence and absence of hydrogen in the ambient:

$$\Delta\rho = \left(\rho_{alloy} + K' P_{H_2}^{1/2}\right) - \rho_{alloy} = K' p_{H_2}^{1/2} \tag{5.16}$$

$$\text{Sensitivity,} \frac{\Delta\rho}{\rho_{alloy}} \left(= \frac{\Delta R}{R_{alloy}} \right) = \left(\frac{K'}{\rho_{alloy}} \right) p_{H_2}^{1/2} \tag{5.17}$$

Since $\frac{K'}{\rho_{alloy}}$ is constant at a given temperature, the sensitivity of the sensor would be directly proportional to square root of hydrogen partial pressure in the gas phase (eqn. 5.17).

Experimental data in literature indicates that hydrogen adsorption capability of palladium increases with reduction in grain size of the metal [123 – 125]. For example, Adams reported the ratio of H/Pd ratio in hydrogen saturated α phase (i.e. in α_{max}) at 300 K increased to 0.1 with 7.0 nm sized palladium nanoparticles (cf. H/Pd value in case of bulk palladium metal = 0.017) [126]. The plateau hydrogen partial pressure where α_{max} and β_{min} phases coexist at 300 K was measured as 1 x 10^{-2} atm (= 10000 ppm). The author also reported H/Pd ratio in β phase to be 0.7 at a hydrogen partial pressure of 1.5 x 10^{-2} atm. [127].

Hydrogen solubility in substitutional alloys of palladium depends on the size, structure and nature of the alloying element. The properties of some of the alloying elements along with their effect on hydrogen solubility are shown in Table 5.1.

When palladium is alloyed with elements having higher atomic radii (e.g. Ag and Au), the lattice parameters increase leads to an increase in the unit cell volume. Solubility of hydrogen (which occupies the interstitial positions) in these alloys is higher than that in pure palladium. In case of alloys with iron, cobalt, nickel and copper whose atomic radii are smaller than that of palladium, the lattice parameters get reduced and hence the unit cell volume reduces. Solubility of hydrogen in these alloys is lower than that in pure palladium. Hence the volume expansion in the alloy on saturating it with hydrogen to form α_{max} is higher when Au and Ag are the alloying elements than when Fe, Co, Ni and Cu are employed. When an alloy with high volume expansion is used as sensor material for hydrogen detection in thin film configuration, the film would be prone to disintegrate during hydrogen absorption-desorption cycles. Hence, alloys of palladium with Fe, Co, Ni and Cu can be considered as candidates for use as sensor material. Among these alloys, hydrogen in Pd–Fe and Pd–Cu alloys have shown to deviate negatively from Sievert's law (i.e. bonding of hydrogen in the alloy is stronger), while the Pd–Ni and Pd–Co alloys showed positive deviation [128]. A strong bonding of hydrogen in the alloy would result in slow desorption kinetics and this would not be desirable for a sensor. Hence, Pd–Ni and Pd–Co alloys are considered as the materials for hydrogen sensing. Figures 5.3 and 5.4 show the binary phase diagrams of Pd–Ni and Pd–Co systems [129]. In the Pd–Ni system, homogenous solid solution with FCC structure exists at all compositions. In case of Pd–Co system, ε-phase with hexagonal structure exits below 695 K (422^{o}C shown in fig. 5.4) in cobalt rich regions and this transforms to α phase at higher temperatures. The temperature range of stability of ε-phase decreases with increase in Pd content and in palladium rich regions, α phase is stable at low temperature itself.

Table: 5.1

Properties of alloying elements and their effect on the solubility of hydrogen in palladium [128]

Element	Metallic radii (pm)	Crystal Structure	Effect on solubility of hydrogen
Au	144	FCC	increases
Fe	126	BCC	decreases
Co	125	Simple hexagonal	decreases
Ni	125	FCC	decreases
Ag	144	FCC	increases
Cu	128	FCC	decreases
Pd	137	FCC	

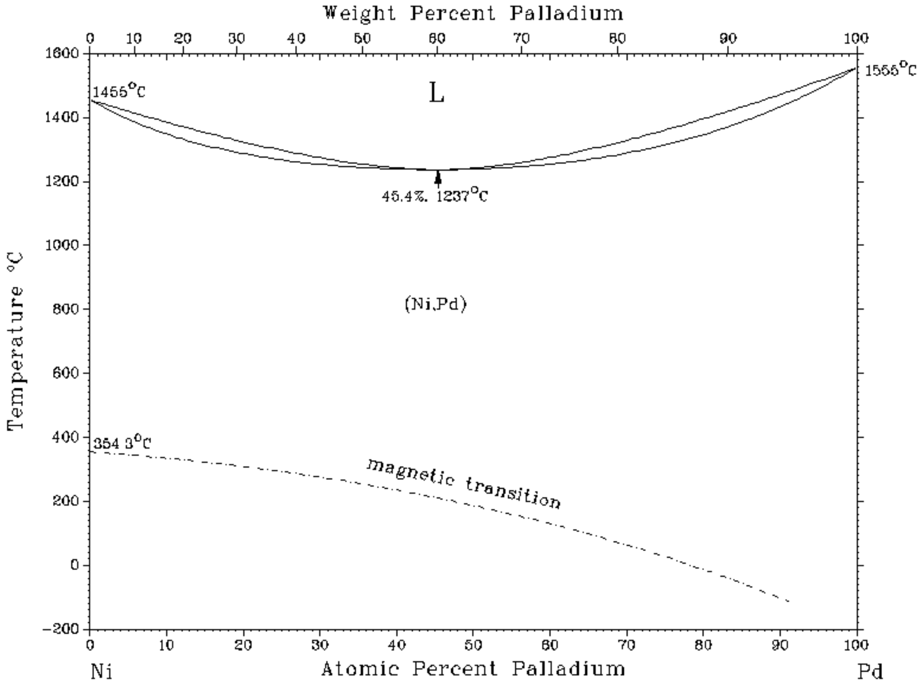

Fig. 5.3 Binary phase diagram of Ni – Pd system [129]

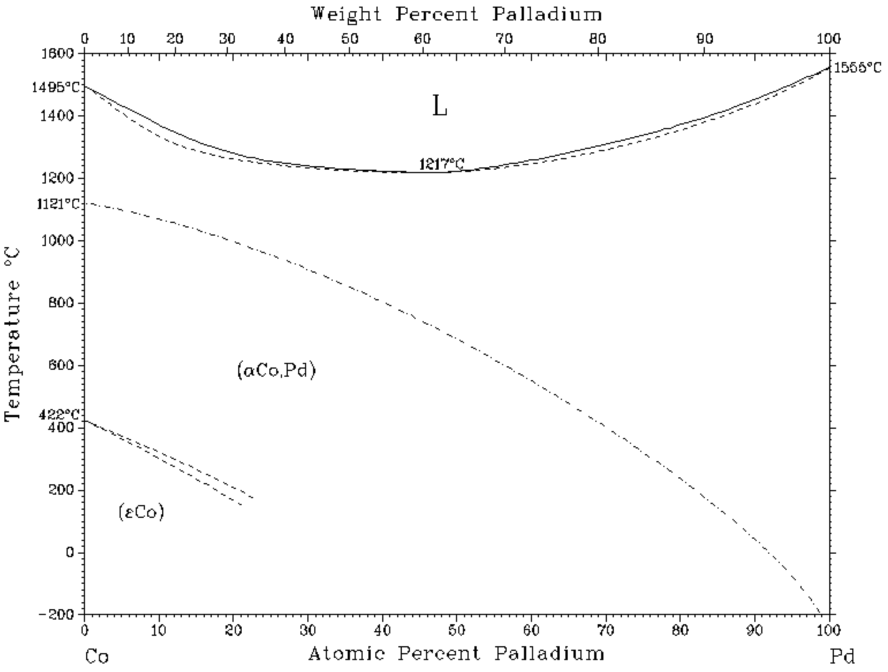

Fig. 5.4 Binary phase diagram of Co – Pd system [129]

This chapter deals with preparation of thin films of alloys of Pd–Ni and Pd–Ni–Co by pulsed laser deposition and studying them as sensors for hydrogen gas. For deposition of these alloys as thin films by PLD, a target of the alloy of homogeneous composition is required. As seen from the phase diagram of the Pd–Ni and Pd–Co systems, preparation of the target of these alloys either by arc melting or by conventional metallurgical route starting from pure metals would involve melting and homogenizing them at temperatures higher than 1773 K. Further, composition change due to vapourisation and oxygen pick up would be significant at these high temperatures. To circumvent these experimental problems, nano particles of the alloys of palladium with nickel as well as with nickel and cobalt were prepared by a novel low temperature chemical reduction (LTCR) technique. Literature survey was carried out to know about the hydrogen interaction studies of Pd—Ni and Pd—Co binary alloys and Pd—Co—Ni ternary alloy. From the survey, hydrogen interaction studies were done on Pd – Ni and Pd – Co system. But, there was no experiment was carried out on the ternary Pd – Ni – Co system. Hence, in this work, substitution of cobalt along with nickel in palladium was taken up and an interaction study with hydrogen was performed.

5.2 Experimental

Nano particles of palladium, nickel, cobalt and alloys of nominal compositions $Pd_{0.95}Ni_{0.05}$, $Pd_{0.9}Ni_{0.1}$ and $Pd_{0.9}Ni_{0.05}Co_{0.05}$ were prepared by LTCR technique in this work. Generally, these reductions are carried out by dissolving the precursors of these metals in water and are reduced using hydrazine or sodium borohydride. Nickel salts cannot be reduced either by hydrazine or sodium borohydride at 300 K in water [38]. They can be reduced by hydrazine or sodium borohydride at pH 13 only above 343 K [130, 131]. During the reduction with hydrazine, nickel first forms nickel hydroxide which then gets reduced to nickel [131]. While Pd^{2+} in aqueous solution can be reduced to metallic Pd by hydrazine or sodium borohydride at 300 K, an increase of temperature to 343 K leads to formation of mixture of Pd and PdO. Hence, synthesis of Pd-Ni alloy using hydrazine or sodium borohydride in water at 300 K would not be possible. Further sodium borohydride violently reacts with water (and reaction of hydrazine with water is slow). In addition to reducing the metal ions to metal, it gets used up in reacting with water. Hence, complete reduction of metal ion to metal (even if excess reagent is added) or detection of end point of this process becomes difficult. This may not be a serious issue when nano particles of pure metal are prepared, except for non-quantitative reduction and loss of material. In case of preparation of alloy powders, this could lead to inhomogeneity in composition. To minimize this problem, the reduction process was carried out by using acetone and/or ethanol as solvent for the metal ion precursors instead of water [37, 132]. Although both acetone and ethanol also react with sodium borohydride, the rate of their reactions is slower than the reaction of water. Acetone is very reactive with hydrazine and forms complex, which is an explosive in the presence of metal ions in the solution. Hence acetone is a not good choice for use with hydrazine.

Palladium (II) acetate, trimer of M/s Alfa Aesar, nickel (II) acetate tetrahydrate (M/s Merck, Germany) and cobalt (II) nitrate hexahydrate (M/s Merck, Germany) were the metal precursors used. Palladium II acetate, trimer and cobalt (II) nitrate hexahydrate were dissolved separately in analytical grade acetone. The nickel II acetate tetrahydrate was dissolved in ethanol and then it was transferred in to large volume of acetone. Powders of pure metals of Pd, Ni and Co were prepared independently by reducing the metal ions by adding finely ground and oven dried (383 K) sodium borohydride (M/s Merck, Germany) under continuous stirring at 300 K. For synthesis of the alloys of nominal compositions $Pd_{0.95}Ni_{0.05}$, $Pd_{0.9}Ni_{0.1}$ and $Pd_{0.9}Ni_{0.05}Co_{0.05}$, stoichiometric quantities of the respective precursors in the solution were reduced with sodium borohydride. The reduction of palladium and nickel acetates to the respective metals and that of cobalt nitrate to cobalt by $NaBH_4$ are shown in eqns. 5.18 to 5.20. For all the above synthesis, a slight excess of $NaBH_4$ was added. After the completion of the reaction, the liquid containing the precipitated powders was digested for 30 min. at 323 K. Later, about 200 ml of distilled water was added to the liquid at 353 K to remove $NaNO_3$, $NaBH_4$ (unreacted), H_3BO_3, $NaBO_2$ and NaOH by dissolving them or by reacting with them, as shown in eqn. 5.21 to 5.24.

$$Pd^{2+}(CH_3COO^-)_2 + NaBH_4 \xrightarrow{300\ K} Pd + 2CH_3COONa + BH_2^- + H_2 \qquad 5.18$$

$$Ni^{2+}(CH_3COO^-)_2 + NaBH_4 \xrightarrow{300K} Ni + 2CH_3COO\,Na + BH_2^- + H_2 \qquad 5.19$$

$$Co(NO_3)_2 + 2NaBH_4 \xrightarrow{300\text{ K}} Co + 2NaNO_3 + B_2H_6\,(g) + H_2 \qquad 5.20$$

$$Na^+ + 2BH_2^- \xrightarrow[H_2O]{353K} NaBO_2 + 2H_2 \qquad 5.21$$

$$NaBO_2 + H_2O \xrightarrow{353K} HBO_2 + NaOH \qquad 5.22$$

$$HBO_2 \xrightarrow[H_2O]{353K} H_3BO_3 \qquad 5.23$$

$$NaBH_4 \xrightarrow[H_2O]{353K} H_3BO_3 + NaOH + H_2 \qquad 5.24$$

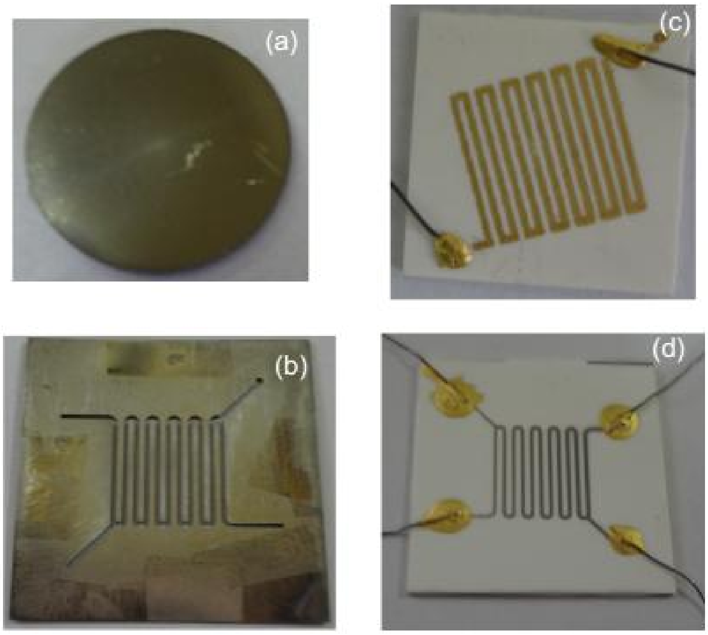

Fig. 5.5 Photograph of a) Pd - Ni alloy disc, b) SS template for thin film deposition c) Au heater (bottom side) and d) Pd – Ni alloy thin film with four probe on alumina substrate (top side)

The precipitated metals and alloys were filtered and washed thoroughly with hot water to remove the adsorbed impurities followed by washing the precipitates with ethanol and acetone. The powders were dried at room temperature for 12 h. In case of the alloys, their compositions were analyzed by atomic absorption spectroscopy (AAS) using M/s GBC Avanta PM AAS, Australia and by inductively coupled optical emission spectroscopy (ICP-OES, M/s Horiba Jobin Yvon, France). These powders were also characterized by X-ray diffraction using PANalytical, Model: X'Pert Pro MPD. From the

XRD pattern, the crystallite size and strain were also calculated. The morphologies of the alloys were elucidated using Ultra 55 Scanning Electron Microscopy, Germany.

The powders were compacted into the form of a disc of 16 mm diameter and 3 mm thickness which in turn were heated at 673 K in vacuum at a pressure of 2.0 X 10^{-5} mbar for 4 h. The discs of Pd and alloys were used as targets (disc) to deposit the thin films over alumina substrate using pulsed laser deposition (PLD). The photograph of $Pd_{0.9}Ni_{0.1}$ (theoretical composition) alloy disc is shown in fig. 5.5a. A stainless steel template (fig. 5.5b) with a uniform cut of 0.4 mm width for a total length of 124 mm (in 11 nearly equal and folded lengths) was fabricated and used to deposit these thin films of palladium and its alloys. Before depositing the thin films, gold electrical pads for making electrical contacts to them were made on the top surface of the alumina substrate by screen printing followed by fired at 1073 K for 1h. The gold paste was purchased from M/s Electro Science Laboratories, USA, (part no. ESL 5544). A thick film Au heater was also made in a similar manner on the bottom surface. The photograph of the gold heater is shown in fig. 5.5c. The deposited palladium and alloy thin films were heated at 373 K in argon ambient using gold heater to desorb the adsorbed moisture from the surface for 3h.

The conditions optimized for the deposition of thin film of Pd and its alloys are given in Table. 5.2. The photograph of a thin film deposited with contacts on the electrical pads is shown in fig. 5.5d. These thin films were characterized by glancing incidence X-ray diffraction (Cu $K\alpha_1$) using INEL XRG-3000 equipped with curved position sensitive detector (CPS 590) covering angle of 10 – 100^o (2θ). The incident angle was chosen 5^o with parallel beam. The surface morphology of the thin film deposited on alumina substrate was scanned using AFM, model Solver Pro, M/s NT – MDT, Russia.

Table: 5.2

In-situ growth parameters for deposition of thin films using PLD

Deposition conditions	
Target	Palladium and alloys of palladium
Fluence (J cm^{-2})	4 - 5
Repetition rate (Hz)	10
Pre-ablation (min.)	5
Ablation (min.)	10
Pressure (mbar)	2×10^{-5}
Substrate-Target distance (cm)	4 – 5
Substrate Temperature (K)	373
Substrate	Polycrystalline Al_2O_3

The thicknesses of thin films were measured using profilometer Dektak^3 of M/s Veeco, USA. The deposited thin film was assembled in small compact glass chamber of 50 ml volume with the provision of gas inlet and outlet. The photograph of the assembled thin film in the glass chamber is shown in fig. 5.6. The resistance of the thin film at 300 K under flowing argon (50 ml/min) containing 2000 and 20000 ppm of hydrogen was measured by the four probe method. Using the four electrical pads (fig. 5.5d) of the thin film, a precisely known current (1×10^{-6}A) was applied across the two electrodes using a high current source measure unit (Model 238 of M/s Keithley Instruments, UK) and voltage drop was measured using the other two leads using a data acquisition switch unit (model 34970 M/s Agilent, USA).

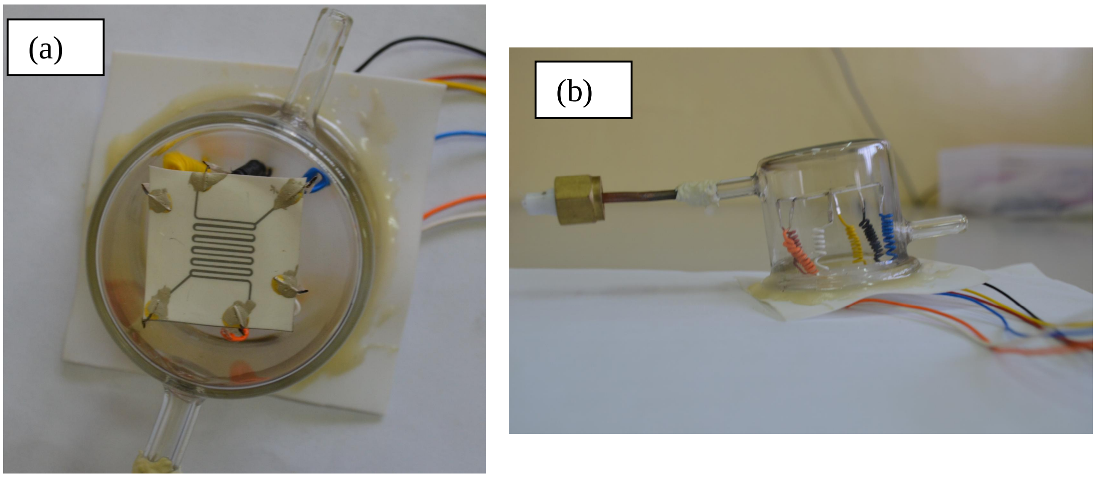

Fig. 5.6 Photograph of Pd thin film installed in a glass chamber a) top view and b) side view

5.3 Results and Discussion

5.3.1 Compositional analysis of alloys

The characterization of synthesized powder was dealt in detail in Appendix 1. The chemical compositions of the alloys obtained by analysis using AAS and ICP-OES techniques are shown in Table. 5.3. The results show that the nickel content in all the three alloys was lower than that expected from the concentration of the precursors in the solution. This indicates the partial reduction of nickel precursor by $NaBH_4$ although an excess of sodium borohydride was added during reaction. The composition elucidated by AAS will be used in subsequent discussions.

Table: 5.3

Chemical composition of alloys of palladium

using atomic absorption spectroscopy

S No.	Composition expected from composition of precursor solution	Composition of the film based on chemical analysis by AAS (Accuracy: ± 5 %)
1.	Pd	-
2.	$Pd_{0.95}Ni_{0.05}$	$Pd_{0.97}Ni_{0.03}$
3.	$Pd_{0.9}Ni_{0.1}$	$Pd_{0.93}Ni_{0.07}$
4.	$Pd_{0.9}Ni_{0.05}Co_{0.05}$	$Pd_{0.91}Ni_{0.04}Co_{0.05}$

5.3.2 Crystallographic elucidation of palladium and its alloys using XRD

Figures 5.7a to d show the XRD (glancing incidence) patterns of Pd, $Pd_{0.97}Ni_{0.03}$, $Pd_{0.93}Ni_{0.07}$ and $Pd_{0.91}Ni_{0.04}Co_{0.05}$ thin films deposited on alumina substrates. In fig. 5.7a, 2θ positions at 40.11 and 46.65 are characteristic reflections of (111) and (200) corresponding to palladium. Analysis of these patterns of the alloys that they also show characteristic reflections of palladium except for a gradual shift of the peak positions to higher 2θ with increase in Ni content. Similar increase in 2θ shift positions is observed in case of $Pd_{0.91}Ni_{0.04}Co_{0.05}$. These shifts in 2θ for the metal and alloy thin films are in agreement with the shifts observed in case of the powders synthesized. Using Scherrer equation, the average crystallite size in thin film was calculated and is in the range of 20 – 30 nm. The average thickness of the thin films is around 7 μm (± 5%).

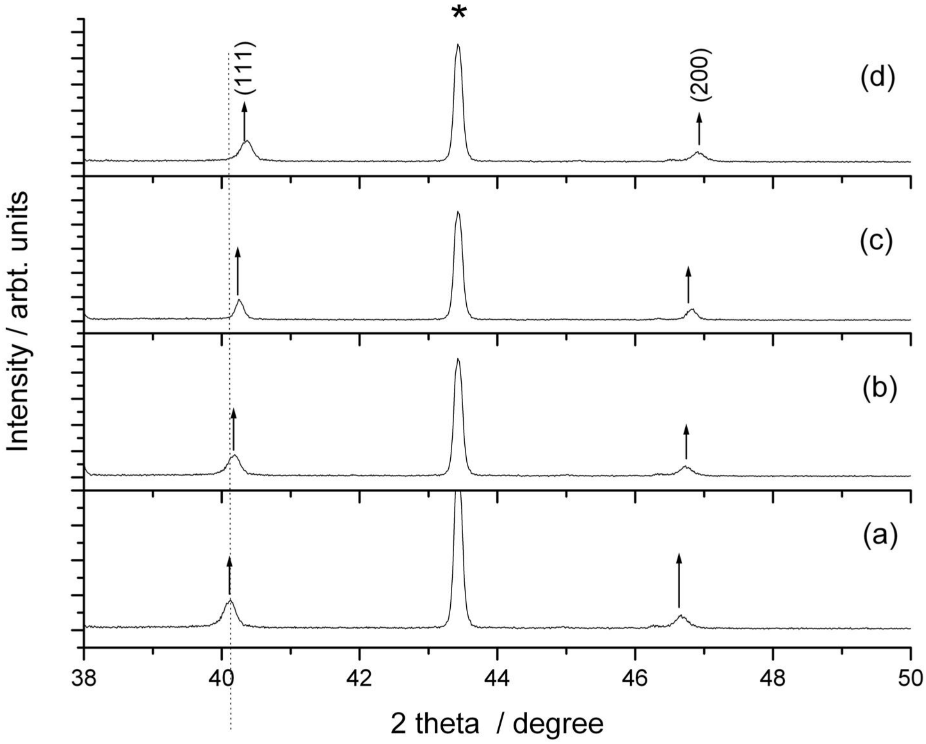

Fig. 5.7 X-ray diffraction pattern of a) Pd, b) $Pd_{0.97}Ni_{0.03}$, c) $Pd_{0.93}Ni_{0.07}$, and d) $Pd_{0.91}Ni_{0.04}Co_{0.05}$ thin film on Al_2O_3 substrate at 373 K. * peak corresponding to Al_2O_3 substrate.

5.3.3 Morphological characterization of palladium and its alloys using AFM

Figures 5.8a and b show the two dimensional AFM images of plain polycrystalline alumina substrate and that of $Pd_{0.93}Ni_{0.07}$ thin film on polycrystalline alumina substrate. The alloy thin film (fig. 5.8b) shows the signatures of the grains having an average grain size of 100 – 150 nm. Whereas the AFM image of uncoated polycrystalline alumina shows the average grain size of 1.0 to 1.5 micron. As seen from the image of the thin film, every grain is connected by a grain boundary. Apart from the uniform distribution of grains (thin film) on a bulk grain (Al_2O_3), grains (thin film) are also grown on grain boundaries aligning with alumina substrate. The porous network (open pores) and grain growth on the grain boundaries of Al_2O_3 provide larger surface area for the gas to adsorb and for the reaction to occur on the surface.

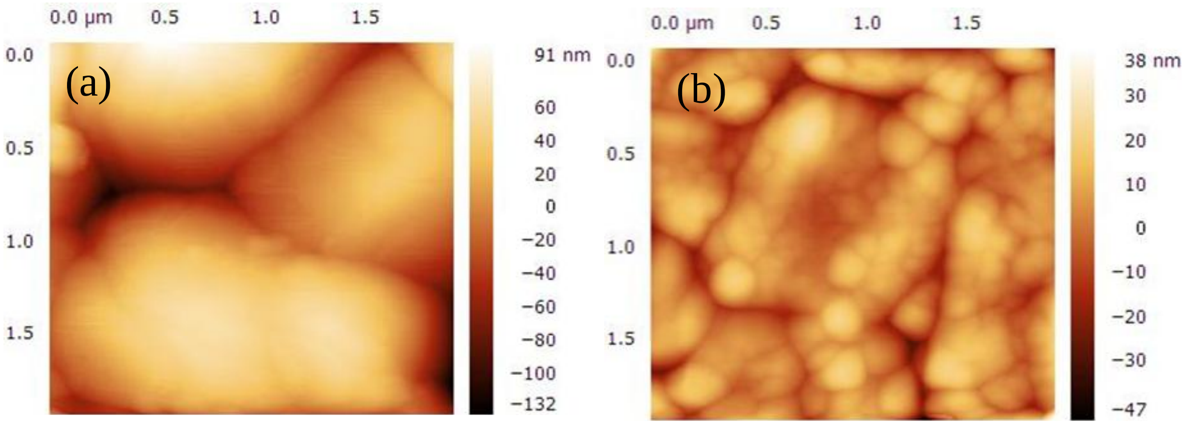

Fig. 5.8 Two dimensional AFM image of a) polycrystalline alumina substrate and b) $Pd_{0.93}Ni_{0.07}$ thin film deposited on polycrystalline alumina substrate

5.3.4 Studies on interaction of hydrogen with thin films of Pd and its alloys

Figures 5.9 (a and b) and 5.10 (a and b) show the change in resistance (four probe) of palladium, $Pd_{0.97}Ni_{0.03}$, $Pd_{0.93}Ni_{0.07}$ and $Pd_{0.91}Ni_{0.04}Co_{0.05}$ thin films on their exposure to argon containing hydrogen in the concentration range of 2000 - 20000 ppm at 300 K. Before the introduction of sample gas, baseline resistance of the film was recorded in pure argon ambient. After establishing a stable baseline, known concentrations of argon containing hydrogen in steps of 2000 ppm was introduced in to the thin film housed chamber. After the introduction of sample containing hydrogen, there was a gradual increase in the resistance of the film. After establishing a stable resistance in the given gas ambient, another sample of argon containing known concentration of hydrogen was introduced and the experiment was continued up to 20000 ppm of H_2 in argon.

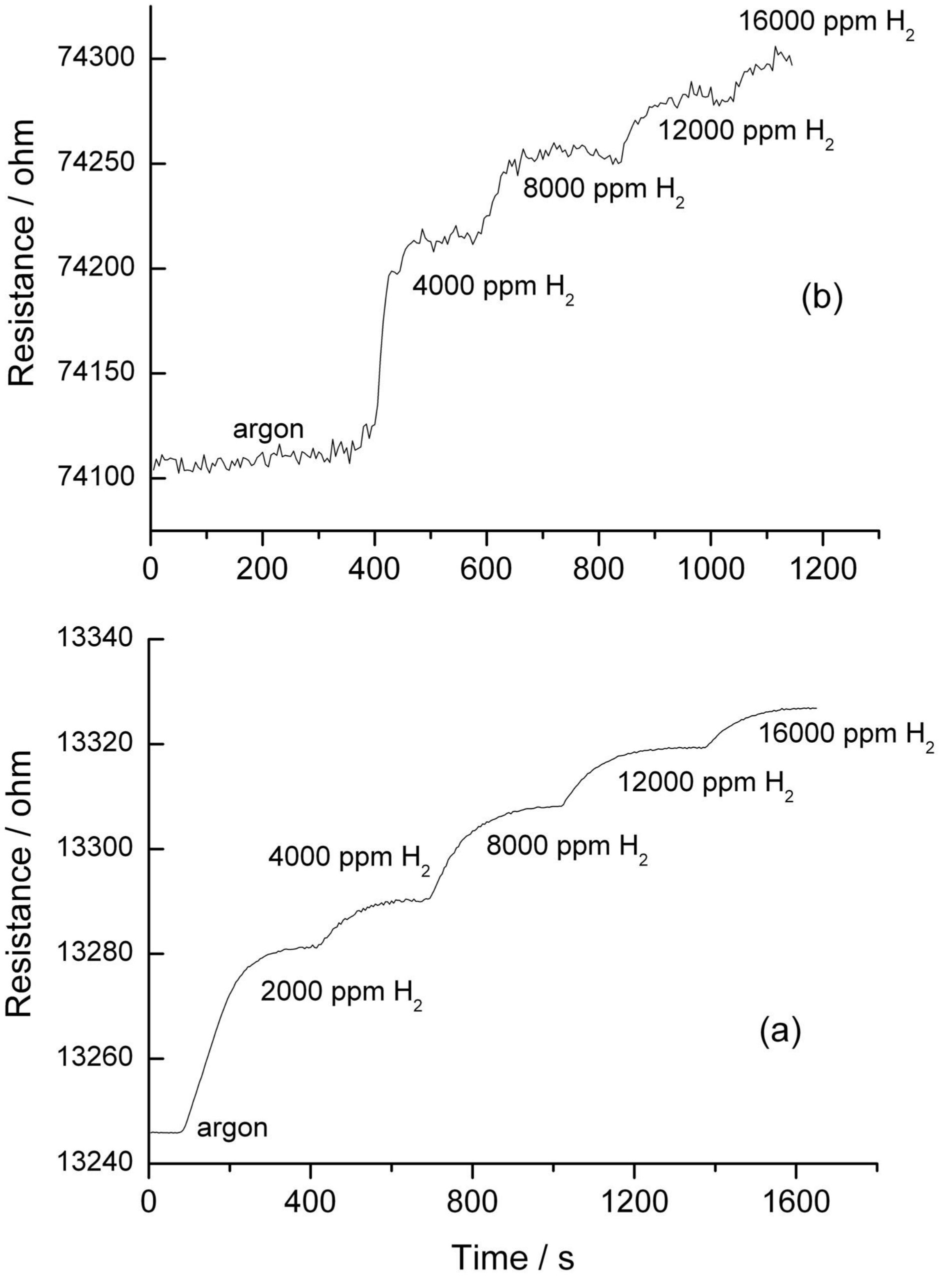

Fig. 5.9 Typical change in resistance of a) Pd and b) $Pd_{0.97}Ni_{0.03}$ thin films towards different concentrations of hydrogen in argon at 300 K

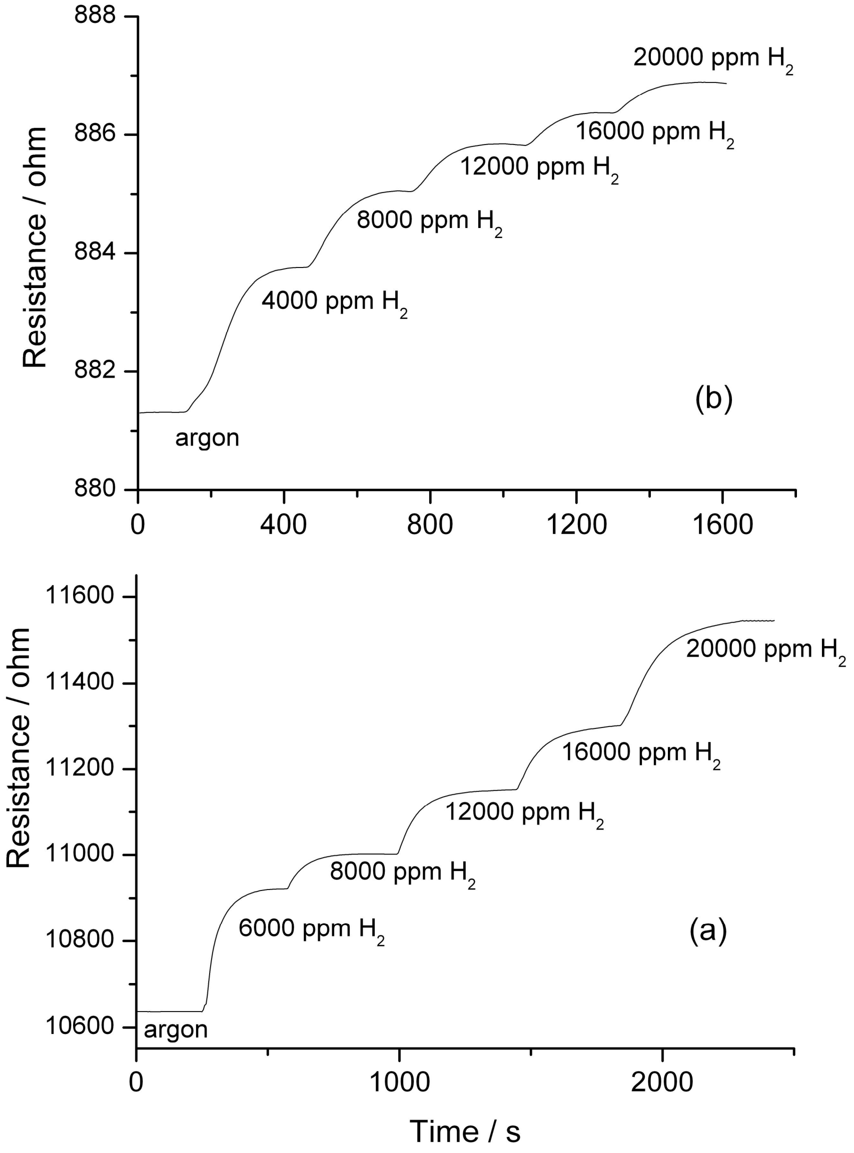

Fig. 5.10 Typical change in resistance of a) $Pd_{0.93}Ni_{0.07}$ and b) $Pd_{0.91}Ni_{0.04}Co_{0.05}$ thin films towards different concentrations of hydrogen in argon at 300 K

Figure 5.11, shows the typical response of palladium thin film on exposure to argon containing 2000 ppm of H_2. The response time (t_{90}) for reaching stable resistance in the presence of hydrogen is about 60 s. The recovery time (t_{90}) of the film was obtained by admitting pure argon into chamber and was found to be 180 s. Figure 5.12 shows the typical response of $Pd_{0.93}Ni_{0.07}$ thin film towards argon containing 2000 ppm of hydrogen at 300 K. These experiments were repeated to evaluate the reproducibility of the response of the thin film towards hydrogen. The response time (t_{90}) of the film was observed to be around 120 s and the recovery time (t_{90}) was around 550 s, which are higher than those of pure palladium film exposed to identical concentration of hydrogen in argon. The higher response and recovery times may be attributed to slower kinetics of interaction of hydrogen with $Pd_{0.93}Ni_{0.07}$ film. The response and recovery times (t_{90}) of $Pd_{0.91}Ni_{0.04}Co_{0.05}$ thin film towards 2000 ppm of hydrogen was observed to be around 80 s and 200 s. The response and recovery times shown by both Pd and $Pd_{0.91}Ni_{0.04}Co_{0.05}$ thin films were close indicating the kinetics of hydrogen interaction with Pd and the ternary alloy film to be of the same order.

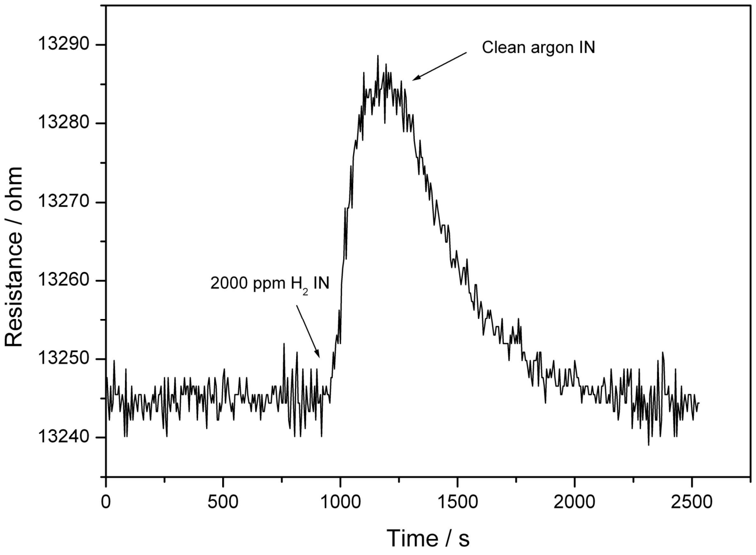

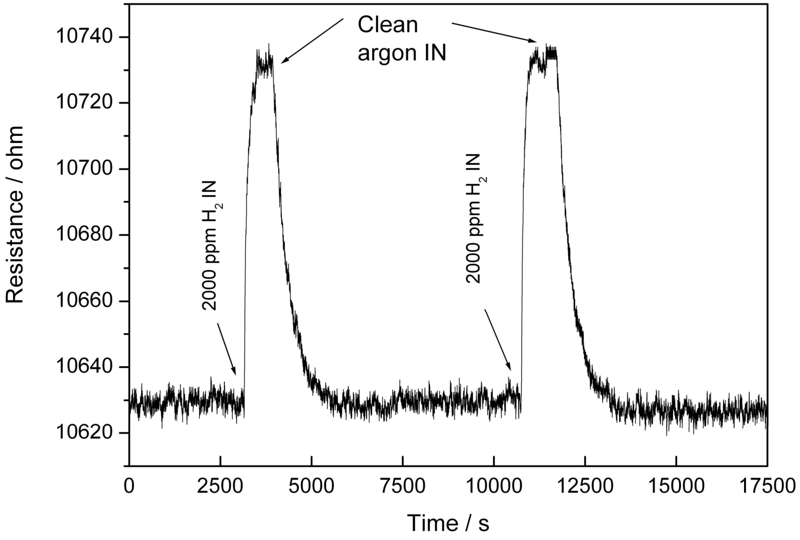

Fig. 5.11 Typical response of palladium thin film on exposure to 2000 ppm of H_2 in argon at 300 K.

Fig. 5.12 Typical response of $Pd_{0.93}Ni_{0.07}$ thin film on exposure to 2000 ppm of H_2 in argon at 300 K.

From the experimental data on resistance of thin films under different hydrogen partial pressures, sensitivity values were calculated. Figure 5.13 shows the plot of sensitivity $\left(\frac{\Delta R}{R}(\%)\right)$ as a function of square root of partial pressure of hydrogen ($atm^{1/2}$) for Pd, $Pd_{0.97}Ni_{0.03}$, $Pd_{0.93}Ni_{0.07}$ and $Pd_{0.91}Ni_{0.04}Co_{0.05}$ thin films at 300 K. A linear relationship between sensitivity and $pH_2^{1/2}$ is exhibited by all the films between 2000 and 20000 ppm of hydrogen. From the figure, it is evident that the sensitivity towards hydrogen increases with increase in the nickel content in the alloy, when compared with pure palladium thin film. On the other hand, both Pd and $Pd_{0.91}Ni_{0.04}Co_{0.05}$ thin film exhibited similar sensitivities.

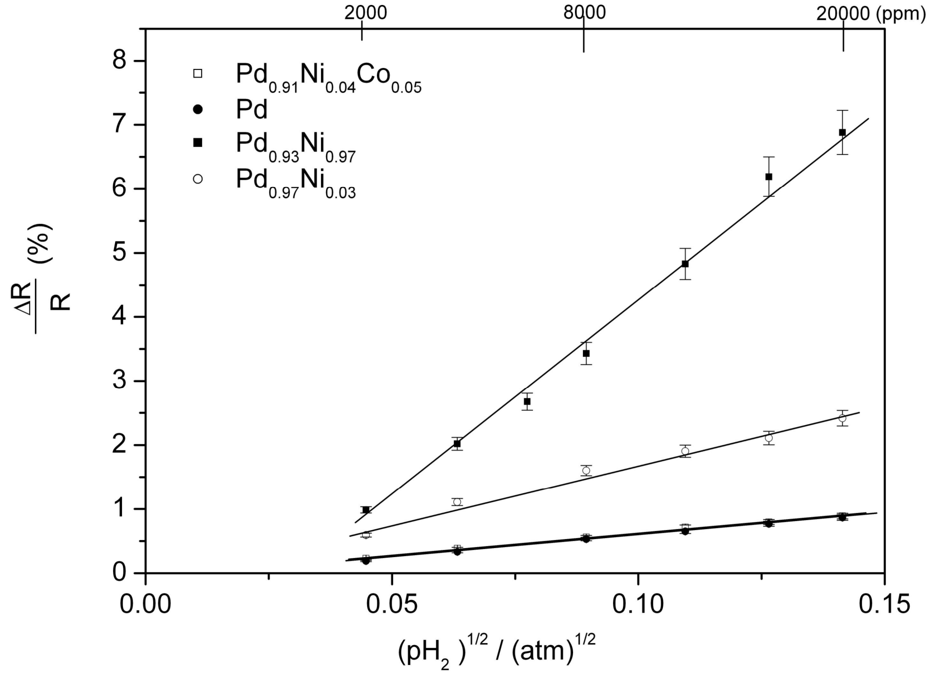

Fig. 5.13 Sensitivity vs $(p_{H_2}/atm.)^{1/2}$ plot for thin films of • Pd, ○ $Pd_{0.97}Ni_{0.03}$, ■ $Pd_{0.93}Ni_{0.07}$ and □ $Pd_{0.91}Ni_{0.04}Co_{0.05}$ at 300 K [Error bar: < 0.5%]

In order to highlight the finer differences in the sensitivity, plots corresponding to Pd and $Pd_{0.91}Ni_{0.04}Co_{0.05}$ thin films are shown separately in fig. 5.14. Although addition of nickel in palladium increased its sensitivity towards hydrogen, addition of cobalt to Pd – Ni alloy reduces this sensitivity. $Pd_{0.91}Ni_{0.04}Co_{0.05}$ thin film showed a marginal increase in sensitivity compared to thin film of pure palladium.

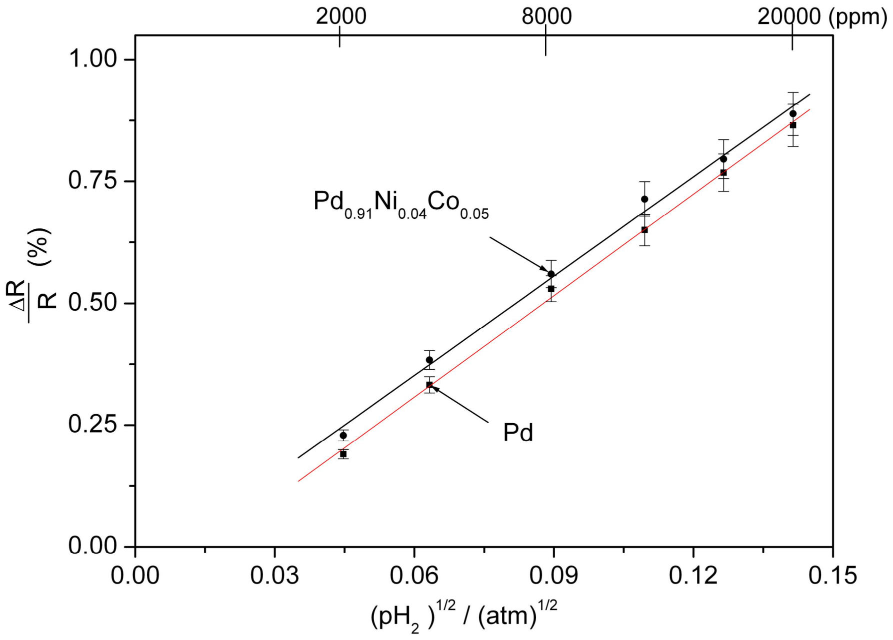

Fig. 5.14 Sensitivity vs $(p_{H_2}/atm.)^{1/2}$ plot for the thin films of ■ Pd and • $Pd_{0.91}Ni_{0.04}Co_{0.05}$ at 300 K [Error bar: < 0.5%]

Figure 5.15 shows the plot of sensitivity $\left(\frac{\Delta R}{R}(\%)\right)$ as a function of square root of partial pressure of hydrogen ($atm^{1/2}$) for the palladium thin film of present results and those reported by Hughes et al [27, 133, 134], Yoon et al [135] and Lee et al [136]. The experimental conditions employed by them during their studies are compared with those employed in the present studies in Table. 5.4. Hughes et al reported an enhanced sensitivity but their studies were restricted between 100 and

1500 ppm of hydrogen. Lee et al observed a linear increase in sensitivity with hydrogen concentration in the range of 1000 - 12500 ppm. As evident from the figure, sensitivity per unit concentration of hydrogen obtained by Hughes et al and Lee et al are much higher than that observed in the present studies. Lee et al further reported that there was a sudden increase in the sensitivity when hydrogen concentration exceeded 15000 ppm. Authors also indicated the rapid increase in sensitivity in case of Pd thin film was due to the phase transition from α to β phase. Yoon et al also reported a linear behavior in sensitivity between 100 and 1500 ppm of hydrogen. The results from the present investigations closely match with those of Yoon et al. It is to be pointed out that Yoon et al carried out the experiments at 423 K, while the present investigations were performed at 300 K.

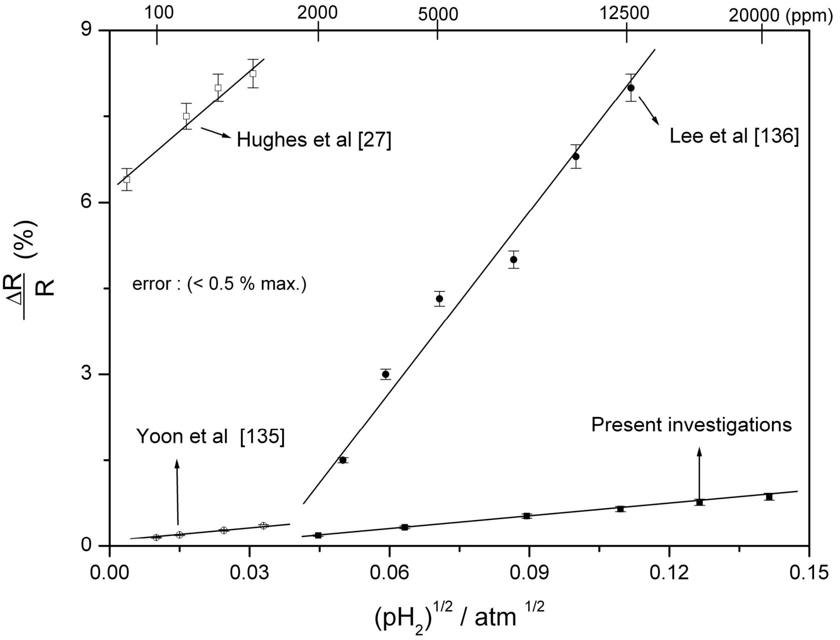

Fig. 5.15 Sensitivity vs $(p_{H_2}/\text{atm.})^{1/2}$ plot for the thin films of Pd, data of (□) Hughes et al, (•) Lee et al, (○) Yoon et al and (■) present investigation [Error bar: < 0.5%]

TABLE. 5.4

Comparison of experimental conditions employed during the studies of the interaction of hydrogen with Pd and its alloys

Alloys (thin film)	Method for analysis of composition	Thickness (Å)	Substrate	Operating Temperature (K)	Deposition technique	Reference
Pd	-	~ 7 x 10^4	Polycrystalline alumina	300	PLD	Present studies
$Pd_{0.93}Ni_{0.07}$	AAS	~ 7 x 10^4	Polycrystalline alumina	300	PLD	Present studies
$Pd_{0.97}Ni_{0.03}$	AAS	~ 7 x 10^4	Polycrystalline alumina	300	PLD	Present studies
$Pd_{0.91}Ni_{0.04}Co_{0.05}$	AAS	~ 7 x 10^4	Polycrystalline alumina	300	PLD	Present studies
Pd	-	500	SiO_2	298	Dual electron beam evaporation	Hughes et al [27, 133]
$Pd_{0.97}Ni_{0.03}$	In-situ Auger profile	500	SiO_2 or SiN	298	Dual electron beam evaporation	Hughes et al [134]
$Pd_{0.92}Ni_{0.08}$	In-situ Auger profile	500	SiO_2 or SiN	298	Dual electron beam evaporation	Hughes et al [134]
Pd	-	500	Silicon	423	R.F. magnetron sputtering	Yoon et al [135]
Pd	Not mentioned	50 – 4000	Silicon (100)	300	DC magnetron sputtering	Lee et al [136]
$Pd_{0.96}Ni_{0.04}$	Not mentioned	50 – 4000	Silicon (100)	300	DC magnetron sputtering	Lee et al [136]
$Pd_{0.93}Ni_{0.07}$	Not mentioned	50 – 4000	Silicon (100)	300	DC magnetron sputtering	Lee et al [136]

Figure 5.16 compares the variation of sensitivity with $p_{H2}^{1/2}$ in case of $Pd_{0.93}Ni_{0.07}$ (present studies and Lee et al), $Pd_{0.97}Ni_{0.03}$ (present studies), $Pd_{0.96}Ni_{0.04}$ (Lee et al) and $Pd_{0.91}Ni_{0.04}Co_{0.05}$ (present studies) thin films 300 K (Concentration range: 2000 - 20000 ppm). All the alloy films showed a linear increase in sensitivity with hydrogen. Lee et al ($Pd_{0.96}Ni_{0.04}$ and $Pd_{0.93}Ni_{0.07}$) reported a marginal decrease in sensitivity with increase in concentration of nickel in the alloy. On the contrary, the results of the present studies showed considerable increase in sensitivity with increase in nickel concentration in the alloy.

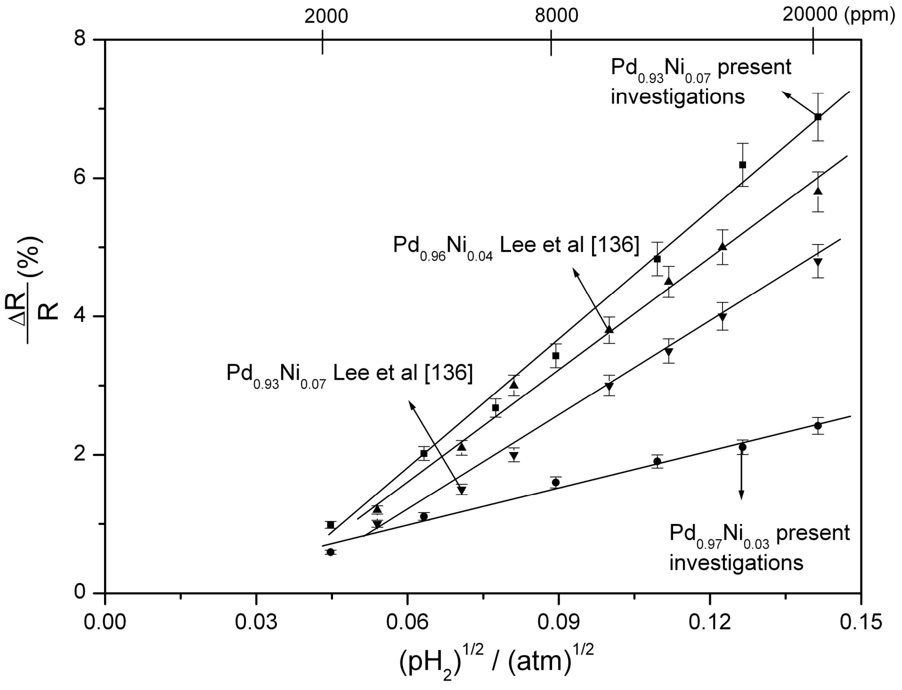

Fig. 5.16 Comparison of sensitivity vs (p_{H_2}/atm.)$^{1/2}$ plots thin films of (●) $Pd_{0.97}Ni_{0.03}$, (■) $Pd_{0.93}Ni_{0.07}$, (▼) $Pd_{0.93}Ni_{0.07}$ (Lee et al) and (▲) $Pd_{0.96}Ni_{0.04}$ (Lee et al) [Error : [< 0.5 %]

Figure 5.17 shows the comparison of sensitivity response plot of $Pd_{0.93}Ni_{0.07}$ (present studies), $Pd_{0.92}Ni_{0.08}$ (Hughes et al), $Pd_{0.97}Ni_{0.03}$ (present studies) and $Pd_{0.97}Ni_{0.03}$ (Hughes et al) thin films as a function of square root of hydrogen partial pressure. Hughes et al also reported lowering of sensitivity towards hydrogen when nickel concentration was increased in the alloy.

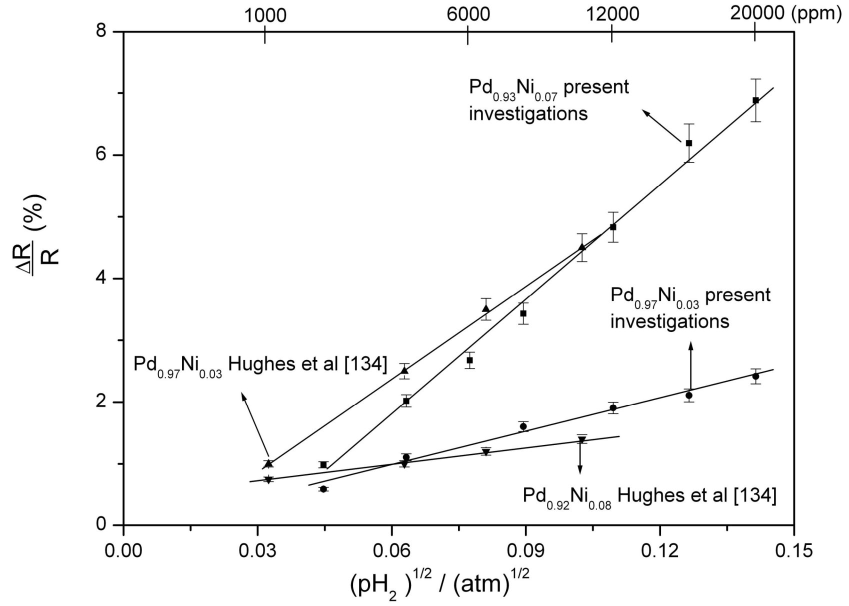

Fig. 5.17 Comparison of sensitivity vs (p_{H_2} /atm.$)^{1/2}$ for the thin films of (●) $Pd_{0.97}Ni_{0.03}$, (■) $Pd_{0.93}Ni_{0.07}$, (▼) $Pd_{0.92}Ni_{0.08}$ (Hughes et al) and (▲) $Pd_{0.97}Ni_{0.03}$ (Hughes et al) [Error bar: < 0.5%]

Lee et al deposited the alloys using DC magnetron sputtering using targets Pd and Ni. Composition of the alloy films was not experimentally determined. Hughes et al deposited alloy thin films using dual electron beam evaporation using Pd and Ni targets. In the present investigations, all the alloy thin films were deposited by PLD by using alloys of known stoichiometry. The reasons for the observed reversal in trend in sensitivity, towards hydrogen on increasing nickel concentration, from the present investigations are not known.

5.4 Conclusions

The present investigations show that palladium and its alloys can be prepared using LTCR technique. From the crystallographic elucidation, increase in the 2θ positions of thin films of $Pd_{0.97}Ni_{0.03}$, $Pd_{0.93}Ni_{0.07}$ and $Pd_{0.91}Ni_{0.04}Co_{0.05}$ when compared with palladium thin film provides the clear crystallographic evidence that the substituted nickel and cobalt enters in the position of palladium. X-ray diffraction studies indicate, PLD deposited thin films are nano-structured. The grain size of 100 – 150 nm, elucidated from AFM images of the thin films, is the evidence that the PLD deposited thin films are in nano dimensions. The response time in the presence of hydrogen and recovery time in the presence of argon of nickel in palladium films were found to be more when compared with palladium thin film at 300 K. The sensitivity towards hydrogen increases with increase in the nickel content in the alloy, when compared to that of pure palladium film. On the other hand, incorporation of cobalt along with nickel in $Pd_{0.91}Ni_{0.04}Co_{0.05}$ drastically decreased the sensitivity towards hydrogen when compared with nickel substituted alloys.

CHAPTER 6

Studies on preparation and characterization of $Ag_6Mo_{10-X}W_XO_{33}$ (X = 0 – 2) and selective sensing behavior of $Ag_6Mo_{10}O_{33}$ thick film towards NH_3 by AC impedance technique

6.1 Introduction

Semi-conducting metal oxides are promising sensor materials for online monitoring of low concentrations of pollutants, hazardous and flammable gases in industrial environments [137 – 149]. A thin or thick film of these materials is placed in ambient air and its electrical resistance can be continuously monitored. When trace level reducing gases are introduced in air, the resistance of the film changes: a decrease in the case of n-type material and an increase in case of p-type material. These resistances are measured by a 2-probe DC method. Silver decamolybdate ($Ag_6Mo_{10}O_{33}$), a mixed conductor with Ag^+ and e^- as carriers is one of these sensor materials which can sense NH_3 in the concentration range of 2 to 25 ppm (TLV of NH_3: 25 ppm) [150]. A thick film of this compound exhibited a decrease in resistance in the presence of NH_3 [151]. However, the resistance of the film was observed to drift continuously. During the 2-probe resistance measurement, a small DC current is passed through the film and the voltage drop across the film is measured. If the charge carriers in the material are either electrons or holes only, then no material is transported through the film. However, when a DC current is passed through a material that has ions as mobile charge carriers, the element corresponding to the ion gets transported from one electrode to another. In case of $Ag_6Mo_{10}O_{33}$, Ag^+ get transported and deposited. This would result in change in the composition of the film and hence in continuous drift in the resistance. Among the various desired characteristics to be possessed by a sensor, baseline stability is an important parameter. The continuous baseline drift can lead to false indication of the presence of pollutant in air.

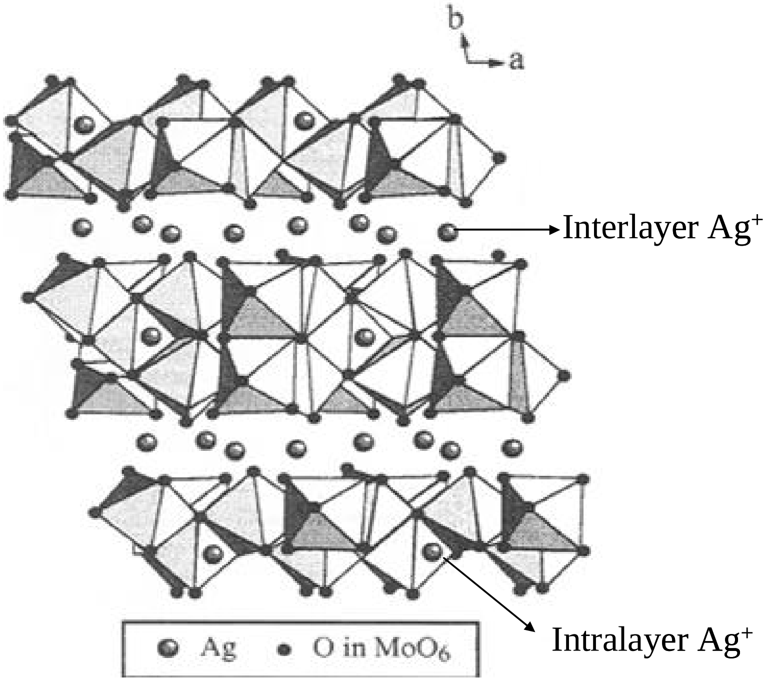

Fig. 6.1 Structure of $Ag_6Mo_{10}O_{33}$ showing the silver ion containing plane sandwiched between MoO_6 layers [152]

In order to improve the baseline stability of $Ag_6Mo_{10}O_{33}$, two approaches have been employed. In the first approach, tungsten was used as substitute for molybdenum. Based on the extensive crystallographic analyses of $Ag_6Mo_{10}O_{33}$, Gatehouse et al showed that silver ion in this compound is bonded as $O-Ag-O$ and is present as separate layers flanked by MoO_6 octahedra on both sides as shown in the Fig.6.1. Such crystallographic arrangement facilitates easy movement of Ag^+ in the layer [152, 153]. It is known that tungsten also forms WO_6 octahedra like MoO_6. It is expected that tungsten substitution for molybdenum may alter the silver ion mobility in the layer. Nominal compositions of $Ag_6Mo_{10-X}W_XO_{33}$ [X = 0 – 2.0] were synthesized and characterized using XRD. Electrical conductivity was measured by AC impedance method. Transport number of ions and electrons in tungsten substituted compounds were delineated through Wagner polarization technique.

In the second approach, resistance of $Ag_6Mo_{10}O_{33}$ was measured by AC impedance technique which would overcome the net transport of Ag^+ and decomposition of the material. AC impedance technique is a promising technique to resolve the contributions of different conduction modes to total electrical conductivity of a material [154 – 157].

The melting point of $Ag_6Mo_{10}O_{33}$ is 800 K [158]. Generally low melting elements like Ga, In etc. exhibit high vapor pressure (highly volatile). MoO_3 is known to be highly volatile. During deposition of thin films of $Ag_6Mo_{10}O_{33}$ decomposes and hence, the film does not contain phase pure $Ag_6Mo_{10}O_{33}$. In this work, $Ag_6Mo_{10}O_{33}$ was therefore made fabricated as thick film. The experimental aspects of thick film fabrication are given elsewhere [150]. The thick film impedance was measured in the temperatures range of 373 – 648 K and in the frequency region of 100 kHz to 100 Hz in clean air. H_2, NH_3 and PG were the analyte gases studied.

6.2 Experimental

6.2.1 Studies on $Ag_6Mo_{10-X}W_XO_{33}$ (x = 0 – 2)

Pure and tungsten incorporated silver decamolybdates with the nominal compositions $Ag_6Mo_{10-X}W_XO_{33}$ (x = 0, 0.25, 0.5, 1.0, 1.5 & 2.0) were prepared by solid state reaction method. Stoichiometric quantities of silver, molybdenum oxide and tungsten trioxide were mixed thoroughly using agate mortar and pestle. The pellets made by compacting the mixture were heated at 773 K for 24 h in air. The products were characterized by X-ray powder diffraction. The reaction leading to the formation of $Ag_6Mo_{10-X}W_XO_{33}$ is shown by eqn. 6.1.

$$6Ag + (10\text{-}x)MoO_3 + xWO_3 + 3/2O_2 \text{ (air)} \xrightarrow[24h]{773\,K} Ag_6Mo_{10-X}W_XO_{33} \qquad (6.1)$$

Electrical conductivities of $Ag_6Mo_{10}O_{33}$, $Ag_6Mo_{9.75}W_{0.25}O_{33}$ and $Ag_6Mo_{9.5}W_{0.5}O_{33}$ were measured using impedance spectroscopy and electronic transport number of these samples was measured using Wagner polarization technique. In order to carry out these investigations, powders were made in the form of pellets and heated to 723 K for 10 h. The details of impedance analysis and Wagner polarization studies are discussed in the experimental section of chapter 2. The baseline resistances of $Ag_6Mo_{10}O_{33}$, $Ag_6Mo_{9.75}W_{0.25}O_{33}$ and $Ag_6Mo_{9.5}W_{0.5}O_{33}$ in clean air were measured as a function of time at 573 K. The electron transport numbers in these samples were measured by Wagner polarization technique in the temperature range of 473 to 698 K. For this measurement, sample in the form of a pellet was sandwiched between two gold foils, which act as blocking electrodes. A constant DC potential of 50 mV was applied across the sample and resultant current was measured as a function of time using Keithley electrometer (Model No. 6517). The decrease in current as a function of time was recorded until it reached steady value. Similarly, conductivity of these samples was measured using AC impedance technique between 473 and 698 K in the frequency range of 1 Hz to 1 MHz. Surface morphology and phase composition were studied using SEM and backscattering electron image.

6.2.2 Studies on gas sensing behavior of $Ag_6Mo_{10}O_{33}$ thick film using AC impedance measurements

The details of the design of the thick film, its preparation and fabrication are explained in the experimental section in Chapter 2. The screen printed $Ag_6Mo_{10}O_{33}$ thick film was first heated to 393 K for 1 h and then it was heated at a heating rate of 5 K per min. to 773 K in air and was maintained at 773 K for 24 h. The thick film was cooled and then characterized by X-ray diffraction. The surface morphology of the thick film was characterized using SEM and EDAX.

The impedance of the thick film was measured by AC impedance technique in the frequency range between 0.1 MHz and 100 Hz, with an applied V_{rms} of 200 mV, in air. The change of impedance of the thick film during its interaction with different concentrations of NH_3 was measured at temperatures between 523 and 623 K. These studies were carried out with H_2 and petroleum Gas (PG) also. The experimental setup used for the gas interaction studies have been dealt in detail in chapter 2.

6.3 Results and Discussion

6.3.1 Characterization of $Ag_6Mo_{10-X}W_XO_{33}$ (x = 0 – 2)

6.3.1.1 Crystallographic elucidation of $Ag_6Mo_{10-X}W_XO_{33}$

Figures 6.2a ($2\theta = 0 – 30^o$) and Fig. 6.4a ($2\theta = 29 – 57^o$) show the XRD (step size: 0.05^o) pattern of $Ag_6Mo_{10}O_{33}$ powder sample. The sample showed the characteristic reflections corresponding to triclinic structure of $Ag_6Mo_{10}O_{33}$ and is in agreement with the JCPDS card no. 04 – 013 – 7646 (Symmetry: $P\bar{1}(2)$, a = 7.59 Å, b

= 8.31 Å, c = 11.42 Å, α = 82.6°, β = 102.9 °, γ = 106.4°). Figures 6.2b and 6.2c show the XRD patterns of $Ag_6Mo_{9.75}W_{0.25}O_{33}$ and $Ag_6Mo_{9.5}W_{0.5}O_{33}$ which are similar to that of $Ag_6Mo_{10}O_{33}$. Examination of these XRD patterns shows no shift in 2θ positions of these tungsten substituted compounds. This indicates, substituted tungsten occupies the position of molybdenum without altering the lattice parameters, which may be attributed similar ionic sizes of Mo^{6+} $(0.59\,\overset{o}{A})$ and W^{6+} $(0.60\,\overset{o}{A})$.

Figures 6.3a to d (2θ = 0 – 30°) and fig. 6.4a to 4d (2θ = 29 – 57°) show the XRD patterns of $Ag_6Mo_{10}O_{33}$, $Ag_6Mo_{9.0}W_{1.0}O_{33}$, $Ag_6Mo_{8.5}W_{1.5}O_{33}$ and $Ag_6Mo_{8.0}W_{2.0}O_{33}$. As seen in fig 6.3b and fig. 6.4b, XRD patterns of $Ag_6Mo_{9.0}W_{1\cdot0}O_{33}$ contain additional peaks at 28.35, 28.41, 32.03 and 32.95 in addition to those corresponding to $Ag_6Mo_{10}O_{33}$, XRD pattern of $Ag_6Mo_{9.0}W_{1\cdot0}O_{33}$, indicating precipitation of a new phase. The new peaks match with the high intense peaks of triclinic of $Ag_2Mo_2O_7$ (JCPDS no. 75 – 1505), and are marked as * in Fig. 6.3b and 6.4b.

Figure 6.3c and fig. 6.4c show XRD patterns for the nominal composition, $Ag_6Mo_{8.5}W_{1.5}O_{33}$. Apart from reflections of $Ag_6Mo_{10}O_{33}$ and $Ag_2Mo_2O_7$, additional peaks are observed at 23.15, 23.6 and 24.35. These peaks are marked as # and correspond to monoclinic phase of WO_3 (JCPDS no. 83 – 0950). From XRD analysis it is clear that the tungsten content in $Ag_6Mo_{10-X}W_XO_{33}$ (X = 1 & 1.5), monoclinic phase of WO_3 is precipitating out along with $Ag_2Mo_2O_{7.}$ Figure 6.3d and fig. 6.4d show the diffraction patterns of the samples of nominal composition $Ag_6Mo_{8.0}W_{2.0}O_{33}$ and is similar to that of $Ag_6Mo_{8.5}W_{1.5}O_{33.}$

Equation 6.2 accounts for the formation of $Ag_6Mo_{9.5}W_{0.5}O_{33}$ along with $Ag_2Mo_2O_7$ and precipitation of WO_3 when MoO_3 to WO_3 ratio is 9:1. However, the finger print reflections of WO_3 could not be identified from the XRD in fig. 6.3b.

$$6Ag + 9MoO_3 + WO_3 \rightarrow 0.86Ag_6Mo_{9.5}W_{0.5}O_{33} + 0.43Ag_2Mo_2O_7 + 0.57WO_3 \quad (6.2)$$

XRD patterns of $Ag_6Mo_{10-X}W_XO_{33}$ indicate that WO_3 is present as solid solution in $Ag_6Mo_{10}O_{33}$ up to 0.5. At high concentrations of WO_3, $Ag_2Mo_2O_7$ and WO_3 precipitate out. To confirm these results additional slow scan XRD patterns with step size of 0.02^o (2θ) were recorded for $Ag_6Mo_{10}O_{33}$, $Ag_6Mo_{9.75}W_{0.25}O_{33}$ and $Ag_6Mo_{9.5}W_{0.5}O_{33}$. These XRD patterns are shown in fig. 6.5a to c ($2\theta = 0 – 30^o$) and 6.6a to c ($2\theta = 29 – 57^o$).

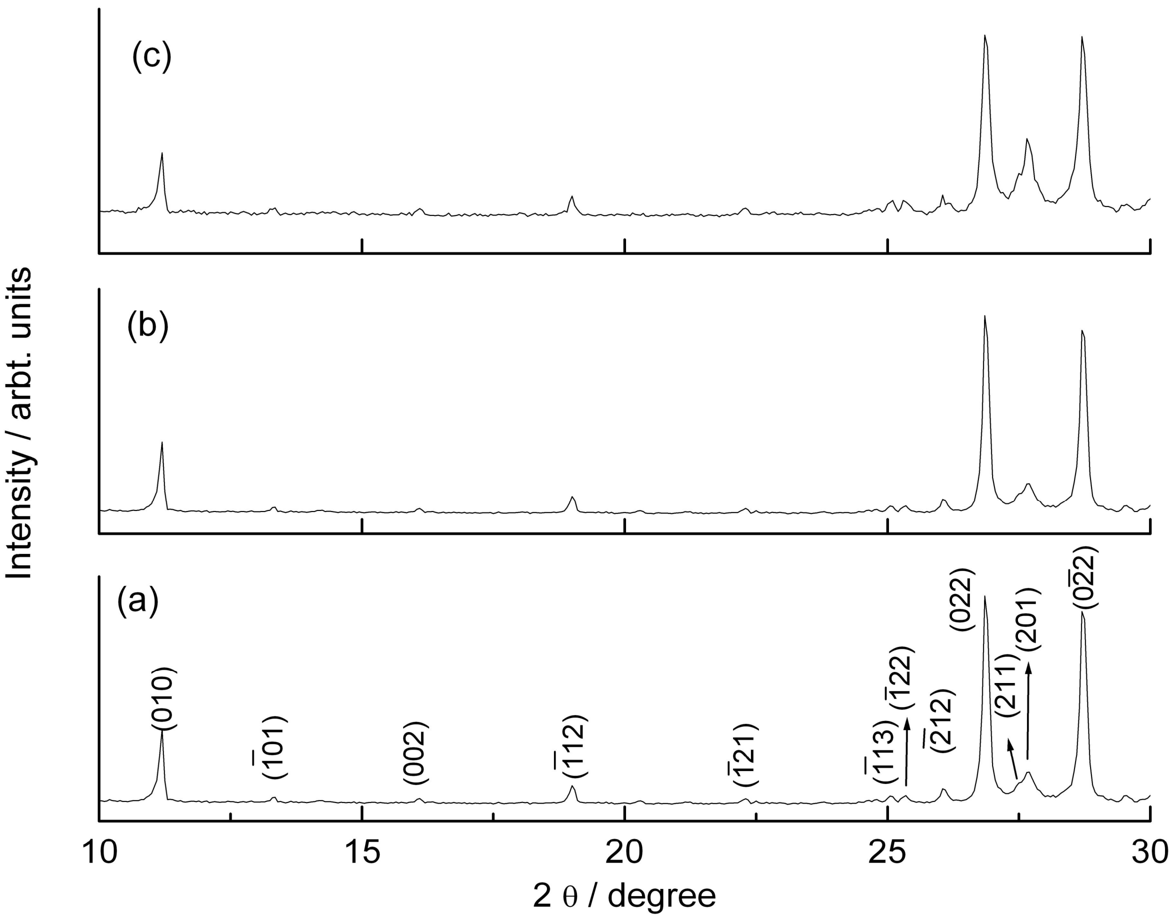

Fig. 6.2 XRD patterns for the nominal compositions a) $Ag_6Mo_{10}O_{33}$, b) $Ag_6Mo_{9.75}W_{0.25}O_{33}$ and c) $Ag_6Mo_{9.5}W_{0.5}O_{33}$

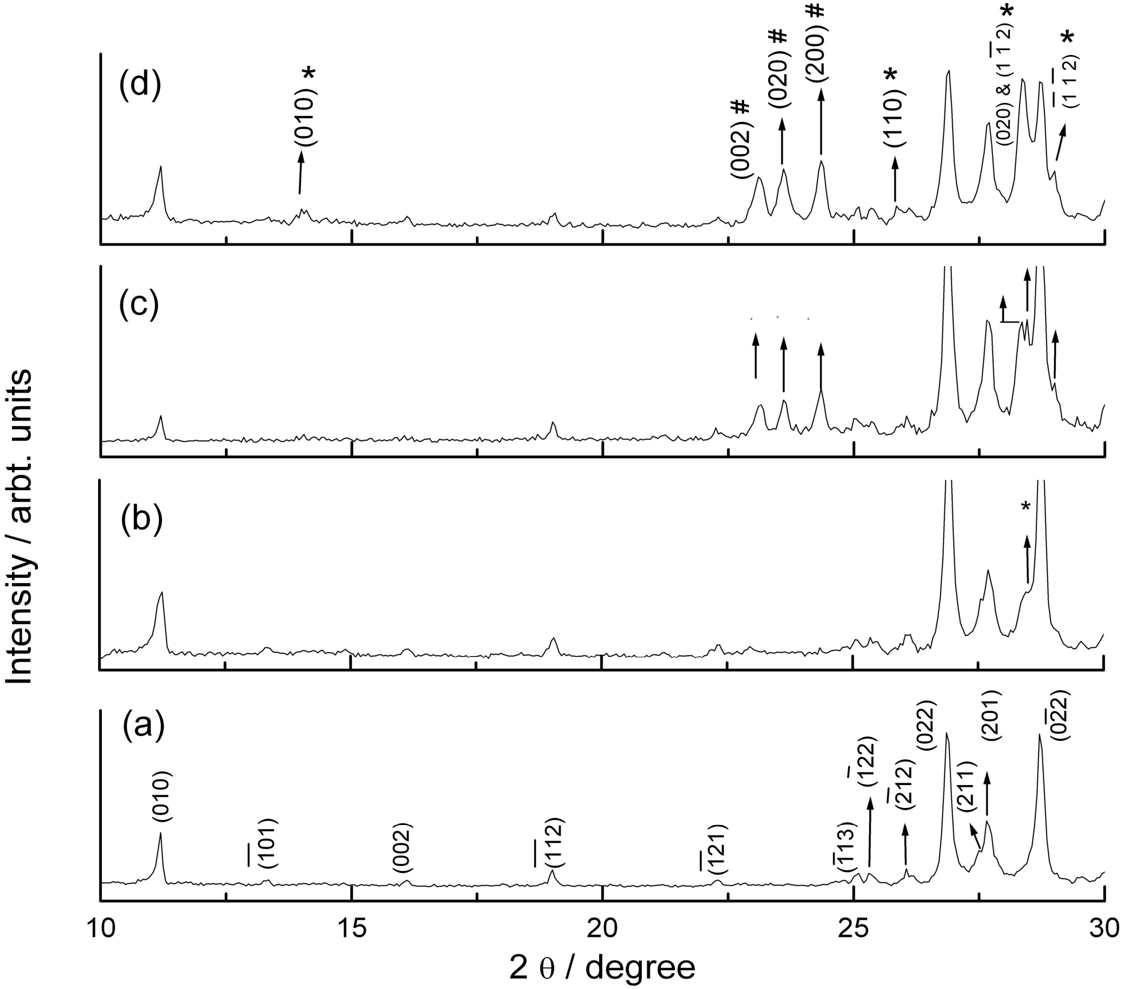

Fig. 6.3 XRD patterns for the nominal compositions a) $Ag_6Mo_{10}O_{33}$, b) $Ag_6Mo_{9.0}W_{1.0}O_{33}$, c) $Ag_6Mo_{8.5}W_{1.5}O_{33}$ and d) $Ag_6Mo_{8.0}W_{2.0}O_{33}$

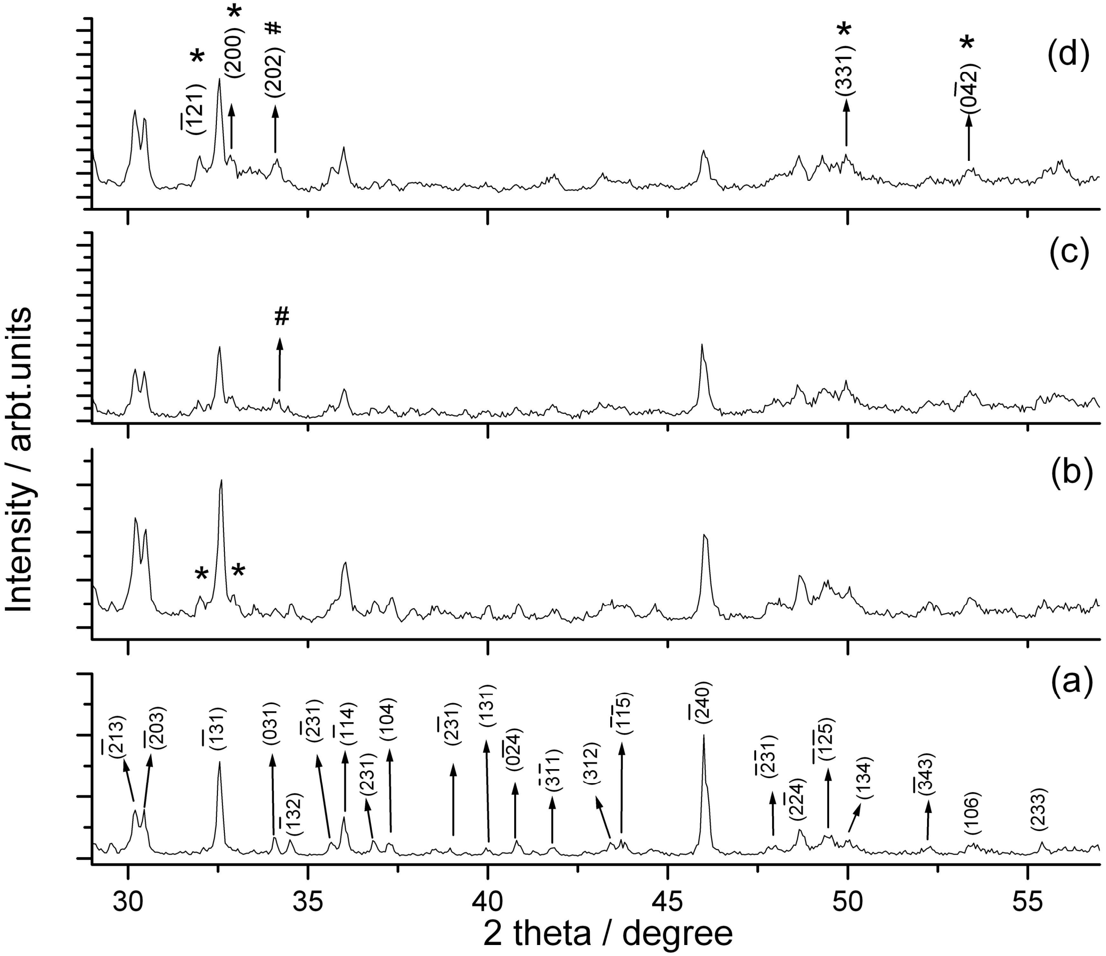

Fig. 6.4 XRD patterns for the nominal compositions a) $Ag_6Mo_{10}O_{33}$, b) $Ag_6Mo_{9.0}W_{1.0}O_{33}$, c) $Ag_6Mo_{8.5}W_{1.5}O_{33}$ and d) $Ag_6Mo_{8.0}W_{2.0}O_{33}$

6.3.1.2 Regular and backscattering scanning electron microscope images of $Ag_6Mo_{10-X}W_XO_{33}$ (0 – 1.0)

Examination of these patterns shows them to be identical and there was no shift in the 2θ positions of the peaks of $Ag_6Mo_{9.75}W_{0.25}$ and $Ag_6Mo_{9.5}W_{0.5}O_{33}$ in comparison with those of $Ag_6Mo_{10}O_{33}$. To confirm the absence of any other phases, regular and backscattering scanning electron microscope images were recorded for $Ag_6Mo_{10}O_{33}$, $Ag_6Mo_{9.75}W_{0.25}$, $Ag_6Mo_{9.5}W_{0.5}O_{33}$ and $Ag_6Mo_{9.0}W_{1.0}O_{33}$ and images are shown in fig. 6.7a to d and fig. 6.8a to d. As seen from the SEM images, all samples exhibit needle shaped grains having non uniform size. Backscattering electron images are strongly related to the atomic number (Z) of the elements in the specimen. The method would distinguish the presence of different phases present in the compound by exhibiting different color contrast. Larger is the difference in atomic number of the elements better would be the resolution of the images. Elements with higher atomic number which backscatter more efficiently appear brighter than the lower atomic number. The backscattering coefficient (η) of molybdenum (atomic number: 42) and tungsten (atomic number: 74) are 0.4 and 0.5 [159]. As seen from the backscattering images (fig. 6.8a – d), all the samples exhibit similar contrasting images. Even though there was a significant difference in the atomic number and backscattering coefficients for molybdenum and tungsten, it was not reflected in the backscattering images of tungsten substituted samples. This indicates there are no separate phases with tungsten enrichment. These results show that tungsten occupies the lattice position of molybdenum in $Ag_6Mo_{10}O_{33}$ up to $Ag_6Mo_{9.5}W_{0.5}O_{33}$. Further experiments to measure electrical conductivity and transport number of Ag^+ and electron were carried out with samples of $Ag_6Mo_{10}O_{33}$, $Ag_6Mo_{9.75}W_{0.25}$ and $Ag_6Mo_{9.5}W_{0.5}O_{33}$.

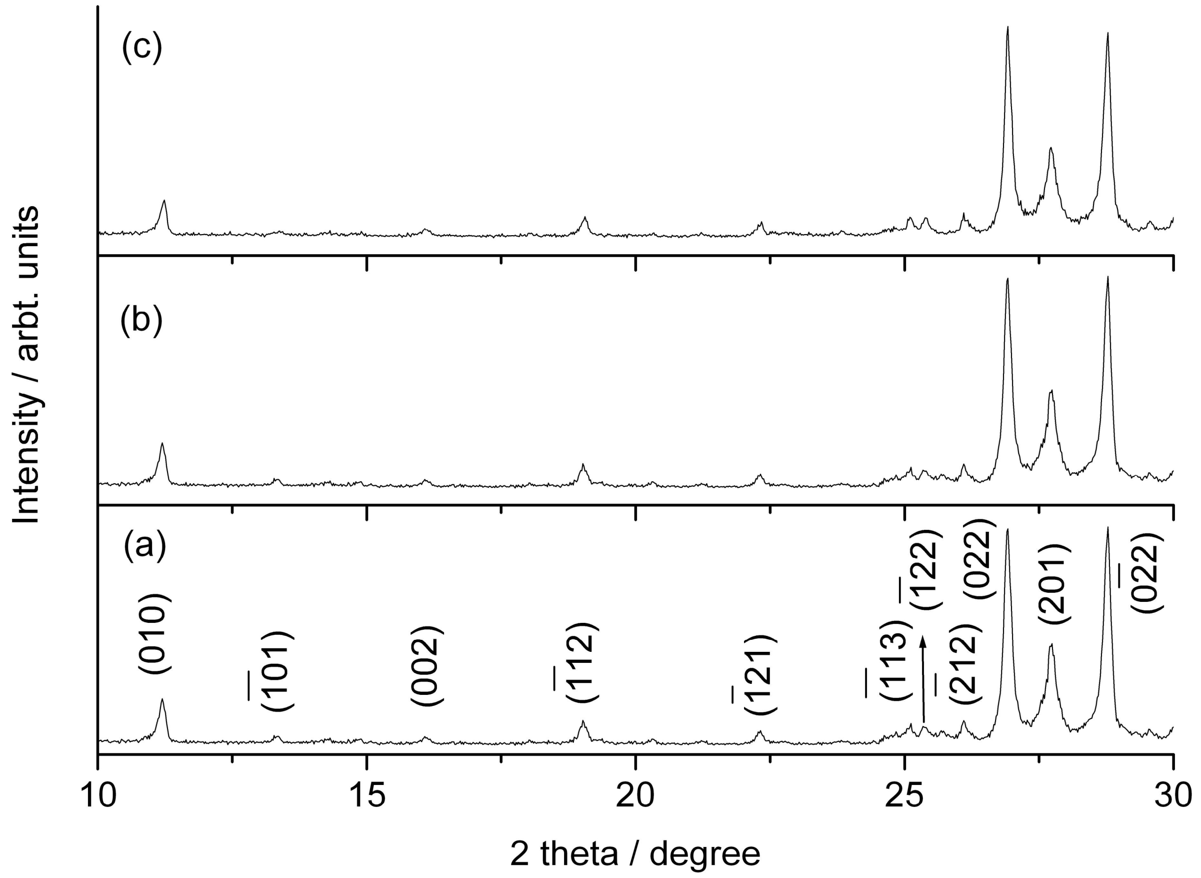

Fig. 6.5 XRD patterns for the nominal compositions a) $Ag_6Mo_{10}O_{33}$, b) $Ag_6Mo_{9.75}W_{0.25}O_{33}$ and c) $Ag_6Mo_{9.5}W_{0.5}O_{33}$

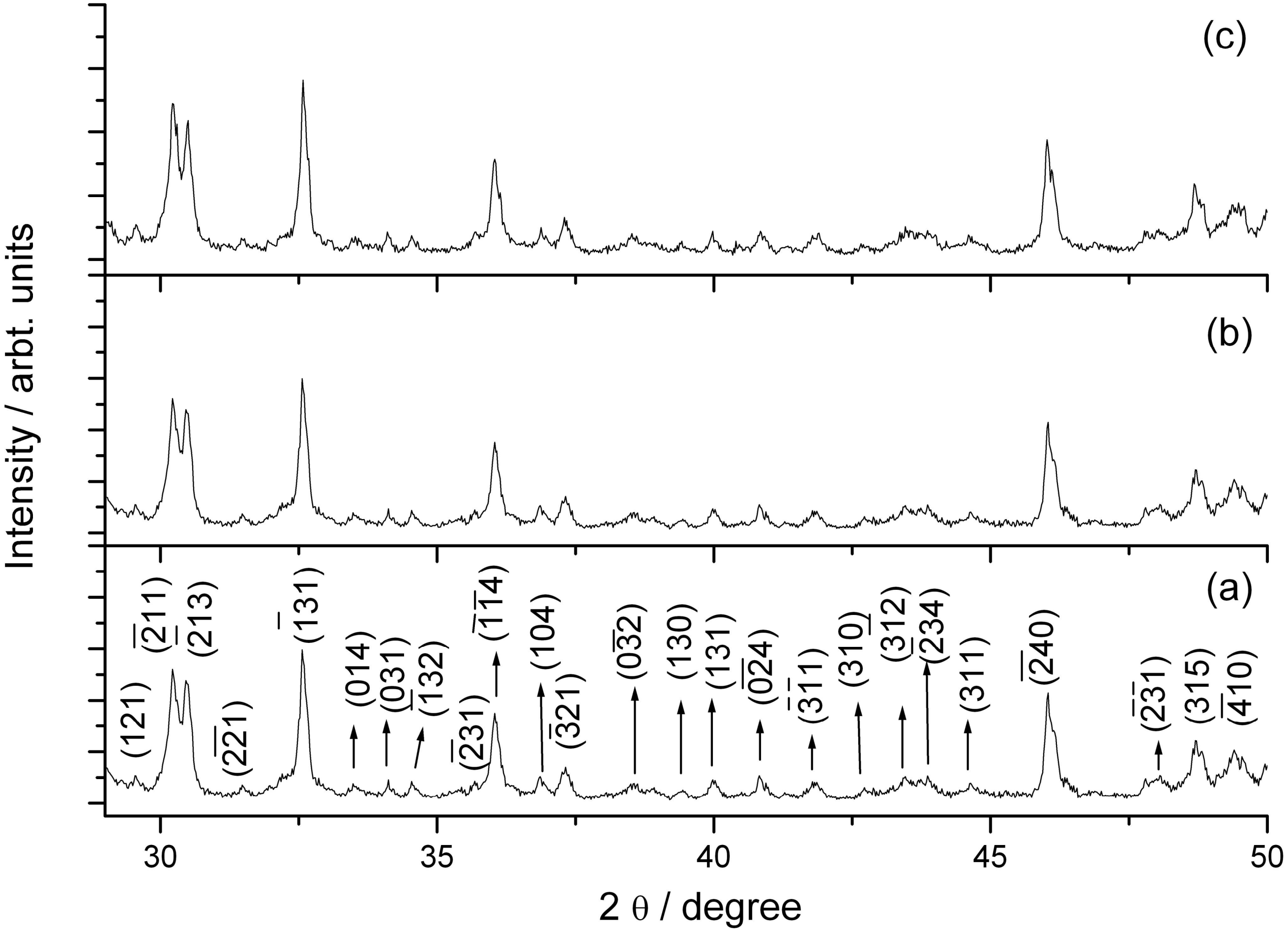

Fig. 6.6 XRD patterns for the nominal compositions a) $Ag_6Mo_{10}O_{33}$, b) $Ag_6Mo_{9.75}W_{0.25}O_{33}$ and c) $Ag_6Mo_{9.5}W_{0.5}O_{33}$

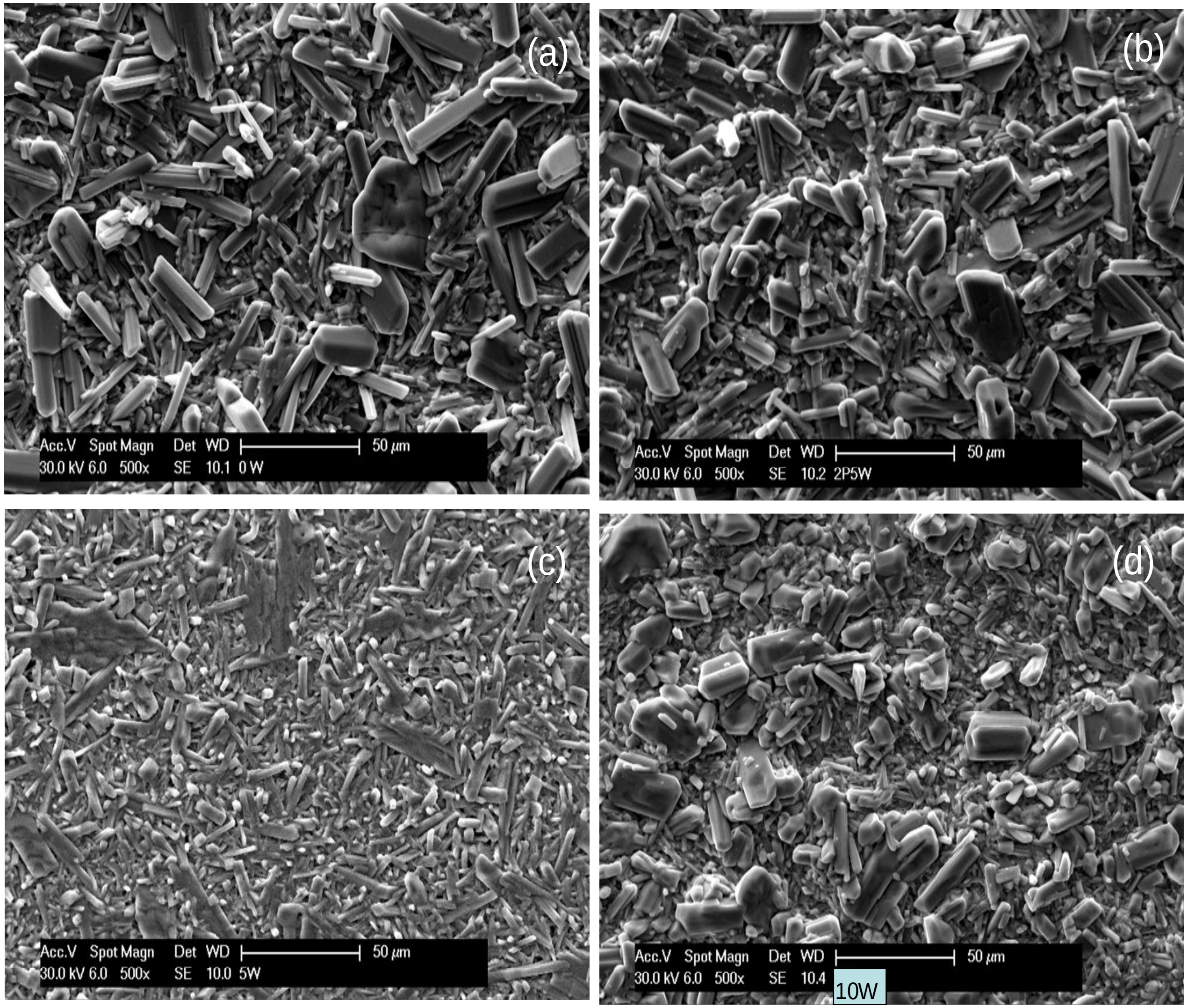

Fig. 6.7 SEM images of a) $Ag_6Mo_{10}O_{33}$, b) $Ag_6Mo_{9.75}W_{0.25}O_{33}$, c) $Ag_6Mo_{9.5}W_{0.5}O_{33}$ and d) $Ag_6Mo_{9.0}W_{1.0}O_{33}$

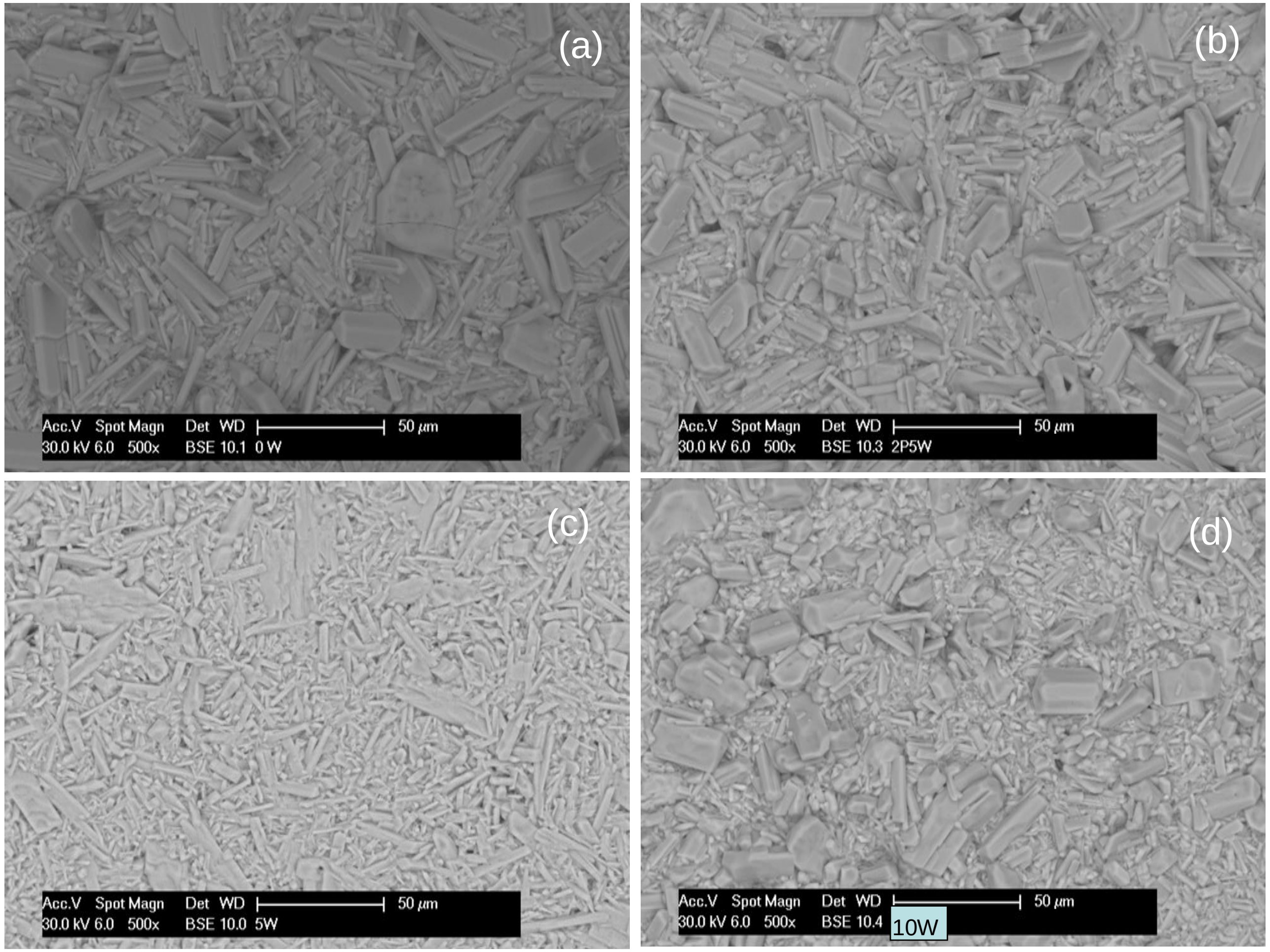

Fig. 6.8 Backscattering electron images of a) $Ag_6Mo_{10}O_{33}$, b) $Ag_6Mo_{9.75}W_{0.25}O_{33}$, c) $Ag_6Mo_{9.5}W_{0.5}O_{33}$ and d) $Ag_6Mo_{9.0}W_{1.0}O_{33}$

6.3.1.3 Silver ion transport behavior in $Ag_6Mo_{10-x}W_xO_{33}$ (x = 0, 0.25 and 0.5)

The transport no. for Ag^+ in $Ag_6Mo_{10}O_{33}$, $Ag_6Mo_{9.75}W_{0.25}O_{33}$ and $Ag_6Mo_{9.5}W_{0.5}O_{33}$ was measured by Wagner polarization technique using the cell configuration: (–) Au/ $Ag_6Mo_{10-x}W_xO_{33}$/Au (+) [x = 0, 0.25 & 0.5] between 473 and 698 K. Sample in the form of pellet was sandwiched between two gold electrodes, which act as blocking electrodes with an applied voltage of 0.5. Typical polarization plot for $Ag_6Mo_{9.5}W_{0.5}O_{33}$ at 586 K is shown in fig. 6.9. The initial current is high and is due to ions and electrons and the current decreases with time. Finally it reaches a constant value after prolonged period under steady state conditions. I_{final} is the steady-state current and this is only due to electrons.

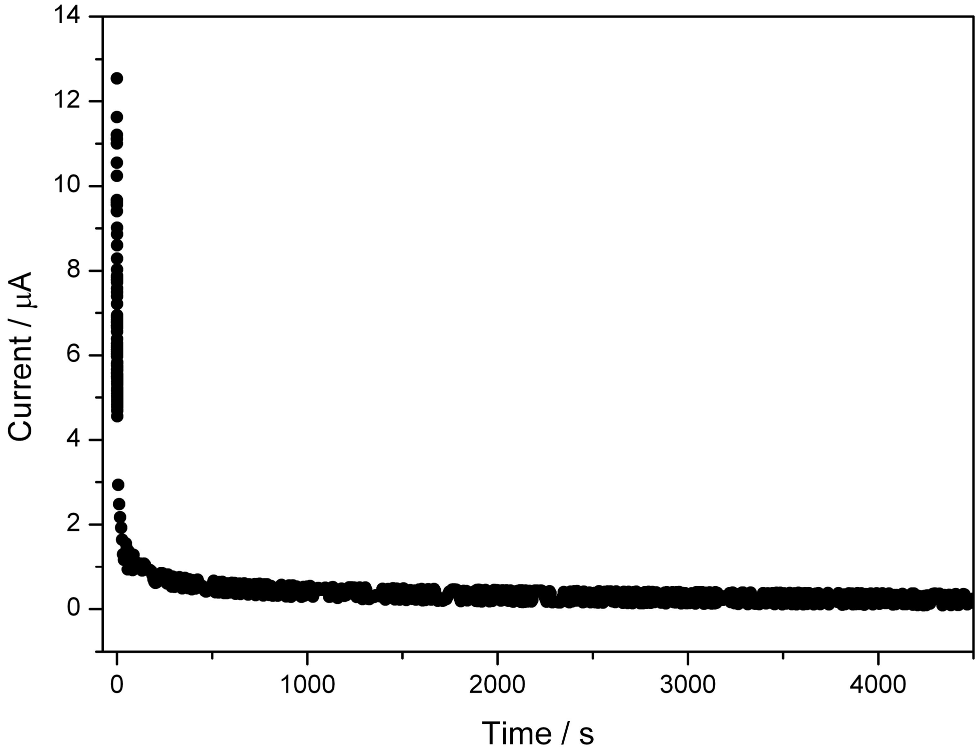

Fig. 6.9 Typical plot of current vs time for the estimation of ionic transport number for the composition $Ag_6Mo_{9.5}W_{0.5}O_{33}$ at 586 K

The ionic transport number (t_i) for the samples is determined and calculated using the eqn. 6.3. Where $I^{o}_{initial}$ is the current at t = 0.

$$\text{Ionic transport number}\,(t_i) = \frac{I^{o}_{initial} - I_{final}}{I^{o}_{initial}} \tag{6.3}$$

$I^{o}_{initial}$ was obtained by extrapolating the current at the initial duration of the experiments i.e. I initial to zero time as shown in fig. 6.10 for $Ag_6Mo_{9.5}W_{0.5}O_{33}$ at 586 K.

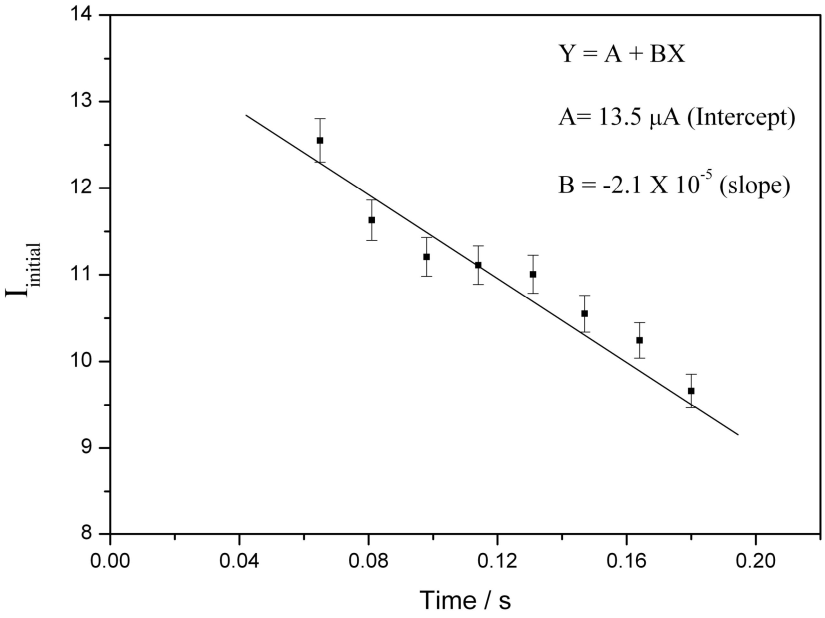

Fig. 6.10 Variation of current with time during Wagner's polarization experiment with $Ag_6Mo_{9.5}W_{0.5}O_{33}$ at 586 K [Error bar: < 0.5%]

Silver ion transport nos. in $Ag_6Mo_{10}O_{33}$, $Ag_6Mo_{9.75}W_{0.25}O_{33}$ and $Ag_6Mo_{9.5}W_{0.5}O_{33}$ were determined from these experimental data and are plotted as a function of temperature in fig. 6.11a. As seen from the figure, t_{Ag^+} of $Ag_6Mo_{10}O_{33}$

is 0.81 at 486 K and increases steeply to 0.90 at 510 K. It increases further to 0.94 at 550 K and to 0.97 at 698 K. For $Ag_6Mo_{9.75}W_{0.25}O_{33}$, t_{Ag^+} is 0.91 at 490 K and gradually it increases with increase in temperature to 0.98 at 692 K as shown in fig.6.11b. For $Ag_6Mo_{9.5}W_{0.5}O_{33}$, t_{Ag^+} is 0.93 at 490 K and shows a maximum Ag^+ transport no. of 0.98 at 598 K and thereafter no further increase is observed up to 692 K. As seen from the fig. 6.11, t_{Ag^+} transport no. increases with substitution of tungsten in $Ag_6Mo_{10}O_{33}$.

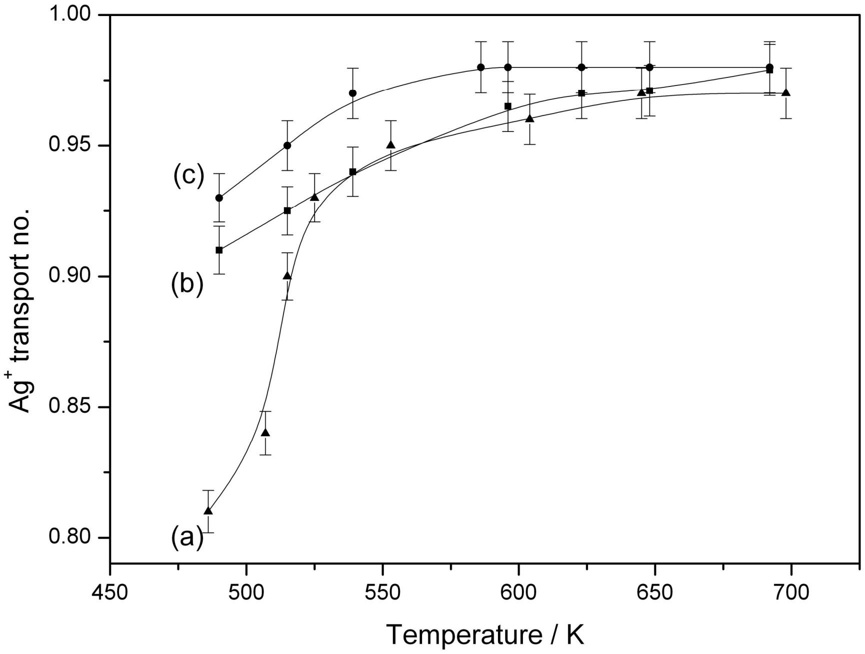

Fig. 6.11 Transport no. of silver ion as a function of temperature for (▲) $Ag_6Mo_{10}O_{33}$, (■) $Ag_6Mo_{9.75}W_{0.25}O_{33}$ and (●) $Ag_6Mo_{9.5}W_{0.5}O_{33}$ [Error bar: < 0.5%]

6.3.1.4 Studies on electrical conductivity of $Ag_6Mo_{10-X}W_XO_{33}$ (x = 0, 0.25 and 0.5)

Figures 6.12a to c show the typical AC impedance (Z' vs Z'') spectrum of $Ag_6Mo_{10}O_{33}$, $Ag_6Mo_{9.75}W_{0.25}O_{33}$ and $Ag_6Mo_{9.5}W_{0.5}O_{33}$ pellets in the frequency range of 300 kHz to 10 Hz at 589 K in air. The spectrum consists of one depressed semicircle followed by an inclined straight line portion which appears in the low frequency region. The semicircular part is attributed to the inherent conduction process (bulk or grain boundary or a combination of both); while the linear portion stems from diffusion of ions/electrons through the bulk to the electrode. From the real axis intercept, resistance of the sample was calculated using Z view® (version 2.70) program and it was employed in Arrhenius plot shown in fig. 6.13.

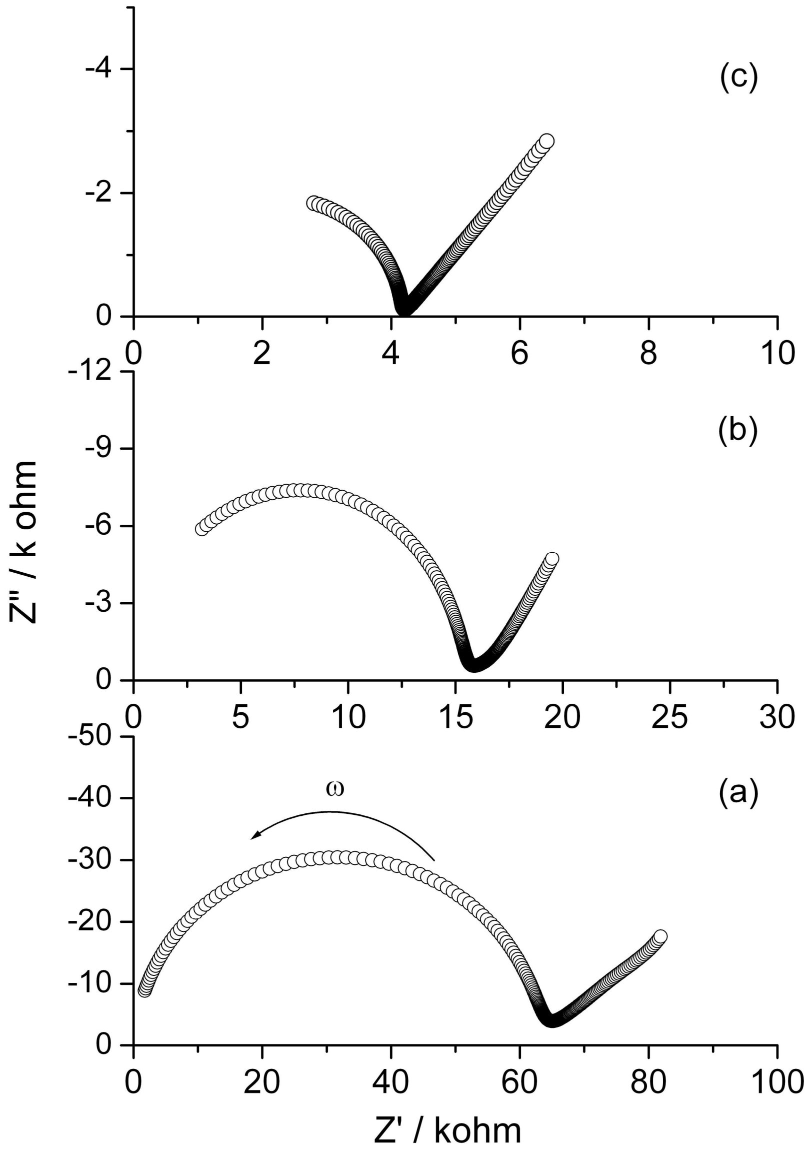

Fig. 6.12 Nyquist plot of a) $Ag_6Mo_{10}O_{33}$, b) $Ag_6Mo_{9.75}W_{0.25}O_{33}$ and c) $Ag_6Mo_{9.5}W_{0.5}O_{33}$ pellets at 589 K

Figure 6.13 shows the Arrhenius plots for the conductivity of $Ag_6Mo_{10}O_{33}$, $Ag_6Mo_{9.75}W_{0.25}O_{33}$ and $Ag_6Mo_{9.5}W_{0.5}O_{33}$ in air between 443 and 689 K. As seen from the figure, all the three samples follow Arrhenius behavior throughout the temperature interval of studies. A systematic increase in conductivity is observed with increase in concentration of tungsten at all temperatures. The activation energies for the conduction process were calculated and are shown in Table 6.1. The data clearly indicate a gradual decrease in activation energy with increase in concentration of tungsten in $Ag_6Mo_{10-X}W_XO_{33}$.

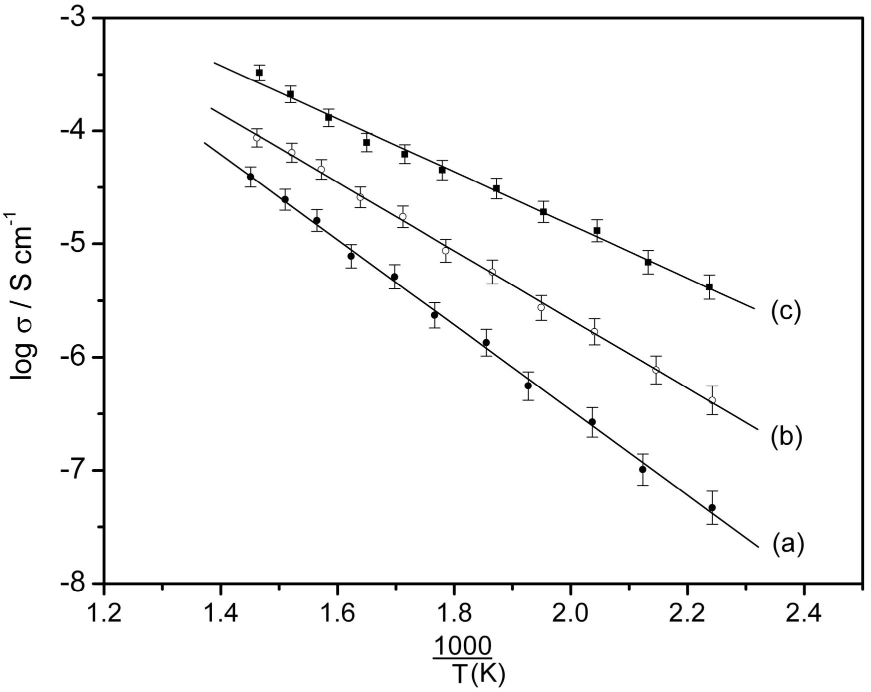

Fig. 6.13 Conductivity vs inverse temperature (Arrhenius) plot for a) $Ag_6Mo_{10}O_{33}$, b) $Ag_6Mo_{9.75}W_{0.25}O_{33}$ and c) $Ag_6Mo_{9.5}W_{0.5}O_{33}$ [Error bar: < 0.5%]

Table: 6.1

Calculated activation energy for the conduction process for pure and tungsten substituted $Ag_6Mo_{10}O_{33}$

Composition	Activation energy E_a (eV)
$Ag_6Mo_{10}O_{33}$	0.32 (± 0.02)
$Ag_6Mo_{9.75}W_{0.25}O_{33}$	0.26 (± 0.02)
$Ag_6Mo_{9.5}W_{0.5}O_{33}$	0.20 (± 0.02)

6.3.1.5 Baseline stability studies of $Ag_6Mo_{10-x}W_xO_{33}$ (x = 0, 0.25 and 0.5)

Figure 6.14a to c shows the resistance of $Ag_6Mo_{10}O_{33}$, $Ag_6Mo_{9.75}W_{0.25}O_{33}$ and $Ag_6Mo_{9.5}W_{0.5}O_{33}$ pellets in air at 573 K measured by two probe DC method as a function of time in air at 573 K using two probe measurements for a period of time to evaluate the stability of the baseline. As seen from the fig. 6.14a to c there is a gradual increase in the resistance of pure and tungsten substituted $Ag_6Mo_{10}O_{33}$ with increase in time. The drift in the resistance shown by the samples are due to slow displacement of silver ion because of high electronic conductivity. As seen from the figure, the rate of change of resistance increases with increase in tungsten substitution in $Ag_6Mo_{10}O_{33}$. This is inline with the increase in silver ion transport number with increase in tungsten substitution in $Ag_6Mo_{10}O_{33}$.

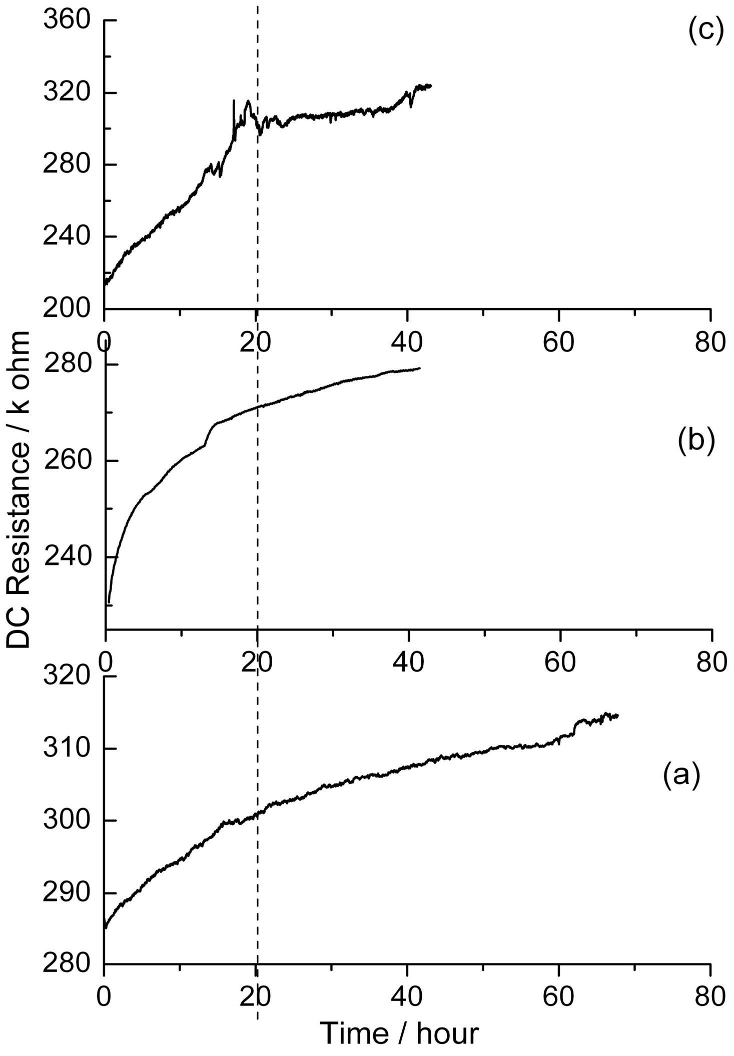

Fig. 6.14 Resistance as a function of time in air at 573 K by DC using two probe measurement for a) $Ag_6Mo_{10}O_{33}$, b) $Ag_6Mo_{9.75}W_{0.25}O_{33}$ and c) $Ag_6Mo_{9.5}W_{0.5}O_{33}$

$Ag_6Mo_{9.75}W_{0.25}O_{33}$ and $Ag_6Mo_{9.5}W_{0.5}O_{33}$ possess higher silver ion transport number and electrical conductivity than those of $Ag_6Mo_{10}O_{33}$. Baseline resistance of these compositions also continuously drifted and hence they would not meet the criteria required for a sensor.

6.3.2 Characterization of $Ag_6Mo_{10}O_{33}$ thick film and studies on its interaction with NH_3, H_2, and PG using AC impedance spectroscopy

6.3.2.1 Crystallographic elucidation of $Ag_6Mo_{10}O_{33}$ thick film

Figure 6.15 shows the XRD pattern of $Ag_6Mo_{10}O_{33}$ thick film on alumina substrate. The thick film exhibited the characteristic reflections of $Ag_6Mo_{10}O_{33}$ and matched well with reflections shown by the bulk $Ag_6Mo_{10}O_{33}$ in fig. 6.2a (JCPDS card no. 04 – 013 – 7646). The reflections due to the polycrystalline alumina substrate are indicated by (*) in the XRD pattern.

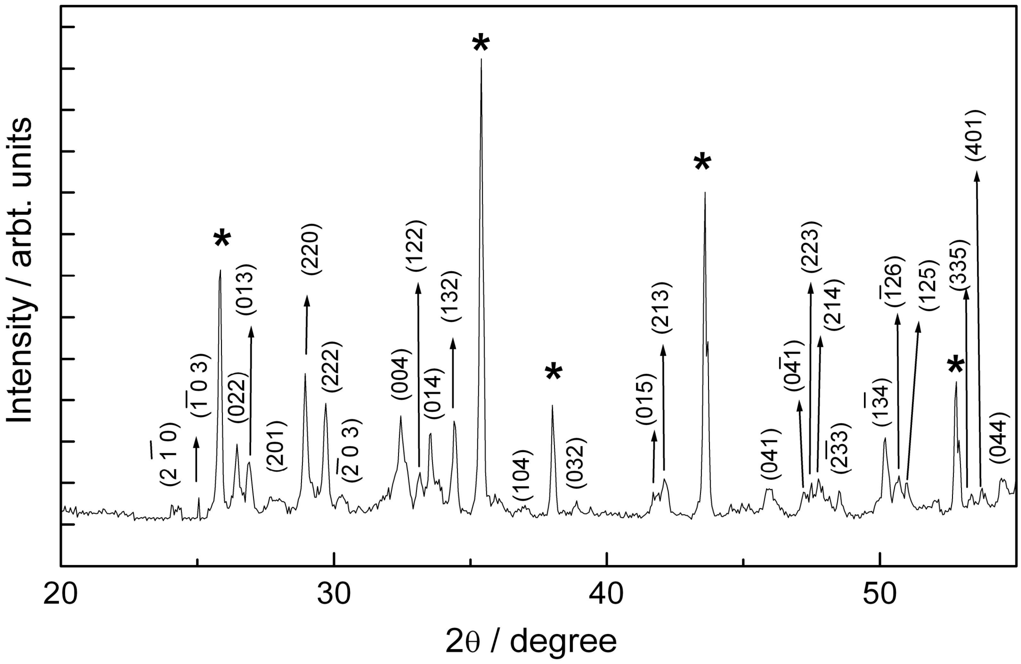

Fig. 6.15 XRD pattern of $Ag_6Mo_{10}O_{33}$ thick film on alumina substrate: (*) peaks corresponding to alumina substrate

6.3.2.2 Surface morphology and EDX analysis of $Ag_6Mo_{10}O_{33}$ thick film

The surface morphology of $Ag_6Mo_{10}O_{33}$ thick film was investigated using scanning electron microscope at the magnification of 100X and the results are shown in Fig. 6.16a. This image shows the surface with uniform distribution of grains of $Ag_6Mo_{10}O_{33}$ as well as open pores in the interior. The porous network is preferred for a metal oxide to adsorb gas molecules on the surface. Figure 6.16b shows the SEM image of the thick film at the magnification of 2000X. As seen from figure, needle shaped grains with non-uniform length and widths are present. The wider plate like shapes provides larger surface area for the gas molecules to adsorb on the surface and EDX spectrum (fig. 6.17) shows Ag and Mo are present at an atomic ratio of 6:10.

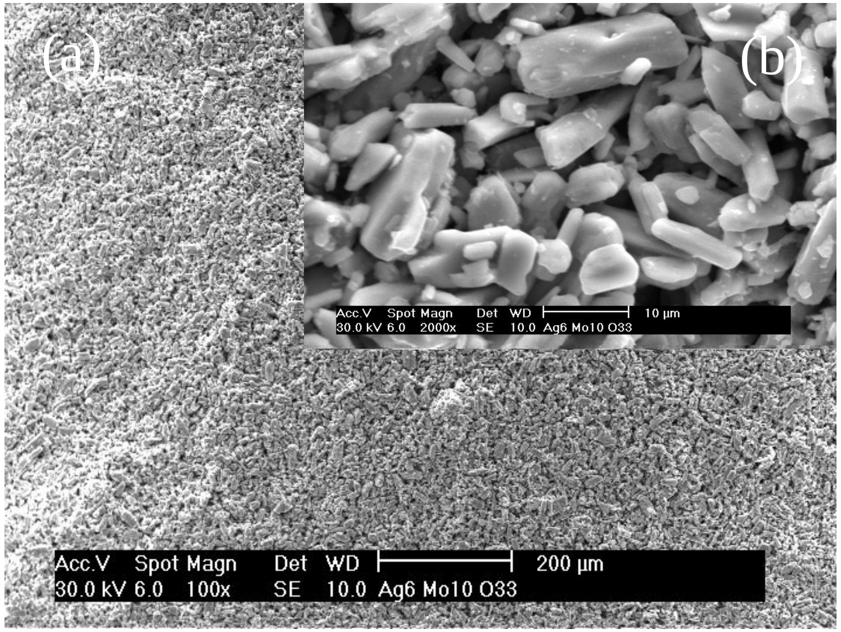

Fig. 6.16 SEM image of $Ag_6Mo_{10}O_{33}$ thick film with the magnification of a) 100 X and b) 2000 X

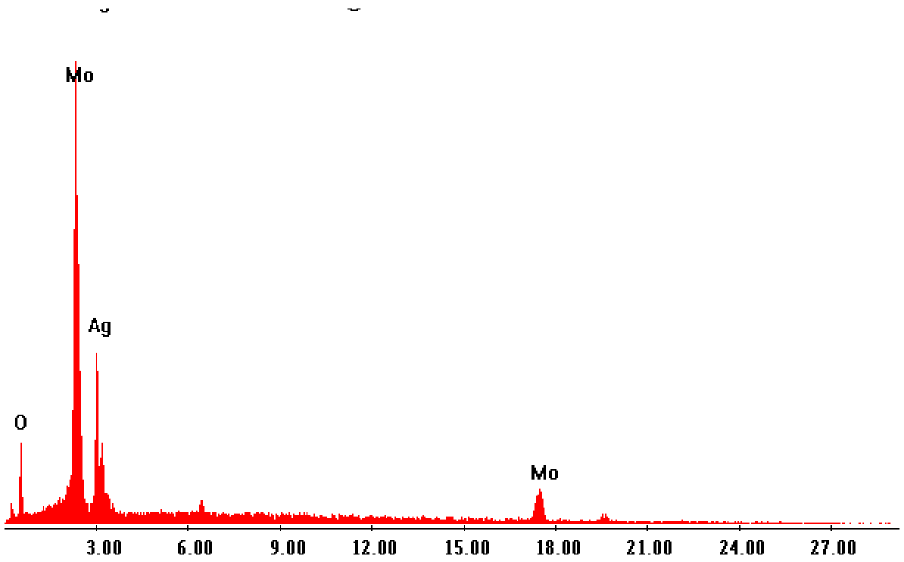

Fig. 6.17 EDX spectrum of $Ag_6Mo_{10}O_{33}$ thick film

6.3.2.3 Impedance studies on $Ag_6Mo_{10}O_{33}$

Figure 6.18 shows the AC impedance (Z' vs Z'') spectrum of $Ag_6Mo_{10}O_{33}$ thick film measured between the frequencies 1 MHz and 1 Hz in the temperature range of 423 to 648 K in air. The compound showed a semi-circular pattern in all the temperatures, which can be modeled by a parallel RC circuit, attributed to grain (g), grain boundaries (gb) and grain – electrode interface (el). Each RC circuit is represented by a semicircle in the complex plot of Z' versus Z'' (Nyquist diagram). The semicircle obtained in the present investigations may correspond to either one or a combination of these processes. The total impedance of the thick film is given by eqns. 6.4 and 6.5. The proposed equivalent circuit model for $Ag_6Mo_{10}O_{33}$ thick film is shown in Fig. 6.19.

$$Z^{total}\,(j\omega) \;=\; \sum_i Z_i\,(j\omega) \tag{6.4}$$

$$Z_i\;(j\omega) = Z_i^{'}\;(\omega) +\; jZ_i^{''}\;(\omega) \tag{6.5}$$

where i = g, gb, el and j = $\sqrt{-1}$

Table: 6.2

Calculated resistance and capacitance of $Ag_6Mo_{10}O_{33}$ thick film using Zview® (version 2.70) program

Temperature K	Resistance (MΩ)	Capacitance (nF)
423	120	0.16
523	5.9	0.21
573	1.9	0.24
648	0.3	0.25

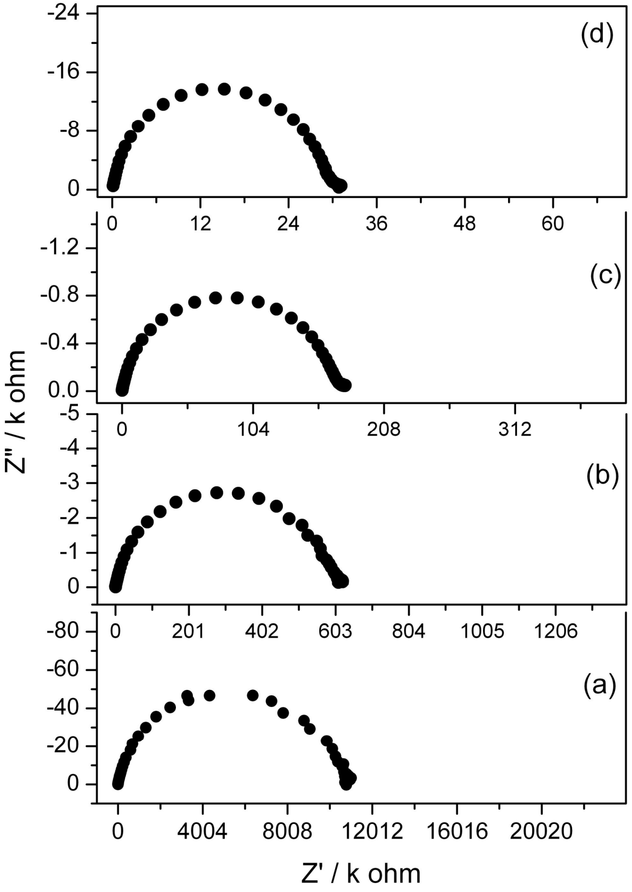

Fig. 6.18 Nyquist plot of $Ag_6Mo_{10}O_{33}$ thick film at a) 423 K b) 523 K c) 573 K and d) 648 K

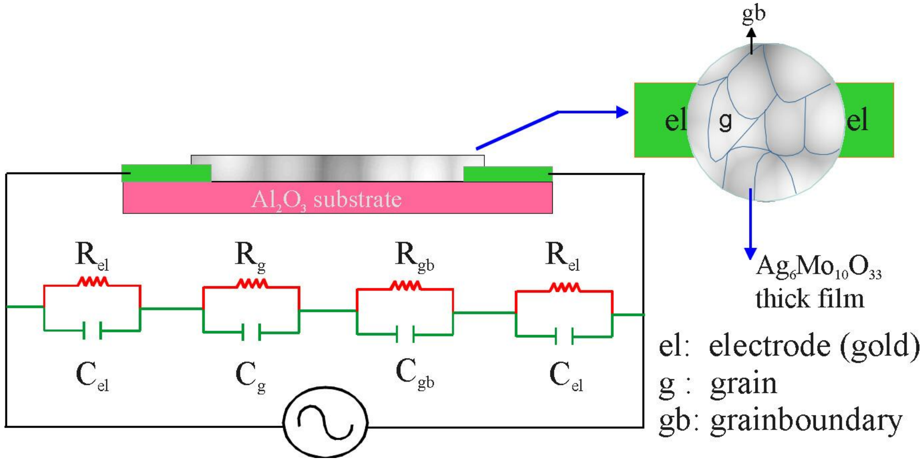

Fig. 6.19 Equivalent circuit proposed for the data obtained from AC impedance measurements of $Ag_6Mo_{10}O_{33}$ thick film

The resistance and capacitance of the thick film in clean air at each temperature for the mentioned temperatures were calculated using Z view® (version 2.70) program using the equivalent circuit and the results are given in Table 6.2. From the table, it is seen that the total resistance of thick film gradually decreases with increase in temperature. But, a gradual increase in the capacitance of the film with increase in temperature was observed. About 500 ppm of H_2, NH_3 and PG were injected independently at 423, 523, 573 and 623 K in to the thick film housed chamber. The film did not respond to any of these gases at 423 and 523 K. The film responded only to NH_3 when its temperature was 573 K or above.

Sunu et al measured the resistance of $Ag_6Mo_{10}O_{33}$ in clean air and air containing ammonia at 573 K [151]. The measurements were carried out by two probe DC technique. They observed the resistance of the film decreased on its exposure to air containing NH_3. When the film was re-exposed to clean air, the resistance traced back to its original value in clean air. They also identified the products of the reaction of $Ag_6Mo_{10}O_{33}$ with NH_3 in air at 573K using XRD as Ag, Mo_2N, MoO_2, and Mo_4O_{11}:

$$\begin{aligned} Ag_6Mo_{10}O_{33} + 12NH_3 \xrightarrow{573K} & \; 6Ag + 2Mo_2N + 2MoO_2 \\ & + Mo_4O_{11} + 18H_2O + 5N_2 \end{aligned} \tag{6.6}$$

On exposure of the products to clean air at the same temperature, the products reacted with oxygen in air to form $Ag_6Mo_{10}O_{33}$ again:

$$6Ag + 2Mo_2N + 2MoO_2 + Mo_4O_{11} \xrightarrow{air} Ag_6Mo_{10}O_{33} + N_2 \tag{6.7}$$

Figure 6.20a shows the impedance (Z' vs Z") plot of $Ag_6Mo_{10}O_{33}$ thick film flowing in clean air (50 ml/min.) at 573 K measured in the frequency range of 100 kHz to 10 Hz in the present work. The resistance (R) and capacitance (C) of the thick film at 573 K were calculated and found to be 1.94 MΩ and 0.24 nF respectively. The relaxation frequency measured from the impedance in clean air is 750 Hz.

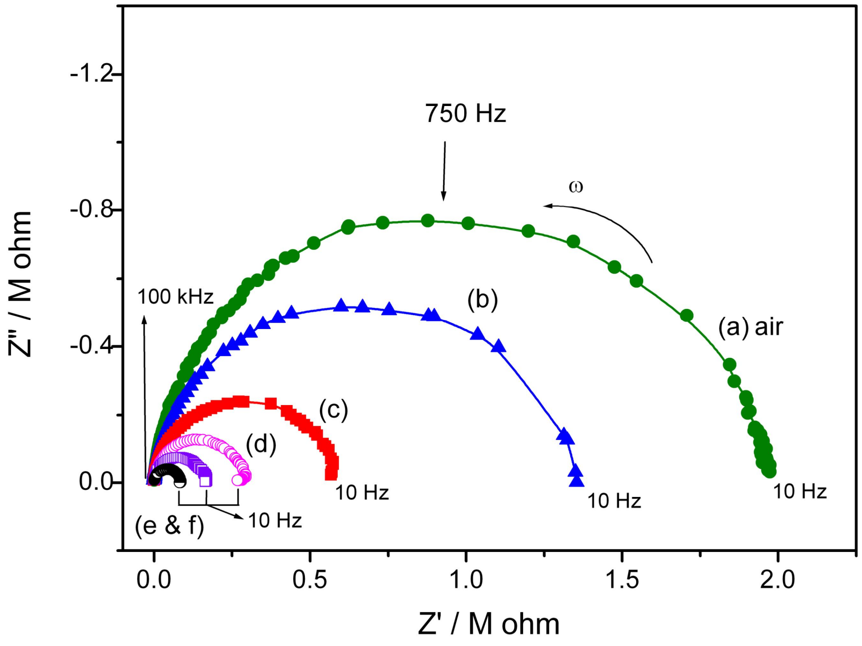

Fig. 6.20 Impedance pattern of $Ag_6Mo_{10}O_{33}$ thick film at 573 K a) air and (b – f) air containing 500 ppm NH_3, Frequency range: 100 kHz – 10 Hz. a – f : cycles

After completing the studies in clean air, air containing 500 ppm of NH_3 was introduced (50 ml/min.) into the chamber housing the thick film. Nyquist scanning was continued in a cyclic mode (Duration of sweep: 205 s). As shown in fig. 6.20b – f, a decrease in the diameter of the Nyquist plot was observed for each sweep in the presence of NH_3 when compared to that obtained in clean air. The R and C components of the film at 750, 263 and 10 Hz during the sweeps, i.e. sweep # 1 and 2 in clean air, sweeps # 3 to 16 in air containing 500 ppm of NH_3 and sweeps # 17 to

22 on re-exposure to clean air are given in Table. 6.3. As seen from the table, there was a gradual change in resistance and capacitance of the thick film after changing the ambient from air to air containing 500 ppm of NH_3. This is due to reaction of NH_3 with $Ag_6Mo_{10}O_{33}$ leading to formation of products (eqn. 6.6). After completion of the chemical interaction and attaining a dynamic equilibrium with the ambient, R and C components attain constant values, as seen from the Table. Because of the new phases appearing in the film, relaxation frequency (which was 750 Hz in clean air) also gets altered. Under the chosen constant experimental conditions, the relaxation frequency was found to be 55.08 kHz [sweep # 14 – 16]). Clean air was introduced into the chamber.

Figure 6.21a – e [sweeps # 18 – 22] shows the Nyquist plot of the thick film after its interaction with air containing 500 ppm of NH_3 followed by reexposure to clean air. The introduction of clean air into the thick film housed chamber leads to the reaction of the products with oxygen to form $Ag_6Mo_{10}O_{33}$ as shown in eqn. 6.7. Figure 6.21f shows the Nyquist plot of thick film before its interaction with 500 ppm of NH_3 in air. As seen from the figure, the diameter of the semi circle increases with each sweep in the presence of clean air. The R and C components vary continuously with time and finally attain constant values. The Nyquist plots of fig. 6.21e and f almost coincide with each other indicating the products formed during the interaction with NH_3 react back to form $Ag_6Mo_{10}O_3$. This is also evident from the relaxation frequency of the compound calculated for the sweep #1 and 22 in Table. 6.3.

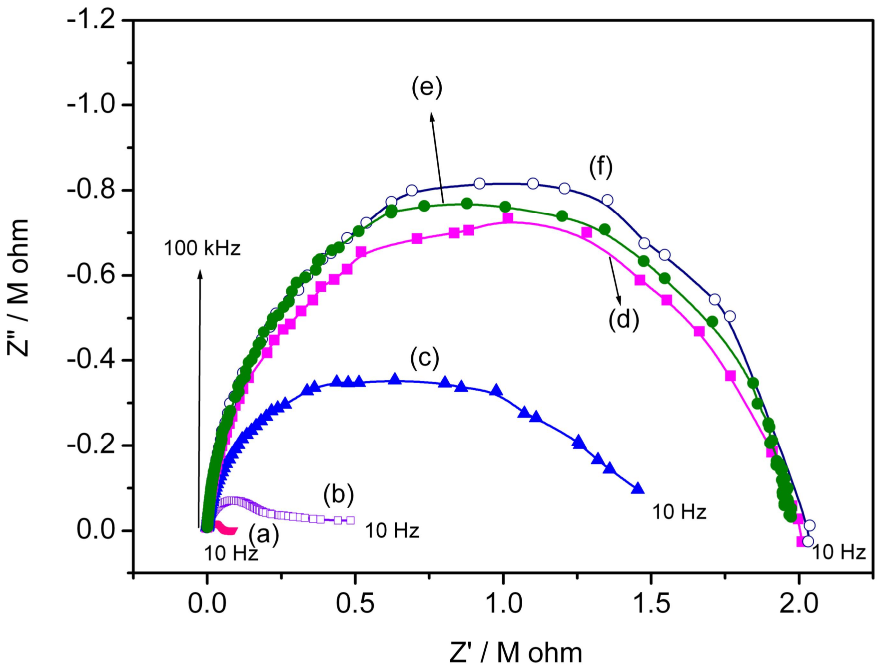

Fig. 6.21 Impedance pattern of $Ag_6Mo_{10}O_{33}$ thick film (a – e) flushing with air after NH_3 exposure f) before exposed to NH_3 in air. , Frequency range: 100 kHz – 10 Hz. a – f : cycles

As seen from fig.6.20, there was a gradual change in R & C component of the thick film in the presence of air containing 500 ppm of NH_3 when compared with impedance of the film in air as a function of frequency. R, C and frequency of all sweeps are found to change during the reaction. To get useful information from $Ag_6Mo_{10}O_{33}$ thick film during gas interaction studies as a sensor point of view, experiments are conducted to observe the change in R and C components of the compound at fixed frequency as a function of time.

To examine the feasibility of employing $Ag_6Mo_{10}O_{33}$ thick film with R and C being measured by AC technique, the frequency at which these measurements are to be made need to be fixed. This frequency should preferably fall in the range where the measured R and C values are nearly frequency independent. Figure 6.22a and Fig. 6.22b show the plot of resistance and capacitance of $Ag_6Mo_{10}O_{33}$ thick film in air as a function of frequency at 573 K (log-log plot of R & C vs frequency). Data for plotting fig. 6.20a was used for this purpose. The resistance and capacitance of $Ag_6Mo_{10}O_{33}$ thick film were deduced using eqn. 6.8 and 6.9.

$$R = \frac{(Z'^2 + Z''^2)}{Z'} \tag{6.8}$$

$$C = \frac{-Z''}{\omega(Z'^2 + Z''^2)} \tag{6.9}$$

As seen from the Fig. 6.22a, film resistance (R) is frequency independent between the frequency region of 800 Hz and 10 Hz in air. Figure 6.22b shows the capacitance (C) of the thick film in air as a function of frequency and it is nearly constant in the frequency range of 550 Hz to 100 kHz i.e. both the measured resistance and capacitance are nearly frequency independent between 550 and 800 Hz. The relaxation frequency of $Ag_6Mo_{10}O_{33}$ thick film (750 Hz) falls in this region (fig. 6.20a). A frequency of 750 Hz was chosen for carrying out further studies.

Table 6.3

R and C components of $Ag_6Mo_{10}O_{33}$ thick film at different frequencies as a function of scanning cycle

No. of cycle (continuous)	Progress of the reaction (s)	ambient	Frequency at 750 Hz		Frequency 263 Hz		Frequency at 10 Hz		Relaxation frequency kHz
			R (kΩ)	Capacitance (nF)	R (kΩ)	Capacitance (nF)	R (kΩ)	Capacitance (nF)	
Impedance in the presence of clean air (sweep 1 & 2)									
1	205	Clean air	964	0.11	1470	0.15	1940	0.24	0.75
2	430		794	0.14	1470	0.16	2151	0.25	0.75
Impedance in the presence of air containing 500 ppm of NH_3 (sweep 3 - 16)									
3	655	Air containing NH_3 (500 ppm)	754	0.13	1100	0.19	1428	0.53	
4	880		468	0.16	541	0.17	542	1.33	
5	1105		263	0.21	284	0.29	267	1.65	
6	1330		162	0.21	169	0.32	163	2.41	
7	1555		115	0.22	116	0.34	111	2.49	
8	1780		84	0.23	85	0.32	81.6	3.97	
9	2005		57	0.25	58	0.36	55.1	4.31	
10	2230		42	0.26	43	0.37	40.8	4.50	
11	2455		36	0.14	36	0.26	35.3	4.48	
12	2680		31	0.14	30	0.26	28.2	4.51	
13	2905		28	0.14	28	0.25	26.9	4.54	
14	3130		26	0.13	26	0.21	24.8	4.70	55.08
15	3335		24	0.13	24	0.20	23.1	4.69	55.08
16	3580		21	0.12	22	0.18	21.2	4.71	55.08
Impedance in the presence of clean air to driven out unreacted ammonia and reaction with oxygen in air to form $Ag_6Mo_{10}O_{33}$									
17	3805	Clean air	56	0.21	63	0.33	90.6	4.03	
18	4030		211	0.19	258	0.32	484.3	1.63	
19	4255		611	0.15	862	0.22	1474	1.10	
20	4480		834	0.13	1350	0.16	2016	0.29	
21	4705		920	0.12	1540	0.14	2125	0.38	0.73
22	4930		924	0.12	1640	0.12	2015	0.23	0.73

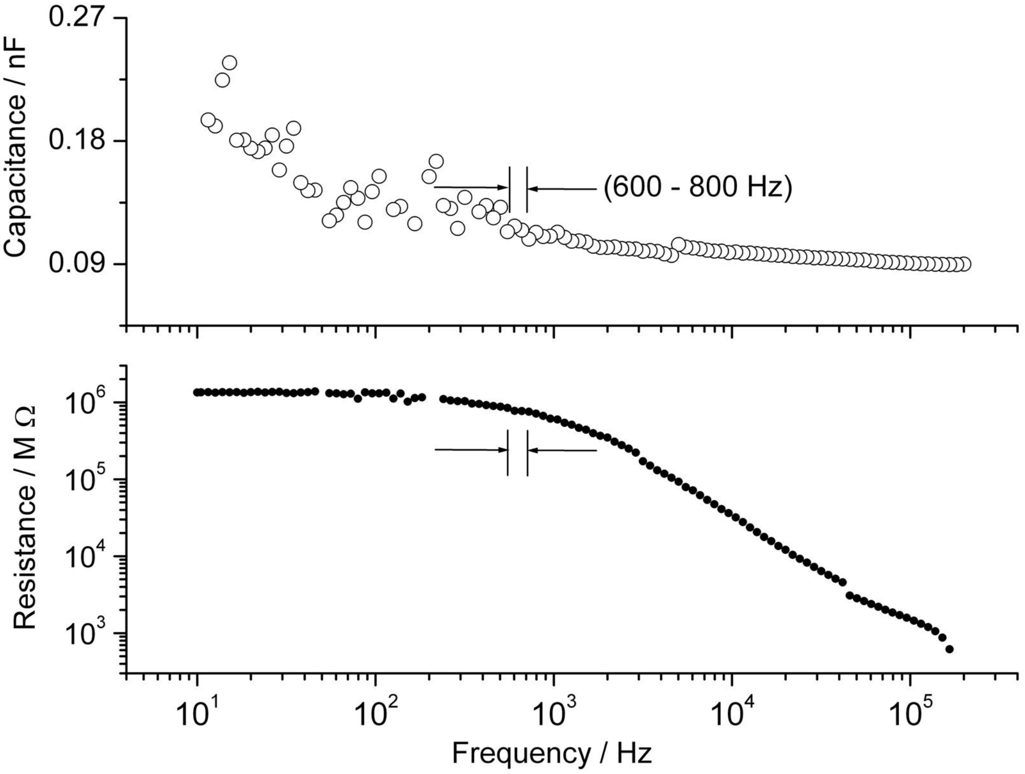

Fig. 6.22 log – log plot of a) resistance and b) capacitance as a function of frequency of $Ag_6Mo_{10}O_{33}$ thick film in air at 573 K

Prior to the studies on gas interaction with $Ag_6Mo_{10}O_{33}$ thick film at 750 Hz, baseline stability of the thick film in clean air was checked. Figure 6.23 shows the resistance and capacitance of $Ag_6Mo_{10}O_{33}$ thick film measured at 750 Hz as a function of time at 573 K. No drift in the resistance and capacitance of the film is observed for a period of 100 h. Hence, measuring R and C components of the film by AC technique would be suitable for use in gas sensor measurements.

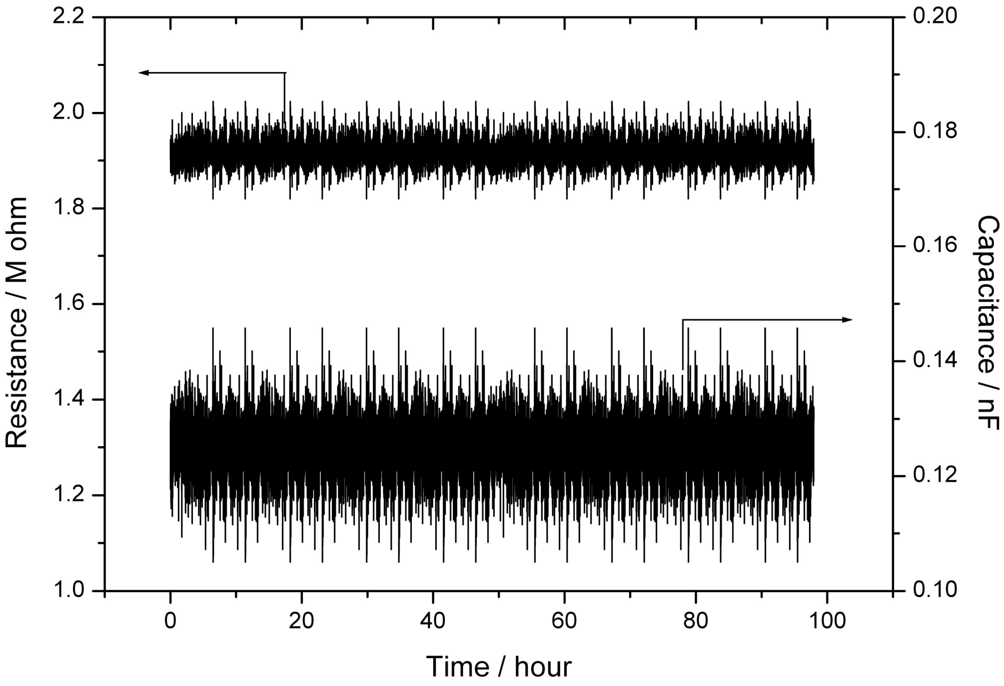

Fig. 6.23 Resistance and capacitance as a function of time plot for $Ag_6Mo_{10}O_{33}$ thick film at 573 K

Figures 6.24a to d show the change in resistance of thick film in the presence of air containing 100, 130, 170 and 500 ppm of NH_3 at 573 K. Figure 6.25a to d shows the changes in capacitance under the same conditions. The resistance of the film decreased in the presence of ammonia and attained a stable value. Similarly the capacitance of the thick film increased in the presence of ammonia. After the resistance and capacitance of the film attained stable values, clean air was introduced into thick film housed chamber. The values of resistance and capacitance retrace back to their original values in clean air. The response and retrace times of the film was calculated from these data and are shown in Table. 6.4.

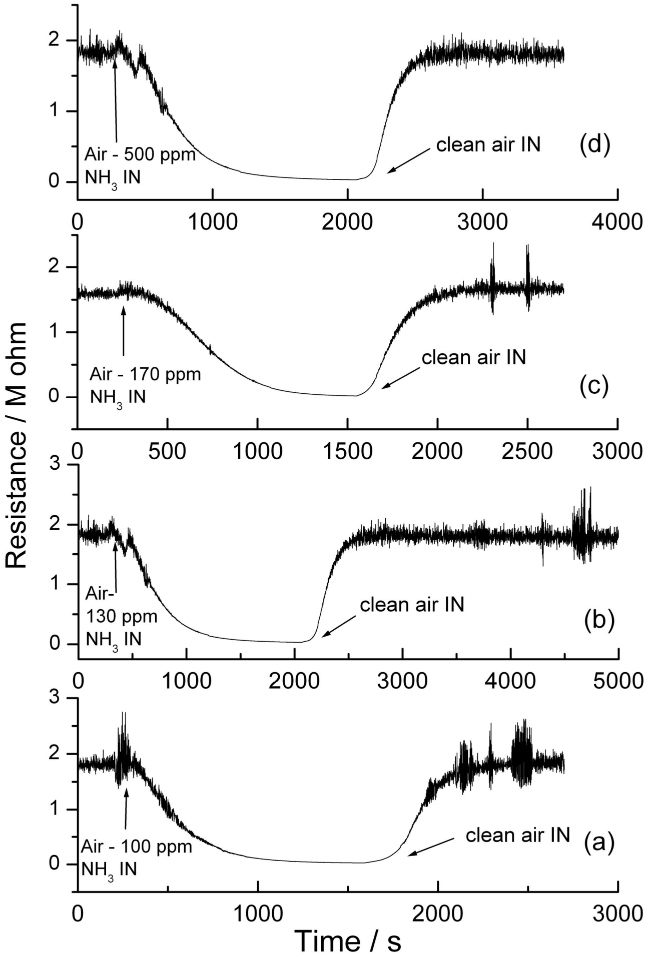

Fig. 6.24 Plot showing the change in resistance of $Ag_6Mo_{10}O_{33}$ thick film at 573 K on exposure to air containing a) 100 ppm NH_3 b) 130 ppm NH_3 c) 170 ppm NH_3 and d) 500 ppm NH_3

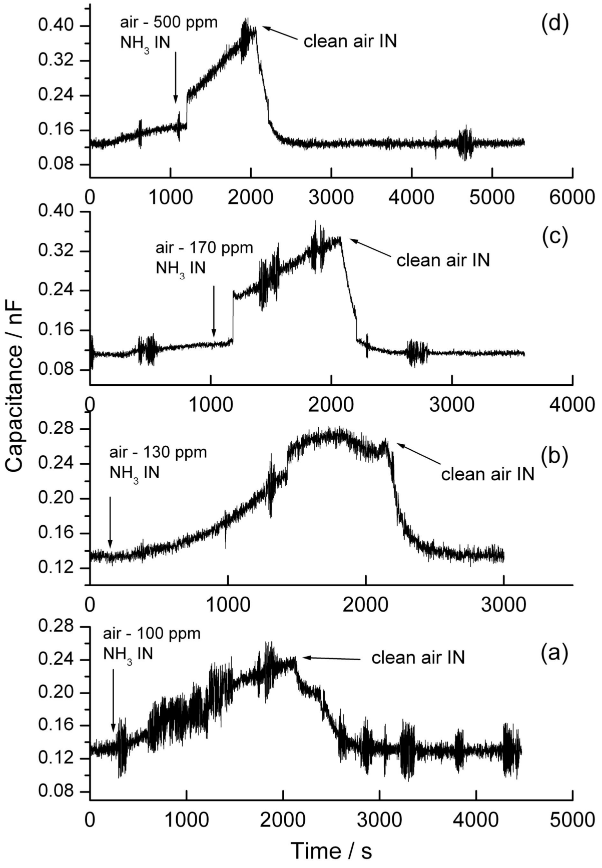

Fig. 6.25 Plot showing the change in capacitance of $Ag_6Mo_{10}O_{33}$ thick film at 573 K on exposure to air containing a) 100 ppm NH_3 b) 130 ppm NH_3 c) 170 ppm NH_3 and d) 500 ppm NH_3

Table: 6.4

Response and recovery time of $Ag_6Mo_{10}O_{33}$ thick film
in the presence of NH_3 at 573 K

Concentration of NH_3 (ppm)	Resistance		Capacitance	
	Response time (min.)	Recovery time (min.)	Response time (min.)	Recovery time (min.)
100	8	8	17	6
130	11	6	18	5
170	12	6.5	11.5	5.0
500	11	10	12.5	6

The response and recovery time for the resistance change shown by the thick film towards ammonia are 12 and 10 min. respectively. The response time for the capacitance based measurements is found higher at 100 and 130 ppm of NH_3.

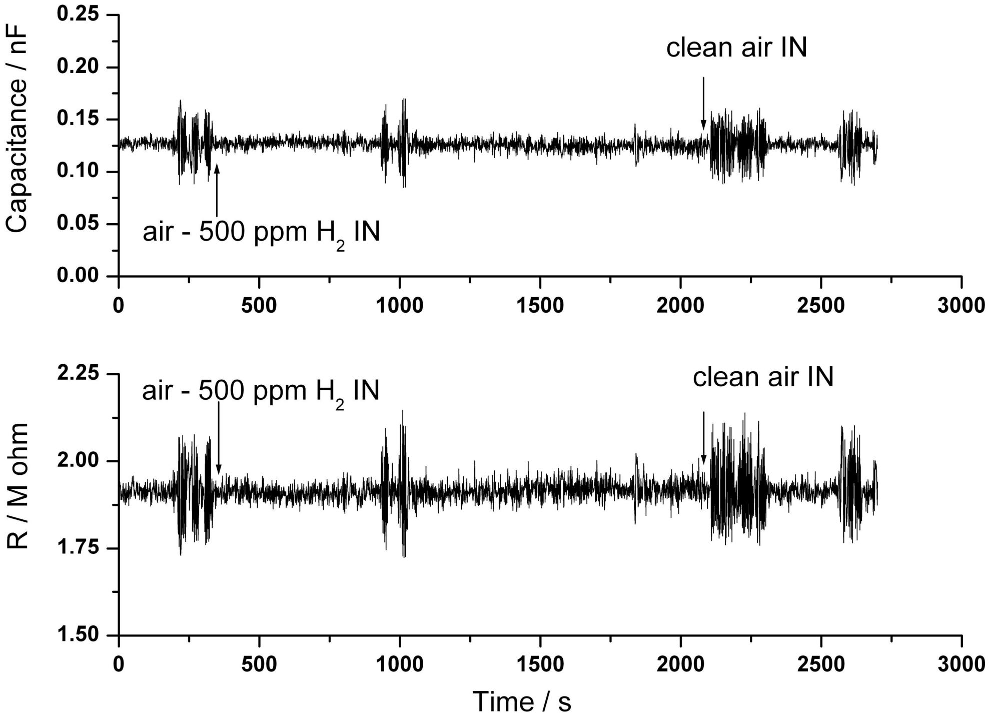

Fig. 6.26 Typical interaction behavior of $Ag_6Mo_{10}O_{33}$ thick film towards air containing 500 ppm of H_2 at 573 K (750 Hz)

The cross sensitivity of the $Ag_6Mo_{10}O_{33}$ thick film towards H_2 was studied at 750 Hz at 573 K. Air containing 500 ppm of H_2 was used as sample gas. Figure 6.26a and b show the resistance and capacitance of the thick film when the sample gas was flowing into the film housed chamber. As seen, the sensor did not respond. Similar experiments were carried out with air containing 500 ppm of PG. The results show that the film has not responded to PG. These studies clearly indicate that the film is selective towards ammonia. However, the response and recovery times were very high at 573 K.

To examine the feasibility of decreasing the response and recovery time by increasing the thick film temperature, the studies on gas sensing were carried out at 623 K. Since the relaxation frequency of $Ag_6Mo_{10}O_{33}$ at 623 K was 14 kHz, it was used for measuring resistance and capacitance of the thick film. The change in capacitance and resistance of $Ag_6Mo_{10}O_{33}$ thick film at 623 K on exposure to air containing 500 ppm of NH_3 at 14 kHz and are shown in fig. 6.27.

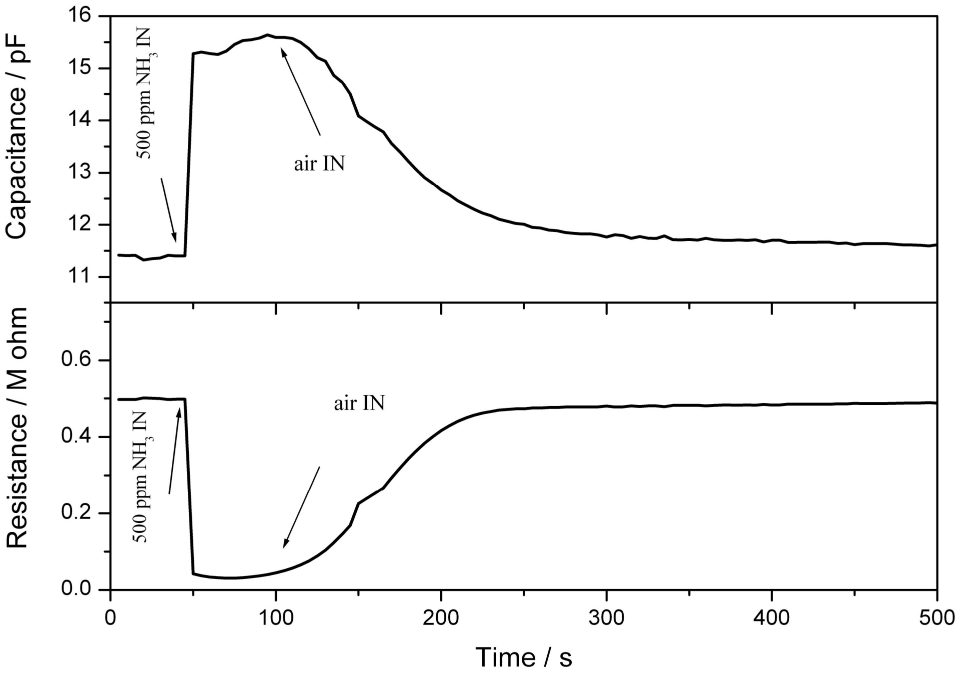

Fig. 6.27 Typical change in the resistance and capacitance plot of $Ag_6Mo_{10}O_{33}$ thick film in air containing 500 ppm of NH_3 at 14 kHz at 623 K

The response and recovery time for the change in resistance and the capacitance of the film towards NH_3 was calculated. The response and recovery time for the change in capacitance of $Ag_6Mo_{10}O_{33}$ is around 1 and 3 min and similarly for the change in resistance was found to be 0.5 and 3 min. respectively. The cross sensitivity of $Ag_6Mo_{10}O_{33}$ thick film towards air containing 500 ppm of H_2 and PG was also tested at 14 kHz at 623 K. Similar experiments were carried out for studying the cross sensitivity towards 500 ppm of PG and 500 ppm of H_2. The thick film did not respond to any of these gases. The typical plot showing the response of $Ag_6Mo_{10}O_{33}$ thick film towards 500 ppm of H_2, NH_3 and PG at 14 kHz is shown in fig. 6.28.

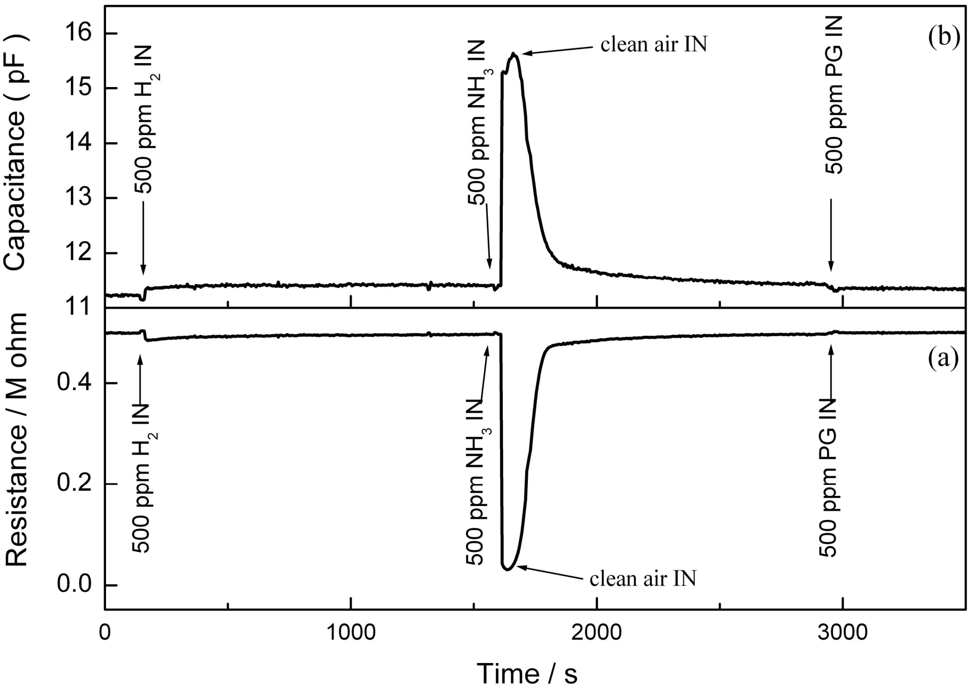

Fig. 6.28 Typical change in a) resistance and b) capacitance of $Ag_6Mo_{10}O_{33}$ thick film as a function of time at 14 kHz in air containing 500 ppm of H_2, NH_3 and PG at 623 K.

The present studies have shown that $Ag_6Mo_{10}O_{33}$ showed good selectivity towards NH_3 by AC technique. The probable reason for such behavior shown by thick film will be discussed here.

Silver decamolybdate ($Ag_6Mo_{10}O_{33}$), belongs to triclinic asymmetric system having the space group of $P\bar{1}(2)$, a = 7.59 Å, b = 8.31 Å, c = 11.42 Å, $\alpha = 82.6^o$, $\beta = 102.9\ ^o$, $\gamma = 106.4^o$. Generally an asymmetric compound would possess permanent dipole moment even in the absence of an electric field. It is a mixed conductor possessing high total conductivity (σ_{total} = 59.5 μS / cm) at 577 K [151]. It has high transport number for Ag^+ ions and Wagner polarization experiments showed t_{Ag^+} at

486 K it is 0.81 and at 550 K it is 0.94. Because of these high σ_{Ag^+} and t_{Ag^+} values, $Ag_6Mo_{10}O_{33}$ would undergo cyclic orientation alignment with respect to applied frequency which is termed as relaxation process. The relaxation effect is usually associated with orientation polarization and it is temperature dependent as shown in eqn. 6.10 [88]. Here, 'α_o' is the orientation polarizability and 'μ' is the dipole moment. The polarizability decreases with increase in temperature.

$$\alpha_o = \frac{\mu^2}{3kT} \tag{6.10}$$

Ammonia is a polar gas ($\alpha = 2.81 \times 10^{-24}$ cm^3) with a permanent dipole moment ($\mu = 1.47$ Debye) and it has a lone pair of electrons. When $Ag_6Mo_{10}O_{33}$ is electrically excited at a fixed frequency (relaxation frequency) to ammonia, the molecules of ammonia first get adsorbed on the surface followed by an orientation of the adsorbed molecules with the applied field. During this phenomenon, processes such as chemisorption of NH_3 molecule and its reaction on the surface (silver ammonia complexes are well known). Owing to chemical reaction at high temperatures, products such as Ag, MoO_2, γMo_2N, Mo_4O_{11}, N_2 and H_2O are formed on the surface. Among these products, Ag, MoO_2 and γ Mo_2N are highly conducting in nature and each has characteristic dielectric constant.

The relation between the dielectric constant (ε_s) and polarizability (α) was derived by Mossoti and Clausius, is shown in eqn. 6.11 Where 'M', 'ρ', 'ϵ_o', 'ϵ_s', 'N_A', 'K_B' and 'T' are molecular weight, density, sample dielectric constant, dielectric constant in vacuum, Avogadro number, Boltzmann constant and temperature (K). In the present case, the values of all these parameters are net value due to the type and quantity of various phases formed by the reaction.

$$\frac{\varepsilon_s - 1}{\varepsilon_s + 2}\frac{M}{\rho} = \frac{1}{3}\frac{N_A}{\varepsilon_O}(\alpha + \frac{\mu^2}{3k_B T}) \tag{6.11}$$

The change in polarizability and dipole moment of a material will reflect in change in its dielectric constant ϵ_s which could alter capacitance [60]. The change capacitance of the material can be deduced from its impedance measured by AC technique.

The relationship of dielectric constant and capacitance is shown in eqn. 6.12. Here, ‘C’ is material capacitance and ‘C_O’ capacitance in vacuum.

$$\varepsilon_s = \frac{C}{C_o} \tag{6.12}$$

As seen in the results and discussion about the gas interaction studies of $Ag_6Mo_{10}O_{33}$ thick film towards H_2, NH_3 and PG (PG is a mixture of propane, butane and isobutane) by AC studies at a fixed frequency, compound showed a selective response towards NH_3 when compared with H_2 and PG. The selective response is due to significant difference in the values of dipole moment and polarizability values of the gases as shown in Table 6.5 [88].

Table: 6.5

Gas phase dipole moments and polarizability of polar and non-polar gases at atmospheric pressure [88]

Gas	Dipole moment (μ) Debye	Polarizability (α) 10^{24} α (cm^3)
H_2	0	0.80
C_3H_8	0.084	6.36
C_4H_{10}	0.132	8.20
NH_3	1.47	2.81

The capacitance change shown by $Ag_6Mo_{10}O_{33}$ in the presence of air containing ammonia is due to ammonia possess significant difference in dipole moment when compared to PG and H_2. Snow et al. also reported their work on the interaction behavior of vapors of dimethylmethylphosphonate (DMMP, μ = 3.62 Debye) with single walled carbon nano-tubes [160, 161]. Authors observed large change in the capacitance of the carbon nano tubes ($\Delta C/C$) during its interaction with DMMP when compared with acetone. Such an enhanced change in capacitance shown by the carbon nano tubes are due to the difference in dipole moment of DMMP (μ = 3.62) and acetone (μ = 2.88). Fan-Li Meng also observed change in the capacitance of single wall carbon nano tubes during their interaction with ammonia, formaldehyde (μ = 2.33 Debye) and toluene (μ = 0.36 Debye) [162]. The carbon nano tubes showed enhanced sensitivity ($\Delta C/C$) towards formaldehyde compared with ammonia and toluene. The larger the dipole moment possessed by the analyte, better the sensitivity exhibited by the material.

6.4 Conclusions

XRD patterns of $Ag_6Mo_{10-X}W_XO_{33}$ indicate that WO_3 is present as solid solution in $Ag_6Mo_{10}O_{33}$ up to 0.5. $Ag_6Mo_{9.75}W_{0.25}O_{33}$ and $Ag_6Mo_{9.5}W_{0.5}O_{33}$ possess higher silver ion transport number and electrical conductivity than those of $Ag_6Mo_{10}O_{33}$. Like $Ag_6Mo_{10}O_{33}$, $Ag_6Mo_{9.75}W_{0.25}O_{33}$ and $Ag_6Mo_{9.5}W_{0.5}O_{33}$ also exhibited baseline resistance drift (DC) as a function of time and hence they would not meet the criteria required for a sensor.

The thick film of $Ag_6Mo_{10}O_{33}$ showed stable baseline resistance as a function of time by AC measurement. The film showed selective response towards NH_3 when compared with H_2 and PG at 573 K. The nature of polarizing property of NH_3 and its reaction probably facilitated the selectivity. The chemical reaction of NH_3 with $Ag_6Mo_{10}O_{33}$, leading to various products formed during the reaction. The reaction leads to change in dielectric constant of $Ag_6Mo_{10}O_{33}$ which reflected in change in the capacitance of the material. Even though the compound exhibited good selectivity towards NH_3 but it showed large response and recovery time with NH_3 at 573 K. There was a marginal improvement in response and recovery time by the film towards NH_3 when the interaction studies carried out 623 K.

CHAPTER 7

Summary, conclusions and scope for future studies

In industries toxic and flammable gases are being handled in very large volumes. There are many polluting species that have drawn special attention. Among the species, the most important are, oxides of nitrogen, CO, Cl_2, H_2S, SO_2, NH_3, CH_4, PG, H_2, etc. The release of such hazardous and flammable gases creates a potential threat to industries, its employees and the environment. In recent years, a great deal of research effort has been directed towards the development of gas sensing devices for off-line and field applications. Gas sensors based on semi-conducting materials have gained an increasing interest due to their advantageous characteristics than traditional systems (based on optical and spectroscopic analysis), which are more cumbersome, expensive and required a careful maintenance by qualified personnel. Physics, chemistry and technology of sensor materials require a better understanding of their bulk and surface properties towards the gases. The criteria required for a material to be a sensor, are high sensitivity and selectivity for the analyte. The sensing compound should show very quick response and reasonable recovery times. It should not undergo any environmental degradation during its usage. But most of the sensing materials lack in selectivity. Research efforts have been initiated to improve the performance of sensing materials by studying their surface chemistry, morphology and microstructure of the materials. The novel synthetic methods have now emerged for the synthesis of nonmaterial for use and handle them as sensing materials. Understanding the reaction mechanism of the sensing materials towards the oxidizing and reducing gases is necessary. The main aim of this thesis is to elucidate some experimental aspects related to the sensing processes of metal oxide semiconductors, synthesis of alloys at low temperatures, and their interaction properties towards H_2,

NH_3, NO_X and PG. The major experimental finding obtained during the studies is described in detail in the chapters 3 – 6 of the thesis and are summarized below.

7.1 Interaction mechanism of In_2O_3 thin film towards NO_X – experimental evidence

The characterization of In_2O_3 thin film using van der Pauw and Hall coefficient studies during NO_X interaction helped in proving the direct evidence of change in carrier concentration of In_2O_3 thin film due to adsorption of NO_X. Similarly, the presence of different N_YO_Z species at various temperatures on the surface of In_2O_3 characterized using laser Raman. In_2O_3 thin film showed good selectivity towards NO_X in the presence of other gases like H_2 and PG. The increase in the resistance of thin film in the presence of NO_X was the clear indication that it was occurring due to abstraction of unoccupied charges by electron withdrawing nature of NO_X on the surface of In_2O_3. Similarly, the increase in the capacitance of In_2O_3 thin film was due to change in the ratio of carrier concentration and barrier height of In_2O_3 was elucidated from the AC measurements.

7.2. Experimental evidence of distinguishing oxidizing and reducing gases using semi-conducting materials

$CuInO_2$ is a meta-stable compound. Such meta-stable compound was deposited as thin film facilitated by PLD technique. $CuInO_2$ thin film a p-type semi-conducting material, showed an increase in resistance during the interaction with H_2 (reducing gas). At the same the thin film exhibited a decrease in resistance in the presence of NO_X (oxidizing gas). XPS results indicated the presence of small fraction of Cu^{2+} in $CuInO_2$ which supports its p-type semiconducting behavior. On the other hand $Cu_2In_2O_5$ thin film (n-type behavior like SnO_2, In_2O_3, etc.), exhibited a just an opposite response trend towards the oxidizing and reducing gases when compared with $CuInO_2$. The gas interaction studies shown by these two different semi-conducting materials towards these oxidizing and reducing gases are the experimental evidences to distinguish these gases.

7.3 A novel soft-chemical approach for the synthesis of palladium alloys and their hydrogen sensing behavior

The present studies showed the possibility of synthesizing palladium and its alloys at 300 K using low temperature chemical reduction technique. X – ray crystallographic studies provided the evidence for the substitution of nickel and cobalt in palladium. The sensitivity towards hydrogen increases with increase in the nickel content in the alloy, when compared with pure palladium film. On the other hand, incorporation of cobalt along with nickel in $Pd_{0.91}Ni_{0.04}Co_{0.05}$ decreased the sensitivity towards hydrogen when compared with nickel substituted alloys. Palladium and alloys of Pd showed linear increase in sensitivity between the concentration of 2000 and 20000 ppm of argon containing hydrogen at 300 K.

7.4 Electrical properties of $Ag_6Mo_{10-X}W_XO_{33}$ and sensing behavior of $Ag_6Mo_{10}O_{33}$ thick film towards NH_3

Crystallographic elucidations of $Ag_6Mo_{10-X}W_XO_{33}$ indicated that W was present as solid solution in $Ag_6Mo_{10}O_{33}$ up to x = 0.5. At higher concentrations of WO_3, $Ag_2Mo_2O_7$ and WO_3 precipitate out. The initial investigations of electrical properties of tungsten substitution in $Ag_6Mo_{10}O_{33}$ indicated an enhancement in the silver ion conduction on comparing with $Ag_6Mo_{10}O_{33}$.

$Ag_6Mo_{10}O_{33}$ thick film showed selectivity towards NH_3 while conducting experiments using AC impedance technique. Polarizing nature of NH_3 and its chemical reaction with $Ag_6Mo_{10}O_{33}$ altered the effective dielectric property of $Ag_6Mo_{10}O_{33}$, products and unreacted ammonia leading to selective sensing of NH_3.

7.5. Scope for future studies

The interaction studies and reaction mechanism of semi-conducting metal oxides and metal/alloys towards gases is a vital research area and the scope for further research in this area is enormous. The stability of the sensing materials in different harsh environments is also one of the challenging research avenues. Some of the work, which will be interesting, can be continued in the future are listed below.

1. The effect of conductivity, charge carrier and charge mobility of In_2O_3 in argon and argon containing different concentrations of NO_X is expected provides valuable information to compare with the effect of In_2O_3 in air and air containing NO_X. Apart from NO_X interaction with In_2O_3, the interaction behavior of the In_2O_3 can be carried out with H_2 or NH_3 to understand the effect on charge carrier concentration and mobility at different temperatures in air / argon ambient.
2. The effect of carrier concentrations and charge carrier mobility of $Cu_2In_2O_5$ and $CuInO_2$ during the interaction with oxidizing and reducing

gases coupled with speciation studies will help in understanding the sensing mechanism.

3. Studies on the interaction behavior of Pd and its alloys will be useful for identifying the compositions suitable for sensing hydrogen between the concentrations of 20000 and 40000 ppm in argon/air streams. Using low temperature novel reduction technique, synthesis of palladium alloys with different concentrations of cobalt and studies on interaction of films of these alloys with hydrogen is needed.

4. Initial investigations of electrical properties of tungsten substitution in $Ag_6Mo_{10}O_{33}$ indicated an enhancement in the silver ion conduction on comparing with $Ag_6Mo_{10}O_{33}$. The tungsten substituted compounds in $Ag_6Mo_{10}O_{33}$ gives some indication about the strong silver ion conductors at lower temperatures. These results can be helpful to handle such compounds as a cationic conductor at low temperature. Studies on $Ag_6Mo_{10-X}W_XO_{33}$ compositions as catalysts for decomposition of ammonia will be useful. Experiments to understand the role played by W in enhancing silver ion conduction will help engineering / tailoring this class of compounds for both gas sensing and catalysis applications. $Ag_6Mo_{10}O_{33}$ thick film has to be tested to low concentrations of NH_3 (< 100 ppm) at 623 K in order to evaluate its detection of NH_3 below the TLV.

References

[1] C. Baird and M. Cann, Environmental Chemistry, 4th edition, Clancy Marshall, USA (2008)

[2] S.C. Bhatia, Text Book of Air Pollution and its Control, Atlantic publishers, India (2007)

[3] P. A. Carson and C.J. Mumford, Hazardous Chemicals Handbook Butterworth – Heinmann Ltd, Linacre House, Jordon Hill, Oxford (1994)

[4] D.J. Davis and G.T. Christianson, Firefigher's Hazardous Materials Reference Book, Van Nostrans Reinhold, New York (1991)

[5] S.A. Kharitnov, B.J.O. Connor, D. J. Evanas and P.J. Barnes, American J. Resp. Crit. Care Med, 151(1995) 1894

[6] J. G. Mohler and C. R. Collier, Handbook of Hazardous Materials, Academic Press, USA (1993)

[7] W. Gopel, J. Hesse and J.N. Zemel, Sensors, Chemical and Biochemical Sensors Part I, Vol.2, VCH publishers, New York (1991)

[8] W. Gopel, J. Hesse and J.N. Zemel, Sensors, Chemical and Biochemical Sensors Part II, Vol.3, VCH publishers, New York (1991)

[9] K. Korotcenkov, Hand book of gas sensing materials, Vol I, Springer publications, New York, (2013)

[10] P.D.C. King, T.D. Veal, F. Fuchs, Ch.Y. Wang, D.J. Payne, A. Bourlange, H. Zhang, G.R. Bell, V. Cimalla, O. Ambacher, R.G. Egdell, F. Bechstedt and C.F. McConville, Physical Review B 79 (2009) 205211

[11] T. Seiyama, A. Kato, K. Fujiishi, and M. Nagatani, Anal. Chem. 34, (1962) 1502

[12] N. Yamazoe and N. Miura in Chemical Sensor Technology, Vol 4, Tokyo (1992)

[13] M. Iwamoto in Chemical Sensor Technology, Vol. 4, Tokyo (1992)

[14] N. Barsan and Udo Weimar, Jrl. of Electroceramics, 7, (2001) 143

[15] M.A. Carpenter, S. Mathur and A. Kolmakov, Metal oxide Nanomaterials for Chemical Sensors, Springer, New York, 2013

[16] S. Andersson and A.D. Wadsley, Nature, 211 (1966) 581

[17] L. A. Bursill and D. J. Smith, Nature, 309 (1984) 319

[18] R. Mars and D.W. van Krevelen, Chem. Eng. Sci. 3(1954) 41

[19] J. V. Bursil, J. De Physique, 35(1974) 7

[20] R. L. Smith and G.S. Rohrer, J. Solid State Chemistry, 124 (1996) 104

[21] D.O. Scanlon, G.W. Watson, D.J. Payne, G.R. Atkinson, R.G. Egdell and D.S.L. Law, J. Phys. Chem. C 114 (2010) 4636

[22] P.L. Gai and E.D. Boyes, Electron Microscopy in Hetergenous Catalysis, Institute of Physics Publishing, Bristol, (2003)

[23] J. Haber, Solid State Chemistry in Catalysis, American Chemical Society, Washington D.C. (1985) 1

[24] W.E. Farneth, R.H. Staley and A.W. Sleight, J. Am. Chem. Soc. 108 (1986) 2327

[25] A. Bielanski and J. Haber, Catal. Rev-Sci. Eng. 19 (1979) 1

[26] T. Hubert, L.B. Brett, G. Black and U. Banach, Sensors and Actuators B 157 (2011) 329

[27] R.C. Hughes and W. K. Schubert, J. Appl. Physics, 71 (1992) 542

[28] F.A. Lewis, The palladium hydrogen system, Academic press, New York, (1967) 65

[29] M. Wang and Y. Feng, Sensors and Actuators B 123 (2007) 101

[30] K. Christmann, Surface Science Reports 9 (1988) 1

[31] Semiconductor Gas Sensors, R. Jaaniso & O.K. Tan, Woodhead Publishing, London, 2013

[32] A. Rothschild and Y. Komem, Jrl. of Applied Physics, 95 (2004) 6374

[33] S. Yamauchi, Chemical Sensor Technology, Vol.4, Elsevier, 1992

[34] G. Eranna, Metal oxide Nanostructures as Gas Sensing Devices, CRC Press, London, 2012

[35] D.E. Williams, J. Chem. Soc., Faraday Trans. I, 83 (1987) 323

[36] A. R. West, Solid State Chemistry and its Applications, John Wiley & Sons, New York (1985) 5

[37] E. L. Holt, Nature, 203(1964) 857

[38] L. Q. Ye, Z. P. Li, H. Y.Qin, J. K. Zhu, B. H. Liu, J.of Power Sources, 196 (2011) 956

[39] S. H. Wu and D. H. Chen, J. of Colloid and Interface Science, 259 (2003) 282

[40] G. N. Glavee, K. J. Klabunde, C.M. Sorensen & G. C. Hadjapnayis, Langmuir, 8 (1992) 771

[41] Y. Chen, K. Y. Liew and J. Li, Applied Surface Science, 255 (2009) 4039

[42] L.V. Azaroff, Elements of X – ray crystallography, McGraw Hill, New York (1968)

[43] B. D. Cullity, Elements of X – ray diffraction, Addison – Wesley Publishing Co., Reading, Massachusetts (1956)

[44] M. Bouroushian and T. Kosanovic, Crystal structure theory and applications, 1 (2012) 35

[45] W.M. Wendlandt, Thermal Methods of Analysis, John Wiley & Sons, New York (1974)

[46] B.B. Chrisey and G. K. Hubler, Pulsed Laser Deposition of thin film, John Wiley, New York (1995)

[47] Hubler, G. K. MRS Bulletin, 17 (1992) 26

[48] J. Cheung, J. Horwitz, MRS Bulletin, 17 (1992) 30

[49] R.J.H. Clark and R.E. Hester, Advances in infrared and Raman Spectroscopy (Vol.1) Heyden publication, London (1975)

[50] B. Bhushan, H. Fuchs and S. Hosaka (Ed.), Applied scanning probe methods, Springer Verlag Publication, Berlin (2004)

[51] D. Briggs and M.P. Seah, Practical Surface Analysis by Auger and X – ray photelectron Spectroscopy, John Wiley and Sons, New York (1990)

[52] J.F. Moulder, W.F. Stickle, P.E. Sobol, K.D. Bomben and J. Chastain, in

Handbook of X – ray Photoelectron spectroscopy, J. Chastain, R.C. Kind Jr. ULVAC – PHI Inc., Chigasaki, Japan (1995)

[53] D.E. Newbury, D.C. Joy, P. Echlen, C.E. Fiori and J.I. Goldstein, Advanced Scanning Electron Microscopy and X – ray microanalysis, Plenum Press, New York (1986)

[54] H.E. Exner in: K. Mills, J.R. Davis and D. A. Dieterich (Eds) Metallography and Microstructure, ASM Handbook Vol. 9, International Soc. ASM., Material park, USA (1998)

[55] D. K. Schroder, Semiconductor material and device characterization, Wiley Interscience, 2004

[56] L. J. Van der Pauw, Philips Technical Review, 26, (1958) 220

[57] L. J. van der Pauw, Philips Res. Rep. 13(1958) 1

[58] O. Lindberg, Proc. of IRE, (1952) 1414

[59] J. R. Mc Donald, Impedance Spectroscopy, John Wiley & Sons, New York (1987)

[60] K. Kao, Dielectric phenomena in solids, Elsevier Academic Press, 2004

[61] M. H. Hebb, J. Chem. Phys. 20 (1952)185

[62] C. Wagner, Z. Elektrochem. 4 (1956) 60

[63] M. Prudenziali, Thick film sensors, Elseveir, Tokyo (1994)

[64] W. Gopel, K.D. Schierbaum, Sensors andActuators B, 26 (1995) 1

[65] D. E. Williams, Solid state gas sensors, P.T. Moseley, B.C. Tofield Editors. Adam Hilger, USA, (1987)

[66] G. Korocenkov, B.K. Cho, Sensors and Actuators B, 156(2011) 527

[67] H. Meixner, J. Gerblinger, U. Lampe, M. Fleischer, Sensors and Actuators B, 23 (1995) 119

[68] G. Sberveglieri, Sensors and Actuators B, 23 (1995) 103

[69] N. Barsan, D. Koziej, U. Weimar, Sensors and Actuators B, 121(2007) 18

[70] K.Wetchakuna, T. Samerjaia, N. Tamaekonga, C. Liewhirana, C. Siriwonga, V. Kruefua, A.Wisitsoraatb, A. Tuantranontb, S. Phanichphanta, Sensors and Actuators B, 160 (2011) 580

[71] G. Korotcenkova, V. Brinzaria, J. R. Stetterb, Iuri Blinova, V. Blajaa, Sensors and Actuators B, 128, (2007) 51

[72] Y.Shimizu, M.Egashira, MRS Bulletin, 24 (1999) 18

[73] C. Shekhar, K.I. Gnanasekar, E. Prabhu, V. Jayaraman, T. Gnanasekaran, Sensor & Actuators B, 155 (2011) 19

[74] D. R. Lide, Hand Book of Chemistry and Physics, CRC Press, (2003 – 2004)

[75] A. Opera, E. Moretton, N. Barsan, W.J. Becker, J. Wollenstin et.al Jrl. Applied Physics, 100, (2006) 033716

[76] T. Bielz, H. Lorenz, W. Jochum, R. Kaindl, F. Klauser, B. Klotzer, S. Penner, J. Phys. Chem. C, 114 (2010) 9022

[77] H. S. Kim, H. G. Na, J. C. Yang, C. Lee, and H. W. Kim, Acta Phys. Pol. A, 119 (2011) 143

[78] M. Lubbe, A. M. Gigler, R. W. Stark, W. Moritz, Surface Science, 604 (2010) 679

[79] J. Laane. J.R. Ohlsen, Prog. Inorganic Chem., L3 (1978) 465

[80] N. Sergent, M. Epifani, T. Pagnier, J. Raman Spec. 37 (2006) 1272

[81] K. Nakamoto, Infrared and Raman Spectra of inorganic and coordination compounds, John Wiley & Sons, New York, (1986)

[82] N. N. Greenwood, A. Earnshaw, Chemistry of Elements, 2nd ed., Butterworths/Heinemann, Oxford, (1998)

[83] H. Tsukahara, T. Ishida, M. Mayumi, Nitric Oxide, 3 (1999) 191

[84] C. N. Hinshelwood, The Kinetics of Chemical Change, Oxford press, (1940)

[85] O. Knacke, O. Kubaschewski and K. Hesselmann, Thermochemical properties of Inorganic substances, 2dn edition, Springer – Virlag (1991)

[86] H. Ogawa, M. Nishikawa and A. Abe, J. Appl. Phys. 53 (1982) 4448

[87] L. Chen and S. Chi Tsang, Sensors and Actuators B, 89 (2003) 68

[88] N. R. Hill, W. E. Vaughan, A. H. Price, M. Davies, Dielectric Properties and Molecular Behavior, Van Nostrand Reinhold Company, London, 1969

[89] M. Seitz, F. Hampton, W. Richmond, M.F. Yan, A.H. Heuer, Advanced in Ceramics, 7, The American Ceramic Society Inc. Ohio, (1983)

[90] M. A. Ponce, C. M. Aldao, M. S. Castro, Materials Science and Engineering B, 123 (2005) 130

[91] X. Zhou, J. Li, Ming Ma, Q. Xue, Physica E (2011) 1056

[92] A. Gurlo, N. Barsan, M. Ivanovskaya, U, Weimar, Gopel, Sensors and Actuators B, 47(1998) 92

[93] C. M. Gonsalez, X. Du, J. L. Dunford, M.L. Post, Sensors and Actuators B, 173 (2012) 169

[94] A. Gurlo, M. Ivanovskaya, N. Barsan, M. Schweizer-Berberich, U. Weimar, W. Gopel, A. Dieguez, Sensors and Actuators B, 44 (1997) 327

[95] Chia-Yu Line, Yueh-Yuan Fang, Chii-Wann Lin, James J. Tunney, Kuo-Chuan Ho, Sensors and Actuators B, 146 (2010) 28

[96] H. Kawazoe, M. Yasukawa, H. Hydo, M. Kurita, H. Yanagi, Hideo Hosono, Nature, 389 (1997) 939

[97] A. N. Banerjee, K.K. Chattopadhyay, Progress in crystal growth and characterization of materials, 50 (2005) 52

[98] V. Jayalakshmi, R. Murugan, Balan Palanivel, J. of alloys and compounds, 388 (2005) 19

[99] H. Ohta, K. Nomura, H. Hiramatsu, K. Ueda, T. Kamiya, M. Hirano, H. Hosono, Solid state electronics, 47 (2003) 2261

[100] H. Kawazoe, H. Yanagi, K. Ueda, H. Ozono, MRS Bulletin, 25 (2000) 28

[101] S. Park and D. A. Keszler, J. of solid state chemistry, 173 (2003) 355

[102] X. Nie, S. Wei and S. B. Zhang, Physical Review Letters, (2002) 066405

[103] H. Yanagi, T. Hase, S. Ibuki, K. Ueda, H. Hosono, Applied Physics Letters, 78 (2001)1583

[104] M. A. Marquardt, N. A. Ashmore, D. P. Cann, Thin Solid Films, 496 (2006) 146

[105] J.C. Lee, Y.W. Heo, J.H. Lee, J.J. Kim, Thin Solid Films, 518 (2009) 1234

[106] O. Garlea, P. Bordet, C. Darie, O. Isnard, R. Ballou, J. Phys. Cond. Matter, 16 (2004) S811

[107] Y. Yao, G. Xie, N.Song, X. Yu and R. Li, Advanced Materials Research, 399 – 401 (2012) 2241

[108] C. W. Teplin, T. Kaydanova, D. L. Young, J.D. Perkins and D.S. Ginley, App. Phy. Letters, 85 (2004) 3789

[109] A. V. Chadwick, A. N. Blacklocks, A. Rougier and C. Yaicle, J. of Physics: Conference Series, 249 (2010) 1

[110] F. Guinneton, O. Monnereau, L. Argeme, D. Stanoi, G. Socol, I.N. Mihailescu, T. Zhang, C. Grigorescu, H.J. Trodahl, L. Tortet, Applied Surface Science, 247 (2005) 139

[111] W. H. Ho, C. F. Li, H. C. Liu, S. K. Yen, J. of Power Sources, 175 (2008) 897

[112] M. Campagna, Rev. Phys. Lett, 34 (1975) 738

[113] Y. Zhang, Z. Liu, D. Zang, L. Feng, Vacuum, 99 (2014) 160

[114] T. H. Fleisch, G. J. Mains, Applications of surface science, 10 (1982) 51

[115] N. Yamazoe and N. Miura in Chemical Sensor Technology, Vol. 4, S. Yamauchi, Editor, Kodansha, Tokyo (1992)

[116] A. Gurlo, N. Barsan, M. Ivanovskaya, U. Weimar, W. Gopel, Sensors and Actuators B, 47 (1998) 92

[117] E. Prabhu, V. Jayaraman, K.I. Gnanasekar, T. Gnanasekaran and G. Periaswami, Asian, J. Phys. 14 (2005) 33

[118] S. Yun and S.T. Oyama, J. Membran Science, 375 (2011) 28

[119] D. P. Smith, Hydrogen in Metals, University of Chicago Press, Chicago, 1948

[120] T. B. Massalski, Binary Alloy Phase Diagram, ASM International, 1990, USA

[121] W. M. Muller, J.P. Blackledge, G.G. Libowitz, Metal Hydrides, Academic Press, New York, 1967

[122] J. S. Galsin, Impurity scattering in metallic alloys, 2002, Punjab Agricultural University, India

[123] T. Mutschele and R. Kirchheim, Scripta Metallurgica, 21 (1987) 1101

[124] J. A. Eastman, L.J. Thompson and B. J. Kestel, Physcial Review B, 48 (1993) 84

[125] M. Yamauchi, R. Ikeda, H. Kitagawa and M. Takata, J. Phys. Chem. C, 112 (2008) 3294

[126] B. D. Adams, A. Chen, Materials Today, 14 (2011) 282

[127] M. Yamauchi, H. Kobayashi and H. Kitagawa, ChemPhysChem, 10 (2009) 2566

[128] M. Shamsuddin, J. Less common metals, 154 (1989) 285

[129] W. G. Moffertt, The Handbook of Binary Phase Diagrams, Genium Publishing Corp. 1979, USA

[130] Z. G. Wu, M. Munoz, O. Montero, Adv. Powder Tech. 21 (2010) 165

[131] J. W. Park, E.H. Chae, S.H. Kim, J.H.Lee, J.W.Kim, S.M. Yoon, J.Y. Choi, Mat. Chem. and Phy. 97 (2006) 371

[132] Y. Chen, K.Y. Liew, J. Li, Applied Surface Science, 255 (2009) 4039

[133] R. C. Hughes, W.K. Schubert, T.E. Zipperian, J.L. Rodriguez and T.A. Plut, J. Appl. Phys. 62 (1987) 1074

[134] R. C. Hughes, W.K. Schubert and R.J. Buss, J. Electrochem. Soc. 142 (1995) 249

[135] J. H. Yoon, B. Joon, J.S. Kim, Mat. Chem. and Phys. 133 (2012) 987

[136] E. Lee, J.M. Lee, E. Lee, J.S. Noh, J.H. Joe, B. Jung, W. Lee, Thin Solid Films, 519 (2010) 880

[137] D. J. Lee, J. Park, H.S. Kim, D.H. Lee, M. Park, H. Chang, J.H. Jin, J.R. Sohn, K. Heo and B.Y. Lee, Sensors and Actuators B, 216 (2015) 482

[138] F. Rigoni, G. Drera, S. Pagliara, A. Goldoni, L. Sangaletti, Carbon, 80 (2014) 356

[139] H. J. Kim, J.H. Lee, Sensors and Actuators B, 192 (2014) 607

[140] N. Ramgir, N. Datta, M. Kaur, S. Kailasaganapathi, A.K. Debnath, D.K. Aswal, S.K. Gupta, Colloids and Surfaces A: Physicochem. Eng. Aspects, 439 (2013) 101

[141] B. Renganathan, D. Sastikumar, G. Gobi, N.R. Yogamlar, A.C. Bose, Optics and Laser Technology, 43 (2011) 1398

[142] C. W. Lin, H. I. Chen, T.Y. Chen, C.C. Huang, C. S. Hsu, R.C. Liu, W.C. Liu, Sensors and Actuators B, 160 (2011) 1481

[143] V. Bhasker Raj, A.T. Nimal, Yashoda Parmar, M.U. Sharma, K. Sreenivas, Vinay Gupta, Sensors and Actuators B, 147 (2010) 517

[144] T. Nagai, S. Tamura, N. Imanaka, Sensors and Actuators B, 147 (2010) 735

[145] W. Y. Weng, S. J. Chang, T. J. Hsueh, C. L. Hsu, M. J. Li, W. C. Lai, Sensors and Actuators B, 140 (2009) 139

[146] J. Huang, J. Wang, C. Gu, K. Yu, F. Meng, J. Liu, Sensors and Actuators A, 150 (2009) 218

[147] B. Timmer, W. Olthuis, A. v. d. Berg, Sensors and Actuators B, 107 (2005) 666

[148] R. S. Gates, H. Xin, K.D. Casey, Y. Liang, E.F. Wheeler, J. Applied Polutry, Resource, 14(2005) 622

[149] A. Jerger, H. Kohler, F. Becker, H.B. Keller, R. Seifert, Sensors and Actuators B, 81 (2002) 301

[150] E. Prabhu, S. Muthuraja, K.I. Gnanasekar, V. Jayaraman, S. Sivabalan and T. Gnanasekaran, Surface Engineering, 24 (2008) 170

[151] S. S. Sunu, V. Jayaraman, E. Prabhu, K.I. Gnanasekar and T. Gnanasekaran, Ionics, 6 (2000) 244

[152] B. M. Gatehouse and P. Leverett, J. Solid State Chemistry, 1 (1970) 484

[153] C. Rosner and G. Lagaly, J. Solid State Chemistry, 53 (1984) 92

[154] M. Miyayama, K. Hikita, G. Uozumi and H. Yanagida, Sensors and Actuators B, 24 – 25 (1995) 383

[155] M. E. H. Amrani, P.A. Payne, K.R. Persaud, Sensors and Actuators B, 33 (1996) 137

[156] P. Lauque, J.M. Laugier, C. Jacoline, M. Bendahan, C. Lemire and P. Knauth, Sensors and Actuators B, 87 (2002) 421

[157] M. Kaur, S.K. Gupta, C.A. Betty, V. Saxena, V.R. Katti, S.C. Gadkari and J.V. Yakhmi, Sensors and Actuators B 107 (2005) 360

[158] S.S. Sunu, PhD. Thesis, University of Madras (2004)

[159] J. I. Goldstein, D.E. Newbury, Scanning Electron Microscopy and X-ray Microanalysis, Springer, New York (2003)

[160] E.S. Snow, F.K. Perkins, E.J. Houser, S.C. Badescu and T.L. Reinecke, Science, 307 (2005) 1942

[161] E.S. Snow and F.K. Perkins, Nano Letters, 5 (2005) 2414

[162] F. L. Meng, L. Zhang, Y. Jia, J. Liu, Y. Sun, T. Luo, M. Li, Sensors and Actuators B, 153 (2011) 103

APPENDIX – 1

Characterization of nano-powders of Pd and its alloys prepared by low temperature chemical reduction (LTCR) method

The characterization of powders of Pd, $Pd_{0.97}Ni_{0.03}$, $Pd_{0.93}Ni_{0.07}$ and $Pd_{0.91}Ni_{0.04}Co_{0.05}$ synthesized through LTCR method is discussed in this section. Figure A1.1a shows the XRD pattern for the nickel powder prepared by reducing nickel II acetate tetrahydrate (dissolved in ethanol) in acetone using sodium borohydride at 300 K. The 2θ peak at 44.43 is characteristic reflection corresponding to (111) plane of nickel. Figure A1.1b and A1.1c show the XRD patterns of these nickel powders heated at 473 K and 673 K respectively in vacuum of 2.0×10^{-5} mbar. The 2θ positions at 44.43, 51.93 and 76.36 correspond to the reflections of cubic system of nickel (JCPDS No. 04-0850, Symmetry; Space Group; Fm3m (225)). These results show that the nickel powder prepared by LTCR method crystallizes and heated at 673 K under vacuum exists in cubic phase only.

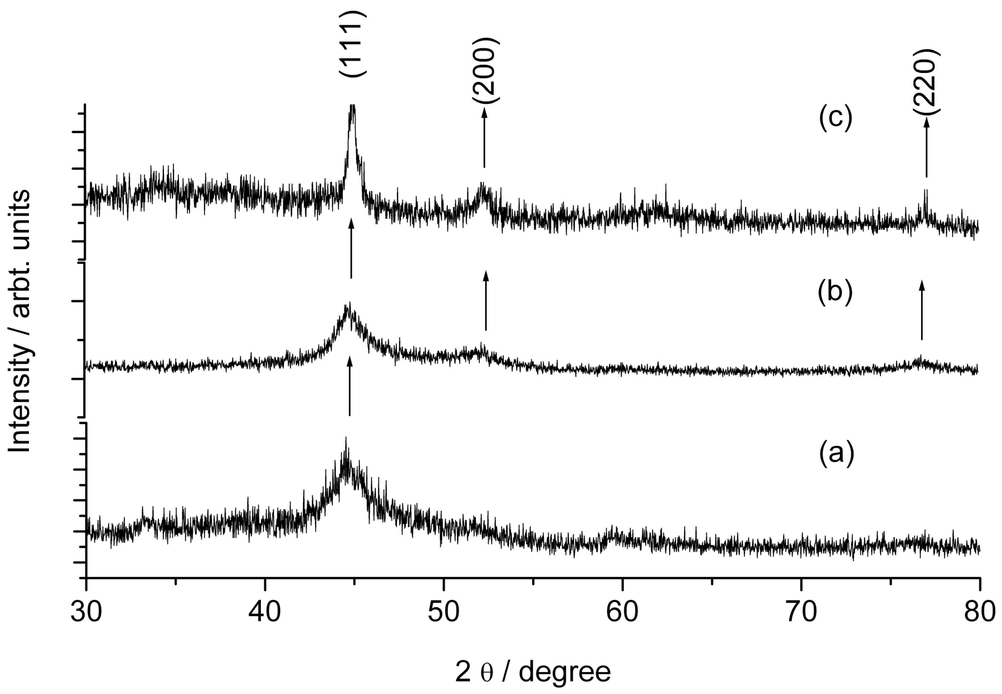

Fig. A1.1 X-ray diffraction pattern of nickel powder; a) as synthesized at 300 K and b) heated at 473 K under vacuum (2 X 10^{-5} mbar) & c) heat at 673 K under vacuum (2 X 10^{-5} mbar)

Figure A1.2a to c show the XRD patterns of the powders of palladium, $Pd_{0.97}Ni_{0.03}$ and $Pd_{0.93}Ni_{0.07}$ synthesized at 300 K. Peaks in XRD pattern shown in fig. A1.2a are broadened are assigned with the characteristic reflections of (111), (200) and (220) of palladium (JCPDS No. 46-1043, Symmetry; cubic, Space Group; Fm3m(225)). XRD patterns of the alloys shown in figures A1.2b and A1.2c do not contain any reflection due to impurity nickel. This shows nickel forms a substitution solid solution with Pd in the composition ranges studied.

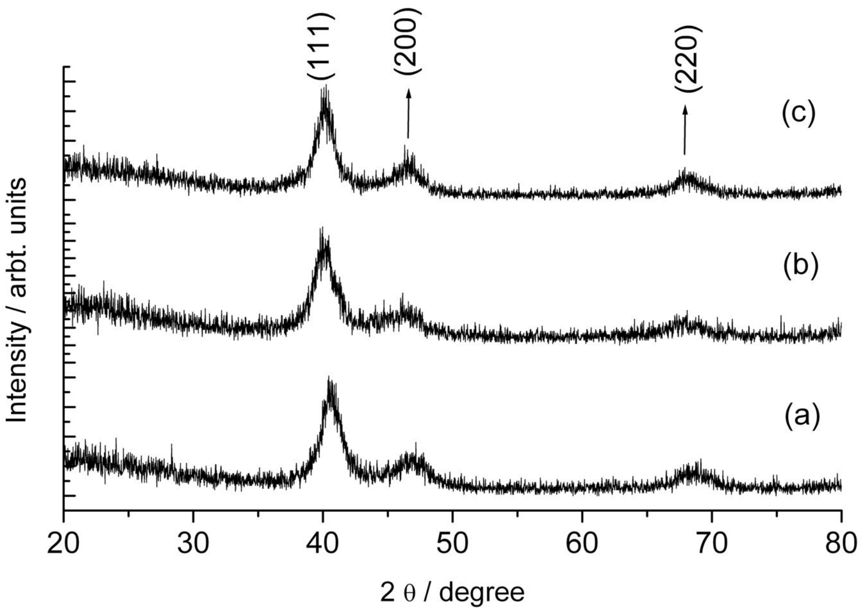

Fig. A1.2 X-ray diffraction pattern of a) Pd, b) $Pd_{0.97}Ni_{0.03}$, and c) $Pd_{0.93}Ni_{0.07}$ powder synthesized at 300 K

Figure A1.3a shows the XRD pattern of cobalt powder synthesized at 300 K. As seen from the pattern, the synthesized powder is amorphous in nature. When this amorphous powder heated in vacuum (2 X 10^{-5} mbar) at 673 K for 4 h, amorphous nature retained (fig. A1.3b). Figure A1.3c shows the XRD patterns of the alloy of composition $Pd_{0.91}Ni_{0.04}Co_{0.05}$ synthesized at 300 K. The pattern show the characteristic reflections of cubic phase of palladium (JCPDS No. 46-1043) and has no reflections corresponding to nickel and cobalt.

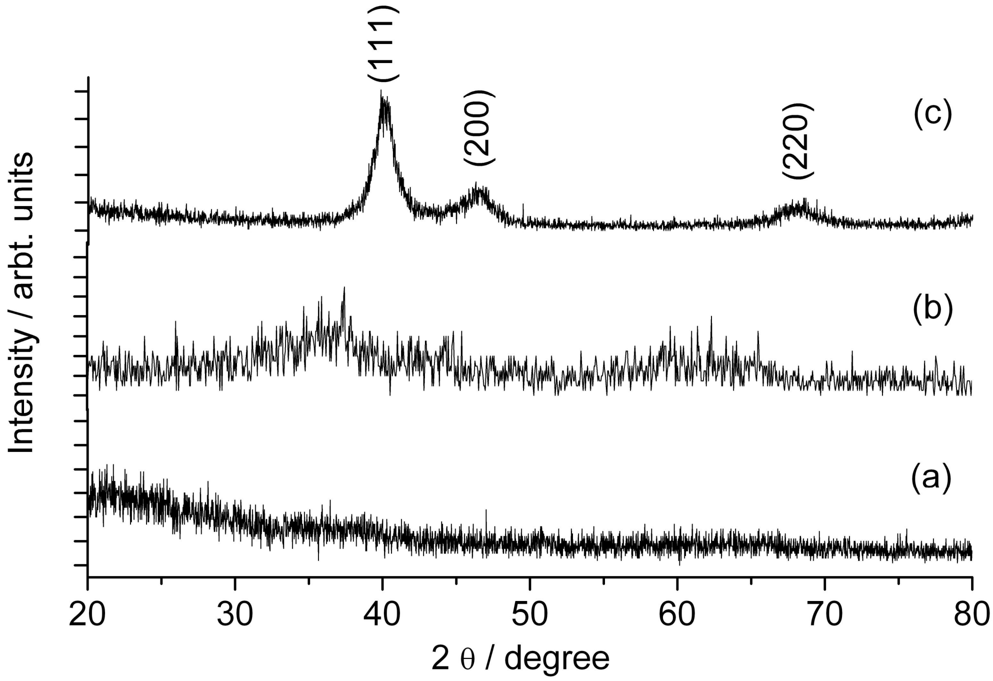

Fig. A1.3 X-ray diffraction pattern of cobalt synthesized at a) 300 K, b) heated in vacuum (2 X 10^{-5} mbar) at 673 K and c) $Pd_{0.91}Ni_{0.04}Co_{0.05}$ powder synthesized at 300 K.

The sizes of the crystallite of the powders of Pd, $Pd_{0.97}Ni_{0.03}$, $Pd_{0.93}Ni_{0.07}$ and $Pd_{0.91}Ni_{0.04}Co_{0.05}$ powders synthesized using LTCR technique at 300 K were estimated using peak broadening of the XRD reflections of the samples. The crystallite size was calculated using the Scherrer equation shown in eqn. A1.1. Here, 'D' is the crystallite size in 'Å', 'K' is the Scherrer constant (shape factor), 'λ' is X- ray (CuK_{α}) wavelength in 'Å' and 'β_{hkl}' is the measured line broadening of the sample. Many factors contributed to XRD peak broadening: (i) crystallite size, (ii) micro strain of the sample and (iii) due to instrumental broadening. The difference between the peak width (FWHM) of the sample (measured) and peak width of the instrument (measured) will give the contribution of crystallite size and micro strain to the peak broadening (eqn A1.2). The instrumental peak broadening was calculated using the Cagliotti equation given in eqn. A1.3. Here $H_{k,}$ is Cagliotti fit function (FWHM of standard silicon powder), U, V and W are refinable parameters. Figure A1.4 shows the plot of 2θ (degrees) versus peak width profile for the NIST silicon standard powder. The crystallite size ‘D’ was calculated using eqn. A1.1 and strain ‘ε’ (eqn. A1.4) by substituting β_{hkl} of the sample obtained from eqn. A1.2.

$$D = \frac{K\lambda}{\beta_{hkl}\mathrm{Cos}\theta} \tag{A1.1}$$

$$\beta_{hkl} = \left[(\beta_{hkl})^2_{measured} - (\beta_{hkl})^2_{Instrumental}\right]^2 \tag{A1.2}$$

$$H_k = \left(U\tan^2\theta + V\tan\theta + W\right)^{\frac{1}{2}} \tag{A1.3}$$

$$\varepsilon = \frac{\beta_{hkl}}{4\tan\theta} \tag{A1.4}$$

The crystallite size and strain of palladium, $Pd_{0.97}Ni_{0.03}$, $Pd_{0.93}Ni_{0.07}$ and $Pd_{0.91}Ni_{0.04}Co_{0.05}$ were calculated and are shown in Table A1.1. The results show that nanoalloys with average crystallite size in the region of 5 – 8 nm at 300 K with strain limit of < 1.5% can be synthesized using low temperature chemical reduction technique.

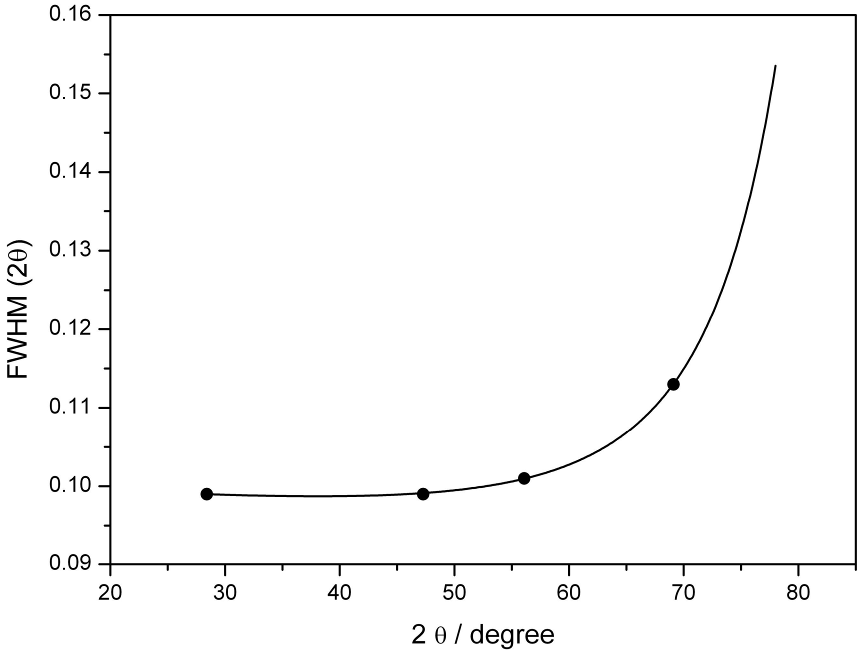

Fig. A1.4 Plot showing 2θ versus peak width for the NIST standard silicon powder and profile obeys Cagliotti function.

Table: A1.1

Calculated crystallite size and micro-strain values of palladium and its alloys synthesized at 300 K

Atomic % of element in Pd		Average crystallite Size (nm) (Tolerance: ± 0.1)	Strain %
Ni	Co		
0	0	7.7	< 1.0
0.03	0	6.5	< 1.0
0.07	0	7.1	< 1.0
0.04	0.05	5.9	<1.5

Figures A1.5a to d show the XRD pattern of Pd, $Pd_{0.97}Ni_{0.03}$, $Pd_{0.93}Ni_{0.07}$ and $Pd_{0.91}Ni_{0.04}Co_{0.05}$ heated in vacuum at 673 K. All the patterns match well with the cubic phase of Pd (JCPDS No. 46-1043). As seen from the figure, peak positions in the alloy gradually shift to higher 2θ when Ni concentration in the alloy increases. Similar shift in 2θ value is also seen in the case of $Pd_{0.91}Ni_{0.04}Co_{0.05}$. The lattice constants of the alloys were calculated and are shown in Table A1.2. Data in the table show a decrease in the lattice constant of the alloys and is due to incorporation of nickel atom of smaller size (metallic radii: 124 pm) and cobalt (126 pm) into palladium lattice (139 pm). Lee et al reported a similar shift in 2θ position with increase in nickel substitution in palladium [1].

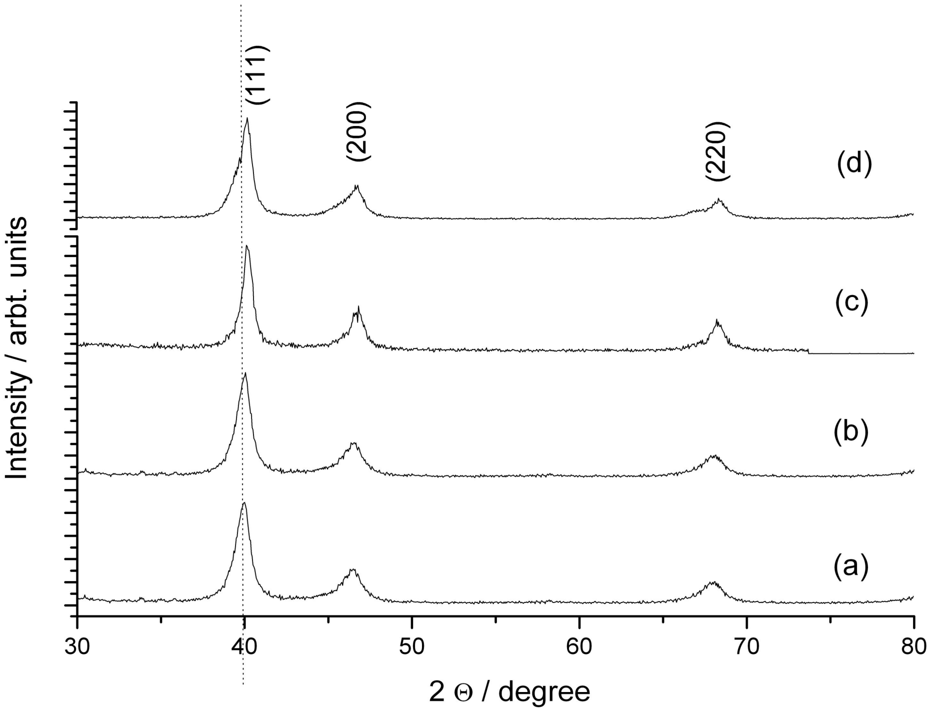

Fig. A1.5 X-ray diffraction pattern of a) Pd, b) $Pd_{0.97}Ni_{0.03}$, c) $Pd_{0.93}Ni_{0.07}$ and d) $Pd_{0.91}Ni_{0.04}Co_{0.05}$ powder heated in vacuum at 673 K

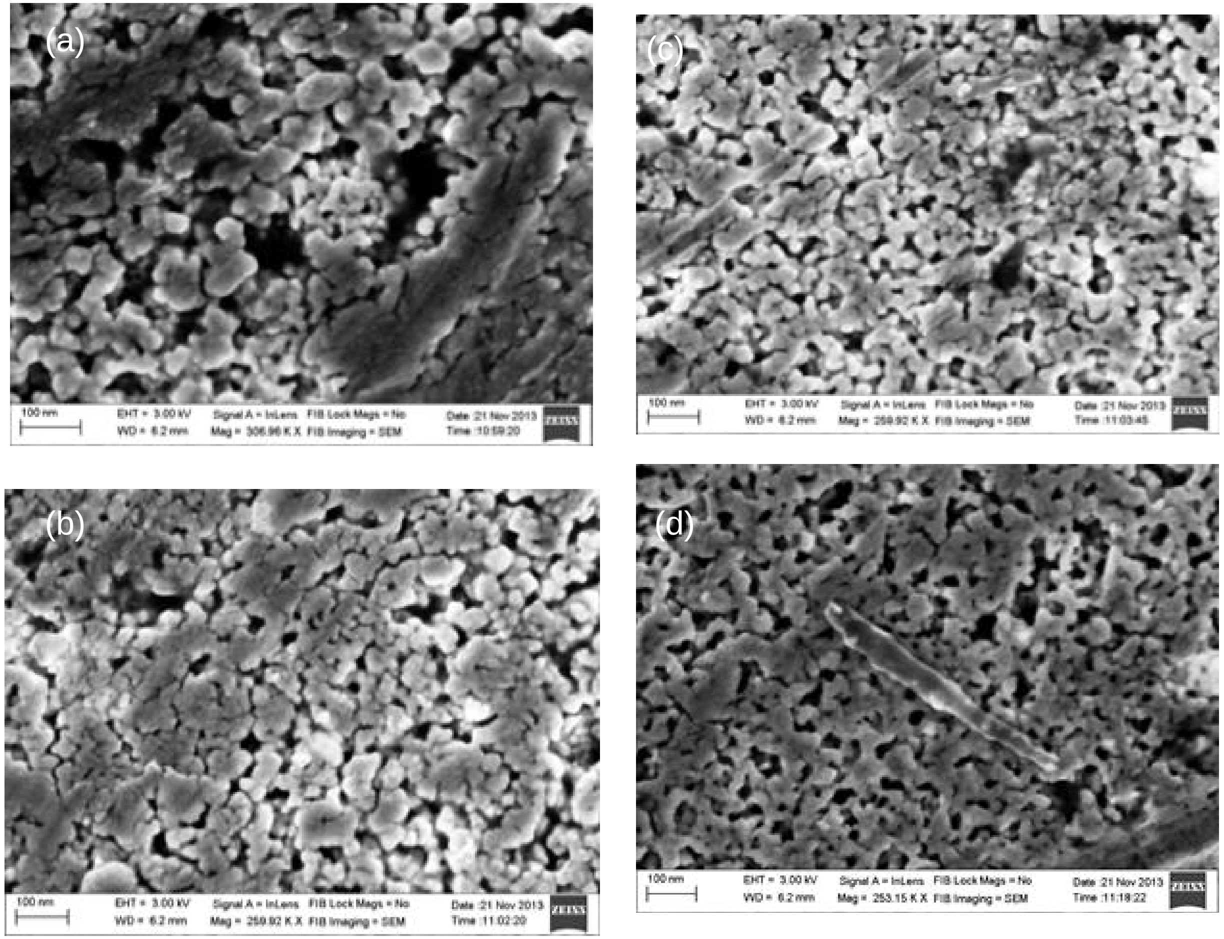

Fig. A1.6 SEM image of a) Pd, b) $Pd_{0.97}Ni_{0.03}$, c) $Pd_{0.93}Ni_{0.07}$ and d) $Pd_{0.91}Ni_{0.04}Co_{0.05}$ heated in vacuum at 673 K.

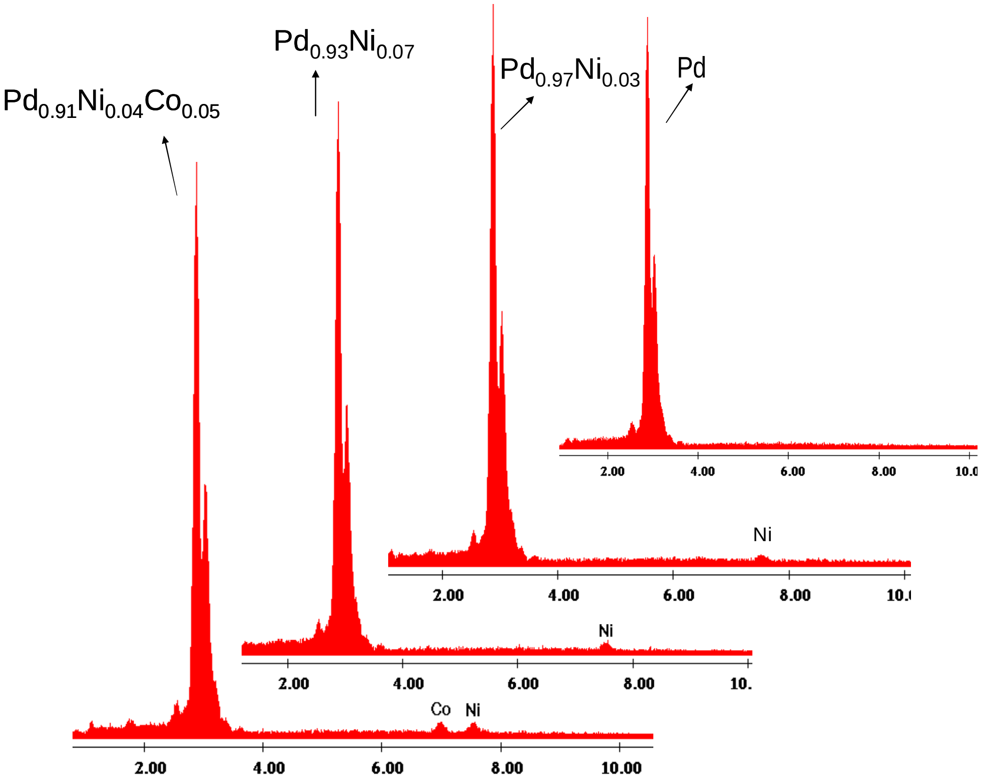

Fig. A1.7 EDX analysis of a) Pd, b) $Pd_{0.97}Ni_{0.03}$, c) $Pd_{0.93}Ni_{0.07}$ and d) $Pd_{0.91}Ni_{0.04}Co_{0.05}$ heated in vacuum at 673 K.

Table: A1.2

Lattice constant change due to incorporation of nickel and cobalt in palladium

Composition at 673 K	Lattice constant (Å) (Error : ± 0.002 Å)
Pd	3.901
$Pd_{0.97}Ni_{0.03}$	3.894
$Pd_{0.93}Ni_{0.07}$	3.885
$Pd_{0.91}Ni_{0.04}Co_{0.05}$	3.873

Figures A1.6a to d show the SEM images of powders of Pd, $Pd_{0.97}Ni_{0.03}$, $Pd_{0.93}Ni_{0.07}$ and $Pd_{0.91}Ni_{0.04}Co_{0.05}$ heated at 673 K in vacuum of 2 X 10^{-5} mbar. As seen from the figure, the surface is a porous network with an average grain size of 20 – 30 nm. Scans at few locations of the samples showed the presence of nanotubes or nanorods with the dimensions of 300 X 10 nm. Figures A1.7a to d show the results of EDX analysis of Pd, $Pd_{0.97}Ni_{0.03}$, $Pd_{0.93}Ni_{0.07}$ and $Pd_{0.91}Ni_{0.04}Co_{0.05}$, analysis elucidate the presence of nickel and cobalt in the alloys.

References

1. E. Lee, J.M. Lee, E. Lee, J.S. Noh, J.H. Joe, B. Jung, W. Lee, Thin Solid Films, 519 (2010) 880